Physics of Polariton Condensates in GaN-based Planar Microcavities

THÈSE N^{O} 5449 (2012)

PRÉSENTÉE LE 14 SEPTEMBRE 2012

À LA FACULTÉ DES SCIENCES DE BASE

LABORATOIRE EN SEMICONDUCTEURS AVANCÉS POUR LA PHOTONIQUE ET L'ÉLECTRONIQUE

PROGRAMME DOCTORAL EN PHOTONIQUE

ÉCOLE POLYTECHNIQUE FÉDÉRALE DE LAUSANNE

POUR L'OBTENTION DU GRADE DE DOCTEUR ÈS SCIENCES

PAR

Jacques LEVRAT

acceptée sur proposition du jury:

Prof. C. Moser, président du jury
Prof. N. Grandjean, directeur de thèse
Prof. B. Deveaud-Plédran, rapporteur
Prof. J. Faist, rapporteur
Prof. D. Le Si, rapporteur

ÉCOLE POLYTECHNIQUE
FÉDÉRALE DE LAUSANNE

Suisse
2012

Le savant n'est pas l'homme qui fournit les vraies réponses;
c'est celui qui pose les vraies questions.
— Claude Lévi-Strauss, *Le Cru et le Cuit* (1964)

À mes parents, Canisia et Michel…

À ma future épouse Bruna…

Remerciements

En premier lieu, je souhaite remercier mon directeur de thèse Nicolas Grandjean pour m'avoir donné l'occasion et la confiance de mener mes projets à ma guise pendant ces quatre années au LASPE. J'ai beaucoup apprécié nos discussions, que ce soit de physique - domaine dans lequel sa curiosité et son imagination débordante m'ont permis d'avancer dans de nouvelles directions - ou d'autres sujets parmi lesquels il faut citer les confrontations culturelles franco-suisses, animées mais très amusantes.

Ensuite, je voudrais remercier Christophe Moser pour avoir accepté la responsabilité de présider mon jury de thèse ainsi que tous les membres qui ont eu la lourde tâche de lire et juger le travail présenté dans ce manuscrit: Dang Le Si, Jérôme Faist et Benoît Deveaud.

Avant de commencer ce travail, j'ai eu le plaisir de faire mon stage de master avec Pierre Corfdir, un grand ami que je tiens à remercier tout spécialement ici car durant les années qui ont suivi, nous avons eu l'occasion de collaborer à plusieurs reprises dans une atmosphère vraiment agréable, sans oublier - bien sûr - l'*after work*. Mon travail de thèse a démarré avec la précieuse aide de Gabriel Christman dont les travaux antérieurs ont fondé les bases de cette thèse et avec qui j'ai passé de très bons moments, donc merci *Dr. Gab* ! Deux ans plus tard, j'ai eu l'immense plaisir de pouvoir travailler avec Georg Rossbach, un allemand qui réside - selui lui - pile au centre de masse de l'Allemagne. Je tiens à lui rendre honneur ici car notre collaboration fut très fructueuse tant scientifiquement qu'humainement. *So, danke sehr mein Freund! Ich habe es wirklich geschätzt mit dir zu arbeiten, schwatzen, (Motor)rad fahren, delikate Getränke trinken, Würstchen am Strand grillen, Backstageieren, USW. (zufällige Reihenfolge...)*. Je tiens également à remercier ici mon ami, collègue de bureau et companion de galère durant mes études et pendant l'assistanat, Gatien Cosendey, sur qui j'ai toujours pu compter - au travail et en dehors (e.g. les innombrables heures pour l'assistanat - que du bonheur!).

Merci également à Raphaël Butté qui a suivi mon travail, m'a soutenu durant toutes ces années et a toujours été disponible à chaque fois que j'avais besoin d'aide, pour quoi que ce soit. Merci pour les innombrables discussions (scientifiques et autres) et les nombreuses corrections d'articles/présentations que tu as effectuées avec beaucoup d'application (et de rouge...) et grâce à quoi j'ai appris la rigueur de la rédaction scientifique. Il y a encore tellement de personnes à qui je dois rendre honneur ici pour les précieuses discussions scientifiques que j'ai pu avoir durant ces dernières années et en particulier Benoît Deveaud, Jean-Daniel Ganière, Pierre Lefebvre et Vincenzo Savona. Sans oublier bien sûr nos fantastiques croisseurs sans qui je n'aurais pas pu regarder des échantillons aussi intéressants : Jean-François Carlin et Eric Feltin pour la MOCVDE et Amélie Dussaigne pour la MBE.

Merci à tous les gens du labo dans lequel règne une atmosphère vraiment fantastique, que ce soit pour le travail (diverses collaborations) ou pour les sorties - planifiées ou improvisées - en ville, au bord du lac, en montagne, sur la terrasse,... J'en garderai un souvenir impérissable. Donc merci Georg, Gatien, Nicolas, Raphaël, Eric, Nino, Etienne, Munise, Marco R., Marco M., Lorenzo, Marlene, Jean-Mi, Julien, Nils, Alexey, Luca, Noelia, Lise, Yoshi, Marcel, Jean-François, Guillaume et Jérôme, sans oublier ceux qui sont partis en cours de route: Gab, Dob, Sylvain, Amélie, Marcus, Arnaud, Tiankai et Rémy. Merci également à Aline, notre fidèle secrétaire qui m'a sorti du pétrin bien des fois (sans oublier Oana), à Roger Rochat, notre mécano génial sans qui monter une manip aurait été un vrai parcours du combattant ainsi qu'à Nicolas Leiser et aux frères Trolliet (salle blanche). Merci aussi à tous mes amis proches qui ont vécu (indirectement) cette expérience avec moi: Marc & Myriam, Pierre & Kim, Sam & Séverine, Patrick l'Irlandais, Valinou & Pauline, Réjane & Christian, Laura & Mathieu, Laurent & Nathalie... et à tous ce que j'oublie!

Je voudrais encore remercier tout spécialement ma famille, en particulier mes parents Canisia et Michel qui m'ont apporté un soutien permanent et sans qui je ne serais jamais parvenu jusqu'ici, ainsi que ma soeur Marie-Noëlle et mes deux frères, Emmanuel et Sébastien, sur qui j'ai toujours pu compter. Enfin, *last but not least*, un énorme merci à ma petite amie et - au moment où j'écris ces lignes - future épouse, qui a su supporter mes humeurs, parfois bonnes mais souvent aussi mauvaises, et a toujours été là pour moi. Donc merci Bruna! Tu as su mieux que quiconque m'accompagner dans cette aventure et je me réjouis de faire le reste de la route avec toi...

Lausanne, le 23 Juillet 2012 J. L.

Abstract

Since its prediction in 1996 by Imamoğlu and coworkers, the use of a non-equilibrium polariton condensate to produce an intense coherent light source referred to as a polariton laser has attracted a lot of interest in the whole physics community as it should allow the realization of ultralow threshold coherent light-emitting devices due to the release of the Bernard-Duraffourg condition. Excitons-polaritons, admixed particles resulting from the strong coupling between a cavity photon and an exciton, are the eigenmodes of a strongly coupled microcavity and exhibit a very light effective mass at the center of the Brillouin zone (10^5 times lighter that a free electron) inherited from the cavity photon. In the present work, we are interested in III-nitride based microcavities embedding GaN quantum wells in the active region. Thanks to the stability of the excitons at room temperature in this system and a large oscillator strength, polariton condensation has been observed up to 340 K under optical excitation, paving the way toward the realization of the first electrically injected polariton laser.

The goal of the present study is to provide a detailed analysis of the system properties accounting for nitride specificities, to describe the mechanisms leading to the formation of polariton condensates and to give the key elements for the optimization of devices relying on polariton nonlinearities. For this purpose, a Fourier-imaging setup allowing for the simultaneous monitoring of real space and far-field energy dispersions was carefully designed to operate in the UV spectral range in order to probe the sample emission at various temperatures.
The first main result of this thesis is the establishment of the complete polariton phase diagram of our multiple quantum well-based GaN microcavity, which provides a comprehensive tool to favor or inhibit the condensation threshold by adjusting the microcavity parameters. The condensation is shown to be governed either by the kinetics or by the thermodynamics depending on the strength of the interactions. As polaritons are half-light, half-matter particles, the mechanisms leading to the nonlinear threshold are totally different from those of a conventional semiconductor laser. In particular, the possibility to tune the interactions in the system by changing the photonic fraction of the polaritons or the lattice temperature allows discriminating between different relaxation regimes.
Then the spin of the polariton condensate is discussed. It is shown that the dimensionality of the system plays a major role in the polarization state of the emitted light. In particular above threshold, for a bulk microcavity, the polarization is randomly oriented whereas for a GaN multiple quantum well based microcavity, the polarization is pinned by the system anisotropy originating from the static disorder. With increasing pumping power, a depinning of the polarization is observed resulting in a progressive decrease in the polarization degree of the emitted light. These two results are well accounted for by a stochastic model of the condensate formation taking into account the in-plane anisotropy caused by the stationary photonic disorder, the self-induced Larmor precession of the condensate pseudospin and the interplay between energy and polarization relaxation rates.

In the last part of this work, the case of nonpolar m-plane GaN based microcavities is addressed. In these structures, the optical axis lies in the plane of the cavity leading to a twofold anisotropy: the birefringence is responsible for the anisotropy of the cavity mode and the distribution of the exciton oscillator strength causes different coupling constants between light and matter along the two orthogonal directions. In such structures different selection rules and optical constants for light polarization perpendicular and parallel to the optical axis can lead to the coexistence of weak and strong coupling regimes with a transition to nonlinear emissions.

Key words: Gallium nitride, III-nitrides, microcavities, polaritons, polariton condensate, strong coupling regime, polariton lasing, Bose-Einstein condensate, biexciton, polariton relaxation, phase diagram, thermodynamics, kinetics, polarization, in-plane disorder, pinning, order parameter, self-induced Larmor precession, nonpolar microcavities, anisotropic coupling regime, optical anisotropy.

Résumé

Depuis sa prédiction en 1996 par Imamoğlu *et al.*, l'utilisation d'un condensat de polaritons hors-équilibre afin de produire une source de lumière cohérente, appelée laser à polaritons, a suscité un vif intérêt dans l'ensemble de la communauté en physique. En effet,un tel dispositif ne nécessite pas de satisfaire la condition de Bernard-Duraffourg pour basculer vers le régime d'émission non-linéaire. Les polaritons excitoniques, particules composites résultant du couplage fort entre un photon de cavité et un exciton, sont les modes propres d'une microcavité opérant en régime de couplage fort. Ces quasi-particules ont la particularité de présenter une très faible masse effective au centre de la première zone de Brillouin (environ 10^5 fois plus légère que celle d'un électron libre) à cause de leur composante lumière. Dans cette thèse, nous allons nous intéresser à des microcavités à base de nitrures d'éléments III comportant des puits quantiques GaN dans la région active. Grâce à la stabilité et à la grande force d'oscillateur des excitons dans ce système, la condensation de polaritons a pu être observée jusqu'à 340 K sous excitation optique, ouvrant ainsi la voie vers la réalisation du premier laser à polaritons injecté électriquement.
Le but de cette étude est de fournir une analyse détaillée des propriétés du système en tenant compte des particularité des nitrures, de décrire les mécanismes conduisant à la formation d'un condensat de polaritons, et de donner les éléments-clés pour l'optimisation de dispositifs utilisant les nonlinéarités polaritoniques. Afin de servir ce but, un dispositif d'imagerie de Fourier permettant l'observation simultanée de l'espace réel et des courbes de dispersion en champ lointain a été élaborée. Le système a été conçu pour fonctionner dans la partie UV du spectre éléctromagnétique à différentes températures.
Le premier résultat important de cette thèse est l'établissement du diagramme de phase de notre microcavité à multi-puits quantiques GaN opérant en régime de couplage fort. Ce diagramme représente une description complète concernant la formation d'un condensat de polaritons en ajustant les paramètres du système. Nous montrons ainsi que la condensation est gouvernée soit par la cinétique, soit par la thermodynamique selon l'intensité des interactions mises en jeu dans le système. Comme les polaritons sont des particules moitié-lumière moitié-matière, les mécanismes conduisant au seuil laser sont totalement différents de ceux mis en œuvre dans un laser semiconducteur conventionnel. En particulier, la possibilité d'ajuster l'intensité des interactions en modifiant la composante photon des polaritons ou en changeant la température du réseau permet de faire basculer le système entre les différents régimes de relaxation.
Dans un deuxième temps, le spin du condensat de polariton est étudié. Il a été montré que la dimensionnalité du système joue un rôle important dans l'état de polarisation de la lumière émise. Au-dessus du seuil, cette polarisation est aléatoire pour une microcavité massive alors qu'elle est toujours orientée dans la même direction pour une microcavité à puits quantiques à cause du désordre statique. Lorsque la densité de porteurs injectés augmente, la lumière émise se dépolarise peu à peu. Ce résultat est expliqué grâce à un modèle décrivant la nature aléatoire de la formation du condensat de polaritons et la compétition entre différents phénomènes antagonistes. D'une part la relaxation énergétique tend à

amener le système vers un état d'énergie minimum polarisé linéairement et d'autre part, la précession de Larmor agissant sur le pseudospin du condensat tend à détruire cette polarisation.
Dans la dernière partie de ce travail, le cas des microcavités non-polaires est étudié. Dans ces structures, l'axe optique se trouve dans le plan de la cavité produisant une anisotropie optique double. D'une part la lumière se propageant dans la cavité va subir l'effet de la biréfringence menant à la formation de différents modes de cavité selon la polarisation (parallèle ou ou perpendiculaire à l'axe optique). D'autre part les règles de sélection excitoniques vont également être différentes selon chaque direction. La combinaison de ces deux effets a conduit à l'observation de la coexistence des couplages fort et faible suivant les deux polarisations. Pour chaque direction, une transition vers le régime nonlinéaire est observée.

Mots-clé : Nitrure de gallium, nitrures d'éléments III, microcavités, polaritons, condensat de polaritons, régime de couplage fort, laser à polaritons, condensation de Bose-Einstein, biexcitons, relaxation polaritonique, diagramme de phase, thermodynamique, cinétique, polarisation, désordre d'interface, paramètre d'ordre, précession de Larmor, microcavités non-polaires, anisotropie optique.

Contents

Remerciements . . . v

Abstract (English/Français) . . . vii

Table of contents . . . xiv

Introduction . . . 1
From Bose-Einstein condensates to ultra-low threshold coherent emitters . . . 1
Polariton condensation and its way toward room temperature . . . 2
III-nitrides for strong light-matter coupling . . . 3
State of the art of planar GaN-based microcavities before this PhD thesis . . . 4
Outline . . . 5

1 Planar microcavities . . . 9
1.1 Optical properties of semiconductors . . . 9
1.1.1 Interband transitions . . . 10
1.1.2 Bulk and quantum well excitons . . . 11
1.1.3 Broadening of the excitonic transition . . . 13
1.1.4 Exciton localization . . . 14
1.1.5 Excitons in the high density regime . . . 14
1.1.6 Excitonic nonlinearities . . . 16
1.1.7 Interaction with the electromagnetic field . . . 17
1.2 Optics of cavities . . . 21
1.2.1 The Fabry-Perot resonator . . . 21
1.2.2 The semiconductor planar cavity . . . 23
1.3 Light-matter coupling in planar microcavities . . . 26
1.3.1 Analogy with the classical mechanical oscillator . . . 27
1.3.2 Classical description of the light-matter interaction: the linear dispersion model . . . 28
1.3.3 Quantum description of the light-matter interaction: coupled quantum oscillators . . . 30
1.3.4 Strong to weak coupling regime transition . . . 34
1.3.5 Impact of the quantum well number . . . 38
1.4 Nonlinearities in strongly coupled planar microcavities . . . 39
1.4.1 The ideal non-interacting Bose gas: case of the Bose-Einstein condensation 39
1.4.2 Polariton BEC . . . 41

2 III-nitride materials ... 43
2.1 A brief history ... 43
2.2 Structural properties ... 44
2.2.1 Crystalline structure ... 44
2.2.2 Crystal orientations ... 46
2.2.3 Growth ... 47
2.2.4 Mechanical properties ... 49
2.2.5 Pyroelectric properties ... 51
2.2.6 Polarization: quantum confined Stark effect in heterostructures ... 53
2.3 Optical properties ... 54
2.3.1 Band structure and radiative properties ... 54
2.3.2 Refractive index and birefringence ... 57

3 Polariton condensation in polar GaN-based microcavities ... 59
3.1 Fourier imaging ... 59
3.1.1 Principle ... 59
3.1.2 Setup specificities ... 61
3.2 Sample presentation ... 62
3.2.1 Design and structural properties ... 62
3.2.2 Optical properties of the bare active medium ... 63
3.2.3 Optical properties of the full microcavity ... 69
3.2.4 Biexcitons: the bare cavity section and the full microcavity ... 72
3.3 Formation of the polariton condensate ... 78
3.3.1 Formation and thermalization of polaritons: the classical picture ... 78
3.3.2 Biexciton-assisted relaxation ... 80
3.4 Renormalization of the polariton branches ... 82
3.4.1 The standard picture ... 82
3.4.2 Impact of the lattice temperature, detuning and disorder ... 86
3.4.3 Impact of interactions and saturation ... 88
3.4.4 Nonlinear renormalization of the polariton condensate: possible contribution of biexcitons ... 91
3.5 The nonlinear regime ... 93
3.5.1 Condensation in real and momentum spaces ... 93
3.5.2 Output power efficiency ... 95
3.5.3 Kinetically driven polariton condensation ... 97

4 Polariton condensation phase diagram ... 103
4.1 Introduction ... 103
4.1.1 Phase transition in the weak coupling regime ... 104
4.1.2 Phase transition in the strong coupling regime ... 107
4.2 Specificities of GaN-based microcavities ... 108
4.3 A pedestrian approach to the phase diagram: kinetic vs. thermodynamic regimes ... 110
4.3.1 Effect of detuning and temperature on the polariton relaxation time ... 110
4.3.2 Impact of the thermodynamics on the threshold power density ... 111
4.4 Theoretical description of polariton relaxation ... 114
4.4.1 The thermodynamic limit ... 114
4.4.2 The kinetic limit ... 115
4.5 Phase diagram: experimental results vs. theory ... 117

4.6 Impact of temperature on the electronic populations ... 120
4.7 LO-phonon mediated relaxation ... 122
4.8 Polariton laser vs. VCSEL: evidence of the matter-like character of polaritons ... 123

5 Polariton polarization properties: evolution of the order parameter ... 125
5.1 Introduction ... 125
5.1.1 Representation of the polariton spin state ... 125
5.1.2 Spontaneous symmetry breaking and polariton BEC ... 126
5.1.3 Pseudospin dynamics ... 128
5.2 Polarization properties of III-nitride-based microcavities ... 129
5.2.1 The bulk microcavity: spontaneous build-up of the order parameter ... 129
5.2.2 The multiple quantum well microcavity: pinning of the order parameter ... 130
5.3 Evolution of the order parameter with carrier density ... 132
5.3.1 Theoretical description ... 132
5.3.2 Theory vs. experiments ... 134
5.3.3 Some polarization features in other semiconductor systems: comparison and perspectives ... 137

6 Polariton condensation in anisotropic nonpolar GaN-based microcavities ... 139
6.1 Introduction ... 139
6.1.1 Motivation: why going for nonpolar? ... 139
6.1.2 Optical anisotropy, a fair price to pay ... 140
6.1.3 State of the art before this work ... 141
6.2 Growth and structural properties ... 141
6.3 Samples of first generation: Bragg polaritons ... 143
6.3.1 Sample design ... 143
6.3.2 Half-microcavity ... 144
6.3.3 Full microcavity ... 147
6.4 Samples of second generation: Anisotropic polariton lasing ... 149
6.4.1 Sample design ... 149
6.4.2 Half-microcavity: investigation of the optical in-plane anisotropy ... 150
6.4.3 Full microcavity: the linear regime ... 155
6.4.4 Full microcavity: the nonlinear regime ... 160

7 Conclusion and perspectives ... 167
7.1 Summary of the experimental results ... 167
7.2 Perspectives ... 169
7.2.1 Room temperature polariton condensation ... 169
7.2.2 Polariton lasing in systems with lower dimensions ... 170
7.2.3 Toward electrically injected polariton lasers ... 170
7.2.4 Applications in biology ... 171

Bibliography ... 173

Appendices ... 191
A Envelope function calculation in the Numerov approximation ... 191
B Band structure calculation: an introduction to the $k \cdot p$ formalism ... 192
C Optical simulation in homogeneous planar multilayer systems: the transfer matrix formalism ... 194

C.1 Isotropic structures: the 2 × 2 matrix formalism 194
C.2 Anisotropic structures: the 4 × 4 matrix formalism 196

Curriculum Vitae 199

Introduction

From Bose-Einstein condensates to ultra-low threshold coherent light emitters

In 1925, Einstein stated that in a non-interacting Bose gas at thermal equilibrium something happens, similar to the isothermal compression of a vapor across the saturation volume. A separation occurs; one part "condenses", the remaining part stays a "saturated" ideal gas [1, 2]. Below a specific critical temperature, any bosonic system adopts a collective behavior and spontaneously collapses into a single quantum state. This surprising effect called *Bose-Einstein condensation* (BEC) is often referred to as the fifth state of matter as the system no longer behaves classically but is described by a macroscopic quantum wave function. The first experimental evidence of this new state of matter occurred only 70 years after in the research groups of Wolfgang Ketterle, Eric Cornell and Carl Wieman in a dilute vapor of atoms at ultra-low temperatures ($T \approx 10^{-7}$ K). They were awarded the Nobel prize in Physics in 2001 [3, 4].

In the present work we are interested in a specific kind of bosonic system appearing in semiconductor optical microcavities operating in the strong coupling regime: cavity polaritons. These particles result from the strong interaction between cavity photons and excitons and simultaneously share the properties of light and matter. In particular, they exhibit a very light effective mass, typically one billion times lighter than that of an atom, inherited from their photonic component. As the critical temperature for the observation of BEC directly depends on the ratio between the particle mass and the temperature, it is then possible to expect polariton condensation at ambient conditions. In 1996, Imamoğlu *et al.* [5] suggested the use of a non-equilibrium polariton condensate to produce a coherent light source referred to as a *polariton laser*. Due to the release of the Bernard-Duraffourg condition limiting the threshold current density in standard semiconductor lasers, polariton-based devices potentially present a significantly lower threshold current.

Figure 0.1(a) highlights the development of electrically driven III-nitride laser diodes during the last two decades for the blue-violet spectral range. The threshold current density J_{thr} has been gradually improved for edge emitting laser diodes [6–9], a device structure relying on cleaved edges that act as cavity. The surface emitting alternative, the vertical cavity surface emitting laser (VCSEL) was only demonstrated very recently [10], and is out of this trend as it still needs a larger driving threshold current density. The decrease in J_{thr} seems to saturate to about $1-2\,\text{kA/cm}^2$ due to intrinsic reasons. In this respect, III-nitride-based devices cannot compete with their arsenide counterpart. An alternative option to further reduce J_{thr} is to switch to a new physical concept, where, for example the large excitonic mass is circumvented while being easy to fabricate. In this context, the polariton laser appears as a promising candidate. Such an electrically driven III-nitride-based device would present a threshold current density between 10 and $100\,\text{A/cm}^2$ [11], i.e., two orders of magnitude below state-of-the art values reported for edge emitting laser diodes (see Fig. 0.1(a)). The success of this approach is

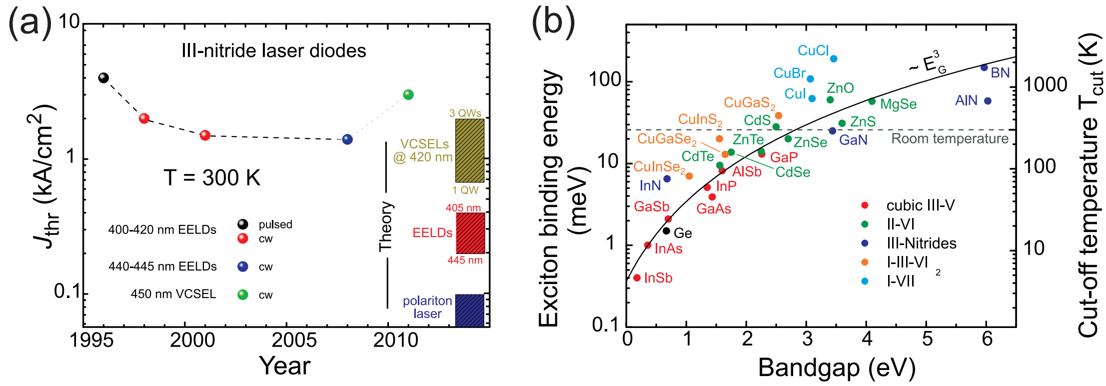

Fig. 0.1: (a) Threshold current density (J_{thr}) of edge emitting laser diodes (EELDs) [6–9] and VCSELs [10] operating at room temperature over the last years. The blue square at the bottom right corner corresponds to the estimated limit, which could be achieved in a nitride polariton-laser based on the approach described in Ref. [11]. For comparison, the optimum value of J_{thr} is also shown for EELDs (calculated for $\lambda = 405$ and 445 nm following Ref.[15]) and for a VCSEL ($\lambda = 420$ nm) embedding different quantum well numbers [16]. (b) Exciton binding energy vs. band gap energy (E_G) for various inorganic bulk semiconductors: III-V (red), II-VI (green), I-VII (light blue), chalcopyrites I-III-VI$_2$ (orange), and III-nitrides (blue). A guide to the eye (black solid line) reproduces the power-law $E_X^b \propto E_G^3$ and the horizontal gray dashed line defines the room-temperature limit.

closely linked to that of the blue III-nitride VCSELs, which were already demonstrated under electrical pumping at room temperature [12, 13] as they share very similar sample designs [14].

Polariton condensation and its way toward room temperature

After the first report of the strong coupling regime in planar GaAs microcavities in 1992 by Weisbuch and coworkers [17] and the proposal of polariton condensation as a driving force for the realization of novel low threshold laser-like emitters by Imamoğlu and co-workers in 1996 [5], the polaritonic field has grown very fast. In particular, the first demonstration of polariton BEC in a CdTe microcavity [18] and the subsequent observations, including integer [19] and half-integer quantum vortices [20], superfluidity [21–23], and solitons [24] in polariton fluids, attracted a lot of attention. Cavity-polaritons exhibit unique characteristics inherited from their mixed light-matter nature. Thus, their photonic component confers them a very low effective mass, while their excitonic one allows them to interact causing nonlinearities.

From the point of view of integrated optoelectronics, cavity-polaritons are of high interest as they can carry information *via* their pseudospin **S**, their phase, their amplitude and their energy. When decaying, an exact copy of this information is transferred to the emitted photons allowing the readout of the polariton state. Another important aspect of cavity-polaritons is that the light-matter content can be controlled *via* the detuning δ between cavity-photons and excitons, e.g., by varying the cavity thickness or the lattice temperature. Thus, the way polaritons interact with each other can be modified: for negative δ-values the lowest energy polariton state is mainly photon-like, while for positive ones the situation is reversed. Based on these unique properties, cavity-polaritons were proposed as promising candidates for several applications in optoelectronics and spinoptronics, including the generation of entangled photon pairs [25, 26], the realization of micro-optical parametric oscillators [27] and ampli-

fiers [28, 29], ultrafast optical spin switches [30, 31], new coherent light sources [5, 32–35], mesoscopic optical Berry-phase interferometers [36], Sagnac interferometers [37], exciton-polariton BEC mediated high-temperature superconducting circuits [38], logic gates [39], polarization/spin-sensitive devices [30, 40–43], THz emitters [44, 45] and devices using spin-independent bistability [46]. Most of those phenomena or concepts have been proposed based on the properties of GaAs and CdTe microcavities, which exhibit on the one hand an advanced structural and optical quality but on the other hand a limited exciton binding energy (E_X^b) restricting their experimental demonstration to cryogenic temperatures and thus preventing the realization of practical devices. Indeed, despite the demonstration of an electrically-injected polariton light-emitting diode, a system operating in the linear emission regime at room temperature in a GaAs-based microcavity, it seems that the cut-off temperature T_{cut} for the observation of polariton related nonlinearities is set by the thermal stability of excitons, i.e., $T_{cut} \approx E_X^b / k_B$ [29]. To overcome this issue E_X^b has to exceed the thermal energy at room temperature ($\sim 26\,\text{meV}$), which defines the main figure of merit to bring polariton nonlinearities up to ambient conditions.

Figure 0.1(b) shows E_X^b values for a variety of inorganic bulk semiconductor materials as a function of their band gap energy E_G. Within the hydrogen-like approximation the relation $E_X^b \propto m_{eff}^*/\epsilon_r^2$ holds, where m_{eff}^* is the reduced effective mass of the exciton and ϵ_r is the static dielectric constant of the material of interest. Both quantities are a function of E_G: as a first approximation $m_{eff}^* \propto E_G$ and $\epsilon_r \propto 1/E_G$ [47]. The resulting power law $E_X^b \propto E_G^3$ is shown as a guide to the eye in Fig. 0.1(b) and highlights the limited number of bulk semiconductor microcavities for high temperature exciton-based applications. This situation can be significantly improved if quantum-well based structures are considered instead of bulk ones. Indeed, due to carrier-confinement effects the value of E_X^b can theoretically be enhanced by a factor of up to four compared to the bulk case in perfectly two-dimensional (2D) quantum wells [48]. However, owing to deviations from the ideal 2D-character real structures exhibit a maximum enhancement factor of about two.

III-nitrides for strong light-matter coupling studies

Motivated by the pioneering work of Shuji Nakamura from Nichia Corporation on blue light-emitting diodes [49] and laser diodes [6] in the early 1990s, the research on III-nitride materials has experienced an impressive development. Recently these materials became the second largest market in the semiconductor industry after silicon. This development is now guided by the rapid progress in the III-nitride technology into many applications of everyday life based on certain material specificities. In the hexagonal phase III-nitride compounds have a direct band gap, which is continuously tunable from the ultraviolet down to the infrared spectral range by ternary alloying and thus also span the whole visible spectrum. Taking into account the well-established possibility of p-type doping for Ga-rich alloys, these characteristics make III-nitrides extremely suitable for optoelectronic applications. Besides the blue-violet laser diodes for optical data storage systems the market of white light-emitting diodes increases most rapidly. They exhibit record luminous efficacies and will progressively revolutionize general lighting. On the basis of their chemical and thermal robustness III-nitrides are further used for high-power and high-temperature electronics, e.g. in power supplies.

Despite the notorious difficulty of achieving high quality layers, III-nitrides offer major advantages for the study of light-matter interaction and in particular a robust excitonic transition ($E_{X,bulk}^b \approx 26\,\text{meV}$ [50]) and an oscillator strength more than five times higher than in III-arsenides [51], which allowed to demonstrate polariton lasing [33] and BEC of exciton-polaritons [52] at room temperature in a bulk GaN-based microcavity. However, with respect to Fig. 0.1(b) and the previous discussion, a lattice

temperature of 300 K roughly corresponds to T_{cut} for this active material. Since the device operating temperatures are usually exceeding the ambient one, a structure relying on a bulk GaN layer seems thus hardly probable. This intrinsic limitation can be effectively overcome by switching to appropriate multiple quantum well-based active regions. Quantum confinement enhances the exciton oscillator strength and the robustness of excitons: E_X^b values of up to 50 meV have been obtained [53]. This approach also induces a reduction in the critical density for condensation n_c by at least one order of magnitude [54] and the observation of polariton condensation over a wider range of detunings δ and temperatures T [55, 56].

State of the art of planar GaN-based microcavities before this PhD thesis

The first demonstration of the strong coupling regime in III-nitride planar microcavities was achieved in 2003 by Antoine-Vincent and coworkers on a bulk GaN microcavity grown on a silicon substrate with a top dielectric distributed Bragg reflector (DBR) at cryogenic temperature ($T = 5$ K) [57]. Two years after, the same group reported the strong coupling regime on a similar structure but with a metallic top DBR up to room temperature and with a vacuum Rabi splitting of 30 meV [58]. Unfortunately, the relatively low quality factors obtained in III-nitride microcavities due to the difficulty of growing a crack-free structure prevented the observation of polariton nonlinearities, even at cryogenic temperatures. Thanks to the pioneering work of Carlin and coworkers who developed the growth of crack-free nitride-based DBRs using the (Al,In)N alloy lattice-matched to GaN [59], with reflectivities above 99%, significant advances in the fabrication of high quality factor microcavities were demonstrated [60, 61].[1] The development of such lattice-matched DBRs allowed the observation of strong coupling regime at room-temperature in a bulk [63] and in a multiple quantum well GaN-based microcavity [64].

The relatively large disorder present in III-nitride-based microcavities compared to arsenide ones makes the study of polaritons a bit more complex. In particular, the impact of photonic [65] and excitonic [66] disorder on the coupling regime was addressed in 2006 by Christmann and coworkers. They showed that the strong coupling regime cannot be sustained when the exciton inhomogeneous broadening becomes comparable to the vacuum Rabi splitting. Another particularity of presently available GaN-based microcavities is the possibility of reaching the nonperturbative regime up to room temperature. Such conditions were shown to favor the polariton relaxation kinetics along the lower polariton branch. Stokker-Cheregi and coworkers have observed in 2008 the thermal suppression of the polariton relaxation bottleneck [67], highlighting the possibility of tuning the interactions in a polariton gas by changing the lattice temperature. The influence of the mirror type (metallic, dielectric or nitride-based ones) is also of paramount importance for the design of III-nitride microcavities due to the relatively high price of the commercially available substrates for homoepitaxial growth. In this context, Réveret and coworkers have shown in 2008 the strong relation between the decrease in the vacuum Rabi splitting and the increase in the light penetration depth of the bottom mirror [68].

At the beginning of the present PhD thesis, polariton condensation had been observed in a bulk [33, 52] and in a multiple quantum well-based [34] microcavity grown on c-plane oriented sapphire substrate at room temperature. The latter structure is the one investigated in the Chapters 3 to 5. In the last chapter, the anisotropic properties of multiple quantum well based microcavities grown along the nonpolar m-orientation are also addressed.

[1] For a review on III-nitride DBRs, the reader can refer to Ref. [62].

Outline

The first part of the present work is devoted to the presentation of theoretical concepts, including the physics of microcavities and the description of III-nitride material properties.

- **Chapter 1: Planar microcavities.** The first chapter is divided into four sections. The first one describes the optical properties of semiconductors and also the impact of the carrier density on the exciton behavior. The second one is devoted to the physics of optical microcavities, including the ideal Fabry-Perot case (metallic mirrors) and the impact of dielectric Bragg reflectors. Finally the physics of optical microcavities with an embedded active region is discussed both in the linear and in the nonlinear regime.

- **Chapter 2: III-nitride materials.** The second chapter briefly presents the properties of III-nitride based semiconductors, including structural, optical and electronic ones. A special attention is paid to the role of the crystal orientation. For heterostructures grown along the polar c-orientation, the impact of the built-in electric field is addressed. For polarization-free structures, i.e. those grown along the nonpolar a or the m-plane orientations, the anisotropic optical response is discussed.

The second part is devoted to the presentation of the experimental results as well as the theoretical modeling and consists of four chapters.

- **Chapter 3: Polariton condensation in polar GaN-based microcavities.** The third chapter is divided into several sections. First the experimental setup is presented and the structural and optical properties of the polar multiple quantum well microcavity sample are discussed in details. Then the polariton dynamics leading to the formation of polariton condensates is presented and a particular attention is paid to the role of biexcitons on the relaxation kinetics. In the next section, the impact of the carrier density on the polariton branch renormalization is discussed. A simple model is presented and confronted to the experimental results, highlighting the specificities of GaN-based microcavities in comparison with other semiconductor material systems. In the last section, some features of polariton condensates are presented.

  Contributions:

  All the time-resolved measurements presented in this chapter have been performed by P. Corfdir (Group of Prof. B. Deveaud-Plédran, EPFL, Lausanne, Switzerland).

  Related publications:

  F. Stokker Cheregi, A. Vinattieri, E. Feltin, D. Simeonov, J. Levrat, J.-F. Carlin, R. Butté, N. Grandjean, and M. Gurioli, Impact of quantum confinement and quantum confined Stark effect on biexciton binding energy in GaN/AlGaN quantum wells, Appl. Phys. Lett. **93**, 152105 (2008).

  P. Corfdir, J. Levrat, G. Rossbach, R. Butté, E. Feltin, J.-F. Carlin, G. Christmann, P. Lefebvre, J.-D. Ganière, N. Grandjean, and B. Deveaud-Plédran, *Impact of biexcitons on the relaxation mechanisms of polaritons in III-nitride based multiple quantum well microcavities*, Phys. Rev. B **85**, 245308 (2012).

- **Chapter 4: Polariton condensation phase diagram.** The fourth chapter is devoted to the phase diagram of polariton condensation in the present polar microcavity (described in Chapter 3). In particular, the relative role played by the kinetic and thermodynamic regimes in relation with

the critical threshold density are discussed both experimentally and theoretically. The additional contributions of thermal depopulation, thermal free electrons, LO-phonons and biexcitons on the polariton dynamics are also addressed.

Contributions:

The simulation of the semiclassical Boltzmann equations has been performed in the group of G. Malpuech (Univ. Blaise Pascal, Clermont-Ferrand, France).

Related publications:

J. Levrat, R. Butté, G. Christmann, E. Feltin, J.-F. Carlin, and N. Grandjean, Invited paper, *Tailoring the strong coupling regime in III-nitride based microcavities for room temperature polariton laser applications*, Proceedings of the 15th Semiconducting and Insulating Materials Conference, phys. stat. sol. (c) **6**, 2820 (2009).

R. Butté, J. Levrat, G. Christmann, E. Feltin, J.-F. Carlin, and N. Grandjean, *Phase diagram of a polariton laser from cryogenic to room temperature*, Phys. Rev. B **80**, 233301 (2009).

J. Levrat, R. Butté, E. Feltin, J.-F. Carlin, N. Grandjean, D. Solnyshkov, and G. Malpuech, *Condensation phase diagram of cavity polaritons in GaN-based microcavities: experiment and theory*, Phys. Rev. B **81**, 125305 (2010) + Erratum: Phys. Rev. B **84**, 199908(E) (2011).

- **Chapter 5: Polariton polarization properties: evolution of the order parameter.** The fifth chapter describes the polarization properties of the polariton emission above the condensation threshold. As in other quantum well-based semiconductor systems, a pinning of the order parameter is observed at threshold. When the excitation power density is increased, a rapid decrease in the linear polarization degree is reported, which is understood in terms of competition between static disorder and self-induced Larmor precession.

  Contributions:

  The simulation of the stochastic Langevin equation have been performed by D. Read in the group of A. Kavokin (Univ. Southampton, UK).

  Related publication:

  J. Levrat, R. Butté, T. Christian, M. Glauser, E. Feltin, J.-F. Carlin, N. Grandjean, D. Read, A.V. Kavokin, and Y.G. Rubo, *Pinning and depinning of the polarization of exciton-polariton condensates at room temperature*, Phys. Rev. Lett. **104**, 166402 (2010).

- **Chapter 6: Polariton condensation in anisotropic nonpolar GaN-based microcavities.** The last chapter focuses on the study of nonpolar multiple quantum well GaN-based microcavities. Due to the intrinsic in-plane optical anisotropy, which affects both the cavity mode and the optically active excitons, the description of the light-matter interaction is richer and more complex than in isotropic cavities. In this chapter, a microcavity featuring the coexistence of strongly and weakly coupled modes along orthogonal polarization planes is investigated. Lasing is observed for both directions well below the exciton saturation density with different threshold power densities along extraordinary and ordinary directions, respectively.

Contributions:

The $k \cdot p$ simulations have been performed by G. Rossbach using the formalism presented in Appendix B. The top DBR deposited on the full microcavity have been developped by G. Cosendey.

Related publications:

G. Rossbach, J. Levrat, A. Dussaigne, M. Glauser, M. Cobet, R. Butté, N. Grandjean, H. Teisseyre, M. Bockowski, I. Grzegory, and T. Suski, *Tailoring the light-matter coupling in anisotropic microcavities: redistribution of oscillator strength in strained m-plane GaN/AlGaN quantum wells*, Phys. Rev. B **84**, 115315 (2011).

J. Levrat, G. Rossbach, A. Dussaigne, G. Cosendey, M. Glauser, M. Cobet, R. Butté, N. Grandjean, H. Teisseyre, M. Bockowski, I. Grzegory, and T. Suski,*On the nature of the non-linear emission properties of an optically anisotropic GaN-based microcavity*, submitted to Phys. Rev. B.

1 Planar microcavities

Planar microcavities are of major interest as they offer a direct way to enhance the light-matter interaction by confining the electromagnetic field in a small volume where emitters are located. In this work, we are interested in the case of multiple quantum well-based structures due to the possibility of tuning the radiative properties of the active region. In the first section, the optical properties of excitons in semiconductors are presented, and a careful attention is paid to their coupling with the vacuum field. As we are interested in the particular case where the coupling occurs with a well defined cavity resonance, the basic properties of ideal Fabry-Perot cavities are first summarized and transposed in the case where mirrors are replaced by distributed Bragg reflectors. The third section is dedicated to the study of semiconductor planar microcavities and the nature of the light-matter interaction depending on the system specificities is carefully addressed. When the system operates in the so-called strong coupling regime, i.e., when the light-matter interaction strength exceeds the damping of the bare modes, the normal modes are described by quasi-particles referred to as *polaritons*. As these quasi-particles have an integer spin, they behave as bosons and can undergo a Bose-Einstein-like phase transition. Some specific features of polariton condensation are discussed in the last section.

1.1 Optical properties of semiconductors

A crystalline solid results from the periodic stack of atoms or molecules arranged following a Bravais lattice (see Section 2.2.1). In isolated atoms, electrons have discrete energy levels and occupy atomic orbitals around the nucleus. Bringing a huge number of them close together to form a solid (typically $10^{22} - 10^{23}$ atoms/cm^3 or more), a high number of orbitals interact and couple to each other leading to the formation of continuous energy bands rather than discrete levels. Some energy ranges are forbidden to electrons and for these reasons are referred to as *band gaps*. According to Pauli principle, electrons accommodate all available states by increasing energy.

In this thesis, we are interested in intrinsic semiconductors where the Fermi level lies within the band gap. By definition, the highest occupied band is named *valence band* and the lowest unoccupied band is the *conduction band*. The difference between the minimum energy of the conduction band E_C^0 and the maximum energy of the valence band E_V^0 defines the band gap energy of the material $E_G = E_C^0 - E_V^0$, which is a fundamental property of semiconductors.[2] All bands in a semiconductor have a well-defined

[2] 0 in E_C^0 and E_V^0 stands for the $\mathbf{k} = \mathbf{0}$ wave vector, i.e., the center of the first Brillouin zone. The position of the minimum of the conduction band and that of the maximum of the valence band in reciprocal space coincide only for direct band gap semiconductors, which are considered in this thesis.

k-dependence accounting for the kinetic energy of electrons propagating in the solid with a given wave vector **k**. In the free-electron model, i.e. when the perturbation due to atoms is neglected, the electronic energy dispersion is parabolic:

$$E_{C,V}\left(\mathbf{k}_{e,h}\right) = E^0_{C,V} + \frac{\hbar^2 \mathbf{k}^2_{e,h}}{2m_{e,h}}, \tag{1.1}$$

where $m_{e,h}$ and $\mathbf{k}_{e,h}$ are the mass and the wave vector of an electron (hole) in the conduction (valence) band, respectively. It is convenient to introduce the concept of *hole*, which is a virtual particle corresponding to this missing electron in the Fermi sea, which behaves as a particle of negative mass ($m_h < 0$). Relations 1.1 are exact in the free electron approximation only. However, the electrons cannot be treated independently from the periodic potential created by atoms in the lattice $\hat{V}_{at}(\mathbf{r})$[3] and the bands E_i (with $i \in \{1,..,N\}$ the index of the band and N the number of electrons in the solid) and electronic wave functions follow from the Schrödinger equation for the periodic crystal:

$$\left[-\frac{\hbar^2\nabla^2}{2m_0} + \hat{V}_{at}(\mathbf{r})\right]\Psi_{i,\mathbf{k}} = E_i(\mathbf{k})\,\Psi_{i,\mathbf{k}}, \tag{1.2}$$

where m_0 is the free electron mass, ∇^2 is the Laplacian operator and $E_i(\mathbf{k})$ corresponds to the energy dispersion of band i. The ensemble of solutions $\left\{E_i(\mathbf{k}), \Psi_{i,\mathbf{k}}\right\}$ is referred to as the band structure of the material and contains important information about the electronic properties of the solid.[4] Relations 1.1 describe free electrons and are therefore not a general solution to equation 1.2. However, as the optical properties of semiconductors are dominated by small wave vectors near the Γ-point, a linearization of the solutions $\left\{E_i(\mathbf{k}), \Psi_{i,\mathbf{k}}\right\}$ around $\mathbf{k} \approx \mathbf{0}$ is convenient. In this region of reciprocal space, the dispersion of the bands is quasi-parabolic and the deviation from the free-electron case is described by substituting the electron and hole masses by effective ones in relations 1.1, i.e., $m_{e,h} \to m^*_{e,h}$. This approximation accounts for the first-order effect of the periodic potential on the electronic motion. The wave functions (or Bloch functions) for electrons and holes are now expressed as:

$$\Psi_{e,h,\mathbf{k}}\left(\mathbf{R}_{e,h}\right) = \exp\left(i\mathbf{k}_{e,h}.\mathbf{R}_{e,h}\right) u_{e,h}\left(\mathbf{R}_{e,h}\right), \tag{1.3}$$

where $\mathbf{k}_{e,h}$ is the wave vector of the electron (hole) in the conduction (valence) band and $u_{e,h}\left(\mathbf{R}_{e,h}\right)$ is the periodic fast varying component of the Bloch function and $\exp\left(i\mathbf{k}_{e,h}.\mathbf{R}_{e,h}\right)$ is its slow component.

1.1.1 Interband transitions

The crystal ground state for a semiconductor corresponds to the case where the N electrons are in the valence band and the conduction band is empty. An optical excitation can promote an electron from the valence band to the conduction band if its energy $\hbar\omega$ is at least equal to the band gap E_G. This transition is quasi-vertical due to the small wave vector of the absorbed photon $\mathbf{k}_{photon} \approx \mathbf{0}$, i.e., initial and final states have nearly the same wave vector $\mathbf{k}_e = \mathbf{k}_h + \mathbf{k}_{photon} \approx \mathbf{k}_h$. In the limit of independent electrons (uncorrelated electron-hole pairs), the state with energy $E = E_G$ corresponds to the first excited state. Due to the coupling to the vacuum field fluctuations *via* the dipole interaction, this state acquires a finite lifetime. When recombining, a photon with the same energy $\hbar\omega = E_G$ is emitted.

[3] $\hat{V}_{at}(\mathbf{r})$ is a one-electron potential, which accounts for the contribution of the other electrons in the mean-field approximation.

[4] The specificities of the GaN band structure are presented in Section 2.3.1.

1.1.2 Bulk and quantum well excitons

1.1.2.1 The bulk exciton

When the Coulomb interaction between electrons and holes is considered, the first excited state is still described by a single electron in the conduction band and a hole in the valence band but they are now correlated and form a bound state called an *exciton*. Its Hamiltonian is the sum of that of the electron and the hole plus the Coulomb interaction term:

$$\hat{\mathscr{H}}_{\mathrm{X}}^{\mathrm{bulk}} = -\frac{\hbar^2 \nabla_{\mathrm{e}}^2}{2m_{\mathrm{e}}^*} - \frac{\hbar^2 \nabla_{\mathrm{h}}^2}{2m_{\mathrm{h}}^*} - \frac{e^2}{4\pi\epsilon_0\epsilon_{\mathrm{r}} \left\| \mathbf{R}_{\mathrm{e}} - \mathbf{R}_{\mathrm{h}} \right\|}, \tag{1.4}$$

where $\mathbf{R}_{\mathrm{e,h}}$ is the coordinate of the electron (hole), $\nabla_{\mathrm{e,h}}^2$ is the Laplacian operator expressed in terms of the particle coordinates, ϵ_0 is the vacuum permittivity and ϵ_{r} is the relative permittivity of the material. As a first approximation, this problem is isomorphic to that of the hydrogen atom where the hole plays the role of the proton. To express the solution of the excitonic problem in terms of that of the hydrogen one, one has to rescale the physical quantities of interest, i.e., the binding energy $E_{\mathrm{X,3D}}^{\mathrm{b}}$ and the Bohr radius a_{B}:

$$\begin{aligned} E_{\mathrm{X,3D}}^{\mathrm{b}} &= \frac{\mu}{m_0\epsilon_{\mathrm{r}}^2} Ry = \frac{\mu}{m_0\epsilon_{\mathrm{r}}^2} \times 13.6\,\mathrm{eV}, \\ a_{\mathrm{B}} &= \frac{m_0\epsilon_{\mathrm{r}}}{\mu} a_{\mathrm{B}}^{\mathrm{H}} = \frac{m_0\epsilon_{\mathrm{r}}}{\mu} \times 0.53\,\mathrm{nm}, \end{aligned} \tag{1.5}$$

where the indices X and H refer to the exciton and hydrogen cases, respectively,[5] $\mu = \left(\frac{1}{m_{\mathrm{e}}^*} + \frac{1}{m_{\mathrm{h}}^*}\right)^{-1}$ is the exciton reduced mass and $Ry = 13.6\,\mathrm{eV}$ is the Rydberg constant. A calculation gives the exciton eigenenergies:

$$E_{\mathrm{n}}^{\mathrm{bulk}} = E_{\mathrm{G}} + \frac{\hbar^2 K^2}{2M_{\mathrm{X}}} - \frac{E_{\mathrm{X,3D}}^{\mathrm{b}}}{n^2}, \tag{1.6}$$

where $M_{\mathrm{X}} = m_{\mathrm{e}}^* + m_{\mathrm{h}}^*$ is the exciton translational mass, $\mathbf{K}$ is the center of mass wave vector and $n = 1, 2, 3...$ is the principal quantum number. Interestingly, as for the hydrogen case, the exciton energy only depends on n meaning that states with the same angular momentum number $l \in \{0, 1, 2, ..., n-1\}$ are degenerate. Note that the quantity $E_{\mathrm{X,3D}}^{\mathrm{b,n}} = -\frac{E_{\mathrm{X,3D}}^{\mathrm{b}}}{n^2}$ corresponds to the exciton binding energy for a bulk exciton with principal quantum number n. In Tab. 1.1, values for E_{G} at low temperature ($T < 10\,\mathrm{K}$), a_{B} and $E_{\mathrm{X,3D}}^{\mathrm{b}}$ are given for the 1s exciton ($n = 1$) for various semiconductor materials. The correlation between the robustness of the exciton and the band gap energy clearly appears and suggests that wide band gap semiconductor materials such as GaN are well adapted for the observation of excitonic effects at elevated temperatures.

Table 1.1: Experimental excitonic parameters for bulk GaAs, CdTe and GaN for $T < 10\,\mathrm{K}$.

	GaAs	CdTe	GaN
E_{G} (eV)	1.519 [69]	1.606 [70]	3.499 [50, 71]
a_{B} (nm)	11.2 [72]	7 [72]	2.7 [73]
$E_{\mathrm{X,3D}}^{\mathrm{b}}$ (meV)	3.9 [69]	9.5 [70]	24.8 [50]

[5] For convenience, these indices will be omitted in the following and will always refer to the exciton.

1.1.2.2 The quantum well exciton

The growth of high quality two-dimensional (2D) GaAs-based heterostructures in the early 80s came along with the surprising observation that the luminescence was dominated by free excitons [74] in opposition to the bulk case. To understand this behavior, the details of the light-matter coupling should be considered (see Section 1.1.7). In a perfect bulk system interactions between photons and excitons lead to the formation of polaritons whose complete radiative decay is forbidden since their radiative lifetime is infinite [75]. This remarkable feature comes from the fact that 3D-excitons transform into 3D-photons, which are reabsorbed and so on and so forth. The luminescence becomes allowed only if this symmetry is broken at least in one direction.[6] In the case of a quantum well 2D-excitons interact with 3D-photons, opening a radiative channel: the radiative lifetime becomes finite, allowing an extremely fast exciton luminescence. In addition, the exciton binding energy and the oscillator strength are enhanced due to quantum confinement, which also contributes to the high efficiency of the excitonic luminescence in quantum well based structures, as will be shown hereafter.

Contrary to bulk excitons, the translation symmetry is broken along the growth direction quantum wells and is responsible for the energy renormalization of the electron and hole states due to quantum confinement. The Hamiltonian for 2D-excitons should be thus corrected with respect to equation 1.4 by adding the electron and hole confinement potentials along the growth direction z, i.e., $\hat{V}_{\mathrm{e,h}}^{\mathrm{conf}}\left(z_{\mathrm{e,h}}\right)$:

$$\mathscr{H}_{\mathrm{X}}^{\mathrm{QW}} = -\frac{\hbar^2\nabla_{\mathrm{e}}^2}{2m_{\mathrm{e}}^*} - \frac{\hbar^2\nabla_{\mathrm{h}}^2}{2m_{\mathrm{h}}^*} + \hat{V}_{\mathrm{e}}^{\mathrm{conf}}(z_{\mathrm{e}}) + \hat{V}_{\mathrm{h}}^{\mathrm{conf}}(z_{\mathrm{h}}) - \frac{e^2}{4\pi\epsilon_0\epsilon_{\mathrm{r}}\left\|\mathbf{R}_{\mathrm{e}} - \mathbf{R}_{\mathrm{h}}\right\|}\,. \tag{1.7}$$

It is convenient to separate the electron (hole) motion in the plane of the quantum well ($\boldsymbol{\rho}_{\mathrm{e,h}}$) from that along the growth direction ($z_{\mathrm{e,h}}$). If the width of the quantum well (L_{QW}) is of the order of the exciton Bohr radius ($L_{\mathrm{QW}} \approx a_{\mathrm{B}}$), the 1s exciton wave function can be written in the form [48]:

$$\Psi\left(\mathbf{R}_{\mathrm{e}}, \mathbf{R}_{\mathrm{e}}\right) = \frac{1}{\sqrt{S}} \exp\left(i\mathbf{k}_{\parallel}\boldsymbol{\rho}\right) f_{\mathrm{e}}\left(z_{\mathrm{e}}\right) f_{\mathrm{h}}\left(z_{\mathrm{h}}\right) \Phi\left(\boldsymbol{\rho}\right), \tag{1.8}$$

where S is the surface of the quantum well plane, $\mathbf{k}_{\parallel} = \mathbf{k}_{\mathrm{e}} + \mathbf{k}_{\mathrm{h}}$ and $\boldsymbol{\rho} = \frac{m_{\mathrm{e}}^*\boldsymbol{\rho}_{\mathrm{e}} + m_{\mathrm{h}}^*\boldsymbol{\rho}_{\mathrm{h}}}{m_{\mathrm{e}}^* + m_{\mathrm{h}}^*}$ are the in-plane components of the exciton wave vector and the position of its center-of-mass, $f_{\mathrm{e,h}}\left(z_{\mathrm{e,h}}\right)$ is the envelope function for the electron (hole) obtained by solving the 1D-dimensional Schrödinger equation for the confinement potential along the growth direction z and $\Phi\left(\boldsymbol{\rho}\right)$ is the solution of the 2D-hydrogenoid-like Hamiltonian. For the 1s exciton, $\Phi_{1s}\left(\boldsymbol{\rho}\right) = \frac{1}{a_{\mathrm{B}}}\sqrt{\frac{2}{\pi}}\exp\left(-\frac{\rho}{a_{\mathrm{B}}}\right)$, where a_{B} is the effective 2D-Bohr radius.[7] In the exact 2D-limit, the eigenenergies of the Hamiltonian 1.7 are given by:

$$E_{\mathrm{n}}^{\mathrm{QW}}\left(k_{\parallel}\right) = E_{\mathrm{G}} + E_{\mathrm{e}}^{\mathrm{conf}} + E_{\mathrm{h}}^{\mathrm{conf}} + \frac{\hbar^2 K_{\parallel}^2}{2M_{\mathrm{X}}} - \frac{E_{\mathrm{X,3D}}^{\mathrm{b}}}{\left(n - \frac{1}{2}\right)^2}\,, \tag{1.9}$$

where $E_{\mathrm{e,h}}^{\mathrm{conf}}$ is the confinement energy of the electron (hole) extracted from the envelope function calculation (see Appendix A). Note that the exciton binding energy is now expressed as $E_{\mathrm{X,2D}}^{\mathrm{b,n}} = -\frac{E_{\mathrm{X,3D}}^{\mathrm{b}}}{\left(n-\frac{1}{2}\right)^2}$ meaning that for the 1s exciton, the binding energy is enhanced by a factor of 4 with respect to the bulk case for $n = 1$. However, this situation corresponds to the perfect 2D-case when $L_{\mathrm{QW}} \to 0$ and confinement effects progressively vanish when the structure dimension tends to the bulk case [48].

[6] Note the exciton luminescence is also allowed in bulk epilayers due to symmetry breaking at the sample surface.

[7] The effective Bohr radius for the 2D-exciton is one half that of the bulk exciton [76]. As only 2D-excitons will be considered in this work, the notation a_{B} will always refer to the bidimensional case.

1.1.3 Broadening of the excitonic transition

The broadening of a transition, excitonic or atomic ones, is a physical phenomenon, which modifies the spectral emission profile of a single or an ensemble of emitters, i.e., excitons in the present case. The emission process consists in the radiative decay of a quantum transition from an excited state to a lower energy one, denoted as i and f in the following. In the ideal case, the emission is quasi-monochromatic and the system emits a photon at a well defined energy $E_{\mathrm{if}} = E_{\mathrm{f}} - E_{\mathrm{i}}$ with a broadening limited by the Heisenberg principle only. However, this situation is never achieved experimentally and an additional broadening of the transition ΔE_{if} is systematically observed, which is a direct measure of the indeterminacy of the transition energy. ΔE_{if} can have two possible origins depending on the nature of this indeterminacy: if all emitters are equivalent, the broadening is said to be *homogeneous* whereas it is *inhomogeneous* otherwise.

1.1.3.1 The homogeneous broadening

The homogeneous linewidth γ_{h} of a transition is directly related to its lifetime: a transition $i \rightarrow f$ has a finite probability $1/\tau_{\mathrm{if}}$ per time unit to spontaneously decay and cannot be determined with an accuracy better than $\Delta E_{\mathrm{if}} \approx \hbar/\tau_{\mathrm{if}}$. In addition to the intrinsic lifetime of each level, τ_{i} and τ_{f}, the main contribution to the homogeneous broadening comes from collisions (inelastic and elastic ones) between the emitters and γ_{h} reads for the transition $i \rightarrow f$:

$$\gamma_{\mathrm{h,if}} = \hbar\left(\frac{1}{\tau_{\mathrm{i}}} + \frac{1}{\tau_{\mathrm{f}}} + \frac{2}{\tau_{\mathrm{coll}}}\right), \tag{1.10}$$

where τ_{coll} is the mean time between two collisions. Note that this collisional contribution depends on the density of excitons and will play an important role in optically or electrically pumped semiconductors [77]. In particular, the homogeneous broadening was found to linearly depend on the injected carrier density in high quality GaAs quantum wells [78]. A similar trend was also observed in bulk GaN epilayers [79]. When the lattice temperature is increased an additional contribution to the homogeneous broadening due to scattering with longitudinal acoustic (LA) and optical (LO) phonons should be considered:

$$\begin{aligned} \gamma_{\mathrm{h,LA}}(T) &= \alpha_1 T, \\ \gamma_{\mathrm{h,LO}}(T) &= \alpha_2 f_{\mathrm{BE}}(T) = \frac{\alpha_2}{\exp\left(E_{\mathrm{LO}}/k_{\mathrm{B}}T\right) - 1}, \end{aligned} \tag{1.11}$$

where $\alpha_{1,2}$ are proportionality coefficients, E_{LO} is the LO-phonon energy (which amounts to 92 meV in GaN) and $f_{\mathrm{BE}}(T)$ is the Bose-Einstein distribution.

1.1.3.2 The inhomogeneous broadening

Let us now consider the case where the quantum well excitons are not equivalent due to structural non-idealities, usually well width fluctuations and alloy disorder. The potential energy for the carriers is thus randomly modulated in space, which results in a Gaussian distribution of the exciton energies. As a consequence, at low temperatures and densities, the broadening does not converge to zero as suggested by relations 1.11 but to the inhomogeneous broadening γ_{inh}, i.e., $\lim_{(T,n)\rightarrow(0,0)} \Delta E_{\mathrm{if}} = \gamma_{\mathrm{inh}}$.

1.1.4 Exciton localization

In an inhomogeneously broadened system, excitons experience a randomly disordered potential landscape. As a consequence, at low temperatures, the lowest energy states act as localization centers and the emission energy observed in photoluminescence experiments does not correspond to the free exciton one: this energy difference is referred to as the *Stokes shift* and is a good indicator of the material quality. In III-nitride systems, the inhomogeneous contribution γ_{inh} to the total broadening can be very large (typically 15 – 25 meV for low aluminum content GaN/(Al,Ga)N quantum wells) and should be considered when simulating the optical properties as it modifies the imaginary part of the dielectric function. In the transfer matrix simulation performed in this thesis, the absorption induced by localized states is modeled by a sigmoidal function [80]:

$$\alpha(E) = \frac{\alpha_0}{1 + \exp\left(\frac{E_G - E}{\Delta E}\right)}, \tag{1.12}$$

where α_0 is a fitting parameter accounting free carrier absorption occurring at short wavelengths and ΔE is the Urbach energy describing the width of the exponential absorption edge. Exciton localization was first observed in high quality GaAs/(Al,Ga)As quantum well samples and the inhomogeneous linewidth was essentially due to single atomic layer fluctuations [74]. In the GaN/(Al,Ga)N quantum wells under investigation in this thesis, the situation is different and the inhomogeneous broadening is dominated by alloy disorder occurring in the (Al,Ga)N barriers [81].

1.1.5 Excitons in the high density regime

As the exciton is a composite particle made out of two fermionic particles, it has an integer spin, which suggests that an excitonic system should share very similar properties with a Bose gas [82]. In particular such a system should undergo a Bose-Einstein-like phase transition below a critical temperature (see Section 1.4). For non-interacting bosons, the physical description is quite straightforward but the situation gets more intricate when interparticle interaction is considered. In this Section, we study the impact of the carrier density on the stability of the excitonic transition and the limits of the bosonic picture validity.

1.1.5.1 Validity of the bosonic picture

An ensemble of bosonic particles has specific symmetry properties. In particular, under exchange of two particles, the total wave function remains perfectly symmetric in opposition to a fermionic ensemble where such an exchange reverses the parity of the wave function. It is convenient to describe a bosonic system in the formalism of the second quantization. In this framework, particles (e.g. electrons and holes) with a given quantum state of wave vector $\mathbf{k}$ can be created or destroyed *via* the corresponding creation and annihilation operators $\hat{Q}^\dagger_{\mathbf{k}}$ and $\hat{Q}_{\mathbf{k}}$, respectively. For bosons, the commutator of these two operators must satisfy:

$$\left[\hat{Q}^\dagger_{\mathbf{k}}, \hat{Q}_{\mathbf{k}'}\right] = \delta_{\mathbf{k},\mathbf{k}'}. \tag{1.13}$$

For an electron with a given momentum $\mathbf{k}$, the creation (annihilation) operator $\hat{a}^\dagger_{\mathbf{k}}$ ($\hat{a}_{\mathbf{k}}$) creates (destroys) one electron with the same wave vector $\mathbf{k}$ (for the hole, the corresponding operators are $\hat{b}^\dagger_{\mathbf{k}}$ and $\hat{b}_{\mathbf{k}}$, respectively). Labeling $|0\rangle$ the crystal ground state, the electron hole-pair with one electron of wave

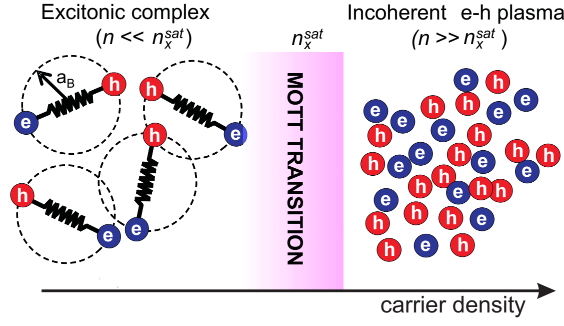

Fig. 1.1: Schematic representation of the Mott transition. Below $n_{\mathrm{X}}^{\mathrm{sat}}$, the electronic population is dominated by excitons. Above $n_{\mathrm{X}}^{\mathrm{sat}}$, the system consists of a degenerate electron-hole plasma.

vector $\mathbf{k}_{\mathrm{e}}$ and a hole of wave vector $\mathbf{k}_{\mathrm{h}}$ is:[8]

$$|\mathbf{k}_{\mathrm{e}},\mathbf{k}_{\mathrm{h}}\rangle = \hat{a}^{\dagger}_{\mathbf{k}_{\mathrm{e}}}\hat{b}^{\dagger}_{\mathbf{k}_{\mathrm{h}}}|0\rangle\,. \tag{1.14}$$

As the exciton is a correlated electron-hole pair, the creation operator of one exciton with wave vector $\mathbf{k}_{\parallel}$, $\hat{d}^{\dagger}_{\mathbf{k}_{\parallel}}$, can be expressed as a linear combination of the uncorrelated hole-pair creation operators. The calculation performed in Ref. [84] for the 1s exciton leads to:

$$d^{\dagger}_{\mathbf{k}_{\parallel}} = \sum_{\mathbf{k}} \frac{\sqrt{8\pi a_{\mathrm{B}}^2/S}}{\left[1+(ka_{\mathrm{B}})^2\right]^{3/2}}\,\hat{a}^{\dagger}_{\frac{m_{\mathrm{e}}^*}{M_{\mathrm{X}}}\mathbf{k}_{\parallel}+\mathbf{k}}\;\hat{b}^{\dagger}_{\frac{m_{\mathrm{h}}^*}{M_{\mathrm{X}}}\mathbf{k}_{\parallel}-\mathbf{k}}\,. \tag{1.15}$$

The calculation of the commutator $\left[\hat{d}^{\dagger}_{\mathbf{k}_{\parallel}},\hat{d}_{\mathbf{k}_{\parallel}'}\right]$ is a challenging task, but its mean value for a 2D-excitonic system with surface density n has been evaluated in [85]:

$$\left[\hat{d}^{\dagger}_{\mathbf{k}_{\parallel}},\hat{d}_{\mathbf{k}_{\parallel}'}\right] = \delta_{\mathbf{k},\mathbf{k}'} + \mathcal{O}\left(na_{\mathrm{B}}^2\right). \tag{1.16}$$

It turns out that the bosonic commutator (equation 1.13) is never completely satisfied for excitons but a good agreement is achieved in the low density regime, i.e., for densities $n \ll 1/a_{\mathrm{B}}^2$. This criterion does not define a clear frontier for the validity of the bosonic picture since the value of the commutator in equation 1.16 continuously decreases with the injected carrier density [86]. The physical origin for the progressive loss of the bosonic character comes from the increasing role played by the exchange term of the fermionic components and the progressive filling of the phase space (Pauli blocking principle).

1.1.5.2 The Mott transition

As detailed in Section 1.1.2, excitons dominate the optical response in quantum well-based structures for all temperatures where the excitonic complex is stable, i.e., when $k_{\mathrm{B}}T < E_{\mathrm{X}}^{\mathrm{b}}$. When increasing the carrier density up to a given saturation value $n_{\mathrm{X}}^{\mathrm{sat}}$, the binding energy of excitons also vanishes and electron-hole bound states are no longer stable. For densities n lower than $n_{\mathrm{X}}^{\mathrm{sat}}$, pairing of electrons and holes in a neutral complex is a stable configuration and screening effects are therefore negligible. Above $n_{\mathrm{X}}^{\mathrm{sat}}$, the system becomes unstable and should be described by an ionized electron-hole plasma (see Fig. 1.1). This transition is referred to as the *Mott transition* [87].

[8] For more information on second quantization, the reader should refer to chapter 3 of Ref. [83].

This transition originates from the composite nature of the exciton. When the carrier density is increased, the distance between excitons decreases and they feel more their fermionic constituents. Originally, Mott claimed that this transition is a first order one (discontinuity in the excitation ionization degree) [88] but this point of view is still quite debated and some experimental evidences tend to show that this transition is rather a continuous one, i.e., the loss of the excitonic character is a progressive process. In bulk semiconductors for instance this point is particularly unclear: some theoretical work claim a first order transition [88, 89] and some others a continuous one [90]. Even experimental reports are contradictory [91, 92]. The situation is different in quantum well-based systems due to confinement effects that affect the range of the Coulomb interaction. In particular, it was shown that the screening of excitons by free electron-hole pairs due to long-range Coulomb interaction is negligible in 2D-systems [93]. The bleaching of excitonic resonances mainly arises from the spatial overlap of particles and the exclusion principle [94]. Finally, even if some theoretical works claim separately an abrupt first order [95] or a continuous Mott transition in quantum wells [96], experiments seem to be in favor of the continuous case [97, 98].

1.1.6 Excitonic nonlinearities

Considering the 1s exciton only, the optical response of a homogeneously broadened quantum well is well accounted for by a complex local dielectric susceptibility of the form:

$$\chi_{1s}(\omega) \propto \frac{f_{osc}^{1s}}{\omega - \omega_{1s} + i\gamma_{1s}}, \tag{1.17}$$

where f_{osc}^{1s} is the 1s exciton oscillator strength, ω_{1s} is the resonance frequency and γ_{1s} is the broadening of the transition. Excitonic nonlinearities occur when one of these quantities is modified by the carrier density [94]. In this thesis we are mainly concerned with the density dependence of f_{osc}^{1s} (saturation of the oscillator strength due to phase space filling and Coulomb interaction) and ω_{1s} (excitonic resonance shift due to interactions). These two effects are discussed in the following Section.

1.1.6.1 Oscillator strength saturation and estimation of the exciton saturation density

The reduction in the 1s exciton oscillator strength f_{osc}^{1s} with increasing carrier density depends on phase space filling (PSF) due to the Pauli blocking principle and to the Coulomb exchange (EX) interaction. Assuming a linear relation between exciton density n_X and the oscillator strength variation δf_{osc}^{1s}, one can write [94]:

$$\delta f_{osc}^{1s} = -\frac{n_X}{n_X^{sat}} f_{osc}^{1s}. \tag{1.18}$$

$1/n_X^{sat}$ has the units of an area and corresponds to the exclusion region around an exciton, i.e., the portion of space, which cannot sustain an extra exciton. As electrons and holes occupy a given wave vector $\mathbf{k}$, states in the phase space are no longer available for the formation of an exciton, the relative change of oscillator strength due to PSF is given by [94]:

$$\left(\frac{\delta f_{osc}^{1s}}{f_{osc}^{1s}}\right)_{PSF} = -\sum_{\mathbf{k}} \left[f_e(\mathbf{k}) + f_h(\mathbf{k})\right] \frac{\Phi_{1s}(\mathbf{k})}{\Phi_{1s}(\mathbf{r}=\mathbf{0})} = -\frac{n_X}{n_{PSF}^{sat}} = -n_X\left(\frac{32}{7}\pi a_B^2\right). \tag{1.19}$$

where $f_{e,h}(\mathbf{k}) = \frac{n_X}{2}|\Phi_{1s}(k)|^2$ is the distribution of electrons (holes) in the case of resonant generation of excitons. In opposition to the PSF term, which does not affect the excitonic resonance ω_{1s}, the exchange term is accompanied with a blueshift in the emission energy. To calculate the reduction in

the oscillator strength associated to this process, the correction of the $1s$ exciton transition due to the Coulomb interaction compared to the unperturbed case is summed over all excited states ($n > 1$) in the mean field approximation [94]:

$$\left(\frac{\delta f_{\mathrm{osc}}^{1\mathrm{s}}}{f_{\mathrm{osc}}^{1\mathrm{s}}}\right)_{\mathrm{EX}} = \sum_{n>1}\left(\frac{\langle 1s|\hat{H}-\hat{H}_0|n\rangle}{\omega_{1\mathrm{s}}-\omega_{\mathrm{n}}}\frac{\Phi_{\mathrm{n}}^*(\mathbf{r}=\mathbf{0})}{\Phi_{1\mathrm{s}}^*(\mathbf{r}=\mathbf{0})}+c.c.\right) = -\frac{n_{\mathrm{X}}}{n_{\mathrm{EX}}^{\mathrm{sat}}} = -n_{\mathrm{X}}\left(\frac{4832}{1225}\pi a_{\mathrm{B}}^2\right), \tag{1.20}$$

where $\hat{H}_0$ and $\hat{H}$ correspond to the unperturbed (no Coulomb interaction) and perturbed Hamiltonians, respectively, and $c.c$ is the complex conjugate of the expression between the parentheses. Finally, the saturation density $n_{\mathrm{X}}^{\mathrm{sat}} = n_{\mathrm{PSF}}^{\mathrm{sat}} + n_{\mathrm{EX}}^{\mathrm{sat}}$ follows from relations 1.19 and 1.20:

$$n_{\mathrm{X}}^{\mathrm{sat}} \approx \frac{0.117}{\pi a_{\mathrm{B}}^2}. \tag{1.21}$$

This relation is the one commonly used to evaluate the saturation density in quantum well based microcavities. It is important to notice that relation 1.21 is derived in the case where the saturating particle is the exciton and neglects the contribution of free electrons and holes on the stability of the bound complexes.

1.1.6.2 Renormalization of the excitonic transition

The excitonic transition $\omega_{1\mathrm{s}}$ is found to shift to higher energy with increasing carrier density in quantum well structures [99]. This effect is attributed to the predominant repulsive interaction between excitons for elevated densities (i.e., the exchange term of the Coulomb interaction). In addition photoluminescence measurements performed under nonresonant excitation indicate that exciton-exciton interactions are also responsible for the collisional broadening of the excitonic line [100].

Even if the renormalization of the exciton energy occurring in quantum wells was first investigated theoretically by Schmitt-Rink and coworkers [94], we rather use in this thesis the approach of Tassone and Yamamoto [101], which is equivalent to that of Ciuti and coworkers [102, 103] and describes in more details the Coulomb interaction. The following expression is commonly used for the exciton blueshift (see Ref. [23] and references therein):

$$\delta E_{\mathrm{X}} = E_{\mathrm{X}}^{\mathrm{b}}\frac{n}{n_{\mathrm{X}}^{\mathrm{sat}}} = E_{\mathrm{X}}^{\mathrm{b}} n\left(2.2\pi a_{\mathrm{B}}^2\right) \tag{1.22}$$

Note finally that the shift of the excitonic transition strongly depends on the dimensionality of the system *via* the term $E_{\mathrm{X}}^{\mathrm{b}}$ and is enhanced when the quantum well thickness is decreased [104].

1.1.7 Interaction with the electromagnetic field

1.1.7.1 Light-matter interaction Hamiltonian

The common way to derive the interaction between Bloch electrons in a crystal and the vacuum field is the semi-classical approach where unperturbed electrons are described by the Schrödinger equation for the crystal (equation 1.2) and the electric $\mathscr{E}(\mathbf{r},t)$ and magnetic $\mathscr{B}(\mathbf{r},t)$ fields at position $\mathbf{r}$ and time t satisfy Maxwell's equations, i.e., the photon field is not quantized. In the presence of an external magnetic field $\mathscr{B}^{\mathrm{ext}}(\mathbf{r},t) = \nabla\wedge\mathscr{A}(\mathbf{r},t)$, the momentum of a moving electron with charge e is changed

by a quantity $\delta \mathbf{p} = -\frac{e}{c}\mathscr{A}$ [72], where c is the speed of light in vacuum and $\mathscr{A}(\mathbf{r}, t)$ is the magnetic vector potential. The interaction Hamiltonian of the electron in the crystal perturbed by an external field is obtained by transforming the Hamiltonian 1.2 with the substitution $\hat{\mathbf{p}} \to \hat{\mathbf{p}} + \delta \mathbf{p}$:

$$\hat{\mathscr{H}}_{\mathrm{int},1}^{\mathrm{X-C}} = \frac{e}{m_0}\mathbf{A}.\hat{\mathbf{p}} + \mathscr{O}\left(\mathbf{A}^2\right), \tag{1.23}$$

where $\hat{\mathbf{p}} = -i\hbar\nabla$ is the momentum operator and the term proportional to $\mathscr{A}^2$ is supposed to be small since the external field is treated as a second order perturbation. It is important to point out that the Hamiltonian 1.23 is not unique and depends on the choice of the gauge. In the case of a globally neutral system whose motion is restricted to small distances (i.e. smaller than the optical wavelength), the dipolar approximation can be made and the use of the Göppert-Mayer gauge (instead of the Coulomb one) transforms $\hat{\mathscr{H}}_{\mathrm{int},1}^{\mathrm{X-C}}$ into:

$$\hat{\mathscr{H}}_{\mathrm{int},2}^{\mathrm{X-C}} \approx -\mathbf{d}.\mathscr{E}, \tag{1.24}$$

where $\mathbf{d} = \sum_{\mathrm{i}} q_{\mathrm{i}}\mathbf{x}_{\mathrm{i}}$ is the electric dipole moment of the considered electric system with $\mathbf{x}_{\mathrm{i}}$ and q_{i} the dipole vector and charge of the ith particle.

1.1.7.2 Oscillator strength of quantum well excitons

In this work, we are interested in the strength of the light-matter coupling between 2D-quantum well excitons and 2D-cavity photons (described in Section 1.2). The relevant physical quantity, which describes the coupling between these two modes, is the oscillator strength per unit area for a given polarization $\boldsymbol{\epsilon} \in \{\hat{x}, \hat{y}, \hat{z}\}$, $f_{\mathrm{osc},\boldsymbol{\epsilon}}^{\mathrm{QW}}/S$, with $\hat{z}$ the unitary vector pointing along the growth direction. Using the interaction Hamiltonian $\hat{\mathscr{H}}_{\mathrm{int},1}^{\mathrm{X-C}}$, the oscillator strength between the initial state $|1\rangle$ corresponding to no photon in the cavity and one exciton with polarization $\boldsymbol{\epsilon}$ and the final state $|2\rangle$ corresponding to one photon with polarization $\boldsymbol{\epsilon}$ in the cavity and no exciton (crystal ground state) reads [105]:[9]

$$\frac{f_{\mathrm{osc},\boldsymbol{\epsilon}}^{\mathrm{QW}}}{S} = \frac{2}{M_{\mathrm{X}}E_{\mathrm{X}}}\left\langle 1\left|\hat{\mathscr{H}}_{\mathrm{int},1}^{\mathrm{X-C}}\right|2\right\rangle = \frac{2}{M_{\mathrm{X}}E_{\mathrm{X}}}\left|\Phi(\boldsymbol{\rho}=0)\right|^2\left|\langle u_{\mathrm{C}}\left|\mathbf{p}.\boldsymbol{\epsilon}\right|u_{\mathrm{V}}\rangle\right|^2\left|\int f_{\mathrm{e}}^*(z)\,f_{\mathrm{h}}(z)\,dz\right|^2, \tag{1.25}$$

where E_{X} is the exciton energy. In the limit where the coupling between light and matter can be treated as a perturbation, Fermi's golden rule can be used to evaluate the interaction matrix element $\left\langle 1\left|\hat{\mathscr{H}}_{\mathrm{int},1}^{\mathrm{X-C}}\right|2\right\rangle$ and the radiative recombination rate for excitons polarized perpendicularly to the growth axis can be calculated:

$$\Gamma_0 = \frac{e^2}{4\epsilon_0 n_{\mathrm{cav}} m_0 c}\frac{f_{\mathrm{osc,xy}}^{\mathrm{QW,1s}}}{S}, \tag{1.26}$$

where n_{cav} is the mean refractive index of the cavity section with embedded quantum wells and $\frac{f_{\mathrm{osc,xy}}^{\mathrm{QW,1s}}}{S}$ is the in-plane exciton oscillator strength for the 1s exciton given by [106]:

$$\frac{f_{\mathrm{osc,xy}}^{\mathrm{QW,1s}}}{S} = \frac{2p_{\mathrm{cv}}^2}{m_0 E_{\mathrm{X}}}\left|\int f_{\mathrm{e}}^*(z)\,f_{\mathrm{h}}(z)\,dz\right|^2\frac{2}{\pi a_{\mathrm{B}}^2}, \tag{1.27}$$

where p_{cv} is the conduction-valence band dipole matrix element at the Γ-point, which is related to the Kane parameter E_{P} of the material (see Tab. 2.5 for III-nitride values) *via* the relation $p_{\mathrm{cv}} = \sqrt{\frac{m_0}{2}E_{\mathrm{P}}}$. Relation 1.27 is only valid for excitons at the center of the Brillouin zone, i.e., for $k_\parallel = 0$. The radiative

[9] Note here that the exciton-cavity photon ensemble is assimilated to a two-level system.

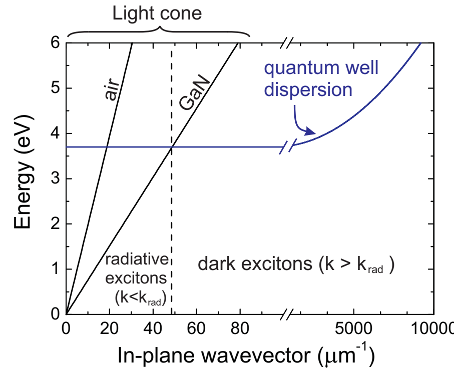

Fig. 1.2: Exciton dispersion curve of a narrow GaN/(Al,Ga)N quantum well ($L_{QW} = 1.2\,\mathrm{nm}$) at room temperature (blue) together with the light cone for air and GaN, which delimits regions where spontaneous photon emission in air or in the substrate is allowed. All the states with momentum beyond k_{rad} are called dark excitons as they cannot recombine radiatively.

decay time for an exciton at the Γ-point is defined as $\tau_{rad} = 1/(2\Gamma_0)$ [107], which amounts to ≈ 1 ps for a polarization-free thick GaN quantum well.

Finally, it is worth mentioning that the oscillator strength in a square quantum well is increased with respect to the bulk case [106] illustrating the advantage of quantum well based microcavities over bulk ones. Note that in III-nitride quantum wells grown along the polar orientation, the presence of a built-in electric field decreases the oscillator strength due to the decrease in the electron and hole wave functions overlap (see Section 2.2.6).

1.1.7.3 Dark excitons

The interaction between light and quantum well excitons in planar microcavities results from the coupling between heavy (hh) or light hole (lh) excitons and a cavity photon.[10] Thereby, the exciton total angular momentum along the growth direction z consists of that of the electron $J_z^e = \pm\frac{1}{2}$ and that of the hole: $J_z^{lh} = \pm\frac{1}{2}$ or $J_z^{hh} = \pm\frac{3}{2}$, respectively. Consequently, the resulting spin projection reads $J_z^X \in \{\pm1, \pm2\}$ for hh-excitons and $J_z^X \in \{0, \pm1\}$ for lh ones. As the photon carries a momentum $J_z^C = 1$ (right-circular polarized, σ^+) or $J_z^C = -1$ (left-circular polarized, σ^-), the coupling of excitonic states with $J_z^X = 0$ and $J_z^X = \pm2$ to the photonic mode is forbidden by spin selection rules. They are thus called *dark excitons*.

In addition to the latter, we also have to consider the nonradiative excitons that cannot emit light because they are out of the light cone. In a perfect 2D-system, excitons with in-plane wave vector $\mathbf{k}_\parallel$ (with modulus $k_\parallel$) couple to photons with the same momentum. In a quantum well, this is realized for all possible values of k_z, which represents a continuum of states. However, if the energy of the excitons $E_X(k_\parallel)$ is below the light cone of the considered material, i.e., if $E_X(k_\parallel) < (\hbar c/n_{cav})\,k_\parallel$, the modes are evanescent in the material and therefore cannot couple to the light. Oppositely, for the excitonic sates with $E_X(k_\parallel) > (\hbar c/n_{cav})\,k_\parallel$, the modes are propagating and can thus radiate out of the structure. The in-plane wave vector delimiting the transition between radiative and nonradiative excitons is given by the condition:

[10] This simple picture is true for zinc-blende semiconductors only such as GaAs or CdTe. In GaN compounds, the crystal-field and spin-orbit splitting lift the valence-band degeneracy at the Γ point: the A-exciton is nearly equivalent to the heavy hole but B and C excitons are mixed, depending on the strain state of the quantum well [108].

$$k_{\text{rad}} = \frac{E_{\text{X}}(k_{\text{rad}})\, n_{\text{cav}}}{\hbar c} = \frac{n_{\text{cav}}}{\hbar c}\left(E_{\text{X}}\left(k_{\parallel}=0\right) + \frac{\hbar^2 k_{\text{rad}}^2}{2M_{\text{X}}}\right) \approx \frac{n_{\text{cav}}}{\hbar c} E_{\text{X}}\left(k_{\parallel}=0\right). \tag{1.28}$$

The situation is depicted in Fig. 1.2 for a GaN-based quantum well. The exciton dispersion curve (blue) is shown together with the light cone for air and GaN, which delimits regions where spontaneous emission in air or in the substrate is allowed. Excitons with $0 < k < k_{\text{rad,air}} \approx 20\,\mu\text{m}^{-1}$ can spontaneously emit light into air and GaN, whereas for $k_{\text{rad,air}} < k < k_{\text{rad}} \approx 50\,\mu\text{m}^{-1}$ spontaneous emission can occur in the GaN substrate only ($k_{\text{rad,air}}$ corresponds to the crossing between the light cone for air and the exciton dispersion curve). It is important to notice that the fraction of radiant states is very small compared to the total exciton population. When investigating the dynamics of excitons in microcavities, one has to consider that the major fraction of the excitonic population is not coupled to the external field and thus acts as a particle reservoir with a lifetime given by the exciton nonradiative lifetime.

Note finally that in a quantum well-based microcavity, other dark excitonic modes appear due to the coupling with the intracavity field. Indeed, the quantum wells located at the nodes of the standing wave do not participate to the light-matter interaction process. In addition, when the number of quantum wells N_{QW} exceeds one, the coupling with the electric field leads to the formation of $N_{\text{QW}} - 1$ dark states (see Sections 1.3.5 and 3.2.3).

1.1.7.4 Dielectric response of the quantum well exciton

In this thesis, we consider the Drude-Lorentz damped harmonic oscillator model to describe the optical response of the quantum well exciton. In this approximation the homogeneous dielectric response of a quantum well of thickness L_{QW} with an excitonic resonance at $E = E_{\text{X}}$ reads:

$$\epsilon_{\text{hom}}(E; E_{\text{X}}) = \epsilon_{\text{B}} + \frac{1}{L_{\text{QW}}} \frac{f_{\text{osc,xy}}^{\text{X}}}{S} \frac{e^2\hbar^2}{\epsilon_0 m_0} \frac{1}{E_{\text{X}}^2 - E^2 + i\gamma_{\text{h}} E}, \tag{1.29}$$

where ϵ_{B} is the background dielectric constant and γ_{h} is the homogeneous broadening of the excitonic transition. The free carrier absorption and the Urbach tail are accounted for by adding the following component to the complex refractive index $n(E) = n_{\text{R}}(E) - i\, n_{\text{I}}(E)$:

$$n_{\text{I}}(E) = -i\frac{\alpha(E)\,\lambda}{4\pi}, \tag{1.30}$$

where $\alpha(E)$ is given by relation 1.12 and λ is the emission wavelength in vacuum. As $\epsilon(E) = n^2(E)$, the following contribution has to be added to the dielectric constant:

$$\Delta\epsilon(E) = n_{\text{R}}^2(E) - n_{\text{I}}^2(E) - 2i\, n_{\text{R}}(E)\, n_{\text{I}}(E). \tag{1.31}$$

However, equation 1.29 fails in describing a system where the inhomogeneous broadening is important as it is the case for III-nitride materials. To account for the emission energy distribution induced by disorder, the homogeneous contribution $\epsilon_{\text{hom}}(E; E_0)$ should be convoluted with a Gaussian distribution with a standard deviation σ related to the inhomogeneous broadening γ_{inh} by the relation $\gamma_{\text{inh}} = 2\sigma\sqrt{2\ln 2}$. The resulting dielectric function finally reads:

$$\epsilon(E; E_{\text{X}}) = \frac{1}{\sigma\sqrt{2\pi}} \int_{-\infty}^{\infty} \exp\left(-\frac{\left(E' - E\right)^2}{2\sigma^2}\right) \epsilon_{\text{hom}}\left(E'; E_{\text{X}}\right) dE'. \tag{1.32}$$

1.2 Optics of cavities

In the previous section, the optical properties of semiconductor epilayers including quantum wells were discussed. The excitonic response in such structures can be treated perturbatively as the resonance is coupled to a continuum of states (vacuum field). In order to increase the efficiency of the light-matter coupling, one should reduce the modal volume of the electric field in resonance with the excitonic transition and increase the photon lifetime, e.g. by increasing the number of passes of a given photon through the active medium before it escapes the active region. A standard way to fulfill these conditions is the use of a planar microcavity, which consists of two mirrors surrounding a spacer whose optical thickness matches a multiple integer of the emitter half wavelength. Here we first describe the ideal Fabry-Perot resonator before discussing the specific case of semiconductor cavities, which differ by the type of mirrors used (see Figs. 1.3(a) and 1.3(b)). These structures allow the control of the emission properties of the semiconductor materials placed inside, such as the spatial distribution of the radiated power, the line shape of the emitted light and a control of the spontaneous emission rate [109].

1.2.1 The Fabry-Perot resonator

Most of the properties of interest in the study of semiconductor resonators such as the resonance frequency, the finesse or the angular dispersion are well accounted for within the Fabry-Perot description. A Fabry-Perot resonator represents the simplest geometry for the confinement of the electromagnetic field and consists of a dielectric spacer of thickness L_{cav} and refractive index n_{cav} sandwiched between two metallic mirrors characterized by their complex reflection $\tilde{r}_{1,2} = r_{1,2}e^{i\phi_{1,2}(\omega)}$ and transmission $\tilde{t}_{1,2} = 1 - \tilde{r}_{1,2}$ (if absorption is neglected) coefficients, where $\phi_{1,2}(E)$ is the phase accumulated at mirrors 1 and 2, respectively. We assume in the following that the resonator is in the air with $n_{\text{cav}} > n_{\text{air}}$.

Considering an incident plane wave with angular frequency ω and complex amplitude $\tilde{E}_{\text{in}}(\omega) = \tilde{E}_0 e^{i\omega t}$ and intensity $I_0 = \left|\tilde{E}_0\right|^2$ coming from the left onto a Fabry-Perot resonator with an angle θ_{ext} (see Fig. 1.3(a)), the transmitted and reflected beams read $\tilde{t}_1 \tilde{E}_{\text{in}}(\omega)$ and $\tilde{r}_1 \tilde{E}_{\text{in}}(\omega)$, respectively. The transmitted component will propagate through the spacer until reaching mirror 2. As no absorption is considered, the norm of the field is left unchanged but its phase is increased by $\Delta\phi = \phi_{\text{cav}} = 2\omega n_{\text{cav}} L_{\text{cav}} \cos(\theta_{\text{in}})/c$, where the internal angle is given by Snell's law $\theta_{\text{in}} = \arcsin[\sin(\theta_{\text{ext}})/n_{\text{cav}}]$. At mirror 2, the incoming complex amplitude of the field reads $\tilde{t}_1 \tilde{E}_{\text{in}}(\omega)\, e^{i\phi_{\text{cav}}(\omega)}$ and splits again into

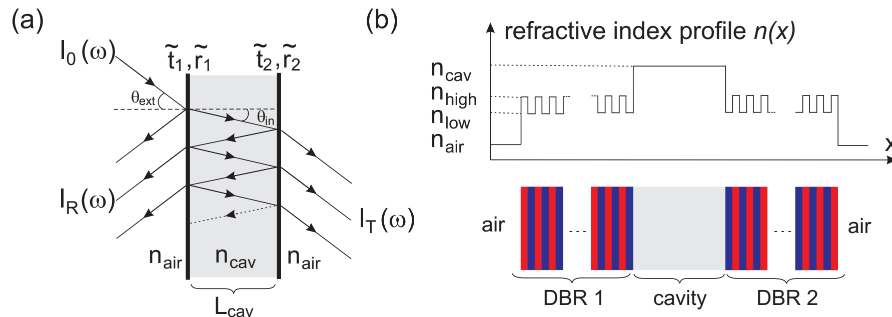

Fig. 1.3: Schematic representation of: (a) a Fabry-Perot interferometer surrounded by air. $I_0(\omega)$, $I_R(\omega)$ and $I_T(\omega)$ are the intensities of the external, reflected and transmitted beams at the energy $\hbar\omega$, respectively. $\theta_{\text{ext,in}}$ is the incident (internal) angle. (b) Schematic description of a Bragg mirror-based microcavity surrounded by air (bottom), together with the refractive index profile (top).

a transmitted beam $\tilde{t}_2\tilde{t}_1\tilde{E}_{\text{in}}(\omega)\,e^{\mathrm{i}\phi_{\text{cav}}(\omega)}$ and a reflected one $\tilde{r}_2\tilde{t}_1\tilde{E}_{\text{in}}(\omega)\,e^{\mathrm{i}\phi_{\text{cav}}(\omega)}$. Overall the field will undergo an infinite number of internal reflections and transmissions. Grouping all the transmitted terms, we end up with a converging geometric series and the transmitted field $\tilde{E}_{\text{out}}(\omega)$ finally reads:

$$\tilde{E}_{\text{out}}(\omega) = \tilde{E}_{\text{in}}(\omega)\,\tilde{t}_1\tilde{t}_2 e^{i\phi_{\text{cav}}(\omega)} \sum_{\text{n}=0}^{\infty}\left(\tilde{r}_1\tilde{r}_2 e^{2i\phi_{\text{cav}}(\omega)}\right)^n = \tilde{E}_{\text{in}}(\omega)\,\frac{\tilde{t}_1\tilde{t}_2 e^{i\phi_{\text{cav}}(\omega)}}{1-\tilde{r}_1\tilde{r}_2 e^{2i\phi_{\text{cav}}(\omega)}}. \tag{1.33}$$

The intensity of the transmitted field is given by:

$$I_{\text{T}}(\omega) = \left|\tilde{E}_{\text{out}}(\omega)\right|^2 = \frac{I_{\max}}{1+\left(\frac{2F_{\text{FP}}}{\pi}\right)^2 \sin^2\left(\phi_{\text{tot}}(\omega)/2\right)}, \tag{1.34}$$

where $\phi_{\text{tot}}(\omega) = \phi_1(\omega)+\phi_2(\omega)+2\phi_{\text{cav}}(\omega)$ is the total phase accumulated in the Fabry-Perot resonator, $I_{\max} = \frac{I_0(t_1t_2)^2}{(1-r_1r_2)^2}$ is the transmitted intensity at the resonance frequency ω_{res}, and F_{FP} is called the *finesse* of the resonator, which is a direct measure of the resonator selectivity. This quantity is completely determined by the resonator losses and is independent of the resonator length. In our case, the losses are only given by the mirrors as absorption is neglected here. F_{FP} is defined as the ratio between the free spectral range ΔE, i.e., the spectral separation between two consecutive modes, over the mode broadening δE. At normal incidence, one thus finds:

$$F_{\text{FP}} = \frac{\Delta E}{\delta E} = \pi\frac{\sqrt{r_1r_2}}{1-r_1r_2}. \tag{1.35}$$

In Fig. 1.4(a), the transmission of a Fabry-Perot resonator with mirrors having the same reflectivity, i.e., $r = r_1 = r_2$ and $I_{\max} = I_0$, is shown for different finesses ranging from 0 to 10. It clearly appears that the spectral selection becomes more accurate when F_{FP} is increased. In Fig. 1.4(b), both finesse and optical mirror losses (α_{m}) are displayed as a function of the reflectivity r highlighting the close link between them and the increasing impact of losses for low r-values. α_{m} is given by the relation:

$$\alpha_{\text{m}} = \frac{1}{2L_{\text{cav}}}\ln\left(\frac{1}{R_1R_2}\right), \tag{1.36}$$

where $R_{\text{i}} = |r_{\text{i}}|^2$ is the reflectance of mirror i. Another quantity of interest in our study is the quality factor of the resonator Q, which corresponds to the rate of energy loss compared to the energy stored. It

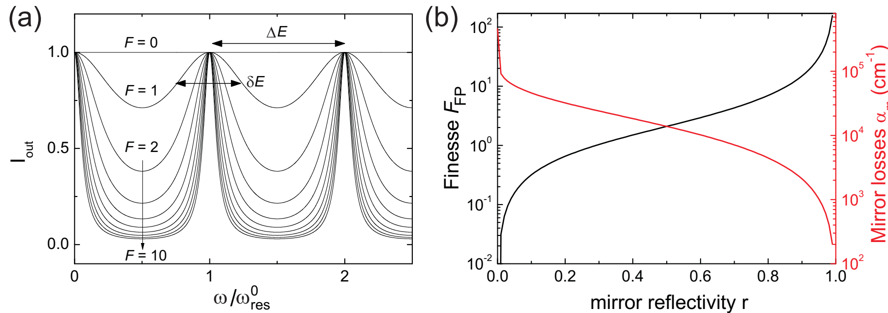

Fig. 1.4: Simulation of a Fabry-Perot interferometer properties: (a) evolution of the transmission spectra for various finesses ranging from 0 to 10 featuring an increase in the spectral selectivity. (b) Evolution of the finesse (black) and mirrors losses (red) vs. mirror reflectivity featuring the strong correlation between these two quantities.

is defined as the mode energy $E_{\mathrm{res}}^{\mathrm{m}}$ (given by relation 1.40) over the mode broadening. For a Fabry-Perot, it reads:

$$Q_{\mathrm{FP}}^{\mathrm{m}} = \frac{E_{\mathrm{res}}^{\mathrm{m}}}{\delta E} = m\pi \frac{\sqrt{r_1 r_2}}{1 - r_1 r_2} = m F_{\mathrm{FP}}, \quad m \in \mathbb{N}. \tag{1.37}$$

Even if the finesse and the quality factor have very similar expressions they have different physical interpretations. Whereas the finesse quantifies the quality of the mode separation (spectral range over broadening), the quality factor is a direct measure of the ability of the cavity to store light. Actually the quality factor can be defined for every oscillator (or resonator), mechanical, electrical or optical one as the energy stored over the energy dissipated per cycle. In the study of light-matter interaction, this parameter is of special interest as it is directly proportional to the cavity photon lifetime τ_{cav} *via* the relation $\tau_{\mathrm{cav}} = \frac{Q}{\omega_{\mathrm{res}}}$. The frequency resonances of the Fabry-Perot $\omega_{\mathrm{res}}^{\mathrm{m}} = E_{\mathrm{res}}^{\mathrm{m}}/\hbar$ are given by the phase-matching condition at the boundaries:

$$e^{i\phi_{\mathrm{tot}}(\omega_{\mathrm{res}})} = 1 \quad \leftrightarrow \quad \phi_{\mathrm{tot}}(\omega_{\mathrm{res}}) = \phi_1(\omega_{\mathrm{res}}) + \phi_2(\omega_{\mathrm{res}}) + 2\phi_{\mathrm{cav}}(\omega_{\mathrm{res}}) = m \times 2\pi, \quad m \in \mathbb{N}. \tag{1.38}$$

In the case of a Fabry-Perot resonator, as $n_{\mathrm{cav}} > n_{\mathrm{air}}$, the wave undergoes no dephasing inside the cavity and $\phi_1(\omega) = \phi_2(\omega) = 0$. Due to the planar geometry and the confinement of light in the growth direction z, it is convenient to write the cavity wave vector as $\mathbf{k}^{\mathrm{cav}} = \mathbf{k}_{\parallel}^{\mathrm{cav}} + \mathbf{k}_{z}^{\mathrm{cav}}$, where the in-plane wave vector $\mathbf{k}_{\parallel}^{\mathrm{cav}}$ is conserved due to the translation invariance in this direction. It is thus conserved at any interface and its norm reads:

$$k_{\parallel}^{\mathrm{cav}} = k_0 \sin(\theta_{\mathrm{ext}}) = k^{\mathrm{cav}} \sin(\theta_{\mathrm{in}}), \tag{1.39}$$

where $k_0 = \frac{E}{\hbar c}$ is the norm of the wave vector of the incident photon with energy E and $k^{\mathrm{cav}} = \frac{E n_{\mathrm{cav}}}{\hbar c}$ the norm of the wave vector in the cavity. As the light is confined in the z-direction, we are interested in the energy dispersion of the in-plane cavity photon. $E_{\mathrm{res}}^{\mathrm{m}}\left(k_{\parallel}^{\mathrm{cav}}\right)$ directly follows from the resonance condition 1.38:

$$\begin{aligned}
\phi_{\mathrm{tot}} = 2k_z^{\mathrm{cav}} L_{\mathrm{cav}} &= m\pi, \\
\sqrt{\left(\frac{E_{\mathrm{res}}^{\mathrm{m}} n_{\mathrm{cav}}}{\hbar c}\right)^2 - \left(k_{\parallel}^{\mathrm{cav}}\right)^2} &= \frac{m\pi}{L_{\mathrm{cav}}}, \\
E_{\mathrm{res}}^{\mathrm{m}}\left(k_{\parallel}^{\mathrm{cav}}\right) &= \frac{\hbar c}{n_{\mathrm{cav}}} \sqrt{\left(\frac{m\pi}{L_{\mathrm{cav}}}\right)^2 + \left(k_{\parallel}^{\mathrm{cav}}\right)^2}, \quad m \in \mathbb{N}.
\end{aligned} \tag{1.40}$$

For small in-plane wave vectors, the cavity photon dispersion is nearly parabolic, which allows defining the effective mass of the cavity photon:

$$m_{\mathrm{eff}}^{\mathrm{cav}} = \frac{\hbar\pi m n_{\mathrm{cav}}}{c L_{\mathrm{cav}}}. \tag{1.41}$$

1.2.2 The semiconductor planar cavity

Because of the relatively low reflectivity of metallic mirrors in the UV energy range considered in this work (typically ~ 90%) and the difficulty of growing high quality semiconductor epilayers on metal, semiconductor planar microcavities usually consist of a cavity section sandwiched between two distributed Bragg reflectors (DBRs). In this section, we briefly review the properties of DBRs and their impact on the properties of semiconductor microcavities compared to Fabry-Perot resonators.

1.2.2.1 Distributed Bragg reflectors (DBRs)

A DBR consists of a stack of bilayers with different refractive indices n_{low} and n_{high}, with $n_{low} < n_{high}$ (see Fig. 1.3(b)). The idea to achieve an arbitrary high reflectivity is to alternate layers with an optical thickness equal to $\lambda_{DBR}/4$, where λ_{DBR} is the targeted wavelength for the DBR. At normal incidence, the waves reflected at each layer interface interfere constructively and the transmitted ones destructively. The maximum reflectivity R_{max} for a DBR is only limited by the number of pairs and the refractive index contrast $\Delta n = n_{high} - n_{low}$. As Δn is usually imposed by the available materials, the only degree of freedom to tune the mirror peak reflectivity is the number of pairs N_{pairs} [110]:

$$N_{pairs} = \frac{1}{2} \log\left(\frac{n_{in}}{n_{out}} \frac{1-\sqrt{R_{max}}}{1+\sqrt{R_{max}}}\right) / \log\left(\frac{n_{low}}{n_{high}}\right), \tag{1.42}$$

where n_{in} and n_{out} are the refractive indices of the medium on the incident and the transmitted side, respectively. In Fig. 1.5(a), the number of pairs is plotted as a function of R_{max} for a dielectric SiO_2/Si_3N_4-based DBR where the incident medium is air and output medium is alternatively air and GaN. Due to the higher refractive index of GaN compared to air, the reflectivity on the last layer of the DBR is lower and a higher number of pairs is required to reach R_{max}. The simulation is performed for a central DBR energy $E_{DBR} = 3.7$ eV, which corresponds to the emission energy at low temperature of the narrow GaN quantum wells investigated in this thesis.

The main difference between metallic mirrors and DBRs comes from the dispersion of the phase after reflection on the mirrors, i.e., $d\phi_{DBR}(E)/dE \neq 0$ whereas $d\phi_{metal}(E)/dE = 0$. However, for $E = E_{DBR}$, $\phi = 0$ and the phase shift is exactly the same as for a metallic mirror. When the energy is slightly different from the targeted one, the interference condition slightly deviates from the optimum case and the reflectivity decreases giving rise to a finite energy domain where the reflectivity is high. This energy region is referred to as the *DBR stopband*. For a small energy range around E_{DBR}, the phase dispersion is linear:

$$\phi_{DBR}(E) = \frac{2 n_{in} L_{DBR}}{\hbar c} (E - E_{DBR}). \tag{1.43}$$

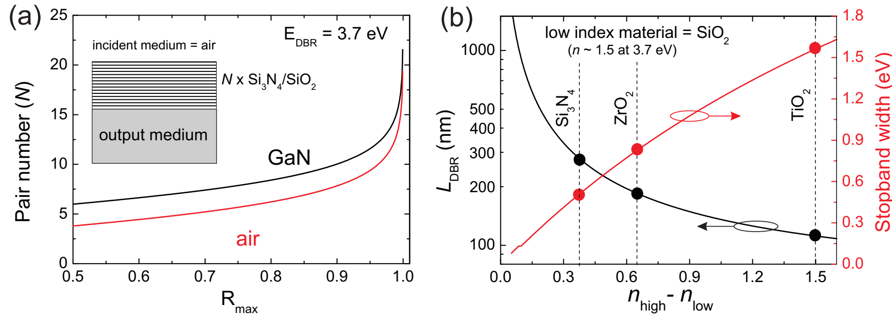

Fig. 1.5: Simulation of DBR properties: (a) impact of the output medium on the pair number for the case of GaN (black line) and air (red line) for a photon energy of 3.7 eV in a Si_3N_4/SiO_2-based DBR. The incident medium is air. (b) Evolution of the penetration depth (black line) and stopband width (red line) as a function of the bilayer refractive index contrast. The low refractive index material considered here is SiO_2 for a photon energy of 3.7 eV. Cases where the high refractive index material is Si_3N_4 ($n \approx 1.88$), ZrO_2 ($n \approx 2.15$) or TiO_2 ($n \approx 3$) are identified with filled circles

In sharp contrast with metallic mirrors, the electric field can penetrate into the DBRs with a characteristic depth L_{DBR}, which makes the effective optical path in the cavity longer. L_{DBR} is given by [110]:

$$L_{DBR} = \frac{\lambda_{DBR}}{4n_{in}} \frac{\min\{n_{in}, n_{low}\}}{\max\{n_{in}, n_{low}\}} \frac{n_{high}}{n_{high} - n_{low}}. \quad (1.44)$$

The stopband width ΔE_{SB} is approximately given by [110]:

$$\Delta E_{SB} \approx \frac{4E_{DBR}}{\pi} \frac{n_{high} - n_{low}}{n_{high} + n_{low}}. \quad (1.45)$$

Relations 1.43 to 1.45 are only valid for an infinite number of pairs but it gives the correct trend for L_{DBR} shorter than the DBR thickness. A more accurate description of the optical properties necessarily requires transfer matrix simulations (see Appendix C).

Note that L_{DBR} critically depends on the choice of the bilayer components, i.e., the larger the refractive index contrast the shorter the penetration depth. In Fig. 1.5(b), L_{DBR} is monitored together with the DBR stopband width as a function of the refractive index contrast $n_{high} - n_{low}$ for a DBR where the low index material is SiO_2 ($n \approx 1.5$ at 3.7 eV). Situations where the high index material is Si_3N_4 ($n \approx 1.88$), ZrO_2 ($n \approx 2.15$) and TiO_2 ($n \approx 3$) are shown with filled circles. It appears that TiO_2 ($n \approx 3$) could be a material of choice to minimize the penetration depth of the electromagnetic field in the DBR while keeping the broadest possible stopband width. However, the absorption occurring in the DBR has not been considered so far and it is mandatory to keep E_{DBR} far below the absorption edge E_{abs} to avoid the damping of the electric field, which prevents the use of TiO_2 ($E_{abs} \approx 3.3$ eV) for GaN-based microcavities.

Let us now have a look at the energy dispersion of DBR structures. In Figs. 1.6(a)-1.6(b), angle-resolved reflectivity spectra calculated with the 2×2 transfer matrix formalism for the TE-polarization are shown for a 10-pair Si_3N_4/SiO_2-based DBR and a 10-pair ZrO_2/SiO_2-based DBR. As expected, the stopband width is larger for the structure presenting the highest refractive index contrast. Another interesting feature is the presence of dispersive modes called *Bragg modes* on each side of the stopband (labeled with white dashed lines). Similarly to the case of the Fabry-Perot resonator, these modes result from constructive interferences occurring in the various layers and present a dispersion, which depends

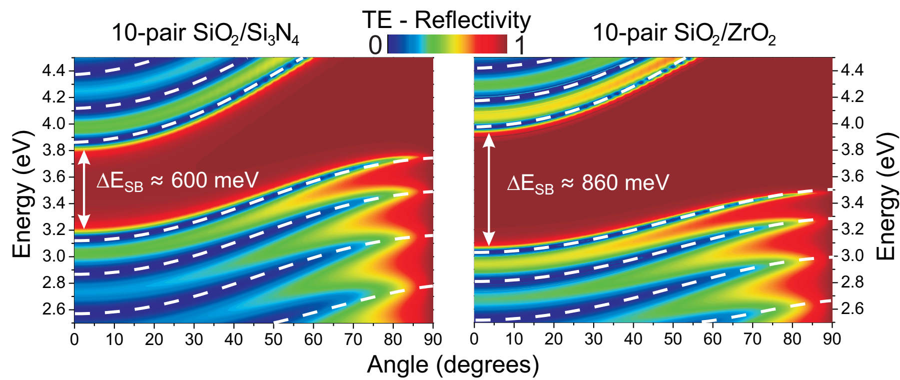

Fig. 1.6: Angle-resolved reflectivity spectra calculated with the 2×2 transfer matrix formalism for the TE-polarization for: (a) 10-pair Si_3N_4/SiO_2-based DBR. (b) 10-pair ZrO_2/SiO_2-based DBR. Both are centered at $E_{DBR} = 3.5$ eV. The energy dispersion of the Bragg modes is indicated by white dashed lines.

on the mean refractive index of the structure. According to relation 1.41, the structure made from the bilayers presenting the lowest mean refractive index, i.e., Si_3N_4/SiO_2 (Fig. 1.6(a)), also presents the lowest effective photonic mass and thus the steepest dispersion. Bragg modes are often referred to as leaky modes as they constitute the main sink of radiation in planar microcavities and will therefore play an important role in the study of polaritons.

Before concluding this section on DBRs, it is worth mentioning that from a pure optical point of view, dielectric DBRs offer the best performances. However, in the present work, we are interested in III-nitride based microcavities where the quality of the active region (i.e. the spacer layer) is critical for the optimization of the light-matter interaction. Unfortunately, coherent growth on dielectric layers is not easily achievable and the quality of the epilayers is strongly reduced. For this reason, the majority of III-nitride based microcavities features a hybrid architecture, i.e., the bottom DBR and the overgrown cavity region consist of a monolithic III-nitride layer stack in order to ensure an optimum optical quality for the active medium. Thereby, the refractive index contrast of the DBR bilayer components $(\Delta n/n)_{\mathrm{nitride}}$ is strongly limited and amounts to about 10% in the best cases [59]. Hence, a high number of pairs (typically > 30) is required to reach a reflectivity as large as 99.5% and a stopband width exceeding 200 meV [111]. This implies a significant penetration depth of the light electric field into the DBR, which detrimentally affects the coupling strength in this geometry. The presence of propagative defects, interface roughness and residual absorption might further decrease the polariton lifetime. For all these reasons a full dielectric microcavity approach providing both a high refractive index contrast, $(\Delta n/n)_{\mathrm{diel}} > 30\%$, and low absorption, which looks better suited to achieve Q-factors exceeding $10'000$ but raises serious challenges in terms of fabrication and processing.

1.2.2.2 Semiconductor microcavities: deviation from the Fabry-Perot resonator

Contrary to Fabry-Perot cavities where the whole electromagnetic field is confined within the spacer, semiconductor microcavities, which usually consist in a spacer sandwiched between two DBRs, suffer from the field penetration in the mirrors. The fraction of light out of the spacer does not participate to the light-matter interaction and the effective cavity length is increased: $L_{\mathrm{eff}} = L_{\mathrm{cav}} + L_{\mathrm{DBR1}} + L_{\mathrm{DBR2}}$. As the longitudinal mode $\xi(z)$ is also partly leaking into the DBRs region, the dispersion of the cavity photon slightly differs from the Fabry-Perot case. In particular, the cavity refractive index dispersion $n_{\mathrm{cav}}(E)$ is modified and should be replaced by an effective one:

$$n_{\mathrm{cav}}^{\mathrm{eff}}(E) = \langle n(z,E)\rangle = \frac{\int_0^{L_{\mathrm{tot}}} n(z,E)\xi(z)\,dz}{\int_0^{L_{\mathrm{tot}}} \xi(z)\,dz}, \tag{1.46}$$

where L_{tot} is the total length of the structure and $n(z,E)$ is the refractive index dispersion profile along the growth direction. All the optical properties such as the quality factor, the cavity mode dispersion and its linewidth are then modified by replacing $L_{\mathrm{cav}} \leftrightarrow L_{\mathrm{eff}}$ and $n_{\mathrm{cav}} \leftrightarrow n_{\mathrm{eff}}$.

1.3 Light-matter coupling in planar microcavities

In this section, we are interested in the description of the light-matter interaction occurring in planar microcavities. The properties of each component, i.e., the cavity photons and the quantum well excitons have been described separately in Sections 1.1.2 and 1.2, respectively. The accuracy of the description will strongly depend on how the light and matter components are treated, i.e., *via* a classical or a quantum approach.

1.3.1 Analogy with the classical mechanical oscillator

An instructive analogy to visualize the dynamics of light-matter interaction is the damped coupled pendula model where light and matter are considered as classical oscillators with eigenfrequencies $\omega_{X,C}$, where X and C correspond to the exciton and the cavity photon, respectively. The exciton is characterized by the angle $\theta_X(t)$ and the cavity photon by $\theta_C(t)$. The friction of each pendulum due to fixation imperfections is represented by a damping rate $\gamma_{X,C}$. The coupling strength g between X and C is modeled by a spring (see Fig. 1.7(a)). The system evolves according to the set of coupled differential equations for $\theta_X(t)$ and $\theta_C(t)$:

$$\begin{aligned}\frac{d^2\theta_X}{dt^2}+2\gamma_X\frac{d\theta_X}{dt}+\omega_X^2\theta_X+g^2(\theta_X-\theta_C) &= 0,\\ \frac{d^2\theta_C}{dt^2}+2\gamma_C\frac{d\theta_X}{dt}+\omega_C^2\theta_C+g^2(\theta_C-\theta_X) &= 0.\end{aligned} \tag{1.47}$$

The energy transfer between the two oscillators occurs *via* the coupling constant g and the damping *via* the constants γ_X and γ_C. Depending on the ratios $g/\gamma_{X,C}$, the coupling might overcome the damping and *vice versa*. The two situations are depicted in Fig. 1.7(b). In the limit $g/\gamma_{X,C} \gg 1$, the system is able to exchange mechanical energy over several periods (strong coupling regime). In the opposite limit where $g/\gamma_{X,C} \ll 1$, the two oscillators behave independently and $\theta_{X,C}(t)$ converge exponentially to zero for each oscillator. The system is said to be in the weak coupling regime as the two oscillators cannot efficiently exchange energy.

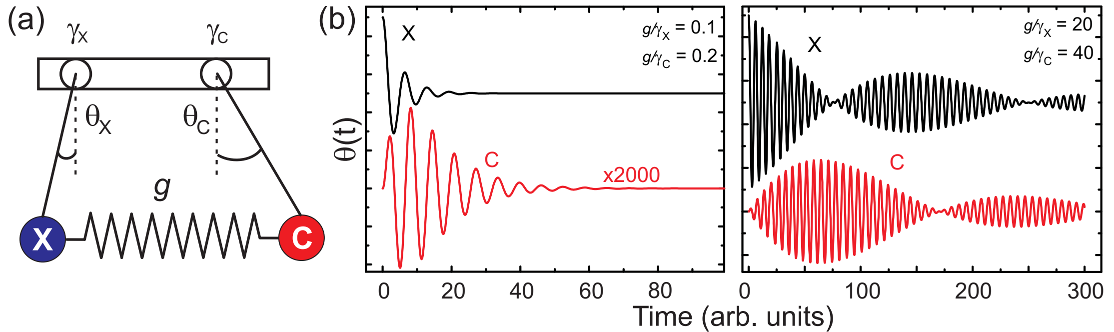

Fig. 1.7: Coupled mechanical oscillator analogy: (a) exciton (X) and cavity photon (C) correspond to damped coupled pendula. The damping is represented by the friction constants γ_X and γ_C and the coupling by a spring with stiffness g. (b) System evolution, i.e., $\theta_X(t)$ and $\theta_C(t)$ in the weakly (left, $g/\gamma_{X,C} \ll 1$) and strongly (right, $g/\gamma_{X,C} \gg 1$) coupled cases.

In the limit where damping is negligible (quasi-periodic regime), the evolution of the system is expressed in terms of the new system eigenmodes, the acoustical one ω_{ac} where X and C oscillate with the same phase and the optical one $\omega_{opt} > \omega_{ac}$ where they oscillate with opposite phases. These two new modes are a characteristic of the coupling between oscillators in classical physics but also for all two-level systems in quantum mechanics and quantum optics [112].

1.3.2 Classical description of the light-matter interaction: the linear dispersion model

The classical description of the light-matter interaction corresponds to the first degree of approximation where both excitons and cavity photons are considered as classical fields and are described by Maxwell's equations. We are interested here in the description of a planar structure made of different layers of various thicknesses with an infinite lateral extension. The optical response of each layer is given by its complex dielectric function $\epsilon(\omega, z)$. For the active layers, the excitonic response is accounted for by the Drude-Lorentz model introduced in Section 1.1.7.4: the dielectric function of the quantum wells is given by relations 1.29, 1.31 and 1.32. The linear dispersion model consists then in solving Maxwell's equations for the electric field for a specific dielectric function profile $\epsilon(\omega, z)$. This is commonly done using the transfer matrix approach developed in Appendix C, which correctly accounts for the mode dispersion of the cavity photon (the exciton is assumed to be non-dispersive[11]).

In Figs. 1.8(a) and 1.8(b), a multiple quantum well microcavity with 3×5 GaN/$Al_{0.2}Ga_{0.8}N$ quantum wells embedded at the 3 electric field maxima of the spacer in a 2λ-microcavity and sandwiched between two dielectric DBRs is investigated. Figure 1.8(a) shows the real and imaginary parts of the refractive index of the active region containing quantum wells at normal incidence ($\theta = 0$) for the case where the exciton-cavity photon detuning δ is zero. δ is an important parameter affecting the nature of the light-matter interaction and is given by:

$$\delta = E_C\left(k_\parallel = 0\right) - E_X\left(k_\parallel = 0\right). \tag{1.48}$$

On the same figure, the energy-dependent resonant refractive index $n_{res}(E)$ is also displayed and is defined by:

$$n_{res}(E) = n_{bg}\frac{E_C}{E}, \tag{1.49}$$

[11] The dispersionless character of the exciton corresponds to a local response for the dielectric constant. This approach was also used e.g. by Kavokin and Gil in Ref. [51].

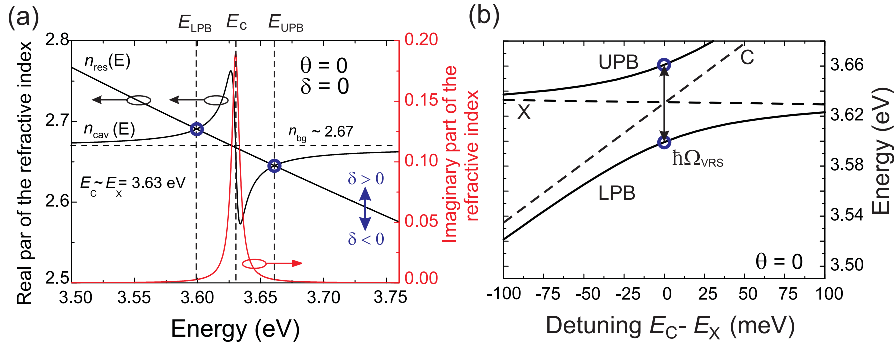

Fig. 1.8: Linear dispersion model: (a) Real (black) and imaginary (blue) refractive index of a microcavity containing 3×5 GaN/$Al_{0.2}Ga_{0.8}N$ quantum wells embedded at the 3 maxima of the electric field and sandwiched between two dielectric DBRs. The resonance condition is fulfilled when $n_{res}(E)$ matches the cavity refractive index $n_{cav}(E)$. When the excitonic response is turned on, two new eigenmodes appear (labeled LPB and UPB). The background cavity refractive index n_{bg} is represented with an horizontal dashed line. (b) Detuning dependence of the system eigenmodes. UPB and LPB anticross with respect to the cavity and exciton modes, which is a fingerprint of the strong coupling regime.

where $n_{bg} \approx 2.67$ is the mean background refractive index of the cavity, which is assumed constant. As shown in Fig. 1.8(a), every time the condition $n_{res}(E) = n_{cav}(E)$ is fulfilled,[12] an optical resonance is allowed in the cavity. Without the excitonic optical response, only the mode $E = E_C$ would be allowed, i.e., when $n_{res}(E)$ is equal to the background refractive index n_{bg}. When the excitonic resonance is turned on, two new eigenmodes appear, labeled E_{LPB} and E_{UPB}, which correspond to the lower (LPB) and upper polariton (UPB) branches. Note that the resonant cavity mode $E = E_C$ is still allowed but is damped by the imaginary part of the refractive index, which corresponds to the absorption occurring in the quantum wells.

When the cavity is slightly detuned with respect to the excitonic resonance, i.e., when $\delta \neq 0$, the resonant refractive index is shifted and the energy of the LPB and the UPB is modified. In Fig. 1.8(b), the lower and upper polariton branch energies E_{LPB} and E_{UPB} (continuous lines) are calculated for several values of δ following the procedure shown in Fig. 1.8(a) but for different detunings ranging from -100 to 100 meV (the case $\delta = 0$ is identified with thick blue circles). A clear anticrossing with respect to exciton and cavity energies (dashed lines) is visible. For negative detunings, $n_{res}(E)$ is shifted down and the resonance condition is fulfilled for values converging to the bare cavity mode energy for the LPB and for values converging to the bare exciton for the UPB. For positive detunings, the situation is reversed: E_{LPB} tends to E_X and E_{LPB} to E_C. The new eigenmode dispersions tend thus to that of the bare modes at large detunings. For the intermediate situation where $\delta = 0$, the energy splitting between bare modes and eigenmodes is maximum and referred to as *the vacuum Rabi splitting* $\hbar\Omega_{VRS} \approx 60$ meV. Note that the observation of $\Omega_{VRS} \neq 0$ is a direct evidence that the system operates in the strong coupling regime and is a measure of the light-matter interaction strength.

The new eigenmodes of the system are also visible in reflection, transmission and absorption spectra (see Fig. 1.9(a)) providing a direct experimental way to probe whether the system is in the strong coupling regime or not. The polariton dispersion, i.e., $E_{LPB}(k_\parallel)$ and $E_{UPB}(k_\parallel)$, can thus be obtained by probing the angular dispersion. In Fig. 1.9(b), the evolution of the reflectivity as a function of the incident angle is calculated using transfer matrix simulations between 0 and 90°.[13] The anticrossing

[12] Note that here n_{cav} corresponds to n_{eff}. However, the notation n_{cav} will be used from now on as we will only consider semiconductor microcavities.

[13] Note that the band-to-band absorption is neglected here to avoid the damping of the UPB.

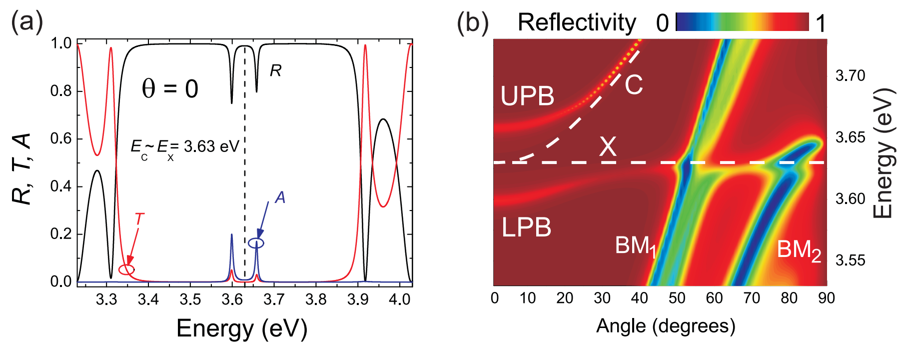

Fig. 1.9: (a) Simulated reflectivity (R), transmission (T) and absorption (A) spectra at normal incidence of the GaN-based microcavity containing 15 quantum wells considered in Fig. 1.8. (b) Calculated reflectivity dispersion between 0 and 90° featuring the optical signature of the upper and lower polariton branches at zero detuning. The bare modes (X and C) are indicated with dashed white lines. The first and second Bragg modes are labeled BM1 and BM2, respectively.

between exciton and cavity photon dispersions is one of the figures of merit for the strong coupling regime. Another interesting feature is the anticrossing of the exciton with the first two Bragg modes (labeled BM_1 and BM_2 in Fig. 1.9(b)), which have a faster dispersion than the cavity mode due to the lower mean refractive index of the dielectric DBRs compared to n_{cav}. As these modes present a reduced quality factor (here $Q_{BM1} \approx Q_{BM2} \approx 50$) compared to the cavity mode one ($Q \approx 1000$), the coupling with the excitonic transition is much weaker and results in a fuzzy anticrossing signature at $\theta = \approx 50°$ and 80° between the exciton and the two first Bragg modes.

In analogy with coupled mechanical oscillators, excitons and cavity photons form a two-level system with an interaction constant g_0 given by [113]:

$$g_0 = \sqrt{\frac{1+\sqrt{R}}{\sqrt{R}} \frac{c\Gamma_0}{n_{cav} L_{eff}}} \approx \sqrt{\frac{2c\Gamma_0}{n_{cav} L_{eff}}}, \tag{1.50}$$

where the exciton radiative emission rate Γ_0 is given by relation 1.26 and $R \approx 1$ is the peak reflectivity of the DBR.

It is worth mentioning that the intrinsic system properties such as the normal mode splitting or the energy dispersion do not require a quantum description and can be probed by means of conventional linear spectroscopy (absorption, reflectivity and transmission measurements). In 1990, Zhu and coworkers successfully explained the splitting of a resonant cavity coupled to an ensemble of barium atoms considered as Lorentz oscillators in a transmission experiment [114]. Two years after, Weisbuch and coworkers reported similar results by means of reflectivity measurements performed on GaAs-based semiconductor microcavities with one or several quantum wells embedded in the spacer layer [17]. They could also account for all experimental observations considering the linear dispersion model presented in this section. However, in this thesis we are mainly interested in properties such as density effects, polariton-polariton interactions, relaxation mechanisms or carrier localization, which are probed by photoluminescence experiments. The classical approach should be thus refined by considering the exciton as an interacting quantum particle.

1.3.3 Quantum description of the light-matter interaction: coupled quantum oscillators

1.3.3.1 Light-matter interaction Hamiltonian in a planar microcavity: the exciton-polaritons

In a full quantum description of the light-matter interaction both optical and matter fields are quantized and treated in the frame of quantum mechanics. The light couples to the field created by the fluctuation of the electric charges. In the dipolar approximation, the electric field is treated classically and the coupling is correctly accounted for by the Hamiltonian 1.24. In analogy with the atomic case, the exciton is considered here as a two-level system $\{|0\rangle, |X\rangle\}$, where $|0\rangle$ corresponds to the crystal ground state and $|X\rangle$, the first elementary excitation, which corresponds to a bound electron-hole pair. In the framework of the second quantization, an exciton with in-plane wave vector $k_\parallel$ is characterized by its creation and annihilation operators $\hat{d}^\dagger_{k_\parallel}$ and $\hat{d}_{k_\parallel}$ and satisfies the bosonic commutation rule in the low density regime (see Section 1.1.5). In this thesis, we consider the case where the exciton is embedded in a planar microcavity, which advantageously filters out the electromagnetic field at the cavity mode energy $E_C(\mathbf{k}_\parallel)$. As a consequence, we can also model the cavity mode with in-plane wave vector $k_\parallel$ by creation and annihilation operators $\hat{c}^\dagger_{k_\parallel}$ and $\hat{c}_{k_\parallel}$. The total Hamiltonian for a given $k_\parallel$ reads:

$$\hat{H}^{\text{pol}}_{k_\parallel} = \hat{H}^{\text{C}}_{k_\parallel} + \hat{H}^{\text{X}}_{k_\parallel} + \hat{H}^{\text{int}}_{k_\parallel} = E_{\text{C}}\left(k_\parallel\right)\hat{c}^\dagger_{k_\parallel}\hat{c}_{k_\parallel} + E_{\text{X}}\left(k_\parallel\right)\hat{d}^\dagger_{k_\parallel}\hat{d}_{k_\parallel} + \hbar g_{k_\parallel}\left(\hat{c}_{k_\parallel}\hat{d}^\dagger_{k_\parallel} + \hat{c}^\dagger_{k_\parallel}\hat{d}_{k_\parallel}\right), \tag{1.51}$$

where the off-resonant terms have been neglected in the interaction Hamiltonian $\hat{H}^{\text{int}}$. Note that in the present work, we will neglect the angular dependence of the coupling strength, i.e., $g_{k_\parallel} \approx g_0$ given by equation 1.50. Hamiltonian 1.51 can be diagonalized using the unitary transformation:

$$\begin{aligned} \hat{p}_{\text{LP,k}_\parallel} &= X_{k_\parallel}\hat{d}_{k_\parallel} + C_{k_\parallel}\hat{c}_{k_\parallel}, \\ \hat{p}_{\text{UP,k}_\parallel} &= -C_{k_\parallel}\hat{d}_{k_\parallel} + X_{k_\parallel}\hat{c}_{k_\parallel}, \end{aligned} \tag{1.52}$$

where $X_{k_\parallel}$ and $C_{k_\parallel}$ are called the Hopfield coefficients [75], which satisfy the condition $\left|X_{k_\parallel}\right|^2 + \left|C_{k_\parallel}\right|^2 = 1$. The variable transformations given by relations 1.52 diagonalize the Hamiltonian 1.51, which reads in the new basis:

$$\hat{H}^{\text{pol}}_{k_\parallel} = E_{\text{LP}}\left(k_\parallel\right)\hat{p}^\dagger_{\text{LP,k}_\parallel}\hat{p}_{\text{LP,k}_\parallel} + E_{\text{UP}}\left(k_\parallel\right)\hat{p}^\dagger_{\text{UP,k}_\parallel}\hat{p}_{\text{UP,k}_\parallel}. \tag{1.53}$$

Operators $\left\{\hat{p}^\dagger_{\text{LP,k}_\parallel}, \hat{p}_{\text{LP,k}_\parallel}\right\}$ and $\left\{\hat{p}^\dagger_{\text{UP,k}_\parallel}, \hat{p}_{\text{UP,k}_\parallel}\right\}$ are the creation and annihilation operators of the new eigenmodes called upper (UPs) and lower polaritons (LPs), which were already introduced to label the resonance observed in the linear dispersion model (see Section 1.3.2). The eigenvalues of the Hamiltonian 1.53 for each $k_\parallel$-vector provide the LPB and UPB energy dispersion:

$$\begin{aligned} E_{\text{LPB}}\left(k_\parallel,\delta\right) &= \frac{1}{2}\delta_{k_\parallel} + E_{\text{X}}\left(k_\parallel\right) - \frac{1}{2}\sqrt{\delta^2_{k_\parallel} + 4g_0^2}, \\ E_{\text{UPB}}\left(k_\parallel,\delta\right) &= \frac{1}{2}\delta_{k_\parallel} + E_{\text{X}}\left(k_\parallel\right) + \frac{1}{2}\sqrt{\delta^2_{k_\parallel} + 4g_0^2}, \end{aligned} \tag{1.54}$$

where $\delta_{k_\parallel} = E_{\text{C}}\left(k_\parallel\right) - E_{\text{X}}\left(k_\parallel\right)$ depends on the exciton and cavity photon effective masses $m^{\text{cav}}_{\text{eff}}$ (equation 1.41) and M_{X}. Note that the vacuum Rabi splitting $\hbar\Omega_{\text{VRS}}$ introduced in the previous section and defined as the energy between the split modes when the bare modes are resonant to each other can be obtained from the polariton energy dispersions:

$$\hbar\Omega_{\text{VRS}} = E_{\text{UPB}}\left(k_\parallel = 0, \delta = 0\right) - E_{\text{LPB}}\left(k_\parallel = 0, \delta = 0\right) = 2g_0. \tag{1.55}$$

In this simple two-level model, the mode broadening is neglected and the vacuum Rabi splitting is directly proportional to the coupling constant g_0. Relation 1.55 is thus only true in the perfect undamped situation and does not strictly apply to realistic structures.

One of the most interesting features of strongly coupled microcavities is the possibility to efficiently tune the light-matter content of the coupled eigenmodes as polaritons are a linear combination of the bare modes with a weight given by the square of the Hopfield coefficients. Thus $\left|X_{k_\parallel}(\delta)\right|^2$ and $\left|C_{k_\parallel}(\delta)\right|^2$ correspond to the excitonic and photonic fractions of the LPB and *vice versa* for the UPB. The Hopfield coefficients depend on the in-plane wave vector $k_\parallel$, the vacuum Rabi splitting Ω_{VRS} and δ *via* the relations:

$$\begin{aligned} X_{k_\parallel}(\delta) &= \frac{\hbar\Omega_{\text{VRS}}}{\sqrt{(\hbar\Omega_{\text{VRS}})^2 + 4\left(E_{\text{LPB}}\left(k_\parallel\right) - E_{\text{X}}\left(k_\parallel\right)\right)^2}}, \\ C_{k_\parallel}(\delta) &= -\frac{4\left(E_{\text{LPB}}\left(k_\parallel\right) - E_{\text{X}}\left(k_\parallel\right)\right)}{\sqrt{(\hbar\Omega_{\text{VRS}})^2 + 4\left(E_{\text{LPB}}\left(k_\parallel\right) - E_{\text{X}}\left(k_\parallel\right)\right)^2}}. \end{aligned} \tag{1.56}$$

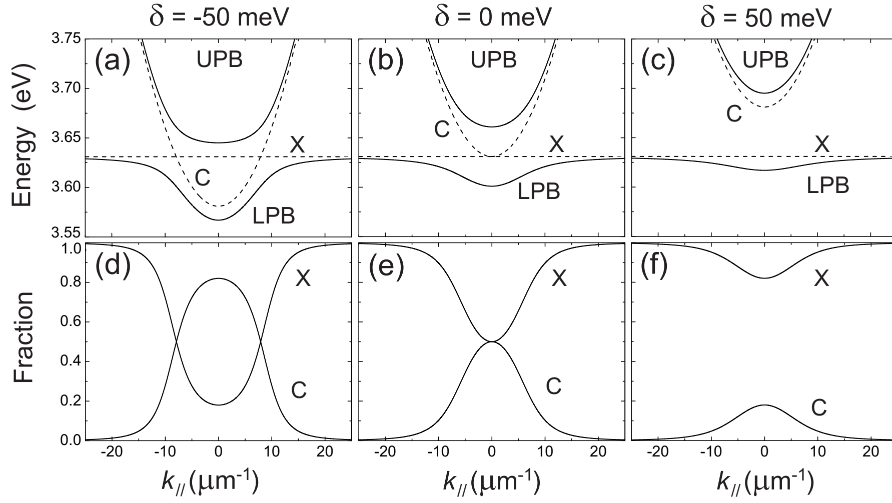

Fig. 1.10: Lower and upper polariton dispersions (solid lines) for (a) $\delta = -50\,\text{meV}$, (b) $\delta = 0\,\text{meV}$ and (c) $\delta = 50\,\text{meV}$. The bare modes (X and C) are indicated with black dashed lines. Excitonic and photonic fractions of the lower polariton branch for (d) $\delta = -50\,\text{meV}$, (e) $\delta = 0\,\text{meV}$ and (f) $\delta = 50\,\text{meV}$. For all curves, $\hbar\Omega_{\text{VRS}} = 60\,\text{meV}$ and $E_{\text{X}} = 3.631\,\text{eV}$, which corresponds to the typical value for a GaN quantum well-based microcavity at room temperature [53].

The exciton-cavity photon detuning is therefore a key parameter that allows changing the excitonic and photonic fractions of polaritons. The effect of δ on the polariton dispersion is depicted in Fig. 1.10. For negative values of δ, the LPB mimics the cavity mode dispersion for small in-plane $k_{\parallel}$ and tends to that of the exciton at large momenta. The opposite situation occurs for the UPB, as they have a complementary light-matter content due to the unitarity of the Hopfield coefficients. When increasing the δ-values toward zero (Figs. 1.10(b) and 1.10(e)) and positive values (Figs. 1.10(c) and 1.10(f)), the LPB and UPB progressively exchange their light and matter content.

The tunability of the polariton content *via* δ offers a unique way to tune the particle behavior and will considerably affect the relaxation dynamics close to the center of the Brillouin zone (see Chapter 4). When the excitonic content is low, i.e., $\left|X_{k_{\parallel}}(\delta)\right|^2 \to 0$, polaritons behave more as photons and conversely, when the excitonic content is high, i.e., $\left|X_{k_{\parallel}}(\delta)\right|^2 \to 1$, polaritons behave more as excitons.

1.3.3.2 Time-dependent Schrödinger equation: Rabi oscillations

The dynamic evolution of a polariton system can be described by the time-dependent Schrödinger equation:

$$i\hbar \frac{\partial \left|\psi(t)\right\rangle}{\partial t} \left|\psi(t)\right\rangle = \hat{H}_{\text{pol}} \left|\psi(t)\right\rangle , \tag{1.57}$$

where $\left|\psi(t)\right\rangle$ is the polariton wave function. Assuming that there is only one photon in the cavity, at a given time t, the polariton state can be written as:

$$\left|\psi(t)\right\rangle = x(t)\left|X\right\rangle + c(t)\left|C\right\rangle , \tag{1.58}$$

where $|X\rangle$ represents the crystal in the excited state (1 exciton, 0 photon), and $|C\rangle$ the crystal ground state (0 exciton, 1 photon). The time-dependent solution shows the dynamic picture of the light-matter

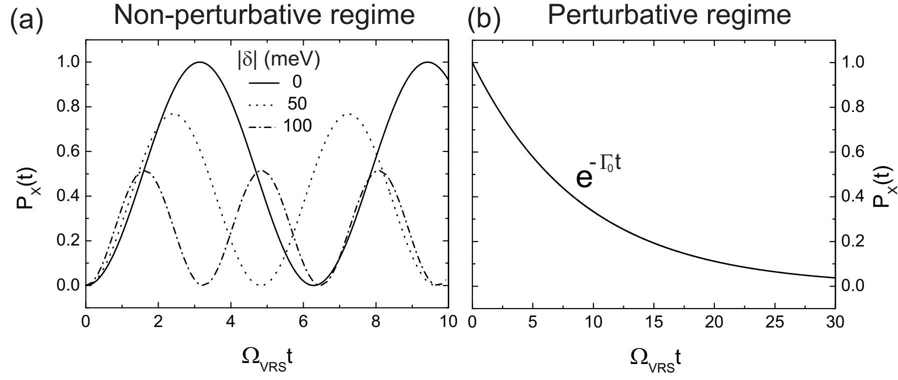

Fig. 1.11: Probability of reabsorption for a photon in a system operating (a) in the strong coupling regime (non perturbative) and (b) in the weak coupling regime (perturbative).

interaction. In particular, the Hopfield coefficients $x(t)$ and $c(t)$ are time-dependent and the system oscillates with a period $\Omega = \sqrt{\Omega_{\mathrm{VRS}}^2 + \delta^2}$ between the states $|X\rangle$ and $|C\rangle$. The figure of merit to visualize the evolution of the system is the probability $P_{\mathrm{X}}(t)$ to find the system in its excited state $|X\rangle$, assuming that the system is initially prepared in the ground state, i.e., $|\psi(t=0)\rangle = |C\rangle$. In other words, $P_{\mathrm{X}}(t)$ corresponds to the probability for an intracavity photon to be reabsorbed by the active medium [76]:

$$P_{\mathrm{X}}(t) = \left|\langle X|\psi(t)\rangle\right|^2 = \frac{\Omega_{\mathrm{VRS}}}{\sqrt{\Omega_{\mathrm{VRS}}^2+\delta^2}} \sin^2\left(\frac{1}{2}\sqrt{\Omega_{\mathrm{VRS}}^2+\delta^2}\right). \tag{1.59}$$

In Fig. 1.11(a), $P_{\mathrm{X}}(t)$ is represented for different values of δ with $\Omega_{\mathrm{VRS}} = 60\,\mathrm{meV}$, which is reasonable for multiple quantum well III-nitride-based microcavities [53]. The associated Rabi period for $\delta = 0$ is $T_{\mathrm{VRS}} = 2\pi/\Omega_{\mathrm{VRS}} \approx 70\,\mathrm{fs}$. The oscillations occurring between the two populations (X and C) are referred to as *Rabi oscillations* and are characteristic of the strong light-matter coupling regime. The first observation of Rabi oscillations was obtained by Norris and coworkers in 1994 in a GaAs-based multiple quantum well-based microcavity operating in the strong coupling regime under femtosecond resonant excitation [115]. A quantum mechanical model accounting for these observations was provided in 1996 by Savona and Weisbuch [116].

The time-dependent description gives a direct interpretation of the square modulus of Hopfield coefficients as the measure of the time spend by the polaritons in the light and the matter components. An exciton-like polariton will thus spent more time as an exciton and *vice versa* for photon-like polaritons. As a result, all polariton properties such as the homogeneous broadening, interaction cross-section or effective mass are weighted by $\left|X_{k_\parallel}(\delta)\right|^2$ and $\left|C_{k_\parallel}(\delta)\right|^2$. Note that the Rabi period defines the timescale of the energy exchange between cavity and exciton modes. In a disordered system such as III-nitride materials, it is interesting to compare this time (~ 70 fs) with the localization time τ_{loc}. For high quality bulk GaN layers with a carrier density of $10^{16}\,\mathrm{cm}^{-3}$, $\tau_{\mathrm{loc}} \approx 25\,\mathrm{ps}$ for X_{A} and X_{B} at 8 K [117]. For quantum wells, this time is likely shorter due to interface disorder but it should definitely be much larger than 100 fs [118], indicating that the Rabi dynamics might prevent carrier localization in the quantum wells and allows the observation of the strong coupling regime in a disordered system if the coupling strength is large enough.

When the damping rates exceed the light-matter coupling strength, the system switches to the weak coupling regime. In this case, the interaction is treated as a perturbation and Fermi's golden rule

applies. This situation is usually achieved when the excitonic resonance is coupled to a continuum of states, or conversely when a single cavity mode is coupled to a broad excitonic resonance. Once the system is in the excited state, the probability of decaying radiatively is increased by the high number of accessible states and the emission process is said to be irreversible. The probability for the emitted photon to be reabsorbed by the active medium is then directly given by the spontaneous radiative rate Γ_0 given by relation 1.26 and exponentially decays with time (see Fig. 1.11(b)[14]). $P_X(t)$ reads in this case:

$$P_X(t) = e^{-i\Gamma_0 t}. \tag{1.60}$$

1.3.4 *Strong to weak coupling regime transition*

In the previous section, cavity photons and excitons were considered as a perfect two-level system, i.e., the lifetime was assumed to be infinite (no homogeneous broadening: $\gamma_h = 0$) and the impact of disorder was neglected (no inhomogeneous broadening: $\gamma_{inh} = 0$). In this Section, the impact of homogeneous and inhomogeneous broadenings of the bare modes on the light-matter interaction is addressed. In particular, it is shown how they can potentially drive the system into the weak-coupling regime. The role of the quantum well number is also treated.

1.3.4.1 Impact of the homogeneous broadening: lifetime limitation

As discussed in Section 1.1.3, the homogeneous broadening γ_h of a given transition is directly related to the decay time τ *via* the time-energy uncertainty relation $\tau\gamma_h \sim \hbar$. Once τ becomes shorter than one Rabi oscillation period $T_{VRS} = 2\pi/\Omega_{VRS}$, the damping overcomes the coupling strength and the system inevitably switches to the perturbative regime. This observation allows defining a very simple criterion for the observation of the strong coupling regime, which can be formulated in two equivalent ways (related to the time and spectral domains, respectively):

$$\begin{aligned} T_{VRS} &\gg \max(\tau_X, \tau_C), \\ \hbar\Omega_{VRS} &\gg \max\left(\gamma_h^X, \gamma_h^C\right), \end{aligned} \tag{1.61}$$

where $\gamma_h^{X(C)}$ corresponds to the homogeneous broadening of the exciton (cavity photon) line. A common way to account for the effect of the finite homogeneous linewidth of the bare modes in the polariton Hamiltonian 1.51 is to phenomenologically introduce an imaginary part to the bare mode energy, i.e., $E_{X,C} \to E_{X,C} - i\gamma_h^{X,C}$. In the bare mode basis $\{|X\rangle, |C\rangle\}$, the time-independent Schrödinger equation for a given in-plane momentum $k_\parallel$ now reads:

$$\hat{H}_{pol}|\psi\rangle = E|\psi\rangle \leftrightarrow \begin{pmatrix} E_C(k_\parallel) - i\gamma_h^C & g_0 \\ g_0^* & E_X(k_\parallel) - i\gamma_h^X \end{pmatrix} |\psi\rangle = E|\psi\rangle. \tag{1.62}$$

The new eigenvalues are similar to expressions 1.54 but are now complex functions:

$$\begin{aligned} E_{LPB}(k_\parallel,\delta) &= \frac{1}{2}\delta_{k_\parallel} + E_X(k_\parallel) - i\left(\frac{\gamma_h^X + \gamma_h^C}{2}\right) - \frac{1}{2}\sqrt{\left[\delta_{k_\parallel} - i\left(\gamma_h^X - \gamma_h^C\right)\right]^2 + 4g_0^2}, \\ E_{UPB}(k_\parallel,\delta) &= \frac{1}{2}\delta_{k_\parallel} + E_X(k_\parallel) - i\left(\frac{\gamma_h^X + \gamma_h^C}{2}\right) + \frac{1}{2}\sqrt{\left[\delta_{k_\parallel} - i\left(\gamma_h^X - \gamma_h^C\right)\right]^2 + 4g_0^2}, \end{aligned} \tag{1.63}$$

[14] For the simulation, a radiative lifetime of 5 ps is considered, which is reasonable for a GaN-based quantum well at room temperature.

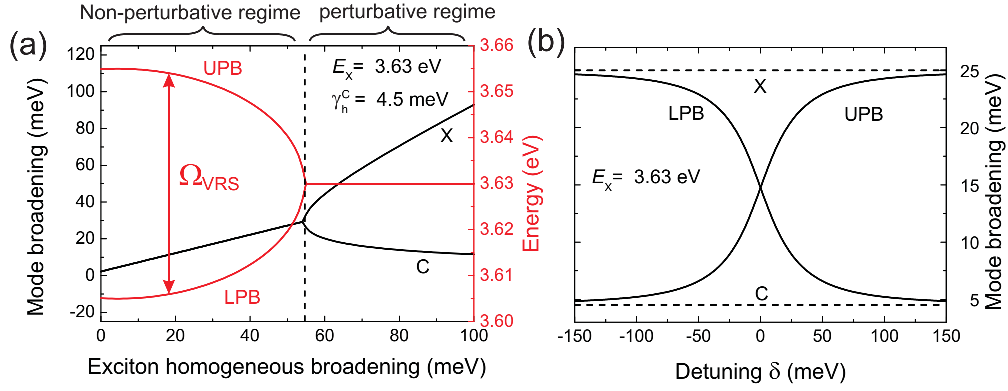

Fig. 1.12: (a) Mode broadening (black) and energy (red) as a function of γ_h^X for $\gamma_h^C = 4.5\,\text{meV}$, $E_X = 3.63\,\text{eV}$ and $g_0 = 25\,\text{meV}$. The vertical dashed line at $\gamma_h^X = 55\,\text{meV}$ sets the transition between the perturbative and non-perturbative regimes. (b) Evolution of the lower and upper polariton homogeneous linewidths as a function of detuning for $\gamma_h^C = 4.5\,\text{meV}$ and $\gamma_h^X = 25\,\text{meV}$.

The main difference between expressions 1.54 and 1.63 is the appearance of a polariton broadening term $\gamma_{LPB/UPB} = -i\text{Im}\left(E_{LPB/UPB}\right)$ associated to the finite lifetime of the bare modes. In addition, the vacuum Rabi splitting will now depend on the relative values of the coupling strength g_0 and the damping rates of the bare modes γ_h^C and γ_h^X:

$$\hbar\Omega_{VRS} = \begin{cases} 0 \text{ for } g_0 \leq \frac{\left|\gamma_h^X - \gamma_h^C\right|}{2} \\ 2\sqrt{g_0^2 - \left(\frac{\gamma_h^X - \gamma_h^C}{2}\right)^2} \text{ for } g_0 > \frac{\left|\gamma_h^X - \gamma_h^C\right|}{2} \end{cases}. \tag{1.64}$$

In Fig. 1.12(a), the real and imaginary parts of the polariton dispersions at $k_\parallel = 0$ for $\delta = 0$ corresponding to the mode broadening and energy, respectively, are plotted as a function of γ_h^X for a microcavity with an excitonic resonance at $E_X = 3.63\,\text{eV}$, a Q-factor of 800 ($\gamma_h^C = 4.5\,\text{meV}$) and an interaction constant $g_0 = 25\,\text{meV}$, which is realistic for a GaN quantum well-based microcavity at room temperature [53]. Interestingly, a discontinuity occurs for both energy and broadening when Ω_{VRS} vanishes, i.e., for $\gamma_{h,\text{lim}}^X = 55\,\text{meV}$. This discontinuity corresponds to the critical exciton damping when the system switches from the weak coupling regime, where the light-matter interaction is treated as a perturbation ($\gamma_h^X < \gamma_{h,\text{lim}}^X$) to the strong coupling one, where the interaction is not perturbative and can be solved exactly ($\gamma_h^X > \gamma_{h,\text{lim}}^X$). Interestingly, in the weak coupling regime, the energies are degenerate, meaning that all emitted photons leak out of the cavity through the cavity mode but their homogeneous linewidth does not correspond to the unperturbed case. This point is of fundamental importance as the weak coupling regime does not correspond to the case of independent modes since they are still correlated *via* the coupling strength g_0. When γ_h^X becomes arbitrarily large the broadenings of the modes at 3.631 eV asymptotically converge to their unperturbed values γ_h^X and γ_h^C.

The linewidths of the lower and upper polaritons is given by the weighted sum of the uncoupled modes:

$$\begin{aligned} \gamma_{LPB}\left(k_\parallel, \delta\right) &= \left|X_{k_\parallel}(\delta)\right|^2 \gamma_X + \left|C_{k_\parallel}(\delta)\right|^2 \gamma_C, \\ \gamma_{UPB}\left(k_\parallel, \delta\right) &= \left|C_{k_\parallel}(\delta)\right|^2 \gamma_X + \left|X_{X_\parallel}(\delta)\right|^2 \gamma_C. \end{aligned} \tag{1.65}$$

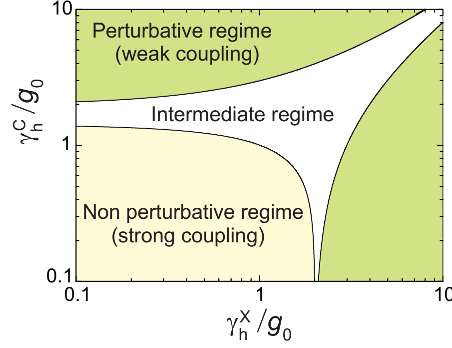

Fig. 1.13: Light-matter coupling diagram featuring the conditions for the observation of the weak (green), intermediate (white) and strong coupling regimes (yellow).

The evolution of the polariton homogeneous linewidths is displayed in Fig. 1.12(b) as a function of detuning for the same material parameters as in Fig. 1.12(a). It highlights the fact that they converge to the uncoupled mode linewidths for $|\delta| \gg 0$. The polariton broadenings are directly related to their radiative lifetime *via* the time-energy relation $\tau_{\mathrm{LPB/UPB}} = \hbar/\gamma_{\mathrm{LPB/UPB}}$.

Experimentally, the vacuum Rabi splitting is accessible *via* reflectivity (R), transmission (T) or absorption (A) measurements (angle-resolved or scans along the sample wedge). However, Savona and coworkers have demonstrated that the splitting might slightly differ in these three situations [113]. In particular, they showed that the corresponding Rabi splittings obey the following order: $\Omega^A_{\mathrm{VRS}} \leq \Omega^T_{\mathrm{VRS}} \leq \Omega^R_{\mathrm{VRS}}$. They also discussed the possibility of observing a normal mode splitting only in transmission and reflectivity spectra but not in absorption. This anomalous situation is referred to as *intermediate coupling regime* and essentially occurs for low quality factor microcavities with $Q < 100$ [119]. This effect can be safely discarded in our study. Since the splitting in absorption is the most restrictive, demonstrating $\hbar\Omega^A_{\mathrm{VRS}} > 0$ is mandatory:

$$\hbar\Omega^A_{\mathrm{VRS}} = \begin{cases} 0 \text{ for } g_0^2 \leq \dfrac{\left(\gamma_h^X\right)^2 + \left(\gamma_h^C\right)^2}{2} \\ 2\sqrt{g_0^2 - \dfrac{\left(\gamma_h^X\right)^2 + \left(\gamma_h^C\right)^2}{2}} \text{ for } g_0^2 > \dfrac{\left(\gamma_h^X\right)^2 + \left(\gamma_h^C\right)^2}{2} \end{cases}. \tag{1.66}$$

From relations 1.64 and 1.66, the phase diagram for the observation of the strong coupling regime in a homogeneously broadened system can be extracted. In Fig. 1.13, distinct regions where weak, strong or intermediate coupling regimes are expected are shown as a function of the ratio between the damping rate of each mode and the light-matter interaction constant g_0.

The diagram shown in Fig. 1.13 is valid in the low density regime, i.e., as long as the coupling strength g_0 is unaffected by the exciton renormalization discussed in Section 1.1.5. When the carrier density increases, the system might switch to the weak coupling regime even if the ratios γ_h^X/g_0 and γ_h^C/g_0 remain small due to the progressive saturation of the exciton oscillator strength (see Section 3.4.1).

1.3.4.2 Impact of inhomogeneous broadening: disorder limitation

The various non-idealities of monolithic microcavities such as defects, monolayer width fluctuations, alloy disorder or DBR imperfections inevitably cause an inhomogeneous broadening of the excitonic and photonic transitions $\gamma_{\mathrm{inh}}^{\mathrm{X}}$ and $\gamma_{\mathrm{inh}}^{\mathrm{C}}$ [65, 81]. As a result different emitters will have different energies, which can be modeled by a Gaussian distribution. Whereas for GaAs-based microcavities the impact of inhomogeneous broadening can often be neglected due to the high quality of the available samples, it is not true for GaN multiple quantum well based ones. Note also that the large effective mass of holes and the small Bohr radius in GaN make excitons more sensitive to in-plane fluctuations.

In opposition to the exciton homogeneous broadening, the inhomogeneous one has a marginal effect on the normal mode splitting, at least as long as $\gamma_{\mathrm{inh}}^{\mathrm{X}} \ll \Omega_{\mathrm{VRS}}$. This can be understood in the framework of the linear dispersion theory by considering the real $(\mathrm{Re}\,(n_{\mathrm{cav}}))$ and imaginary parts of the cavity refractive index $(\mathrm{Im}\,(n_{\mathrm{cav}}))$. It has been shown in the previous section that a resonant mode is allowed each time the optical length of the cavity matches a half-integer multiple of the cavity effective length, i.e., when $n_{\mathrm{res}}(E) = n_{\mathrm{cav}}(E)$, where $n_{\mathrm{res}}(E)$ is given by relation 1.49. In Fig. 1.14(a), $\mathrm{Re}\,(n_{\mathrm{cav}})$ and $\mathrm{Im}\,(n_{\mathrm{cav}})$ are calculated for different values of the $\gamma_{\mathrm{inh}}^{\mathrm{X}}$ spanning from 1 to 90 meV but with a constant homogeneous broadening of 15 meV. The inhomogeneous broadening is taken into account in the excitonic optical response *via* the relation 1.32. The structure considered consists of 15 thin GaN quantum wells ($L_{\mathrm{QW}} = 2$ nm) with an oscillator strength per unit area of $5 \times 10^{13}\,\mathrm{cm}^{-2}$.

In Fig. 1.14(b), the calculated resonances (black filled squares) are displayed for each value of $\gamma_{\mathrm{inh}}^{\mathrm{X}}$. As predicted by Houdré and coworkers [112], the vacuum Rabi splitting remains nearly unaltered by the inhomogeneous broadening until $\gamma_{\mathrm{inh}}^{\mathrm{X}}$ becomes comparable to Ω_{VRS}. The exciton-cavity photon detuning is set to zero so that the energy difference between LPB and UPB corresponds to Ω_{VRS}. This simplified model shows that the transition from the weak to the strong coupling regime can be induced by the inhomogeneous broadening when the exciton disorder energy and the coupling strength become comparable. In the limit where $\gamma_{\mathrm{inh}}^{\mathrm{X}} \ll \Omega_{\mathrm{VRS}}$, the linewidth of the polariton branches

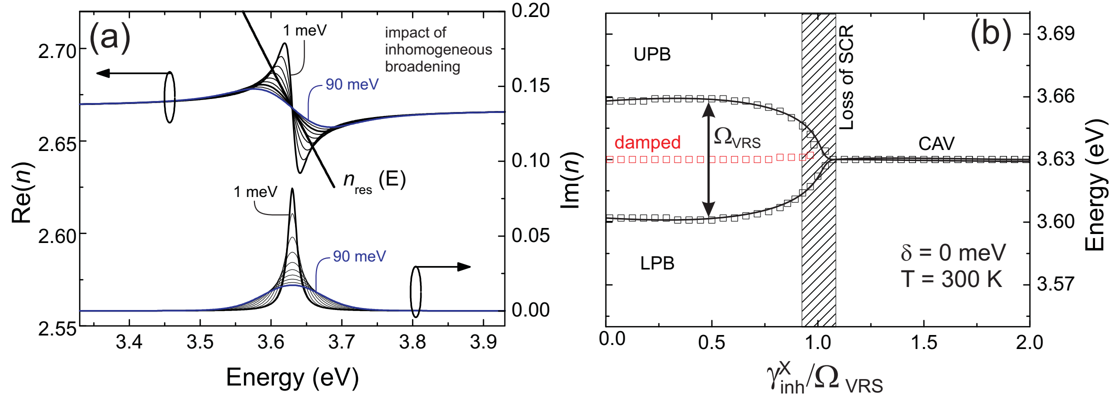

Fig. 1.14: (a) Real (top) and imaginary (bottom) parts of the cavity refractive index calculated for different values of the exciton inhomogeneous broadening spanning from 1 to 90 meV but for a constant homogeneous broadening of 15 meV at zero detuning. The resonance condition is reached when $n_{\mathrm{res}}(E)$ matches the cavity refractive index $n_{\mathrm{cav}}(E)$. (b) The calculated resonances (black filled squares) are displayed for each value of $\gamma_{\mathrm{inh}}^{\mathrm{X}}$. The transition between the strong (SCR) and weak (WCR) coupling regimes is indicated by a dashed area. The mode found in red is damped by the imaginary part of cavity refractive index.

is given by relations 1.65. This interesting feature allows accessing to the exciton and cavity photon homogeneous linewidth of the excitonic resonance by means of linear spectroscopy.

The cavity photon can also be affected by the inhomogeneous broadening $\gamma_{\mathrm{inh}}^{\mathrm{C}}$ due to in-plane fluctuations in the cavity thickness or more generally by a spatially varying cavity effective length $L_{\mathrm{eff}}(x, y)$. Contrary to the exciton mode whose extension is limited by the diffusion length, which is of the order of 100 nm in III-nitride quantum wells at room temperature for both polar [120] and non polar orientations [121], the spatial scale for the inhomogeneous broadening of the cavity mode (with resonance wavelength λ_{C}) is much larger and is given by the Fabry-Perot mode radius [122]:

$$R_{\mathrm{FP}} = \sqrt{\frac{\lambda_{\mathrm{C}} L_{\mathrm{cav}}}{\pi n_{\mathrm{cav}}} \frac{(R_1 R_2)^{1/4}}{1-(R_1 R_2)^{1/2}}}, \tag{1.67}$$

which ranges between 2.5 and 4 μm for GaN microcavities considering values between 90 and 99.9% for R_1 and R_2 (peak reflectivity of the bottom and top DBRs). As a consequence, when probing the sample with an excitation spot of area S, a number of modes $\frac{2S}{\pi R_{\mathrm{FP}}^2}$ will form.[15] As they are all mutually incoherent, the far-field pattern will remain the same as that from a single spatial mode but with a quality factor averaged over the spot size area. In-plane photonic disorder can thus be seen as the coexistence of several independent strongly coupled microcavities. As a consequence, $\gamma_{\mathrm{inh}}^{\mathrm{C}}$ cannot switch the system from the non-perturbative to the perturbative regime.

1.3.5 *Impact of the quantum well number*

In a perfect system containing N_{QW} identical quantum wells of energy E_{X},[16] all excitons are equally coupled to the internal electric field with energy E_{C}. The Hamiltonian of the system reads:

$$\hat{H}_{\mathrm{N=N_{QW}}} = \begin{pmatrix} E_C & g & g & \dots & g \\ g^* & E_X & 0 & \dots & g \\ g^* & 0 & E_X & \dots & g \\ \dots & \dots & \dots & \dots & \dots \\ g^* & 0 & 0 & \dots & E_X \end{pmatrix}. \tag{1.68}$$

The eigenenergies of the system are given by:

$$\begin{aligned} E_{\mathrm{LPB/UPB}} &= \frac{1}{2}\left[(E_X + E_C) \pm \sqrt{(E_X - E_C)^2 + N_{\mathrm{QW}} \cdot 4g^2}\right], \\ E_{\mathrm{dark}}^{1,..,\mathrm{N_{QW}}-1} &= E_X \end{aligned} \tag{1.69}$$

The coupling between this N-fold degenerate set of quantum wells and a single cavity mode results in two bright modes, the lower and upper polaritons, and $N_{\mathrm{QW}} - 1$ degenerate dark states with energy $E = E_{\mathrm{X}}$. The entire oscillator strength is shared between the cavity photon and the totally symmetric excitonic wave function $|X_{\mathrm{S}}\rangle = \frac{1}{N_{\mathrm{QW}}} \sum_{\mathrm{i}} |X_{\mathrm{i}}\rangle$, where $|X_{\mathrm{i}}\rangle$ is the exciton wave function of the ith quantum well. From the solutions 1.69, it is seen that the coupling strength $g_0^{N_{\mathrm{QW}}}$ is increased compared to the case of a single quantum well structure:

[15] The factor 2 accounts for polarization degeneracy.

[16] The quantum wells are assumed to be all independent. In other words, the barriers are thick enough to avoid the formation of mini-bands and their coupling occurs *via* the light-matter interaction constant, which is assumed to be identical for all quantum wells.

$$g_0^{N_{\mathrm{QW}}} = g_0\sqrt{N_{\mathrm{QW}}}. \tag{1.70}$$

This relation is exact in the limit where all quantum wells are located at the antinodes of the electric field, which is never the case when there is more than one quantum well per maximum. In this case, N_{QW} must be replaced by the effective number of quantum wells, which accounts for the position of the quantum wells with respect to the field antinodes [113]:

$$N_{\mathrm{QW}}^{\mathrm{eff}} = N_{\mathrm{set}}\left(\frac{N_{\mathrm{QW}}^{\mathrm{max}}}{2} + \frac{1}{2}\frac{\sin\left(N_{\mathrm{QW}}^{\mathrm{max}} k_z L_{\mathrm{p}}\right)}{\sin\left(kL_{\mathrm{p}}\right)}\right) = \frac{N_{\mathrm{QW}}}{2} + \frac{N_{\mathrm{set}}}{2}\frac{\sin\left(N_{\mathrm{QW}}^{\mathrm{max}} k_z L_{\mathrm{p}}\right)}{\sin\left(kL_{\mathrm{p}}\right)}, \tag{1.71}$$

where L_{p} is the quantum well period, i.e., the sum of the quantum well (L_{QW}) and barrier (L_{b}) thicknesses, $N_{\mathrm{QW}}^{\mathrm{max}}$ is the number of quantum wells located at the N_{set} antinodes of the field, and k_{z} is the wave vector at the resonance for normal incidence. In real structures, the N_{QW} exciton states are not equivalent due to alloy disorder, thickness, strain and electric field fluctuations, which is featured by the inhomogeneous broadening of the excitonic line. These non-idealities of the structure mix up the exciton states and can lead to a redistribution of the oscillator strength from the two optically active states (LPB and UPB) to the $N_{\mathrm{QW}} - 1$ dark ones [123].

1.4 Nonlinearities in strongly coupled planar microcavities

In section 1.1.5, the quantum nature of excitons was addressed. In particular, it was shown that they satisfy the bosonic commutation rule in the low density limit, i.e., when the mean interparticle distance is small compared to the 2D-Bohr radius. As a consequence, polaritons are expected to behave as bosons in a dilute system. In this section, we will briefly summarize the properties of bosons and their singular behavior due to the Bose-Einstein statistics, which leads to a quantum phase transition referred to as *Bose-Einstein condensation* (BEC) when the degeneracy condition is reached. The finite lifetime of polaritons and their ability to interact *via* their excitonic component strongly impacts on the formation of Bose condensates and the thermodynamic description should be refined and replaced by a revised definition of the BEC.

1.4.1 The ideal non-interacting Bose gas: case of the Bose-Einstein condensation

1.4.1.1 Coherence length of massive particles

In his thesis (1924) Louis de Broglie suggested that massive particles also have a wave nature. To every particle with a momentum p, a wave is associated with a wavelength $\lambda_{\mathrm{DB}} = h/p$, where h is the Planck constant. In a non-interacting Bose gas, the momentum p is given by mv_{th}, where v_{th} is the mean velocity of the particles derived from Boltzmann kinetic gas theory and due to the thermal agitation. The thermal wavelength λ_{DB} associated to each particle is given by the relation:

$$\lambda_{\mathrm{DB}} = \frac{h}{\sqrt{2\pi m k_{\mathrm{B}} T}}. \tag{1.72}$$

This relation highlights the fact that both temperature and mass are notorious enemies of quantum effects as λ_{DB} tends to zero when these parameters are increased. For this reason, at ambient conditions, the wave function associated to massive particles have a negligible spatial extent and the quantum behavior is bleached. Conversely, for elementary particles with a small mass and for cryogenic temper-

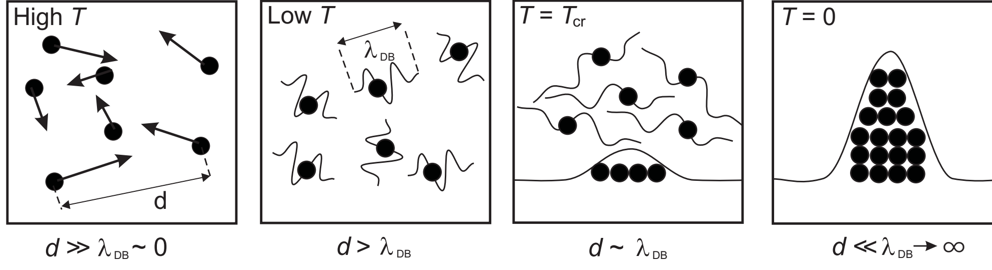

Fig. 1.15: Schematic representation of a Bose gas behavior when the temperature T is decreased. When T is high, particles behave as classical ones. When T is sufficiently decreased, their wave function extension given by λ_{DB} becomes comparable with the mean interparticle distance d. $T = T_{\mathrm{crit}}$ corresponds to the critical situation where $\lambda_{\mathrm{DB}} = d$ and bosons accumulate in the ground state. At $T = 0$, all particles lie in the ground state.

atures, the coherence length defined by λ_{DB} reaches the order of the mean interparticle distance d and the associated wave functions can spatially interfere (see Fig. 1.15).

1.4.1.2 Bose-Einstein condensation: Introduction and definition

Depending on their symmetry, quantum particles can be classified into two categories: fermions have an antisymmetric wave function and bosons a symmetric one. This classification comes from their indistinguishability: two bosons can be exchanged without affecting the system wave function, contrary to fermions. Bosons and fermions thus show drastically different behaviors as their wave function will differently interfere. In particular fermions tend to repel each other due to the destructive interferences between particles having the same state (Pauli blocking principle) whereas bosons tend to attract each other due to constructive interferences. This behavior is directly visible in the shape of the distribution functions: classical particles are distributed according to the Boltzmann distribution $N_{\mathrm{B}}\left(E_{\mathbf{k}}, T, \mu\right)$, fermions according to the Fermi-Dirac one $N_{\mathrm{FD}}\left(E_{\mathbf{k}}, T, \mu\right)$ and bosons according to the Bose-Einstein one $N_{\mathrm{BE}}\left(E_{\mathbf{k}}, T, \mu\right)$:

$$N_{\mathrm{B}}\left(E_{\mathbf{k}}, T, \mu\right) = g_{\mathrm{E}_{\mathbf{k}}} \exp\left(-\frac{E_{\mathbf{k}}-\mu}{k_{\mathrm{B}}T}\right), \tag{1.73}$$

$$N_{\mathrm{FD}}\left(E_{\mathbf{k}}, T, \mu\right) = g_{\mathrm{E}_{\mathbf{k}}} \left[\exp\left(\frac{E_{\mathbf{k}}-\mu}{k_{\mathrm{B}}T}\right)+1\right]^{-1}, \tag{1.74}$$

$$N_{\mathrm{BE}}\left(E_{\mathbf{k}}, T, \mu\right) = g_{\mathrm{E}_{\mathbf{k}}} \left[\exp\left(\frac{E_{\mathbf{k}}-\mu}{k_{\mathrm{B}}T}\right)-1\right]^{-1}, \tag{1.75}$$

where $g_{\mathrm{E}_{\mathbf{k}}}$ is the degeneracy of the state with energy $E_{\mathbf{k}}$ and μ is the chemical potential, which is given by the conservation of the total particle number N_{tot}:

$$\mu \leftrightarrow \sum_{\mathbf{k}} N\left(E_{\mathbf{k}}, T\right) = N_{\mathrm{tot}}. \tag{1.76}$$

It is worth pointing out that when $T \to \infty$, $f_{\mathrm{FD}}\left(E_{\mathbf{k}}, T, \mu\right)$ and $f_{\mathrm{BE}}\left(E_{\mathbf{k}}, T, \mu\right)$ converge to the classical Boltzmann distribution, indicating that the quantum nature of the particles is blurred for high temperatures.

The calculation of the total particle number from relation 1.76 leads to the important physical constraint $\mu < E_{\mathbf{k}=0} = E_0$. Defining the origin of energies E_0 at the minimum of the energy dispersion curve, the

chemical potential μ is a strictly negative quantity. From the shape of the Bose-Einstein distribution (relation 1.75), it appears that when μ approaches zero, the number of particles at $k = 0$ (N_0) becomes increasingly large. This singularity is the physical origin for the BEC.

In 1925, Einstein proposed the idea that for a non-interacting bosonic quantum gas at thermal equilibrium, a critical temperature T_{crit} exists at which a phase transition occurs [1, 2]:

> *Die Behauptung geht also dahin, dass etwas Ähnliches eintritt wie beim isothermen Komprimieren eines Dampfes über das Sättigungsvolumen. Es tritt eine Scheidung ein: ein Teil "kondensiert", der Rest bleibt ein gesättigtes ideales Gas.* (The idea is that something happens, similar to the isothermal compression of a vapor across the saturation volume. A separation occurs; one part "condenses", the remaining part stays a "saturated" ideal gas.) (Einstein, 1925)

The total number of particles N_{tot} in the system is thus the sum of N_0 corresponding to the condensate and the other particles N_{T}, which correspond to the thermal component of the gas, i.e., the uncondensed phase. These particle numbers obviously depend on T and μ. For a given temperature, N_0 is a smooth function of μ and reaches a maximum value N_{crit} when $\mu = 0$. The critical temperature for BEC is defined by the condition [124]:

$$N_{\text{T}}\left(T = T_{\text{crit}}, \mu = 0\right) = N_{\text{tot}}\,, \tag{1.77}$$

where V is the volume occupied by the gas. This condition states that condensation is triggered when N_0 becomes a dominant fraction of N_{tot}: the excited states saturate and $N_0 \approx k_{\text{B}}T/\mu$ becomes macroscopically occupied as $\mu \to 0$. This mechanism is the classical definition of BEC. For a 3D system, relation 1.77 leads to $T_{\text{crit}} = \frac{2\pi\hbar^2}{mk_{\text{B}}}\left(\frac{N_{\text{tot}}}{2.612V}\right)^{3/2}$.

Another way of understanding the BEC is to compare the mean interparticle distance $d = V^{1/3}$ in a Bose gas to the thermal de Broglie wavelength given by relation 1.72. As schematically depicted in Fig. 1.15, when $d = \lambda_{\text{DB}}$, wave packets start to overlap and constructively interfere in the state of minimum energy ($k = 0$). For $T > T_{\text{crit}}$, the particles behave classically whereas for $T < T_{\text{crit}}$, particles accumulate in the ground state. In the limiting case where $T = 0$, λ_{DB} diverges and the vapor phase no longer exists. This situation corresponds to a pure BEC. Experimentally, BEC was observed in 1995 in dilute atomic vapors by the groups of Wieman and Cornell at Boulder [4] and that of Ketterle at MIT [3].[17] However, due to the relatively large mass of atoms, the critical temperature for BEC was of the order 150 nK. According to relation 1.72, the only way for the observation of BEC at elevated critical temperatures is the decrease in the mass of the particles. Several bosonic particles were proposed as good candidates and BEC was claimed in various systems such as indirect excitons [125], magnons [126] or even cavity photons [127]. In this thesis, we will focus on microcavity polariton condensation as they exhibit an extremely low effective mass inherited from the cavity photon dispersion (see relation 1.41).

1.4.2 Polariton BEC

A generalization of the previous discussion for a 2D-system such as a polariton gas is problematic since long-wavelength thermal fluctuations destroy the long-range order [128]. BEC is thus forbidden for an infinite 2D-system at $T \neq 0$. However, in a finite system of lateral dimension L, the critical temperature becomes acquires a finite value and quasi-BEC can take place with:

$$T_{\text{crit}} \propto \frac{N_{\text{tot}}}{L^2 \log\left(N_{\text{tot}}\right)}\,, \tag{1.78}$$

[17] Eric A. Cornell, Wolfgang Ketterle, and Carl E. Wieman shared the Nobel prize in 2001 for this discovery.

and the critical density is given by [129]:

$$N_{\text{crit}} = \frac{2}{\lambda_{\text{DB}}^2} \log\left(\frac{L}{\lambda_{\text{DB}}}\right). \tag{1.79}$$

In opposition to atomic BEC, polaritons have a very short lifetime of the order of the picosecond and a non-negligible interaction cross-section due to their excitonic part content. These specific features significantly alter the thermodynamic description presented before and the definition of BEC should be refined. The role of interactions in the polariton condensate formation, the impact of the short polariton lifetime and the peculiarities of quasi-BEC will be addressed in details in Chapter 4.

Regarding the criterion for the demonstration BEC in a polariton system, observation of the massive occupation of the ground state is mandatory but not sufficient. It was shown that polariton BEC is accompanied by the appearance of long range order and phase coherence in the condensed state [124]. As all particles occupy the same state (delta-function in the Fourier space $\delta(\mathrm{k})$), the coherence is extended over the complete condensate area. This remarkable feature was experimentally observed *via* spatial coherence measurements [18] and was considered as the *smoking gun* for BEC. Another critical aspect of BEC, which should also be observed is the spontaneous symmetry breaking, which is monitored by the spontaneous build-up of the order parameter at threshold [52]. In a polariton system, this spontaneous build-up is directly measurable *via* the polarization of the emitted light (see Chapter 5).

2 III-nitride materials

Due to lack of inversion symmetry in the wurtzite cell, III-nitride semiconductors present peculiar features, including the presence of spontaneous polarization field along the c-axis and an intrinsic optical anisotropy including birefringence and dichroism. In this chapter, a brief history is first presented highlighting how these materials have played an increasing role both in academia and in the industry, due to large panel of applications they cover. Then the main structural and optical properties of III-nitrides are presented and a particular attention is paid to the impact of the crystal orientation.

2.1 A brief history

Even if the first reports on the growth of aluminum nitride date back to the second half of the 19th century, the real story of III-nitrides started in the late 1960s, early 1970s [130]. The possibility of realizing efficient light-emitting diodes (LEDs) operating in the visible range generated a lot of interest for those materials and in particular for GaN that was investigated first. A significant breakthrough was the observation of well-resolved excitonic resonance transitions at low temperature on GaN epilayers grown by hydride vapor phase epitaxy (HVPE) on c-plane oriented sapphire substrate in 1971 [71]. Despite encouraging observations, the available samples suffered from a relatively high defect density and the difficulty to efficiently p-dope the layers rapidly damped the interest of the scientific community for III-nitrides.

The next major breakthroughs, which really marked a revival of the research on III-nitrides occurred in the late 1980s with the pioneering works of Akasaki and coworkers. First, in 1986, this group reported an improvement in the material quality of GaN epilayers grown by metal-organic vapor phase epitaxy (MOVPE) by using an AlN buffer grown on top of sapphire substrates [131]. Then, they obtained for the first time an efficient p-type conductivity in Mg-doped GaN layers post-treated with low-energy electron beam irradiation producing the dissociation of Mg-H complexes, which form during growth due to contamination in the chamber [132]. It paved the way toward the realization of nitride-based electrically injected devices. In 1991, Shuji Nakamura from Nichia Chemical Industries Ltd. showed a subsequent improvement of GaN epilayers when introducing a low temperature GaN buffer layer about 20 nm thick prior to the high temperature growth of GaN by MOVPE [133]. This two-step growth process allowed a significant decrease in the defect density (mainly threading dislocations) while improving the optical and electrical characteristics. This was followed by the first demonstration of candela-class blue LEDs relying on an InGaN/GaN multiple quantum well active medium in 1994 by Nakamura and coworkers [49]. Two years after this *tour de force*, the first blue laser diode (wavelength

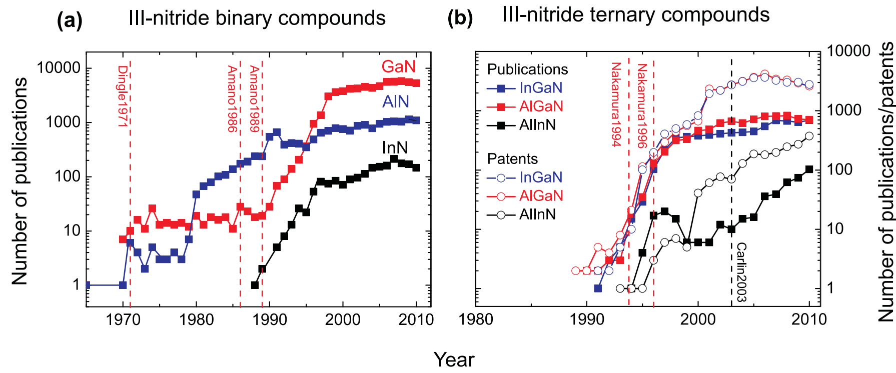

Fig. 2.1: Number of publications during the last decades in the field of III-nitrides: (a) InN, GaN and AlN binary compounds and (b) InGaN, AlGaN and AlInN ternary compounds. The vertical dashed lines indicate the major breakthroughs made by Dingle1971 [71], Amano1986 [131], Amano1989 [132], Nakamura1994 [49], Nakamura1996 [6] and Carlin2003 [59] (source: *ISI Web of Science*). For the ternary compounds, the number of patents is also indicated (source: *Google patents*).

emission $\lambda = 417\,\text{nm}$) operating at room temperature was reported [6]. These major advances triggered the activity on III-nitrides, which was continuously growing over the last decade as evidenced by the increasing number of related patents and publications (see Fig. 2.1). Nowadays, III-nitride-based devices such as LEDs, laser diodes or even HEMTs for high frequency electronics are commercially available and represent the second largest semiconductor market after the silicon one.

2.2 Structural properties

2.2.1 Crystalline structure

A detailed description of the solid crystalline structure is of special interest as many of the material physical properties, such as electronic and mechanical ones, can be can be drawn from symmetry arguments by applying group theory.

Any crystalline structure can be obtained by a periodic repetition of an elementary pattern, called *base*, in all three directions of space, on each point of the structure, called the *Bravais lattice*. Such a lattice is generated by 3 primitive translation vectors, labeled $\mathbf{a}_1$, $\mathbf{a}_2$ and $\mathbf{a}_3$.[18] Directions and planes in a crystal are expressed in this basis by a set of integers h, k and l called the *Miller indices*. Any vector $\mathbf{R}$ of the Bravais lattice can thus be expressed as:

$$\mathbf{R} = h\mathbf{a}_1 + k\mathbf{a}_2 + l\mathbf{a}_3 \,. \tag{2.1}$$

Even if III-nitrides can crystallize in the zinc-blende [134] or even in the rocksalt phase under high pressure [135], only the wurtzite one is thermodynamically stable. Its lattice corresponds to a hexagonal close packed (hcp) structure with a two-atom basis: the metal atoms $\text{M} \in \{\text{In}, \text{Ga}, \text{Al}\}$ are located at positions $(0,0,0)$ and $\left(\frac{1}{3}, \frac{2}{3}, \frac{1}{2}\right)$ and the N-atoms at $\left(\frac{1}{3}, \frac{2}{3}, u + \frac{1}{2}\right)$ and $(0,0,u)$ where u is the internal parameter, which defines the $M - N$ bond length according to:

$$\Delta(M - N) = u \cdot c \,, \tag{2.2}$$

[18] The choice of these vectors spanning the primitive unit cell is not unique but should reflect at best the crystal symmetry.

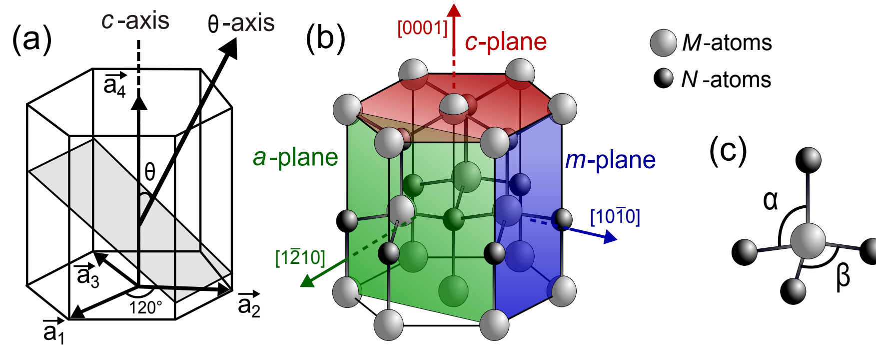

Fig. 2.2: Schematic representation of the wurtzite cell featuring: (a) the basis ($\mathbf{a}_1, \mathbf{a}_2, \mathbf{a}_3, \mathbf{a}_4$) of the Bravais cell. The grey plane represents an arbitrary semi-polar plane forming an angle θ with the c-axis. (b) Polar and non-polar crystal orientations. (c) Angles between metallic (M) and nitrogen atoms (N).

where the distance between two equivalent planes in the stacking direction is c. These four positions form the primitive unit cell for the entire wurtzite family and every vector of the wurtzite Bravais cell can be expressed in the basis ($\mathbf{a}_1, \mathbf{a}_2, \mathbf{a}_4$) (see Fig. 2.2(a)), where $\mathbf{a}_4$ is collinear to the high symmetry direction labeled as c-axis and has a norm given by the c lattice constant. $\mathbf{a}_1$ and $\mathbf{a}_2$ have the same length and form an angle of 120° between them in the orthogonal plane. Because of the hexagonal symmetry of the wurtzite cell, it is common to use a four-vector basis and introduce an additional in-plane vector $\mathbf{a}_3 = -(\mathbf{a}_1 + \mathbf{a}_2)$. In this basis, planes and directions are given by the four-index notation. Note that crystal planes are labeled as $(hklm)$ and directions as $[hklm]$.

The hcp 3D lattice can be seen as a pile up of hexagonally arranged stacks of spheres. After the first plane (labeled as *A*) the second one (*B*) is deposited in order to minimize the total volume, i.e. each sphere is touching the three neighboring ones from the underlying layer. This bilayer stack is then repeated to generate the full 3D-crystalline structure with the period sequence *ABABAB*..., where *C* and *D* correspond to two shifted planar arrangements of vertical $M-N$ bonds whose length is given by the relation 2.2. Labeling a the distance between two adjacent spheres within a given layer, a, c and u constants in a perfect hcp structure satisfy the relations:

$$\begin{aligned} \frac{c}{a} &= \sqrt{\frac{8}{3}} \approx 1.633\,, \\ u &= \frac{3}{8} = 0.375\,. \end{aligned} \tag{2.3}$$

The two bond angles in the tetrahedron, α and β (see Fig. 2.2(c)), are equal in an ideal structure, i.e. $\alpha = \beta = 109.47°$. However, due to non-idealities in the as-grown samples and the strong ionicity of the bonds, these ideal values slightly differ from the experimentally observed for all $In_xGa_{1-x}N$ [136], $Al_xGa_{1-x}N$ [137] and $Al_xIn_{1-x}N$ compounds [138]. In Table 2.1, the relative deviation between the ideal and the real lattice constants is shown.

Despite the complexity of the III-nitride ternary alloys, it appears that a linear interpolation between the binary compounds InN, GaN and AlN (Vegard's law) is valid for the macroscopic structural properties such as the lattice constants a and c [139]. For a given alloy $C_xD_{1-x}N$, where A and B are metal atoms, a given lattice parameter can be expressed, for a given molar fraction x:

Table 2.1: Relative deviation between the ideal and the real lattice parameters calculated from values given in [139]. Values with index 0 correspond to the ideal hcp case.

	InN	GaN	AlN
$(u-u_0)/u_0$	1.07	0.53	1.87
$\left(\frac{c}{a}-\frac{c_0}{a_0}\right)/\frac{c_0}{a_0}$	-0.92	0.06	-1.65
$(\alpha-\alpha_0)/\alpha_0$	-0.71	-0.27	-1.17
$(\beta-\beta_0)/\beta_0$	0.7	0.28	1.15

$$P(x) = P_{\mathrm{CN}}x + P_{\mathrm{DN}}(1-x), \tag{2.4}$$

where P_{CN} and P_{DN} are the values of the parameter P for the binary compounds CN and DN. This linear approximation no longer holds for the nearest-neighbor bond lengths $M-N$, which depend on the internal parameter $u(x)$. A nonlinear bowing term $bx(1-x)$ accounting for the difference in electronegativity between species, the strain and the various non-idealities should be added to equation 2.4 where b is the *bowing parameter*, which is larger for alloys containing indium. In Fig. 2.3, the evolution of the parameters a, c and u is shown for the III-nitride ternary compounds.

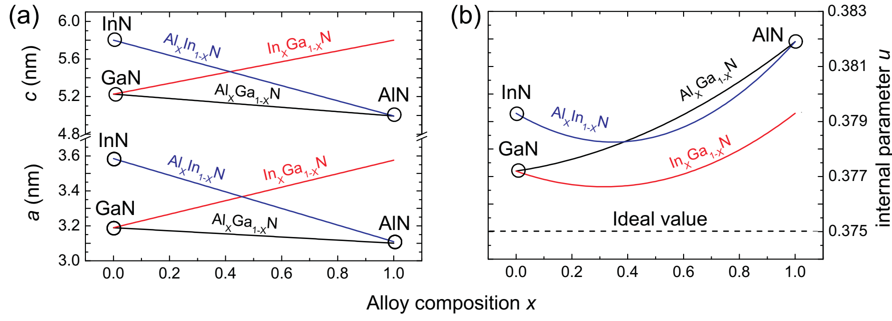

Fig. 2.3: Variations of (a) the lattice constants a and c and (b) the internal parameter u as a function of the alloy composition x following [139].

2.2.2 *Crystal orientations*

The transformation of a coordinate system $(\hat{x},\hat{y},\hat{z})$ into another one $(\hat{x}',\hat{y}',\hat{z}')$ can be made by three successive rotations defined by the three *Euler angles*. In the case of the wurtzite cell, only two angles are needed to rotate the crystal in an arbitrary orientation and the rotation matrix $U(\phi,\theta)$ reads:

$$U(\phi,\theta) = \begin{pmatrix} \cos(\theta)\cos(\phi) & \cos(\theta)\sin(\phi) & -\sin(\theta) \\ -\sin(\phi) & \cos(\phi) & 0 \\ \sin(\theta)\cos(\phi) & \sin(\theta)\sin(\phi) & -\cos(\theta) \end{pmatrix}, \tag{2.5}$$

where θ defines the angle between the $c-$axis [0001] and the normal to the growth plane $(hklm)$ and ϕ corresponds to a rotation around the $c-$axis. Due to the sixfold symmetry of the wurtzite structure, only the θ-dependence can be considered. Most of the crystal properties, including operators (Hamiltonian),

vectors (momenta, positions, etc.) and tensors (strain, stress, stiffness, etc.) can be expressed by means of $U(\theta) = U(\theta, \phi = 0)$ [140]. By convention, the x axis is aligned with the m-direction $[1\bar{1}00]$, the y axis with the a-direction $[11\bar{2}0]$ and the z axis with the principal c-axis [0001] (see Fig. 2.2(b)).

Until 2000, the research on III-nitrides mainly focused on materials grown along the $c-$direction (θ=0), mainly driven by the industry for the realization of blue LEDs. Even if this crystal orientation undoubtedly presents serious advantages due to its mature growth, process handling and the availability of large-area substrates with a relatively low threading dislocation density ($\sim 10^5 - 10^6\,\mathrm{cm}^{-2}$), growth along other crystal orientations also presents serious advantages despite a poorer crystalline quality. Nowadays, the research on mainly focuses on three different types of crystal orientations:

- **$\theta = 0°$: the polar *c*-axis.** The c-axis is always referred to as the polar one due to the presence of spontaneous polarization along the growth direction. It is still the preferred choice in academia and industry because of its higher crystalline quality and in-plane isotropic properties. However, the radiative efficiency of heterostructures is strongly affected by the presence of a built-in electric field in the active medium. This effect, referred to as *quantum confined Stark effect*, detrimentally affects the exciton oscillator strength and binding energy due to the separation of electron and hole wave functions (see Section 2.2.6).
- **$\theta = 90°$: the nonpolar *a*- and *m*-axes.** In contrast with c-plane samples, growth along nonpolar orientations allows to get rid of the quantum confined Stark effect as the projection of the polarization along the growth direction is equal to zero [141, 142]. In addition, due to the in-plane optical anisotropy, the emitted light is spontaneously polarized, which presents a serious advantage for displays such as liquid crystal display screens [143]. Finally, nonpolar orientations are very promising to reduce the threshold current density for UV laser diodes [144].
- **$0 < \theta < 90°$: the semi-polar axes.** A last category of crystal orientation, which has recently attracted a lot of interest in the community is the semi-polar one (e.g. semi-transparent plane in Fig. 2.2(a)). This intermediate situation seems very promising for the realization of LEDs and laser diodes in the green spectral range due to the higher indium incorporation allowing to reach longer wavelengths [145]. Indeed, an electrically injected continuous-wave green laser diode ($\lambda = 520\,\mathrm{nm}$) was demonstrated on the $(20\bar{2}1)$-plane [146]. Another serious advantage of these orientations is that the piezoelectric field along the growth direction can be strongly reduced depending on the alloy composition and the strain state [140].

2.2.3 Growth

One of the major issues for the growth of high quality III-nitride samples is the high price of the commercially available bulk GaN substrates for homoepitaxy, which are mainly used for the fabrication of laser diodes. Industry and research have to cope with this and develop materials and techniques to optimize heteroepitaxial growth. A good substrate has to meet several requirements such as a good thermal expansion coefficient (α) close to that of GaN [147], an appropriate surface chemistry, a good thermal conductivity (κ) and cleavability and last but not least, a good availability and an affordable price (see Table 2.2 for some commonly used substrates). The lattice mismatch in heteroepitaxially grown layers is of major importance as it favors the formation of dislocations, cracks and various defects affecting both the optical and electrical efficiency of optoelectronic devices. A special attention must be also paid to the difference between the thermal expansion coefficients ($\Delta\alpha$) as it introduces

residual stress upon cooling the sample from high growth temperature to the ambient one, resulting in additional structural defects [148, 149].

The most commonly used substrates for the heteroepitaxial growth of III-nitrides are sapphire, silicon (Si) and silicon carbide (SiC): their relevant physical properties are displayed in Tab. 2.2. Growth on sapphire seems inconvenient due to its low thermal conductivity, its relatively important lattice mismatch and thermal expansion difference with respect to GaN. However, it is still nowadays the preferred choice due to its low price and high availability. SiC, used with both 4H- and 6H-polytypes, presents a reduced lattice mismatch to GaN compared to sapphire and has a relatively large thermal conductivity allowing for an efficient heat dissipation. However, GaN can hardly be grown directly on SiC due to the poor wetting between the two compounds [150]. In addition, the price and the availability of SiC substrates still remains not competitive with sapphire ones. Another substrate of choice is silicon, owing to its advantageous physical properties, the ultra-high crystalline quality of the substrates and its mature development making Si substrate widely available and extremely cheap. Despite these obvious qualities, controlling the quality of GaN layers grown on Si substrates for optoelectronic and high power electronic applications remains critical owing to issues encountered with the management of the accumulated tensile strain. Other materials can potentially be used as a substrate such as AlN, AlAs, GaAs, ZnO, MgO, $LiAlO_2$, etc. For a review, the reader can refer to Ref. [151].

Table 2.2: Material properties of various substrates influencing the quality of the overgrown III-nitride material. Values taken from [151].

	Si (111)	α-Al_2O_3	SiC (4H, 6H)
Δ a/a (%)	17	-13.9	-3.5
$\Delta\alpha\left[10^{-6}/K\right]$	-3	1.7	-1.14
κ (W/cm K)	1.56	0.25	3.8

The three main techniques to grow III-nitrides are hybride vapor phase epitaxy (HVPE), molecular beam epitaxy (MBE) and metal-organic vapor phase epitaxy (MOVPE). HVPE is usually preferred for the growth of thick GaN epilayers as it allows for large-size crystal growth with rates exceeding 500 μm/h (at typically 1050° C). Those thick GaN layers often serve as templates for nitride heterostructures grown by the other two techniques. In the present work, heterostructures are grown by both MBE (nonpolar microcavities presented in Chapter 6) and MOVPE (polar microcavity investigated in Chapters 3 to 5). The MBE growth technique requires high or ultra-high vacuum, typically 10^{-8} Pa, and is limited to a relatively low deposition rate (up to about 1 μm/h for GaN) compared to MOVPE ($1-10\,\mu$m/h for GaN) or especially HVPE. However, due to the high vacuum in the growth chamber, MBE offers the possibility of monitoring the growth rate *via in situ* monitoring of RHEED (reflection high energy electron diffraction) oscillations and thus to achieve a high control on the thickness of each layer with a resolution down to a single molecular monolayer. Contrary to the MBE technique, MOVPE presently offers a higher reproducibility and is more commonly used in the industry for the growth of nitride-based optoelectronic devices.

2.2.4 Mechanical properties

The wurtzite cell corresponds to the ideal highly symmetric case where all atoms are fixed at the lattice positions defined by the Bravais structure. However, this situation is rarely achieved permanently as the atoms are elastically bonded and will reorganize themselves under the influence of strain, thermal fluctuations, local or extended defects, etc. A mechanical description of the lattice is thus of high importance to understand the impact of the cell deformation on both electronic and optical properties of the material of interest.

2.2.4.1 Strain in crystals

Due to the large lattice-mismatch between III-nitride compounds and the commercially available substrates, the sample design should fully account for strain effects on the material properties. In opposition to phonons, which correspond to the motion of the lattice, strain affects the electronic and optical properties permanently as it modifies the equilibrium position of the atoms in the primitive cell. A good understanding of the crystal mechanical properties provides a direct way of tuning the properties of optoelectronic devices by strain management, e.g. *via* a careful choice of the crystal orientation, alloy composition, layer thicknesses, etc.

The strain tensor relates the unstrained lattice unit vectors $(\mathbf{a}_1, \mathbf{a}_2, \mathbf{a}_3)$ to the effective ones $\left(\mathbf{a}'_1, \mathbf{a}'_2, \mathbf{a}'_3\right)$ by the relation:

$$\begin{pmatrix} \mathbf{a}'_1 \\ \mathbf{a}'_2 \\ \mathbf{a}'_3 \end{pmatrix} = \begin{pmatrix} \varepsilon_{\mathrm{xx}} & \varepsilon_{\mathrm{xy}} & \varepsilon_{\mathrm{xz}} \\ \varepsilon_{\mathrm{yx}} & \varepsilon_{\mathrm{yy}} & \varepsilon_{\mathrm{yz}} \\ \varepsilon_{\mathrm{zx}} & \varepsilon_{\mathrm{zy}} & \varepsilon_{\mathrm{zz}} \end{pmatrix} \begin{pmatrix} \mathbf{a}_1 \\ \mathbf{a}_2 \\ \mathbf{a}_3 \end{pmatrix}. \tag{2.6}$$

The off-diagonal terms of the strain tensor correspond to shear deformation whereas the diagonal ones correspond to a hydrostatic one, i.e. the relative deformation in a given direction $i \in \{x, y, z\}$ is given by $\varepsilon_{\mathrm{ii}} = \frac{L_{\mathrm{f}} - L_0}{L_0}$ where L_0 and L_{f} correspond to the bond length before and after deformation, respectively. When $\varepsilon_{\mathrm{ii}} < 0$, the strain is compressive and tensile when $\varepsilon_{\mathrm{ii}} > 0$.

2.2.4.2 Hooke's law for solids

Crystal deformation generates internal forces leading to the natural definition of stress as the force responding to strain per unit area [152]. Strain ($\bar{\bar{\varepsilon}}$) and stress ($\bar{\bar{\sigma}}$) are second-rank tensors proportional to each other in the linear elastic theory limit. For a crystal, Hooke's law is generalized by introducing a fourth-rank tensor displaying the elastic stiffness C_{ijkl}, which linearly relates stress and strain components. Due to the crystal symmetries the C_{ijkl} tensor (81 components) can be reduced to a 6×6 matrix C_{ij}. For wurtzite crystals, only five elastic constants are necessary to describe the mechanical properties:

$$C_{\mathrm{ij}} = \begin{pmatrix} C_{11} & C_{12} & C_{13} & 0 & 0 & 0 \\ C_{12} & C_{11} & C_{13} & 0 & 0 & 0 \\ C_{13} & C_{13} & C_{33} & 0 & 0 & 0 \\ 0 & 0 & 0 & C_{44} & 0 & 0 \\ 0 & 0 & 0 & 0 & C_{44} & 0 \\ 0 & 0 & 0 & 0 & 0 & \frac{1}{2}(C_{11} - C_{12}) \end{pmatrix}. \tag{2.7}$$

As $\bar{\bar{\varepsilon}}$ and $\bar{\bar{\sigma}}$ are symmetric tensors, they can be reduced to 6-component vectors with the notation convention $xx \to 1$, $yy \to 2$, $zz \to 3$, $yz = zy \to 4$, $xz = zx \to 5$, and $xy = yx \to 6$. Hooke's law for solids

Table 2.3: Elastic constants for III-nitride binary compounds extracted from [153]. For ternary alloys, the constants can be estimated using Vegard's law (equation 2.4).

	GaN	AlN	InN
C_{11} (GPa)	390	396	223
C_{12} (GPa)	145	137	115
C_{13} (GPa)	106	108	92
C_{33} (GPa)	398	373	224
C_{44} (GPa)	105	116	48
d_{15} (pm/V)	-1.6	-2. 1	-3.5
d_{31} (pm/V)	3.1	5.4	7.6
d_{33} (pm/V)	3.1	3.6	5.5

therefore reads:

$$\sigma_{\mathrm{i}} = \sum_{\mathrm{j}} C_{\mathrm{ij}}\varepsilon_{\mathrm{j}} - \sum_{\mathrm{k}} e_{\mathrm{ik}} F_{\mathrm{k}} \approx \sum_{\mathrm{j}} C_{\mathrm{ij}}\varepsilon_{\mathrm{j}}\,. \tag{2.8}$$

where e_{ik} is the piezoelectric tensor and F_{k} is the electric field along the k-direction. All latin subscripts run over the three spatial directions x, y and z. Note that in expression 2.8, the second term representing the converse piezoelectric effect is neglected, which is justified *a posteriori* by the small deviations (~ 2%) from the complete calculation in the case of heterostructures [154]. In the present work, we are interested in growth of heterostructures, in particular microcavities with multiple quantum wells serving as an active region. Assuming a pseudomorphic growth of the heterostructure on the underlying III-nitride epilayer, the strain is relaxed along the growth direction in order to minimize the elastic energy W given by [155]:

$$W = \frac{1}{2}\sum_{\mathrm{i,j=1}}^{6} C_{\mathrm{ij}}\varepsilon_{\mathrm{i}}\varepsilon_{\mathrm{j}} = \frac{1}{2}\left[C_{11}\varepsilon_{\mathrm{xx}}^2 + C_{11}\varepsilon_{\mathrm{yy}}^2 + C_{33}\varepsilon_{\mathrm{zz}}^2 + 2C_{12}\varepsilon_{\mathrm{xx}}\varepsilon_{\mathrm{yy}} + 2C_{13}\left(\varepsilon_{\mathrm{xx}}\varepsilon_{\mathrm{zz}} + \varepsilon_{\mathrm{yy}}\varepsilon_{\mathrm{zz}}\right) + 4C_{44}\varepsilon_{\mathrm{xz}}^2\right]. \tag{2.9}$$

The assumption of pseudomorphic growth leads to the following conditions on the strain tensor [140]:

$$\bar{\bar{\varepsilon}} = \begin{pmatrix} \varepsilon_{\mathrm{xx}} \\ \varepsilon_{\mathrm{yy}} \\ \varepsilon_{\mathrm{zz}} \\ 2\varepsilon_{\mathrm{yz}} \\ 2\varepsilon_{\mathrm{xz}} \\ 2\varepsilon_{\mathrm{xy}} \end{pmatrix} = \begin{pmatrix} \varepsilon_{\mathrm{xx}}^0 + \varepsilon_{\mathrm{xz}}\frac{\sin(\theta)}{\cos(\theta)} \\ \varepsilon_{\mathrm{xx}}^0 \\ \varepsilon_{\mathrm{zz}}^0 + \varepsilon_{\mathrm{xz}}\frac{\cos(\theta)}{\sin(\theta)} \\ 0 \\ 2\varepsilon_{\mathrm{xz}}(\theta) \\ 0 \end{pmatrix}, \tag{2.10}$$

where $\varepsilon_{\mathrm{xx}}^0 = \frac{a_{\mathrm{s}} - a_{\mathrm{e}}}{a_{\mathrm{e}}}$ and $\varepsilon_{\mathrm{zz}}^0 = \frac{c_{\mathrm{s}} - c_{\mathrm{e}}}{c_{\mathrm{e}}}$ and a_{i} and c_{i} are the lattice constants of the epilayer (index e) and the substrate (s), respectively. The only remaining unknown is $\varepsilon_{\mathrm{xz}}$, which directly follows from the minimization of the elastic energy W in equation 2.9, i.e. $\frac{\partial W}{\partial \varepsilon_{\mathrm{xz}}} = 0$, leading to the expression of $\varepsilon_{\mathrm{xz}}$ for any crystal orientation θ [140]:

$$\varepsilon_{\mathrm{xz}}(\theta) = -\frac{\left[\left(C_{11} + C_{12} + C_{13}\frac{\varepsilon_{zz}^0}{\varepsilon_{xx}^0}\right)\sin^2(\theta) + \left(2C_{13} + C_{33}\frac{\varepsilon_{zz}^0}{\varepsilon_{xx}^0}\right)\cos^2(\theta)\right]\varepsilon_{\mathrm{xx}}^0\sin(\theta)\cos(\theta)}{C_{11}\sin^4(\theta) + 2\left(C_{13} + 2C_{44}\right)\sin^2(\theta)\cos^2(\theta) + C_{33}\cos^4(\theta)}. \tag{2.11}$$

Using expressions 2.10 and 2.11, the strain tensor can be expressed for any crystal orientation and for each layer of the heterostructures. This aspect is of major importance as the strain is considerably

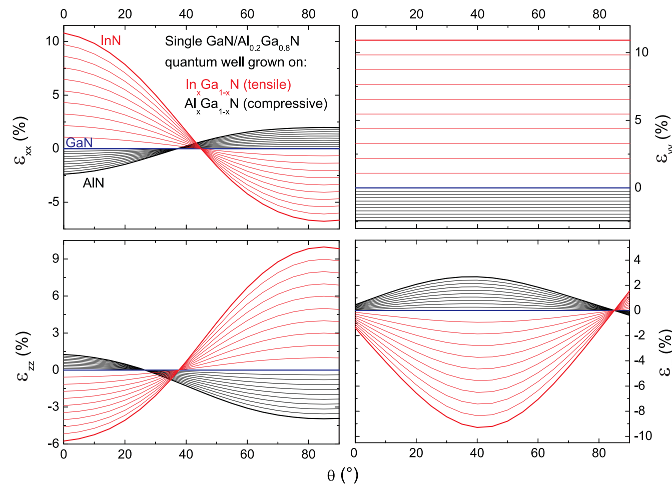

Fig. 2.4: Evolution of the strain tensor in a single $GaN/Al_{0.2}Ga_{0.8}N$ quantum well for different strain states. The buffer is continuously changed by switching from $In_xGa_{1-x}N$ (red thin lines, tensile strain) to $Al_xGa_{1-x}N$ (black thin lines, compressive strain) with $0 < x < 1$. The cases with $x = 0$ correspond to GaN (blue thick line) and to InN (thick red line) and AlN (thick black line) for $x = 1$.

affecting the excitonic properties such as the effective mass, the band gap energy or the oscillator strength. As in this work we will exclusively focus on $GaN/Al_xGa_{1-x}N$ quantum wells with a relatively moderate aluminum composition in the barriers, typically 10 – 20%, we present in Fig. 2.4 the evolution of the strain tensor for different planes, corresponding to the different values of θ between 0 (c-plane) and 90° (a- and m-planes) calculated for a single $GaN/Al_{0.2}Ga_{0.8}N$ quantum well. To simulate the transition from tensile to compressive strain, the buffer is continuously changed by switching from $In_xGa_{1-x}N$ (red thin lines, tensile strain) to $Al_xGa_{1-x}N$ (black thin lines, compressive strain) with $0 < x < 1$. The cases $x = 0$ correspond to growth on GaN (thick blue line) and InN (thick red line). The case $x = 1$ corresponds to growth on AlN (thick black line).

2.2.5 Pyroelectric properties

It is clear from the wurtzite structure symmetry that the III-nitride crystal lacks inversion symmetry. As a consequence, the barycenter of cations and anions does not coincide in the primitive cell, which results in the appearance of very large spontaneous polarization fields along the c-direction. For this reason, III-nitrides belong to the family of pyroelectric materials, i.e. materials exhibiting the ability to generate a voltage due to temperature variations or lattice deformations. One should distinguish between the primary pyroelectric effect or spontaneous polarization $\mathbf{P}_{sp}$, which is normally present in the material due to the lack of inversion symmetry and the secondary pyroelectric or piezoelectric polarization $\mathbf{P}_{pz}$ effect, which arises from any extra stress applied to the material.

2.2.5.1 Spontaneous polarization

For III-nitride binary compounds, the spontaneous polarization is: $P_{sp}^{GaN} = -0.034\,C/m^2$, $P_{sp}^{AlN} = -0.09\,C/m^2$ and $P_{sp}^{InN} = -0.042\,C/m^2$ [153]. For ternary alloys, P_{sp} can be estimated by the use of Vegard's law (equation 2.4). It was shown that P_{sp} linearly depends on the internal parameters u [156],

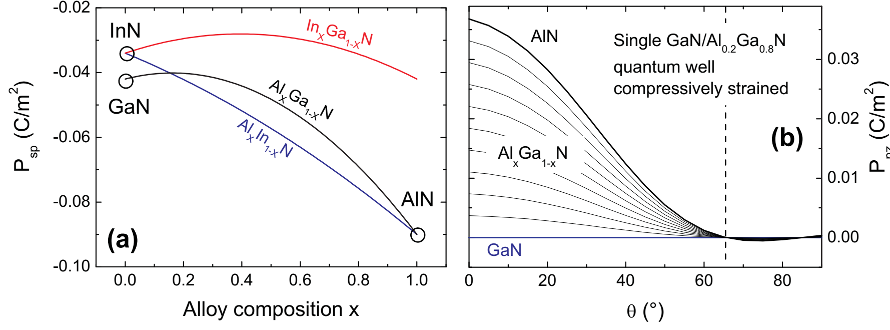

Fig. 2.5: (a) Evolution of P_{pz} of III-nitride ternary alloys: $Al_xGa_{1-x}N$ (black line), $In_xGa_{1-x}N$ (red line), and $Al_xIn_{1-x}N$ (blue line): (b) The evolution of $P_{pz}(\theta)$ is displayed for a single GaN/$Al_{0.2}Ga_{0.8}N$ quantum well from the strain-free (GaN substrate, thick blue line) to the highly compressive strain case (AlN substrate, thick black line). A minimum of P_{pz} is found in this case for $\theta \approx 65°$ (vertical dashed line).

i.e. it is sensitive to the influence of the anion-cation bond length only and not to disorder [139]. As the internal parameter nonlinearly depends on the alloy composition, a bowing parameter b (see Tab. 2.4) must be introduced to correctly describe the spontaneous polarization of ternary alloys (see Fig. 2.5(a)).

As $\mathbf{P}_{sp}$ is oriented along the c-axis, its value along an arbitrary plane $(ijkl)$ forming an angle θ with the c-axis is simply given by $P_{sp}(\theta) = P_{sp}\cos(\theta)$.

Table 2.4: Bowing parameters for III-nitrides. Values taken from [139].

	(Al,Ga)N	(In,Ga)N	(Al,In)N
Bowing parameter of P_{sp} (C/m^2)	0.021	0.037	0.07
Bowing parameter of E_{gap} (eV)	-1	-2.5	-5.4

2.2.5.2 Piezoelectric polarization

The physical origin of the piezoelectric polarization is the same as for the spontaneous case but it only occurs when an additional stress is applied to the material affecting the anion-cation bond length. To first order, the magnitude of the variation of $\mathbf{P}_{sp}$ depends on the stress applied *via* the piezoelectric moduli d_{ij} (see Tab 2.3). The piezoelectric polarization along a given direction i is thus given by:

$$P_{pz,i} = \sum_{jk} d_{ijk}\sigma_{jk}. \tag{2.12}$$

Using Hooke's law (equation 2.8) to relate strain and stress tensors, the polarization along the growth direction for an arbitrary plane is obtained *via* the rotation matrix $U(\theta)$ [140]:

$$P_{sp}(\theta) = 2d_{15}C_{44}\varepsilon d_{xz}\sin(\theta) + [d_{31}(C_{11}+C_{12}) + d_{33}C_{13}](\varepsilon_{xx}+\varepsilon_{yy}) + (2d_{13}C_{13}+f_{33}C_{33})\varepsilon_{zz}\cos(\theta). \tag{2.13}$$

The nonlinear variations of strain with the crystal orientation lead to the appearance of a minimum of the piezoelectric polarization for a semi-polar plane. The evolution of $P_{pz}(\theta)$ is displayed in Fig. 2.5(b)

for a single $GaN/Al_{0.2}Ga_{0.8}N$ quantum well from the strain-free (GaN substrate) to the highly compressive strain state case (AlN substrate). A minimum in P_{pz} is found in this case for $\theta \approx 65°$. It is worth pointing out that this behavior is strongly influenced by the choice of the substrate and the crystal orientation. A careful attention should thus be paid to strain management when designing a sample.

2.2.6 Polarization: quantum confined Stark effect in heterostructures

In heterostructures, the polarization discontinuity at interfaces between two different layers i and j creates charge planes whose sign and amplitude are given by the relation 2.14.

$$\sigma_{i/j} = -\left(\mathbf{P}_j - \mathbf{P}_i\right).\hat{n}_{ij}, \tag{2.14}$$

where $\hat{n}_{ij}$ is the unitary surface vector pointing from medium i to medium j and $\mathbf{P}_{i(j)}$ is the total polarization vector in the layer $i(j)$. In the case of a single quantum well structure, charge planes of opposite sign are formed at each side of the well $\sigma_{QW/B}$ and $\sigma_{B/QW} = -\sigma_{QW/B}$, where the index B stands for barrier and QW for quantum well (labeled σ^+ and σ^- in Figs. 2.6(a)-2.6(b)). The charge planes act as a capacitor resulting in the appearance of a built-in electric field $\mathbf{F}_{bi}$ in the quantum well given by the relation $\mathbf{D}_i = \epsilon_i \mathbf{F}_{bi}$, where $\mathbf{D}_i$ is the electrostatic displacement vector and ϵ_i the dielectric constant of layer i. A generalization to an arbitrary structure and in particular to multiple quantum well active regions is possible but boundary conditions should be chosen carefully. Applying periodic boundary conditions, the field in an arbitrary layer i reads [157]:

$$\mathbf{F}^i_{bi} = \frac{\sum_j l_j \mathbf{P}_j/\epsilon_j - \mathbf{P}_i \sum_j l_j/\epsilon_j}{\epsilon_i \sum_j l_j/\epsilon_j}. \tag{2.15}$$

In Figs. 2.6(a)-2.6(b), the electron and hole wave functions Ψ_e and Ψ_h are calculated for two different quantum well thicknesses using the Numerov approximation for a single $GaN/Al_{0.2}Ga_{0.8}N$ quantum well grown on a GaN substrate along the polar c-orientation (see Appendix A). In Fig. 2.6(c), the

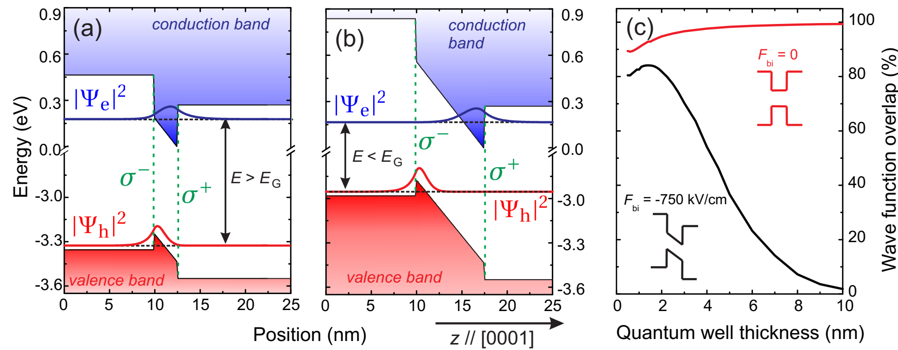

Fig. 2.6: Impact of the quantum confined Stark effect on the electronic properties of a single $GaN/Al_{0.2}Ga_{0.8}N$ quantum well surrounded by infinitely large barriers with: (a) $L_{QW} = 2.5$ nm (emission occurs above the band gap E_G) (b) $L_{QW} = 7.5$ nm (emission occurs below E_G). Electron (blue) and hole (blue) presence probability $|\Psi_e|^2$ and $|\Psi_h|^2$ are calculated in the envelope wave function approximation. The charge planes at the well interfaces are indicated by σ^+ and σ^- (green dashed lines). (c) Impact of the quantum well thickness on the electron and hole wave function overlap in the case where the internal electric field is considered (black) and in the flat band condition (red).

evolution of Ψ_e and Ψ_h is shown alternatively when the built-in electric field ($F_{bi} \approx 750\,kV/cm$) is considered (black curves) and when no electric field is present. The most striking features are (i) the increasing spatial separation between Ψ_e and Ψ_h when the quantum well thickness and the electric field are increased and (ii) the drastic decrease in emission energy $\hbar\omega$, which can even go below the band gap energy for thick enough quantum wells [158] according to:

$$\hbar\omega = E_G - E_X^b + E_e^{conf} + E_h^{conf} - eL_{QW}F_{bi}, \tag{2.16}$$

The quantum confined Stark effect is responsible for the strong decrease in the exciton radiative efficiency due to the drastic decrease in the wave function overlap. It is therefore detrimental to an efficient light-matter coupling and a careful attention should be brought to the design of microcavities in order to minimize its impact. In the case of thin ($L_{QW} < 2\,nm$) polar quantum wells or nonpolar GaN/(Al,Ga)N ones, the overlap integral in equation 1.27 is approximately equal to one, which leads to an optimum oscillator strength per unit area of $7 \times 10^{13}\,cm^{-2}$ considering a 2D-Bohr radius of 2 nm.

2.3 Optical properties

Besides pyroelectricity, the absence of inversion symmetry in the wurtzite cell causes the uniaxial anisotropy of III-nitride materials. As a consequence, the absorption, the emission and the propagation of light in these structures depend on the crystal orientation. Two kinds of anisotropy must be considered: the absorption (dichroism) and emission processes are connected to the symmetry and the shape of the band structure whereas the propagation properties are governed by the birefringence, i.e. the refractive index experienced by the electric fields is different for each polarization direction.

2.3.1 Band structure and radiative properties

2.3.1.1 Energy bandgap

One of the main interests of III-nitride materials is the possibility to cover the spectral range spanning from the mid-infrared with InN to the deep UV with AlN (see Fig. 2.7(a) and values given in Tab. 1.1). The band gap of all ternary alloys between these three compounds are obtained by applying Vegard's law (see equation 2.4) with the bowing parameters given in Tab. 2.4 (see Fig. 2.5). The band gap being closely related to the inter-atomic distance in the crystal, it is thus expected to change with temperature. In particular, it becomes larger when atoms come closer to each other and *vice versa*. The temperature evolution $E_G(T)$ is well accounted for by the semi-empirical Varshni's law [159]:

$$E_G(T) = E_G(0) - \frac{\alpha T^2}{\beta + T}, \tag{2.17}$$

where $E_G(0)$ is the value of the band gap at zero temperature and α and β are coefficients given in Tab. 2.5. Note that these values are adjustable since they depend on the nature of the substrate and should be established for each sample individually by means of reflectivity and photoluminescence experiments. In Fig. 2.7 (b), the evolution of the band gap energy for the different valence bands (labeled A, B and C) are reported for a strain-free bulk GaN layer as a function of lattice temperature according to equation 2.17 with the parameters extracted from Refs. [50, 153]. Note that the GaN band gap exhibits an important redshift of about 70 meV between 0 and 300 K.

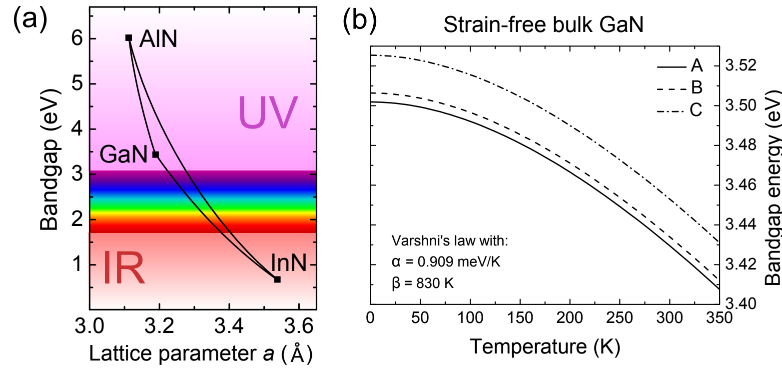

Fig. 2.7: (a) Band gap of the common III-nitride compounds versus lattice constant a emphasizing the possibility of band gap engineering *via* alloying. (b) Evolution of the band gap energy for the three valence bands (labeled A, B and C) in a strain free bulk GaN layer as a function of lattice temperature. The band gap energy at 2 K is taken from [50] and the parameters for the Varshni's fit from [153].

2.3.1.2 Conduction and valence bands: energies, selection rules and strain effects

The anisotropy of the conduction and valence bands and consequently of the optical transitions essentially relies on the symmetry of the bands close to the Γ-point, i.e. the center of the Brillouin zone. The conduction band (Γ_7^c symmetry) being almost isotropic, the selection rules are governed by the energy and symmetry of the three valence bands (with Γ_9^v, Γ_{7+}^v, and Γ_{7-}^v symmetry in order of decreasing energy; the corresponding transitions being labeled as A, B, and C). The fact that A, B and C are non-degenerate comes first from the structural anisotropy, which leads to a non-zero crystal field splitting Δ_{cr} between the two top bands (A and B) and the C bands. The splitting Δ_{so} between heavy and light hole bands (A and B) is obtained by considering the spin-orbit interaction (see Tab. 2.5 for values and Fig. 2.8(a)). Analytical expressions for the conduction and valence bands for unstrained III-nitrides are obtained from the following relations in the case of strained wurtzite structures [162]:

Table 2.5: Band gap parameters for III-nitrides. The values are taken from [153] when not specified.

	GaN	AlN	InN
$E_G\,(0)$	3.507	6.23	0.7 [160]
α (meV/K)	0.909	1.799	0.245
β (K)	830	1462	624
Δ_{cr} (meV)	19	-164	41
Δ_{so} (meV)	14	19	1
D_1 (eV)	-3.7	-17.1	-3.7
D_2 (eV)	4.5	7.9	4.5
D_3 (eV)	8.2	8.8	8.2
D_4 (eV)	-4.1	-3.9	-4.1
D_5 (eV)	-4	-3.4	-4
D_6 (eV)	-5.5	-3.4	-5.5
E_P (eV)	16.9 [161]	23.8 [161]	11.4 [161]

$$
\begin{aligned}
E_{\rm c}(\mathbf{k}=0) &= \Delta_{\rm cr} + \frac{\Delta_{\rm so}}{3} + E_{\rm G}\,,\\
E_{\rm v,A}(\mathbf{k}=0) &= \Delta_{\rm cr} + \frac{\Delta_{\rm so}}{3} + \theta_\varepsilon + \lambda_\varepsilon\,,\\
E_{\rm v,B}(\mathbf{k}=0) &= \frac{1}{2}\left(\Delta_{\rm cr} - \frac{\Delta_{\rm so}}{3} + \theta_\varepsilon\right) + \lambda_\varepsilon + \sqrt{\frac{1}{4}\left(\Delta_{\rm cr} - \frac{\Delta_{\rm so}}{3} + \theta_\varepsilon\right)^2 + \frac{2\Delta_{\rm so}^2}{9}}\,,\\
E_{\rm v,C}(\mathbf{k}=0) &= \frac{1}{2}\left(\Delta_{\rm cr} - \frac{\Delta_{\rm so}}{3} + \theta_\varepsilon\right) - \lambda_\varepsilon + \sqrt{\frac{1}{4}\left(\Delta_{\rm cr} - \frac{\Delta_{\rm so}}{3} + \theta_\varepsilon\right)^2 + \frac{2\Delta_{\rm so}^2}{9}}\,,\\
\lambda_\varepsilon &= D_1\varepsilon_{\rm zz} + D_2\left(\varepsilon_{\rm xx} + \varepsilon_{\rm yy}\right)\,,\\
\theta_\varepsilon &= D_3\varepsilon_{\rm zz} + D_4\left(\varepsilon_{\rm xx} + \varepsilon_{\rm yy}\right)\,,
\end{aligned}
\tag{2.18}
$$

where the $D_{\rm i}$ coefficients are the deformation potentials (see Tab. 2.5). As the excitons closely follow the behavior of the bands they belong to [163], selection rules for the optical excitonic transitions can be obtained from the symmetry of the bands. In the case of relaxed GaN the lowest energy transitions, A and B, dominate the optical response for polarization of the electric field vector **E** perpendicular to the c-axis, i.e. in the ordinary direction $\mathbf{E}\perp c$, while C rules the extraordinary one. The relative oscillator strengths of the corresponding transitions for GaN are found in Tab. 2.6 and obey the Thomas-Reiche-Kuhn sum rule, i.e., $\sum_{\rm i=A,B,C} f_{\rm osc,i}^{\mathbf{E}\parallel c} = \sum_{\rm i=A,B,C} f_{\rm osc,i}^{\mathbf{E}\perp c} = 1$. It appears that exciton A is only coupled to the light polarized perpendicularly to the c-axis whereas B and C radiate in all directions.

Table 2.6: Relative oscillator strength for A, B and C excitons in relaxed GaN [164, 165].

	$f_{\rm osc}^{\mathbf{E}\perp c}$	$f_{\rm osc}^{\mathbf{E}\parallel c}$
A	0.5	0
B	0.44	0.12
C	0.06	0.88

A common approximation used in this work to model the valence band symmetry, energy and effective masses in the $k\cdot p$ formalism (see Appendix B) is the quasi-cubic description where the c-axis is identified with [111] of the cubic zinc-blende structure. This approximation is justified by the fact that the first and second neighbors occupy the same position in both structures.

When growing a structure on a lattice-mismatched substrate, a biaxial strain (compressive or tensile) is applied to the epilayer, which results in the modification of energy, symmetry and the effective masses of the bands. When grown along $c-$axis, the strain in the basal plane does not introduce any extra degeneracy lift as the hexagonal structure is preserved. However, the energy edges, the effective masses and the symmetry of the bands are modified. In particular, it is seen that a compressive strain increases the band gap energy and a tensile strain decreases it [163] (see Fig. 2.8(b)). Oscillator strengths and effective masses of A, B and C bands are also strongly affected [167]. In the present work, we will also focus on GaN-based samples grown along polar and nonpolar orientations. Whereas the crystal symmetry is hexagonal for structures grown along the c-axis, on a nonpolar orientation, the symmetry of the crystal is reduced to the orthorhombic one [166] leading to an extra anisotropy in the structure and to a more complex band structure (see Fig. 2.8(c)). However, these extra lines are not resolved for the relatively low strain in our samples and $k\cdot p$ treatment with a 6×6 Hamiltonian (see Ref. [167] and Appendix B) correctly reproduces experimental data (see Chapter 6).

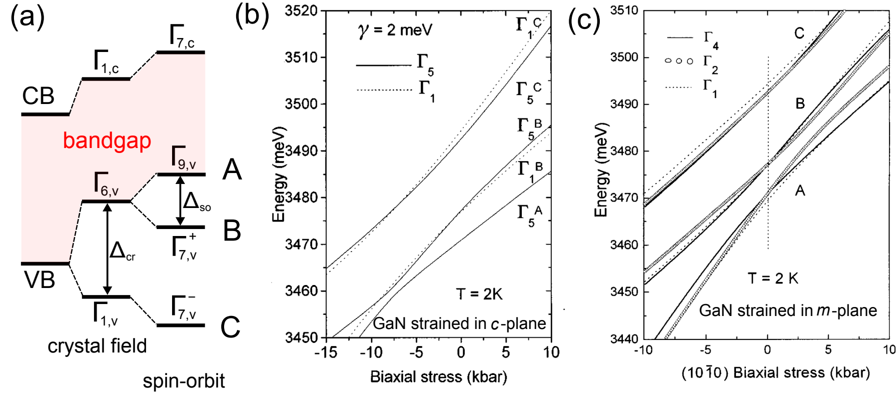

Fig. 2.8: (a) Degeneracy lift of the GaN valence bands due to the anisotropic crystal field Δ_{cr} and spin-orbit interaction Δ_{so} leading to the formation of heavy hole (A), light-hole (B), and spin-orbit (C) excitons. The symmetry of the bands are indicated and the band gap evolution is indicated in red.(b) Evolution of the exciton states in polar GaN as a function of the (0001) biaxial stress (taken from [163]) (c). Evolution of the exciton states in nonpolar-GaN as a function of the $(10\bar{1}0)$ biaxial stress(taken from [166]). In both cases, positive values of stress correspond to compression.

2.3.2 *Refractive index and birefringence*

The uniaxial anisotropy of the wurtzite cell is responsible for the intrinsic birefringence of the III-nitride crystals. Components of the electric field polarized along the ordinary direction ($f_{\mathrm{osc}}^{\mathbf{E}\perp c}$) or along the extraordinary direction ($f_{\mathrm{osc}}^{\mathbf{E}\parallel c}$) do not experience the same dielectric constant ϵ. As a consequence, a convenient description of the light propagation in III-nitride layers is obtained with a tensor and not with a single dielectric constant, i.e. $\epsilon \to \bar{\bar{\epsilon}}$. Assuming an isotropic dielectric constant in the basal plane, which is correct for growth on c-plane substrate, one can write:

$$\bar{\bar{\epsilon}} = \begin{pmatrix} \epsilon_{\mathrm{o}}(E) & 0 & 0 \\ 0 & \epsilon_{\mathrm{o}}(E) & 0 \\ 0 & 0 & \epsilon_{\mathrm{e}}(E) \end{pmatrix}, \tag{2.19}$$

where E is the energy of the optical field, $\epsilon_{\mathrm{e}}(E) = \epsilon_{zz}(E)$ and $\epsilon_{\mathrm{o}}(E) = \epsilon_{xx}(E) = \epsilon_{yy}(E)$ correspond to the dielectric function along the $c-$axis (e-direction) and in the basal plane (o-direction), respectively. Anisotropic dielectric properties of III-nitrides were first investigated on wurtzite and zinc-blende GaN epilayers [168, 169]. But rapidly, the development of laser diodes and LEDs operating from the green to the UV range required a deeper knowledge of the birefringent properties of $In_xGa_{1-x}N$ and $Al_xGa_{1-x}N$ for various alloy compositions. Unfortunately, the reports on birefringence in $In_xGa_{1-x}N$ are quasi inexistent and not reliable [170]. The main difficulty comes from the difficulty of growing high quality thick InGaN epilayers with a high indium content. There are numerous reports on birefringence in $Al_xGa_{1-x}N$ epilayers (see [171] and references therein) but values are available only for long wavelengths ($\lambda > 442\,\mathrm{nm}$). In this work, we consider the ordinary and extraordinary dielectric function for GaN and AlN given in [172]:

$$\epsilon_{\mathrm{i}}(E) = 1 + \frac{2}{\pi}\left[\frac{A_{0,\mathrm{i}}}{2}\log\left(\frac{E_{1,\mathrm{i}}^2 - E^2}{E_{0,\mathrm{i}}^2 - E^2}\right) + \frac{A_{1,\mathrm{i}}E_1}{E_{1,\mathrm{i}}^2 - E^2}\right], \tag{2.20}$$

where the index $i \in \{o, e\}$ indicates the ordinary and extraordinary direction, respectively. This relation directly follows from the Kramers-Kronig relation, assuming a step-like absorption profile for the

imaginary part of ϵ due to excitonic band-to-band transitions [172]. A_0 corresponds to the magnitude of the absorption between energies E_0 and E_1. High energy absorption contributions are modeled by a delta-function at the energy E_1 with amplitude A_1. Values of E_0, E_1, A_0 and A_1 are given in Tab. 2.7. Note that in our study, E_0 is corrected by the confinement energy, the exciton binding energy and the strain induced variations *via* $k \cdot p$ simulations. Note also that the energy E_0 is replaced by a complex value in order to lift the discontinuity in ϵ and simulation artifacts, i.e., $E_0 \to E_0 + i\gamma$, where γ defines the broadening of the absorption edge.

Table 2.7: Fitting parameters for the dispersion of the real dielectric function in equation 2.20. Values are taken from [172].

	GaN (o)	GaN (e)	AlN (o)	AlN (e)
A_0	1.837	1.929	4.664	4.944
E_0 (eV)	3.450	3.504	6.465	6.398
A_1 (eV)	40.65	41.89	27.14	30.28
E_1 (eV)	8.175	8.164	10.81	9.461

Unfortunately, values for $Al_xGa_{1-x}N$ at the energy of GaN are not available and a linear interpolation is a bit hazardous. The ordinary refractive indices given in Ref. [173] are thus preferred.

For c-plane microcavities, the impact of birefringence is not considered in the simulations as it is expected to play a negligible role for the propagation angles of interest. For microcavities grown along a nonpolar orientation, birefringence leads to a splitting of the cavity mode [174]. As the light polarized along the o-direction experiences a smaller refractive index ($\Delta n = n_e - n_o > 0$) the optical cavity length is smaller and the cavity mode appears at higher energy. Assuming an ideal λ-cavity, in the Fabry-Perot approximation the longitudinal-transverse (LT) cavity mode splitting is given by:

$$\Delta E_{LT} \approx \frac{\Delta n}{n_{cav}} E_{cav}. \tag{2.21}$$

This shift was measured to amount to $\Delta E_{LT} = 47$ meV in an a-plane GaN-based microcavity ($\lambda \approx 390$ nm) made out of a 13 pair AlN/GaN DBR, a GaN interlayer and a top dielectric DBR [174]. In Chapter 6, we investigate m−plane nonpolar microcavities operating in the strong coupling regime featuring a LT-splitting of the cavity mode $\Delta\omega_{LT} \approx 35$ meV [175].

3 Polariton condensation in polar GaN-based microcavities

In this chapter, we will focus on the energy relaxation of polaritons in polar GaN-based multiple quantum well microcavities. Intrinsic properties such as density of states, energy or polariton linewidth can be probed *via* reflectivity measurements [17] but the polariton condensate formation dynamics, the impact of disorder and the role of interactions must be probed by means of photoluminescence experiments. In the first Sections, the experimental setup and the sample are introduced. Then the formation of the polariton condensate and the impact of the carrier density on the system behavior are discussed.

3.1 Fourier imaging

3.1.1 Principle

Most of the polariton properties can be obtained from their energy dispersion, which is experimentally accessible by means of angle-resolved measurements including reflectivity, transmission, absorption or photoluminescence. This remarkable property comes from the one-to-one coupling between 2D-excitons and 2D-cavity photons with the same in-plane wave vector $\mathbf{k}_\parallel = \left(k_x, k_y\right)$. According to relation 1.39, the norm of $\mathbf{k}_\parallel$ is related to the external angle θ *via* $k_\parallel = \frac{E}{\hbar c}\sin(\theta)$. Due to the in-plane translation invariance, the azimuthal angle $\phi = \tan^{-1}\left(k_x/k_y\right)$ is conserved during the emission process, meaning that all states in a given band with the same in-plane momentum have the same energy and the far field pattern has a circular symmetry.[19]

In order to have access to the polariton states $\mathbf{k}_\parallel$, all the rays emitted (or reflected) in the same direction (θ, ϕ) from the sample must be focused on the same point (x_F, y_F) at the spectrometer entrance slit. This conjugated plane called the *Fourier plane* corresponds to the Fourier transform of the sample near field emission pattern and can be experimentally obtained by the use of a lens or a microscope objective. If the sample is located at the focal distance of the lens, all the rays emitted in the same direction are focused at the focal point behind the lens. As we use a microscope objective with a high numerical aperture (N.A. = 0.55) corresponding to a maximum detection angle $\theta_{max} \approx 33.4°$ and a short focal length $f_{obj} = 2.5$ mm, the Fourier plane is formed directly on the back of the objective. As a consequence, two other lenses, with focal length $f_1 = 300$ mm and $f_2 = 200$ mm, respectively, are used to image this Fourier plane (FP1) at the entrance of the spectrometer entrance slit (FP2). Due

[19] Note that this property is no longer true in resonant experiments where the emission azimuthal angle is given by the momentum and energy conservation between pump, signal and idler beams [25].

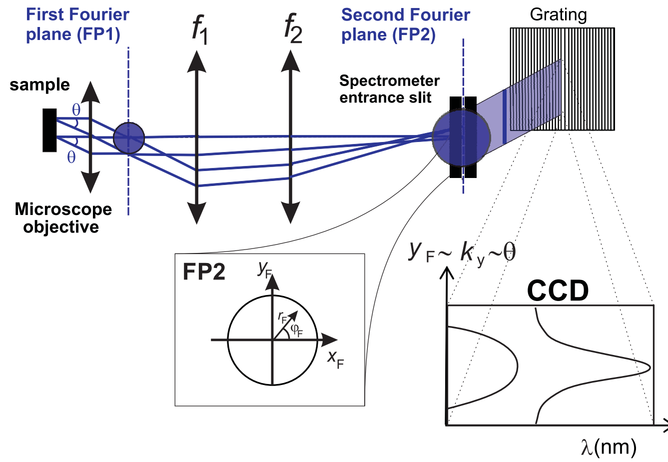

Fig. 3.1: Fourier imaging spectroscopy principle with one high numerical aperture microscope objective (N.A. = 0.55) and two lenses (f_1 and f_2). The two Fourier planes (FP1 and FP2) are indicated. The energy dispersion curve is monitored on the CCD camera after dispersion of the section of FP2 with $k_x = 0$. The plane FP2 is magnified for clarity.

to in-plane invariance, the Fourier plane is circular. The energy dispersion $E(k_\|)$ is then obtained by dispersing a line in the Fourier plane. This is done experimentally by closing the spectrometer slit around the center of FP2 as depicted in Fig. 3.1.

This procedure is exact in the paraxial approximation only, i.e., when the rays make a small angle with respect to the optical axis of the system. In this situation, $\sin(\theta) \approx \tan(\theta) \approx \theta$ and the optical path can be calculated by means of transfer matrices (see Fig. 3.2). The path of rays emitted from the same sample point (off-axis) for angles spanning over the whole numerical aperture, i.e., from -33 to 33° is shown in black. The conjugated plane corresponds to the real space (RS), i.e., a magnified image of the near field. In red, the path of rays emitted with the same angle $\theta = 33°$ from different sample points over a cross-section region of 10 μm is displayed. The corresponding conjugated plane now corresponds

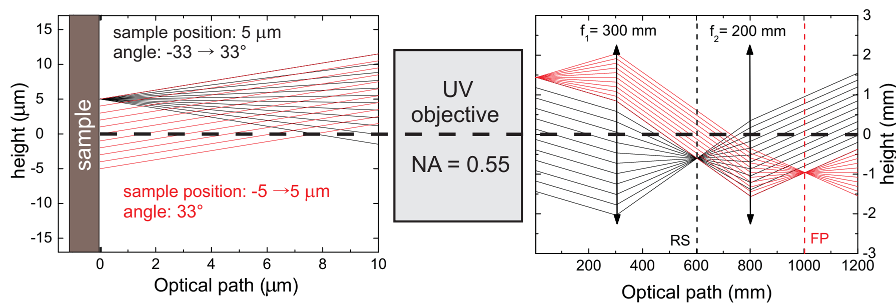

Fig. 3.2: Transfer matrix simulation of the optical path. The red beams originate from different sample spots (between −5 and 5 μm) with the same emission angle ($\theta = 33°$) and the black ones from the same sample position ($x = 5\,\mu$m) but with different emission angles (between −33 and 33°). The left panel shows the rays close to the sample surface (before the objective) and the right panel the beam path through the two lenses (after the objective). The conjugated planes are represented with black (real space, RS) and red (Fourier plane, FP) vertical dashed lines.

to the Fourier plane (FP2) and is formed after the RS-plane. This simulation shows that real space and Fourier planes can be easily obtained with the same experimental configuration. The paraxial approximation is unfortunately not valid over the whole numerical aperture and must be corrected numerically. The radial coordinate $r_{\mathrm{F}} = \sqrt{r_{\mathrm{F}}^2 + y_{\mathrm{F}}^2}$ is related to the emission angle θ by the relation:

$$r_{\mathrm{F}} = G f_{\mathrm{obj}} \tan(\theta) = G f_{\mathrm{obj}} \left[\frac{\hbar c k_{\parallel}}{E(k_{\parallel})} - 1 \right]^{-1/2}, \tag{3.1}$$

where $G = f_2 / f_1$ (see Fig. 3.3) is the magnification factor due to the use of two lenses to image FP2.

3.1.2 Setup specificities

The experimental setup is schematically depicted in Fig. 3.3. The excitation line can be switched between various excitation sources:

- Frequency-quadrupled Nd:YAG laser emitting at 266 nm: 500 ps pulse length and 8.52 kHz repetition rate (nonresonant excitation). This laser is the one used for all the measurements exhibiting optical nonlinearities (i.e. polariton condensation). The averaged threshold power density P_{thr} and the peak power density are linked *via* the duty cycle $D = \tau_{\mathrm{pulse}} \times f_{\mathrm{laser}} = 4.26 \times 10^{-6}$.
- cw frequency-doubled Ar-ion laser at 244 nm (nonresonant excitation)
- Optical parametric oscillator system tunable between 210 and 2300 nm: 7 ns pulse length and 1 kHz repetition rate (allowing resonant and nonresonant excitations)
- White light source (Xenon lamp) for reflectivity and transmission measurements and real space imaging

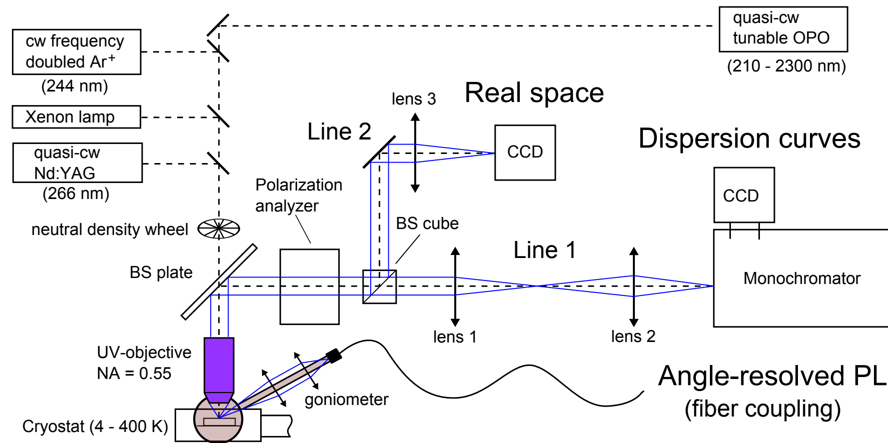

Fig. 3.3: Schematic representation of the experimental setup including the various excitation sources and the collection lines (1 and 2). Temperature, power, and polarization-resolved studies are possible. The goniometer arm is superimposed to the standard Fourier setup showing the possibility of performing conventional angle-resolved measurements. See text for more details.

The light source is then focused on the sample with a typical spot size comprised between 2 and 10 μm depending on the source used and the accuracy of the focusing *via* the UV microscope objective (N.A. = 0.55).[20] The signal is then collected from the sample through the same objective and deflected into the collection line by a non-polarizing beam-splitter plate. Here, the Fourier-plane formed on the backside of the objective is imaged on the entrance slit of a 55 cm focal length monochromator *via* two lenses with a focal length of 30 and 20 cm, respectively (line 1 in Fig. 3.3). After being dispersed on a 150, 1200 or a 2400 gr/mm grating the signal is imaged on a UV-enhanced back-illuminated CCD with a spectral resolution $\Delta\lambda = 0.327$, 0.04 and 0.019 nm, respectively. Polarization-resolution is achieved by combining a $\lambda/2$-wave plate and a linear polarizer placed before the first lens. The emission pattern can be recorded simultaneously by means of a non-polarizing beam-splitter cube located behind the polarization setup and imaged through a 30 cm focal length lens on a UV-enhanced high-resolution CCD camera (line 2). A continuous-flow liquid-helium cryostat allows to tune the temperature from 4 to 400 K. Asymmetric photoluminescence spectra can be recorded by tilting the sample and using the same configuration as described before to extend the range of accessible angles.

Finally, another common configuration to record the dispersion curve is to use a goniometer with a rotating arm (visible in Fig. 3.3). The signal is then collected by means of a fiber coupler and sent to the spectrometer *via* a fiber adapter (not shown). Even if this method presents several advantages such as the absence of aberrations and a wider range of accessible angles (from −10 to ~ 90°), the dispersion curves cannot be recorded in one shot as in the Fourier configuration and the spot size cannot be easily focused below a diameter of ~ 50 μm.

3.2 Sample presentation

3.2.1 Design and structural properties

In the present and following chapters (4 and 5), we will consider separately a GaN-based multiple quantum well 3λ-microcavity and its bare active medium, which consists of a 67-period GaN (1.2 nm)/$Al_{0.2}Ga_{0.8}N$ (3.6 nm) quantum well stack. Both have been grown during the same run by metal organic vapor phase epitaxy [81] on a 3 μm thick GaN buffer deposited on a *c*-plane sapphire substrate. The bare active medium sample, was capped with a $\lambda/4$ $Al_{0.2}Ga_{0.8}N$ thick layer. Concerning

[20] A near-UV objective with a numerical aperture of 0.5 and a small depth of focus (~ 1 μm) is also used for the micro-reflectivity measurements.

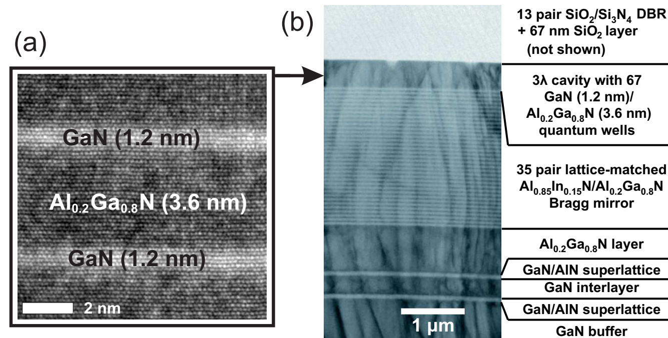

Fig. 3.4: Cross-section transmission electron micrograph of (a) the active region featuring the high quality of the GaN/(Al,Ga)N quantum wells and (b) the half-microcavity structure.

the full microcavity structure shown in the transmission electron microscopy (SEM) image shown in Fig. 3.4(b)), it consists of a high-reflectivity epitaxial 35 pair lattice-matched $Al_{0.85}In_{0.15}N/Al_{0.2}Ga_{0.8}N$ DBR grown on a strain relieving template made of two GaN/AlN superlattices separated by a GaN interlayer followed by an $Al_{0.2}Ga_{0.8}N$ layer. The 3λ active medium, consisting of 67 quantum wells sandwiched between two $\lambda/4$ $Al_{0.2}Ga_{0.8}N$ layers was then grown on top of the bottom DBR. Finally a 67 nm thick Si_3N_4 layer and a 13 pair top dielectric SiO_2/Si_3N_4 DBR have been deposited. The entire structure is crack-free as seen from the TEM images shown in Figs. 3.4(a) and 3.4(b).

Contrary to the common design of multiple quantum well based microcavity structures operating in the strong coupling regime, the present quantum wells are not preferentially located at the antinodes of the standing wave, but they are homogeneously distributed over the full cavity section. This particular design has been chosen to circumvent the geometrical effect that affects the quantum well emission by the variation of the built-in electric field present in the different quantum wells [176]. It also enhances the light-matter interaction *via* the important increase of the effective quantum well number according to relation 1.71. Note finally that both samples exhibit a similar barrier alloy disorder but a different strain state. Compared to the bare multiple active region, the quantum wells in the full microcavity sample are more compressively strained (on a mean in-plane lattice parameter corresponding to that of $Al_{0.2}Ga_{0.8}N$) and thus emit at higher energy ($\Delta E \approx 60$ meV).

3.2.2 *Optical properties of the bare active medium*

3.2.2.1 Highly confined excitons

Even if the present samples have been grown along the polar c-axis, we will hereafter neglect the effect of the quantum confined Stark effect on the excitonic properties. Indeed, these GaN quantum wells are thin enough to ensure an optimal overlap between electron and hole wave functions and are only marginally affected by the built-in electric field along the growth direction. To support this point, envelope function calculations in the effective potential formalism have been performed [177] (see Figs. 3.5(a)-3.5(b)). A variational modeling of the exciton has been included, in which the in-plane and on-axis motions of the exciton are separated. [21] It also appears that the electron and hole

[21] The dynamical de-screening of the built-in electric field after pulsed photo-excitation should neither affect the exciton binding energy nor the overlap between electron and hole wave functions and therefore no time- or excitation-dependent change of the exciton radiative lifetime is expected.

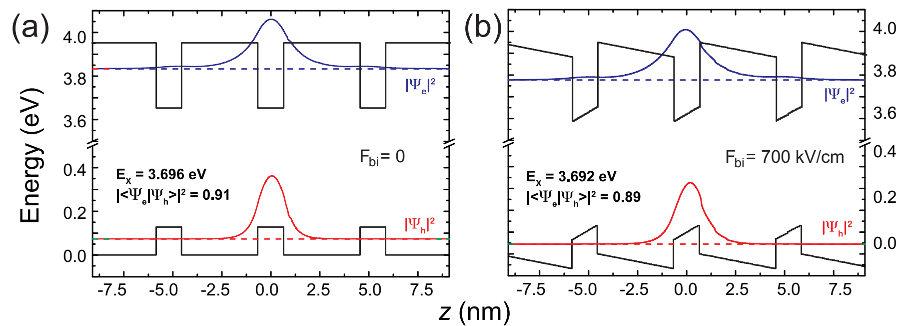

Fig. 3.5: Band-profiles (black line) of electron and hole wave functions (blue and red lines, respectively) for an exciton confined in GaN (1.2 nm)/$Al_{0.2}Ga_{0.8}N$ (3.6 nm) multiple quantum well (a) without and (b) with built-in electric field, $F_{bi} = 700$ kV/cm [158].

wave functions are evanescent in the (Al,Ga)N barriers, preventing the formation of mini-bands. This point is of major importance in our study as all quantum wells can be considered as equivalent and independent. Simulations also feature the high exciton binding energy of such thin quantum wells, which approximately amounts to 46 meV, a value twice larger than that of excitons in bulk GaN layers [50]. We should also mention that for such thin quantum wells, a huge inhomogeneous broadening could be expected due to monolayer width fluctuations and the high confinement energy: the energy fluctuation between 5 and 6 monolayers amounts to $\Delta E \approx 40$ meV, which is not consistent with the measurements reported hereafter. The localization energy is thus not ruled by monolayer fluctuations [178] but rather by alloy disorder [81].

3.2.2.2 Photoluminescence studies: Peak identification, alloy disorder and localization

From the combined reflectivity, photoluminescence excitation (PLE) and nonresonant cw photoluminescence measurements performed at 10 K on the bare active medium (see Fig. 3.6(a)), it appears that the quantum well features are dominated by two transitions lying at 3.655 and 3.639 eV and labeled X_{loc} and XX_{loc}, respectively. X_{loc} is identified with the emission from the fundamental quantum exciton state (exciton A).[22] At low temperatures, the quantum well emission properties are dominated by localized exciton states [74], and the emission energy E_{X}^{PL} observed in photoluminescence is:

$$E_{\text{X}}^{\text{PL}} = E_{\text{X}}^{\text{loc}} = E_{\text{X}} - \delta E_{\text{X}}^{\text{loc}}, \tag{3.2}$$

where $E_{\text{X}}^{\text{loc}}$ corresponds to the energy of the free exciton E_{X} with zero in-plane wave vector minus the localization energy $\delta E_{\text{X}}^{\text{loc}}$. Comparing photoluminescence with reflectivity and PLE, we deduce $\delta E_{\text{X}}^{\text{loc}} \approx 10$ meV, which is also supported by temperature-resolved reflectivity measurements featuring the temperature evolution of the A and B exciton lines (see Figs. 3.7(a)-3.7(b)). This energy is small compared to the 40 meV calculated by envelope function calculations and corresponding to a single monolayer well width fluctuation. As a matter of fact, it has already been shown that in MOVPE grown

[22] The PLE measurements were performed with an OPO-based laser system with an emission wavelength continuously tunable between 200 nm and 2.3 μm pumped by a pulsed Nd:YAG laser (λ = 355 nm with a 1 kHz repetition rate and 3 ns pulse width).

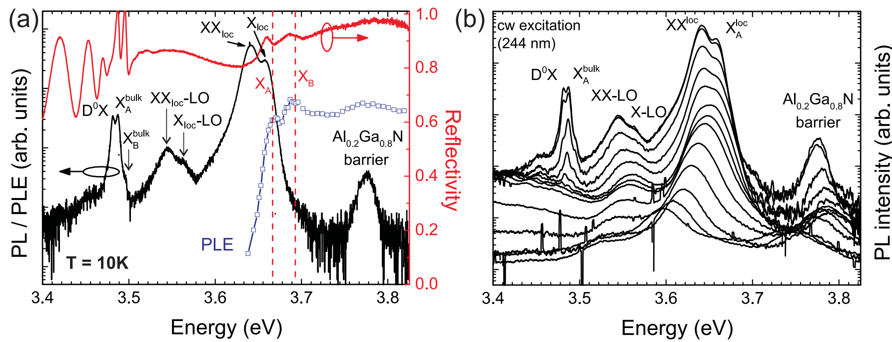

Fig. 3.6: Optical characterization of the bare cavity region. (a) Low temperature (T = 10 K) reflectivity (red), photoluminescence (PL) measured under cw excitation at 244 nm and PLE measurements performed under quasi-cw excitation (open blue squares). (b) Low power PL spectra taken from 10 to 300 K under cw excitation at 244 nm. PL spectra in (a) and (b) were obtained using an excitation power density of 175 W/cm^2.

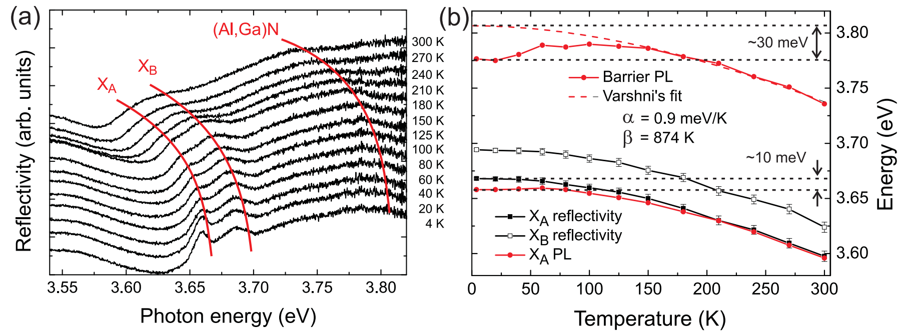

Fig. 3.7: (a) Reflectivity spectra taken for temperatures ranging from 4 to 300 K. Guide to the eyes (red lines) indicate the positions of A and B free excitons and that of the (Al,Ga)N barrier. (b) Temperature evolution of the peak energy measured in photoluminescence and reflectivity for X_A, X_B, and the (Al,Ga)N barrier, featuring localization energies $\delta E^{loc}_{X_A} \approx 10$ meV and $\delta E^{loc}_{(Al,Ga)N} \approx 30$ meV. The Varshni's fit for the (Al,Ga)N barrier is also shown (red dashed line).

GaN/(Al,Ga)N quantum wells, Al-content fluctuations occurring in the (Al,GaN) barriers dominate the quantum well emission inhomogeneous linewidth [81].

Under quasi-cw conditions, increasing the excitation density leads to a superlinear increase in the intensity of the lower-energy transition with respect to the emission at 3.655 eV (see Fig. 3.10(a)). We therefore attribute the emission occurring at 3.639 eV to the emission from biexcitons similarly to the observations reported in Refs. [179–181]. A deeper investigation of this line is presented in a separate section dedicated to the role of biexcitons in the present structure (Section 3.2.4).

From the S-shaped temperature-dependence of the (Al,Ga)N emission energy shown in Figs. 3.6(b) and 3.7(b), we can deduce an exciton localization energy of 30 meV in the barrier due to alloy disorder.[23] Such a high localization energy due to fluctuations in the (Al,Ga)N energy band gap is in relatively good agreement with the experimental value of δE^{loc}_{X} and our calculations: accounting for the penetration length of the exciton wave function in the barrier a localization energy of approximately 12 meV is expected.

In addition to the above-mentioned transition at 10 K, we observe additional lines at 3.564, and 3.548 eV, which lie exactly 91 meV below the emission from the localized exciton and biexciton lines. We therefore attribute these transitions to the first LO-phonon replica of X_{loc} and XX_{loc}, respectively. At lower energies, we also observe the emission lines from the GaN buffer layer, which correspond to the donor-bound A-exciton centered at 3.481 eV and the A and B free exciton lines at 3.488 and 3.497 eV, respectively (see Fig. 3.6(a)). Finally, although we observe a clear signature of exciton B both in reflectivity and PLE , its role on the relaxation and recombination processes of carriers is neglected in the following. This assumption is indeed justified by the energy difference of 21 meV measured between A and B quantum well excitons: for a lattice temperature of 10 K, this higher-energy exciton branch is not significantly thermally populated.

[23] Note that this value is higher than what is reported for similar (Al,Ga)N layers in the literature [182].

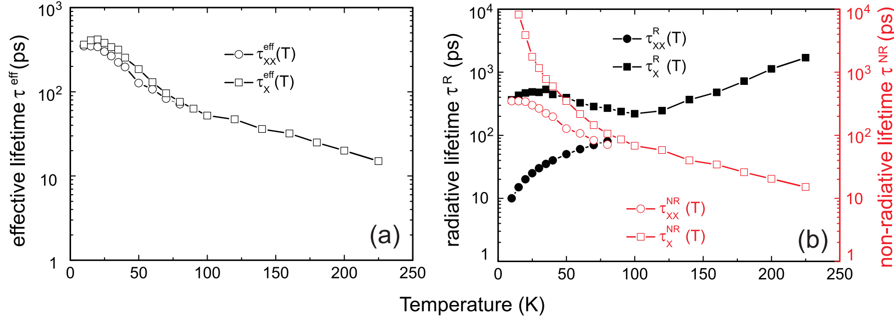

Fig. 3.8: Temperature evolution of (a) the effective lifetime τ^{eff}, (b) the radiative (black) and nonradiative lifetimes τ^{R} and τ^{NR} (red). The exciton is represented by squares and the biexciton by circles.

3.2.2.3 Carrier lifetimes and quantum efficiency

The time-resolved photoluminescence experiments presented in this chapter are carried out with the third harmonic of a Ti:Al_2O_3 mode-locked laser (pulse width and repetition rate of 2 ps and 80.7 MHz, respectively).[24] The laser beam was focused down to a 50 μm diameter spot on the sample surface. The photoluminescence signal was then analyzed with a 1200 grooves/mm grating (spectral resolution of ~ 500 μeV) followed by an Optronis streak camera working in synchroscan mode. In Fig. 3.8, the effective lifetimes τ^{eff} of exciton (X) and biexciton (XX) lines are displayed as a function of lattice temperature. τ^{eff} corresponds to decay times measured in time-resolved photoluminescence experiments and is affected by both radiative (τ^{R}) and nonradiative (τ^{NR}) components *via* the relation:

$$\frac{1}{\tau^{\text{eff}}} = \frac{1}{\tau^{\text{R}}} + \frac{1}{\tau^{\text{NR}}}. \tag{3.3}$$

Assuming that all carriers have reached thermal equilibrium, i.e., the relaxation times are small compared with the recombination times, and that the recombination mechanisms only depend on temperature, it is possible to extract separately the contribution of τ^{R} and τ^{NR} *via* temperature-dependent measurements [183]. One can reasonably assume that the radiative lifetime is short compared to the nonradiative one at low temperature (quantum efficiency η equal to 1) and that the photoluminescence intensity evolves with temperature according to $I_{\text{PL}}(T) = \eta(T) I(T_{\text{min}})$, where $T_{\text{min}} = 10$ K is the minimum experimental lattice temperature. In this situation, one can write:

$$\begin{aligned}
\tau^{\text{R}}(T) &= \underbrace{\frac{I_{\text{PL}}(T_{\text{min}})}{I_{\text{PL}}(T)}}_{1/\eta(T)} \tau^{\text{eff}}(T), \\
\tau^{\text{NR}}(T) &= \frac{I_{\text{PL}}(T_{\text{min}})}{I_{\text{PL}}(T_{\text{min}}) - I_{\text{PL}}(T)} \tau^{\text{eff}}(T).
\end{aligned} \tag{3.4}$$

The evolution of the effective lifetime for the exciton and biexciton transitions are displayed in Fig. 3.8(a). Using the relations 3.4, the radiative and nonradiative contributions to the decay time are extracted (see Fig. 3.8). This information is of high interest for the study of the full microcavity as the relaxation mechanisms of polaritons and the formation of the polariton condensate strongly depend on the exciton lifetime (see Chapter 4).

[24] The excitation wavelength was tuned to 280 nm in order to fall into a reflectivity minimum of the Bragg reflector of the full microcavity sample.

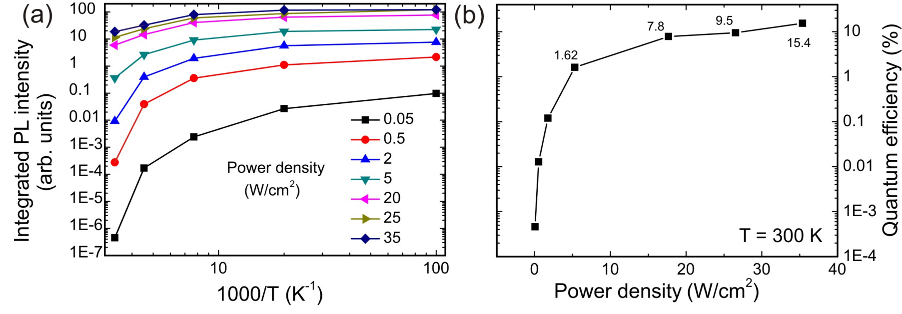

Fig. 3.9: (a) Integrated photoluminescence intensity of the quantum well emission as a function of the inverse temperature for different excitation power densities ranging from 0.05 to 35 W/cm^2. (b) Quantum efficiency displayed as a function of the average injected power density at room temperature.

In Fig. 3.9(a), the integrated photoluminescence intensity of the quantum well emission obtained under quasi-cw excitation condition ($\lambda = 266$ nm) is displayed as a function of inverse temperature for different excitation densities ranging from 0.05 to 35 W/cm^2. It appears that in the medium injection regime, in the 10 – 40 W/cm^2 range, the quantum efficiency is not dramatically affected. In Fig. 3.9(b), the quantum efficiency is displayed as a function of the injected power densities at room temperature. It turns out that for the power used in this work, this value remains above 10%.

3.2.2.4 High density regime: toward the Mott transition

As already discussed in section 1.1.5, the Mott transition is likely continuous in quantum wells. Moreover it is triggered when the carrier density gets close to the n_{sat} value given by relation 1.21, which only depends on the 2D Bohr radius. In the present structure, the Bohr radius was estimated in principle to ~ 1.7 nm [53], which leads to $n_{\text{sat}} \approx 1.3 \times 10^{12}\,\text{cm}^{-2}$ per quantum well. The total 2D carrier density n_{X} injected in the quantum wells can be estimated from the injected laser power through the following formula:

$$n_{\text{X}} = \frac{P_{\text{laser}} \tau_{\text{X}}^{\text{eff}}}{E_{\text{laser}}} A_{\text{cav}} \left(1 - R_{\text{laser}}\right), \tag{3.5}$$

where A_{cav} is the fraction of carriers captured in the quantum wells and $R_{\text{laser}} \approx 0.3$ is the reflection of the pump laser on the structure at the laser energy E_{laser}. Note that, equation 3.5 is hard to evaluate due to the important uncertainties on the exciton lifetime and quantum well absorption. In addition, this relation depends on the laser type (cw or pulsed[25]) and does not account for the inhomogeneous beam profile of the excitation source. As a consequence, any estimation based on relation 3.5 is hazardous.

We present in Fig. 3.10(a), a power-series performed under nonresonant conditions with a quasi-cw excitation source (Nd:YAG laser, $\lambda = 266$ nm) at 4 K. The average excitation power density is varied from 0.5 to 2360 W/cm^2. Considering the duty cycle of the laser the peak power is significantly higher compared to the cw excitation case. We thus assume that the photoluminescence is mainly governed by free excitons due to the saturation of localized states contrary to the case of the measurements displayed in Figs. 3.6(a) and 3.6(b) performed under cw excitation.

[25] In the case of pulsed excitation, this relation is valid only if the exciton effective lifetime is short compared to the pulse duration. In this case, the excitation condition is referred to as *quasi-cw*. In our case, this approximation is nearly valid as $\tau_{\text{X}}^{\text{eff}} < 400$ ps and $\tau_{\text{pulse}} = 500$ ps.

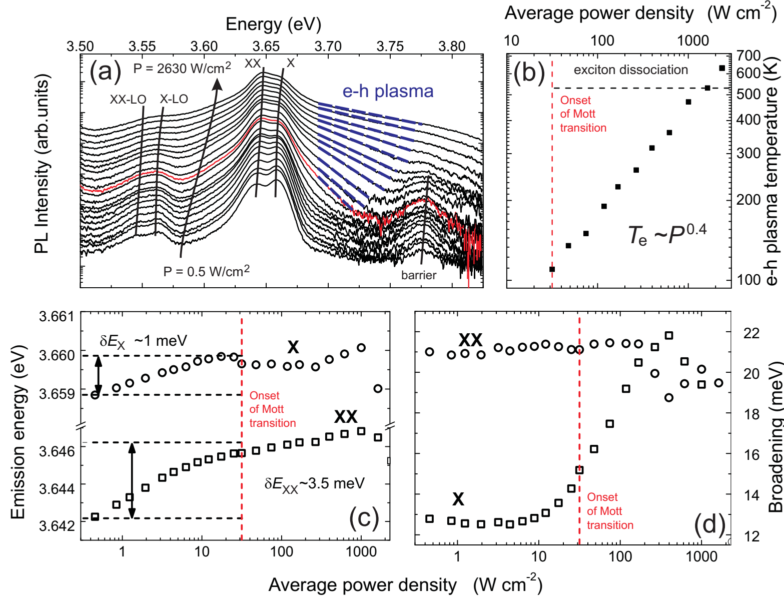

Fig. 3.10: Power-series measured at 4 K for power densities ranging from 0.5 to 2360 W/cm^2. Corresponding evolution of: (a) the photoluminescence spectra (the spectrum highlighted in red corresponds to the onset of the Mott transition). The blue-dashed lines correspond to the contribution from the e-h plasma appearing above the onset of Mott transition (red spectrum). (b) e-h plasma temperature. (c) Emission energy. (d) Mode broadening. The biexciton transition is represented by open circles and the exciton one by open squares.

This power-series highlights several interesting facts. First, for the case corresponding to n_{sat} (likely corresponding to the red spectrum shown in Fig. 3.10(a)), the quantum well emission gets significantly broader and the high-energy tail becomes exponential, which is a characteristic trace of the onset of the Mott transition, as observed on InGaAs/GaAs quantum wells [98]. This emission tail comes from the thermalized electron-hole plasma recombination and extends to higher energies when the carrier density increases. Another interesting feature is the increase in the electron-hole temperature T_{e} (displayed in Fig. 3.10(b)), which scales sublinearly with the pump power density ($T_{\mathrm{e}} \propto P^{0.4}$). In principle the photoluminescence of free carriers above the band edge provides a direct measure of the relative free electrons and holes population n_{free} in the quantum wells according to [184]:

$$n_{\mathrm{free}} \propto \sqrt{I_{\mathrm{plasma}} T_{\mathrm{e}}}, \tag{3.6}$$

where I_{plasma} is the free carrier photoluminescence intensity, which linearly scales with the power density P in the present experiment. Relation 3.6 holds in our system only if $P \propto n_{\mathrm{free}}^{1.4}$, which suggests that either the electron-hole generation rate or the quantum well absorption or the internal quantum efficiency increases with the excitation power density, which could be ascribed to the saturation of the non-radiative centers. Note that the laser absorption profile in our multiple quantum well structure and the quasi-cw excitation regime have to be considered and can significantly alter the behavior of the photoluminescence intensity. Finally, relation 3.6 might not apply to our system as it does not account for the contribution of localized excitons and that of biexcitons, which significantly affect the electronic population distribution at low temperature (see Section 4.6). Below the Mott transition, both excitonic and biexcitonic lines undergo a blueshift of 1 and 3.5 meV, respectively (see Fig. 3.10(c)). The

renormalization of the exciton transition below n_X^{sat} is due to inter-particle collisions [99] and is of fundamental importance in the study of polaritons in the high density limit as it will also affect the shape of the polariton dispersion. Above n_X^{sat}, the blueshift for X and XX lines is much less pronounced, likely due to a partial compensation with the band gap renormalization, which induces a redshift of the band gap energy ΔE_G [185]:

$$\Delta E_G \propto -n^{1/3}, \tag{3.7}$$

where n is the injected carrier density. In Fig. 3.10(d), the linewidth broadening is displayed for both lines after a careful deconvolution of the photoluminescence spectra and shows a drastic increase in the quantum well exciton one above the Mott transition. This broadening is likely due to collisional broadening below n_{sat} and to the progressive loss of the excitonic character above, i.e., electrons and holes progressively populate the valence and conduction bands leading to light emission occurring at higher energy with the effective temperature given in Fig. 3.10(b). As the Mott transition is seen to be continuous for the present quantum wells, excitons coexist with electron-hole pairs until bound complexes are no longer stable. This situation likely occurs when the effective temperature exceeds the exciton binding energy (horizontal black dashed line in Fig. 3.10(b) corresponding to $E_X^b = 46$ meV) or when the exciton oscillator strength is completely bleached due to phase space filling and Coulomb exchange interaction. The fact that the biexciton linewidth is less affected by collisions can be intuitively understood from the smaller probability of biexciton scattering, as it involves 4 excitons but also due to the reduced Coulomb interaction and population compared to the excitonic case. Note that the strong signature of excitons and biexcitons at the highest pump power densities used likely originates from the deeper quantum wells which are less populated.

3.2.3 Optical properties of the full microcavity

3.2.3.1 Demonstration of the strong coupling regime

The demonstration of the strong coupling regime in the present sample was part of the PhD thesis work of G. Christmann [119]. In this subsection, we briefly recall the main features.

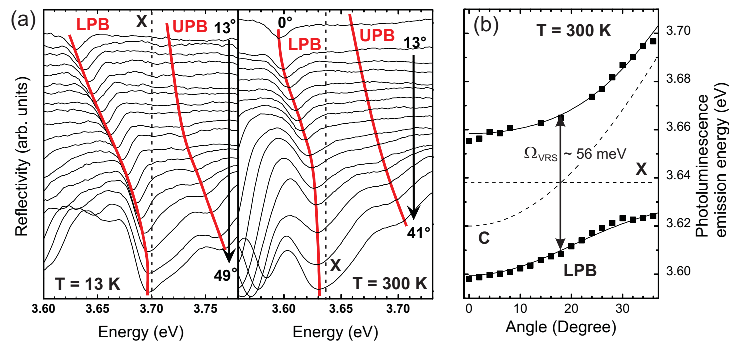

Fig. 3.11: (a) Low (left) and room temperatures (right) angle-resolved reflectivity spectra for various external angles ranging from 0 to nearly 50°. Guides for the eyes (red lines) indicate the position of the lower (LPB) and upper polariton branches (UPB). The position of the bare quantum well exciton (X) is indicated with a black dashed line. (b) Dispersion curve deduced from angle-resolved photoluminescence measurements featuring a vacuum Rabi splitting $\Omega_{VRS} = 56 \pm 4$ meV. Adapted from Ref. [53].

In Fig. 3.11(a), the reflectivity is reported for various emission angles ranging from 0 to nearly 50° at low (left, $T = 13$ K) and room temperatures (right) featuring a clear anticrossing behavior between the cavity photon and exciton modes, which is a clear indication that the system operates in the strong coupling regime. In Fig. 3.11(b), the upper and lower polariton dispersion curves are deduced from angle-resolved photoluminescence measurements revealing a vacuum Rabi splitting $\Omega_{VRS} = 56 \pm 4$ meV, which corresponds to an oscillator strength per surface unit $f_{osc}/S \approx 5 \times 10^{13}$ cm^{-2} [53]. A quality factor in excess of 1000 was reported for this sample, which corresponds to a cavity photon lifetime $\tau_C \approx 0.2$ ps. Note that this value is large compared to the expected duration of a Rabi oscillation $T_{VRS} \approx 70$ fs, which fulfills the requirements for the strong coupling regime observation according to condition 1.61. The interest in working with such multiple quantum well microcavity naturally arises from the fact that:

- the exciton binding energy in such narrow polar quantum wells is increased compared to the bulk case [158].
- the threshold power density is expected to be decreased by a factor of 10 compared to the bulk case [54], while the exciton saturation density is increased owing to the decrease in the exciton Bohr radius.
- the vacuum Rabi splitting is increased as it scales with the square root of the effective quantum well number N_{eff} given by relation 1.71. In the present structure $N_{QW}^{eff} \approx N_{QW}/2 = 33.5$.

3.2.3.2 Optical signature of dark states

As already described in Section 1.3.5, in ideal samples operating in the strong coupling regime with N_{QW} quantum wells located at the field antinode, the system is described by $N_{QW} + 1$ eigenstates: two bright modes, the lower and upper polaritons, which result from the coupling between the cavity mode and the fully symmetric combination of the N_{QW} quantum well excitonic states, and $N_{QW} - 1$ exciton modes not coupled to the light [123]. Those dark excitons are not dark from spin arguments, but only result from the diagonalization of the Hamiltonian 1.68 describing the interaction between a cavity mode with N_{QW} exciton states. Although necessarily present, we will disregard in the present work the

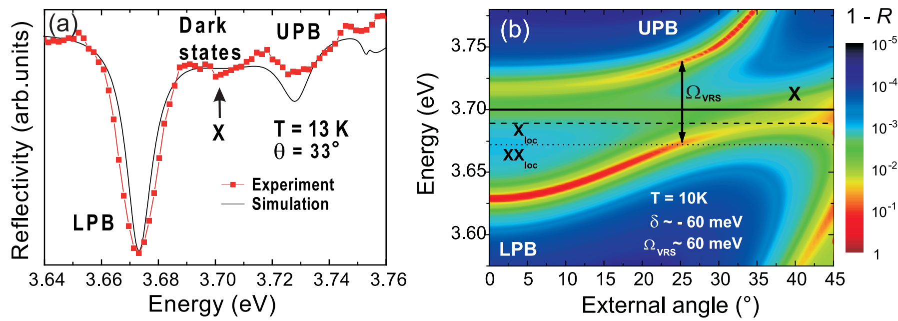

Fig. 3.12: (a) Computed (black line) and measured (red symbols) reflectivity spectra of the full microcavity measured at 13 K for an angle of 33°. Free excitons (X), lower (LPB) and upper polariton (UPB) resonances are indicated. (b) Computed angle-resolved reflectivity spectra at 10 K for $\Omega_{VRS} = 60$ meV and $\delta = -60$ meV. $1 - R$ is displayed in logarithmic scale to enhance the visibility. Solid, dashed and dotted lines show the emission from free excitons, localized excitons and localized biexcitons, respectively. Adapted from Ref. [186].

role played by dark excitons with a total angular momentum $J = 0$ or $J = 2$, as well as that of biexcitons made out of $J = 0$ or $J = 2$ excitons.

In real samples, non-idealities including alloy disorder, quantum well width fluctuations or even defects lead to a redistribution of the oscillator strength between the polariton modes and dark excitons [123]. Even if the strong coupling regime is preserved, dark excitons may thus exhibit an optical signature in absorption, reflectivity or photoluminescence experiments [112]. On top of this an additional non-ideality comes into play for the present structure: quantum wells located apart from the electric field antinodes are partly uncoupled from the photonic cavity mode and are therefore adding an extra contribution to the optical response. The combination of both effects is responsible for the weak dip observed at the energy of the uncoupled exciton mode in reflectivity measurements (see Fig. 3.12(a)). Such measurements are in agreement with the results of transfer matrix simulations shown in Fig. 3.12(b). These simulations show in a logarithmic scale the quantity $1-R$, which is of major importance, especially between the upper and the lower polariton branches, as it gives the fraction of photons allowed to escape from the microcavity in this energy range. In particular, it indicates that localized and free excitons and biexcitons should be visible in the far field.

3.2.3.3 Quantum well exciton energy

As the sample is in the strong coupling regime, the quantum well emission is not easily accessible by means of photoluminescence. As the lower polariton converges asymptotically toward that of the uncoupled exciton at high $k_{\parallel}$-vectors, high angle measurements provide an indirect access to this state. However, the range of accessible angles is limited to ±55° at low temperatures because of the cryostat window. A direct way to probe the quantum well emission is to perform photoluminescence on the sample cross-section. In Fig. 3.13, the photoluminescence emission energy measured on the microcavity section is displayed as a function of temperature. A fit using the semi-empirical Varshni's law (equation 2.17) is also shown with the same parameters as those used for the bare active medium, i.e., $\alpha = 0.9\,\text{meV/K}$, $\beta = 874\,\text{K}$ and $E_X(T=0) = 3.705\,\text{eV}$.

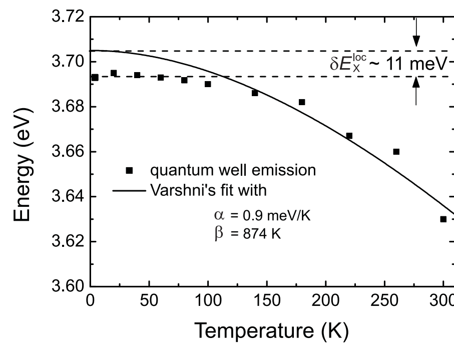

Fig. 3.13: Evolution of the exciton energy in the full microcavity for temperatures ranging from 4 to 300 K measured by photoluminescence performed on the sample cross-section (black squares). The fit of the free exciton energy using Varshni's law is also shown (black line) featuring an exciton localization energy of 11 meV.

Note that the lower limit deduced for the exciton localization energy with this fitting procedure $\delta E_X^{\text{loc}} = E_X(T=0) - E_{\text{PL}}(T=0) \approx 11\,\text{meV}$ is in good agreement with the value observed on the bare active region.

3.2.4 Biexcitons: the bare cavity section and the full microcavity

Even if the biexcitonic transition was briefly mentioned in the previous section, a separate one is devoted to its study as it plays a non-negligible role in the polariton dynamics of III-nitride microcavities. In this section, we will first discuss the general properties of biexcitons in GaN/(Al,Ga)N single quantum wells and then address the case of our two multiple quantum well samples, i.e., the bare cavity section and the full microcavity one. The formation and thermalization dynamics as well as their impact on the polariton condensate formation are discussed.

3.2.4.1 Biexciton in GaN quantum wells: generalities

The first report of biexcitonic emission in III-nitrides was obtained in a bulk GaN layer in 1996 by Okada and coworkers, featuring a biexciton binding energy of 5.3 meV [187]. Later, biexciton luminescence was also observed in disordered (Al,Ga)N layers [179] highlighting the impact of localization (which is more important for larger aluminum contents), which enhances the biexciton binding energy. The demonstration of biexciton recombination in GaN/(Al,Ga)N quantum wells was only recently achieved [180]. Ideally one can think to biexcitons as excitonic molecules in analogy with the hydrogen molecule (H_2), which consists of a bound state of two protons and two electrons. Exactly like atoms, biexcitons are optically active, they can propagate in space and form bound complexes. In an ideal 2D-system, the biexciton binding energy is related to the exciton one by the empirical Haynes rule [188, 189]:

$$E_{\mathrm{XX}}^{\mathrm{b}}/E_{\mathrm{X}}^{\mathrm{b}} \approx 0.228\,. \tag{3.8}$$

In Figs. 3.14(a) and 3.14(b), the photoluminescence spectra of single GaN/$\mathrm{Al_xGa_{1-x}N}$ quantum wells are displayed for two different aluminum contents in the barrier, 5 and 9%, respectively. Due to the relatively low aluminum content, excitons are less affected by alloy disorder at the interfaces resulting in a small localization energy (3.6 and 5 meV, respectively [180]) offering the possibility of observing free exciton emission at relatively low temperatures: 10 K in the case of GaN/$\mathrm{Al_{0.05}Ga_{0.95}N}$ quantum wells and 30 K for the GaN/$\mathrm{Al_{0.09}Ga_{0.91}N}$ ones. The spectra are extracted from time-resolved photoluminescence measurements at short delay. In both samples, exciton (X) and biexciton (XX) lines dominate the photoluminescence spectra at low temperatures. Due to the presence of an intrinsic wedge in the quantum thickness, the energy of both transitions is modified due to quantum confinement as discussed hereafter. The biexciton nature was derived from the superlinear increase in the XX-line in power-dependent photoluminescence experiments.

In Figs. 3.14(c)-3.14(d), the biexciton to exciton binding energy ratio and the biexciton binding energy are reported as a function of quantum well thickness. For the thinnest quantum wells, a drastic enhancement of the biexciton binding energy as well as an important deviation from Haynes rule is seen, whereas for thick quantum wells, this ratio tends to the ideal value of 0.228. Two effects must be considered to account for this behavior. On one side when approaching the 2D-ideal case (narrow quantum wells) excitons become more sensitive to interface disorder and therefore to localization. An increase in the biexciton binding energy induced by disorder was first reported by Langbein and Hvam in GaAs/$\mathrm{Al_xGa_{1-x}As}$ layers [191]. In particular, they demonstrated that the quenching of the kinetic energy of the exciton-exciton motion induced by the localization was responsible for the strengthening of the biexciton complex: the higher the disorder the higher the biexciton binding energy. A similar behavior was also reported in $\mathrm{Al_xGa_{1-x}N}$ epilayers by Yamada and coworkers [179]. Another effect that goes along with the reduction in the dimensionality along the growth direction is the modification in the carrier confinement energy $E_{\mathrm{X}}^{\mathrm{conf}}$. In a quantum well with infinite barriers, $E_{\mathrm{X}}^{\mathrm{conf}}$ continuously increases

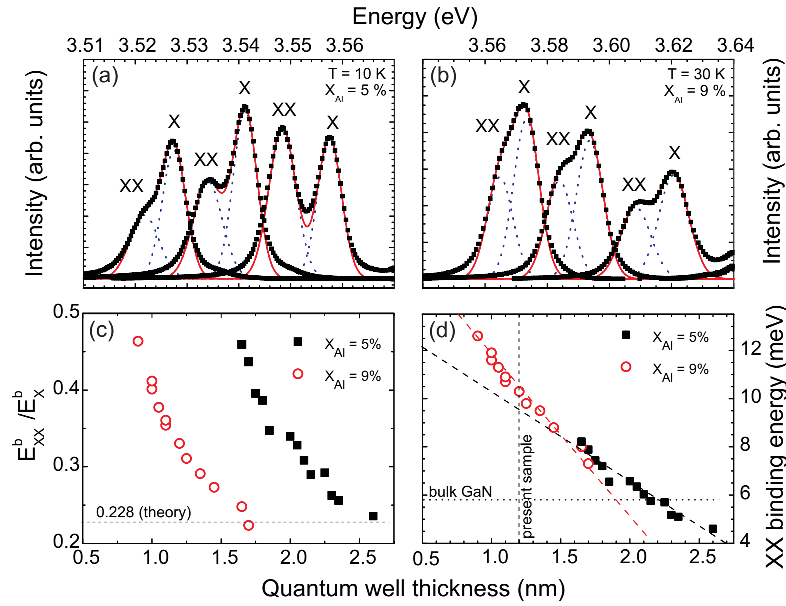

Fig. 3.14: Experimental time-resolved spectra measured at short delays (black squares) for a single (a) GaN/$Al_{0.05}Ga_{0.95}N$ quantum well at 10 K and (b) GaN/$Al_{0.09}Ga_{0.91}N$ quantum well at 30 K measured at different sample positions corresponding to different quantum well thicknesses. Each spectral transition is fitted with a Gaussian line shape (dotted blue lines). Evolution of the (c) biexciton/exciton binding energy ratio and (d) biexciton binding energy as a function of quantum well thickness for the case of the quantum well with 5% (black squares) and 9% (open red circles) aluminum content in the barrier. Adapted from Ref. [190].

when the well thickness L_{QW} tends to zero. However, the present quantum wells are very shallow due to the low Al-content and envelope function calculation indicate that E_X^b is rather decreasing when L_{QW} approaches zero due to the leakage of the wave function into the barriers for the thickness range investigated.

In polarization-free quantum wells, the biexciton binding energy is a monotonically decreasing function of the well width as a consequence of the confinement-enhanced wave function overlap between excitons [192]. In the case of the present polar III-nitride quantum wells, the situation is more intricate due to the presence of the built-in electric field causing the electron and hole wave function separation and the reduction in the exciton binding energy for larger quantum wells. As a consequence in polar III-nitride heterostructures with reduced dimensionality, E_{XX}^b varies in a non-trivial way as it depends on the competition between localization, confinement and quantum confined Stark effect [181]. The variation in the binding energies due to the combined effect of localization, confinement and localization is clearly visible in Fig. 3.14(d): for thin quantum wells, E_{XX}^b increases up 8.1 and 12.6 meV, for the structure with 5 and 9% of aluminum content, respectively. Note that the confinement should affect both exciton and biexciton transitions in a similar way [189, 193] and no significant deviation from the Haynes rule is expected, in opposition to the behavior shown in Fig. 3.14(c). As a consequence, the localization is likely playing the dominant role in these samples. The detrimental impact of the quantum confined Stark effect on the binding energies is unambiguously visible in Fig. 3.14(d): for quantum wells thicker than 2.25 nm (~ 9 monolayers), E_{XX}^b becomes smaller than its value in bulk GaN. A similar transition was predicted for the exciton in GaN/(Al,Ga)N quantum wells with comparable

thicknesses in Ref. [158]. Extrapolating those results to the case of the presently investigated structure, i.e., for GaN/$Al_{0.2}Ga_{0.8}N$ quantum wells with a well width of 1.2 nm (vertical dashed line in Fig. 3.14(d)), a biexciton binding energy between 10 and 15 meV is expected. Finally, note that the observation of a biexciton line in photoluminescence is usually considered as a proof of the high material quality. However, one should be careful with such assessment as the biexciton luminescence can originate from sample regions, which are locally free of defects but presenting an overall low structural quality [194].

3.2.4.2 Biexciton signature in the bare multiple quantum well active medium

Even if the transition at 3.639 eV visible in Fig. 3.6(a) was attributed to biexcitons due to its superlinear increase with pump power (see Fig. 3.10), the emission is not following a quadratic power law as expected for a bimolecular process. However, such a behavior observed in time-integrated photoluminescence spectra is not incompatible with biexciton recombination and can result from the shorter radiative lifetime of the biexciton compared to the exciton one [179] or to the long formation dynamics of the biexciton complex. In order to firmly identify the origin of this transition, time-resolved photoluminescence has been performed at low temperature (see Fig. 3.15(a)).

In a system at quasi-thermal equilibrium, free exciton (I_X) and biexciton emission intensities (I_{XX}) should verify at all times the mass action law, i.e., $I_X^2 \propto I_{XX}$ [195]. The validity of this expression can be extended to the case of localized populations (see Appendix of Ref. [186] for a demonstration):

$$\left(I_X^{loc}\right)^2 / I_{XX}^{loc} \propto \exp\left[-\frac{E_{XX}^b + \delta E_{XX}^{loc} - 2\delta E_X^{loc}}{k_B T}\right] \tag{3.9}$$

From Fig. 3.15(a), it appears that quasi-thermal equilibrium between the populations requires ~ 600 ps to be satisfied. The long delay between biexciton formation and the achievement of a quasi-thermal

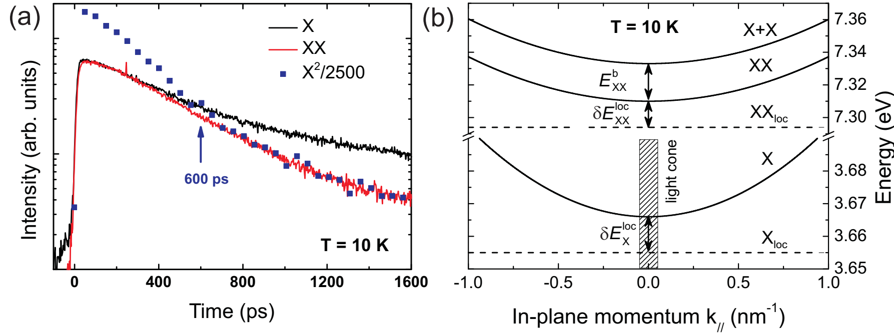

Fig. 3.15: (a) Low-temperature photoluminescence time-decays of the exciton (black) and biexciton (red) emissions. After 600 ps, the XX-intensity follows the same time-dependence as the square of the X-intensity (blue symbols) featuring the thermalization between the two populations. (b) In-plane dispersion of excitons (X) and biexcitons (XX) confined in a GaN/$Al_{0.2}Ga_{0.8}N$ quantum well. Due to the conservation of the in-plane momentum, only excitons lying within the light cone (shaded area) can couple to light. Biexcitons form from the binding of two excitons ($X + X$). The energy difference between the bottom of the two-exciton continuum and a biexciton with zero-kinetic energy is equal to the biexciton binding energy E_{XX}^b. At 10 K, excitons and biexcitons are localized along the quantum well plane, with respective localization energy δE_X^{loc} and δE_{XX}^{loc}. Adapted from Ref. [186].

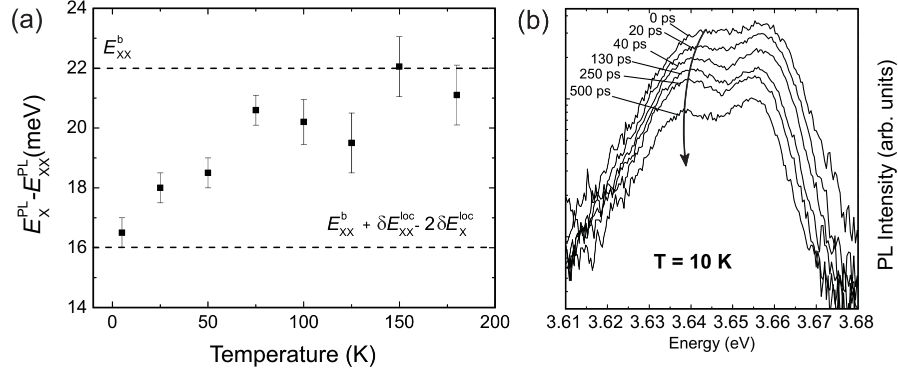

Fig. 3.16: (a) Temperature dependence of the energy difference between exciton and biexciton photoluminescence lines. (b) Time-evolution of the photoluminescence after nonresonant excitation featuring the localization dynamics of the biexciton *via* the redshift of the biexciton emission line (black arrow). Adapted from Ref. [186].

equilibrium between the two populations was previously ascribed to the decoupling of exciton and biexciton dynamics, once these carriers are localized [180]. Similarly to excitons, biexcitons are also bound to potential fluctuations at low temperatures [191, 196] and a biexciton localization energy $\delta E^{\mathrm{loc}}_{\mathrm{XX}}$ can be defined in the same manner as the energy difference between free biexcitons propagating in the quantum well plane and localized ones (see Fig. 3.15(b)). The emission energy observed in photoluminescence spectra resulting from the radiative dissociation of a localized biexciton can be expressed as:

$$\begin{aligned} E^{\mathrm{PL}}_{\mathrm{XX}} &= E^{\mathrm{loc}}_{\mathrm{XX}} - E^{\mathrm{loc}}_{\mathrm{X}} \\ &= E_{\mathrm{X}} + \delta E^{\mathrm{loc}}_{\mathrm{X}} - \delta E^{\mathrm{loc}}_{\mathrm{XX}} - E^{\mathrm{b}}_{\mathrm{XX}}, \end{aligned} \tag{3.10}$$

where $E^{\mathrm{loc}}_{\mathrm{XX}} = 2E_{\mathrm{X}} - E^{\mathrm{b}}_{\mathrm{XX}} - \delta E^{\mathrm{loc}}_{\mathrm{XX}}$ and $E^{\mathrm{loc}}_{\mathrm{X}} = E_{\mathrm{X}} - \delta E^{\mathrm{loc}}_{\mathrm{X}}$ are the energies of the localized biexciton and exciton, respectively. For free carriers, the energy difference between exciton and biexciton photoluminescence emissions directly corresponds to $E^{\mathrm{b}}_{\mathrm{XX}}$ but this is no longer true at low temperatures. Since the recombination of a localized biexciton leaves a localized exciton in the same site [197], one can write:

$$E^{\mathrm{PL}}_{\mathrm{X}} - E^{\mathrm{PL}}_{\mathrm{XX}} = E^{\mathrm{b}}_{\mathrm{XX}} + \delta E^{\mathrm{loc}}_{\mathrm{XX}} - 2\delta E^{\mathrm{loc}}_{\mathrm{X}}. \tag{3.11}$$

When the temperature is increased, both excitons and biexcitons get delocalized, the biexciton binding energy is directly accessible from photoluminescence spectra. The progressive transition from localized to delocalized biexcitons is clearly visible in the temperature evolution of the photoluminescence emission energy shown in Fig. 3.16(a): the energy difference between exciton and biexciton lines shifts from 16 meV at 10 K to 22 meV at 200 K. This observation indicates that both excitons and biexcitons are delocalized at 200 K, which leads to $E^{\mathrm{b}}_{\mathrm{XX}} = 22$ meV and $E^{\mathrm{loc}}_{\mathrm{XX}} = 16$ meV.

Assuming an exciton binding energy of 46 meV as deduced from envelope function calculations (see Fig. 3.5), the biexciton to exciton binding energy ratio $E^{\mathrm{b}}_{\mathrm{XX}}/E^{\mathrm{b}}_{\mathrm{X}}$ amounts to 0.48 in the present sample. This important deviation from Haynes rule (relation 3.8) indicates that the impact of disorder on biexcitons is not specific to bulk ternary alloys but also plays an important role in quantum wells [191]. In addition, from the previously obtained energies, we can extract the free and localized biexciton energy at 10 K that occur at 3.645 and 3.639 eV, respectively. In Fig. 3.16(b), the time-evolution of the

quantum well exciton and biexciton photoluminescence is shown at 10 K after nonresonant excitation. At zero delay, i.e., when the photoluminescence signal starts to rise, the biexciton emission lies at 3.645 eV. It then progressively redshifts to 3.639 eV within 500 ps and finally remains constant for longer delays, giving a clear evidence of the dynamic trapping of biexcitons along the quantum well in-plane disorder potential.[26]

3.2.4.3 Biexciton signature in the multiple quantum well microcavity

The far-field emission pattern measured at 10 K after nonresonant cw excitation is shown in Figs. 3.17(a)-3.17(c) for different detunings. Figures 3.17(a) and 3.17(b) are monitored with the Fourier imaging spectroscopy setup using a microscope objective with a numerical aperture of 0.55 covering the emission angles between −33.4 and 33.4°. Figure 3.17(c) is obtained using the conventional angle-resolved setup characterized by a lower numerical aperture (larger spot size) but allowing to collect the luminescence at higher angles (up to 55° at low temperatures). In the specific case where $\delta = -61$ meV (see Fig. 3.17(a)), the lower polariton photoluminescence at $k_{\parallel} = 0$ lies at 3.629 eV at 10 K. Fitting the lower-polariton dispersion with a vacuum Rabi splitting ∼ 60 meV, we deduce that the uncoupled free exciton and the bottom of the upper polariton branch lie at 3.701 and 3.713 eV, respectively (see Fig. 3.12(b)). In addition to the emission from lower polaritons, we observe two emission lines at 3.671 and 3.690 eV. These lines are dispersionless and correspond in energy neither to the upper polariton branch, nor to the uncoupled free quantum well exciton. Furthermore, it clearly appears in Fig. 3.17(c) that these two transitions cross the lower polariton branch dispersion without any perturbation indicating that they are not coupled to the cavity mode. The fact that these two lines are visible in the far-field emission pattern is due to the reduced reflectivity between the lower and upper polariton modes in this energy range (see Figs. 3.12(a)-3.12(b) and Sections 1.3.5 and 3.2.3). Similarly to the bare cavity section sample, uncoupled excitons efficiently localize due to the quantum well disorder potential at low temperature. As the two samples have been grown during the same run, the potential fluctuations along the quantum well planes as well as the exciton localization energy of ∼ 11 meV are expected to be similar in both cases. Indeed this assumption is confirmed by temperature-resolved photoluminescence measurements performed on the cross-section of the full microcavity (see

[26] Note that the biexciton photoluminescence decay has been spectrally integrated over free and localized states.

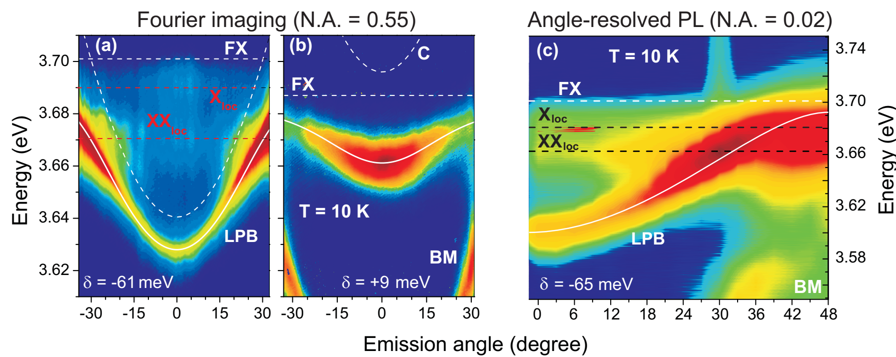

Fig. 3.17: Angle-resolved photoluminescence spectra measured at 10 K either with the Fourier imaging spectroscopy setup ((a) and (b)) or (c) with the conventional angle-resolved setup featuring a numerical aperture of 0.55 (spot size: 2 − 5 μm) and 0.02 (spot size: ∼ 50 μm), respectively, and for different detunings: (a) $\delta = -61$ meV (b) $\delta = 9$ meV and (c) $\delta = -65$ meV. (a) and (b) are adapted from Ref. [186].

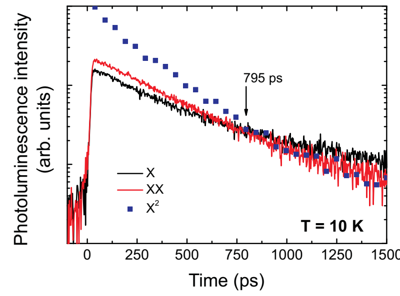

Fig. 3.18: Photoluminescence decays measured at 10 K for the exciton emission (black line) and for the biexciton one (red line) for $\delta = -61$ meV. After 795 ps, the intensity of the biexciton quadratically follows that of the exciton (blue squares). Adapted from Ref. [186].

Fig. 3.13(a)). Since the uncoupled exciton energy lies at 3.701 eV, the corresponding emission energy for localized excitons is expected at 3.690 eV. The non-dispersive transition detected at 3.690 eV is thus attributed to the recombination of excitons localized along the quantum well plane.

As for the bare active region, time-resolved photoluminescence is required to understand the origin of the 3.671 eV line. In Fig. 3.18, the emission intensity decay at normal incidence after nonresonant picosecond excitation is shown together with the one of the localized exciton emission. Interestingly, the emission from localized excitons non-exponentially decays whereas the line at 3.671 eV exponentially decays with a decay time $\tau_{\mathrm{XX}} = 335$ ps. After ~ 795 ps, the emission intensity decay of the 3.671 eV line quadratically follows that of excitons.[27] Again, this characteristic behavior allows to identify the 3.671 eV line with the radiative dissociation of cavity biexcitons. This observation is in agreement with the theoretical description given in Ref. [123], which states that dark excitons in multiple quantum well microcavities efficiently bind into biexcitons, which then recombine and leave either a dark exciton, a lower or an upper polariton. For each of these radiative channels, the emitted photon has a characteristic energy $E_{\mathrm{XX}}^{\mathrm{PL}}$:

1. **Radiative dissociation of a cavity biexciton into a photon and a dark exciton.** The corresponding biexciton emission energy is $E_{\mathrm{XX}}^{\mathrm{PL}} = E_{\mathrm{X}} - E_{\mathrm{XX}}^{\mathrm{b}}$ for free biexcitons, or $E_{\mathrm{XX}}^{\mathrm{PL}} = E_{\mathrm{X}} + \delta E_{\mathrm{X}}^{\mathrm{loc}} - \delta E_{\mathrm{XX}}^{\mathrm{loc}} - E_{\mathrm{XX}}^{\mathrm{b}}$ for localized ones.[28]

2. **Radiative dissociation of a cavity biexciton into a photon and a lower polariton.** Assuming the biexciton as quasi-dispersionless, the biexciton emission energy reads $E_{\mathrm{XX}}^{\mathrm{PL}} = 2E_{\mathrm{X}} - E_{\mathrm{XX}}^{\mathrm{b}} - E_{\mathrm{LPB}}\left(\mathbf{k}_{\parallel}^{\mathrm{LPB}}\right)$, where $\mathbf{k}_{\parallel}^{\mathrm{LPB}}$ is the in-plane wave vector of the remaining lower polariton. Note that two mechanisms should be considered here: either the lower polariton directly feeds the lower polariton branch ground state ($\mathbf{k}_{\parallel}^{\mathrm{LPB}} = 0$) or the exciton reservoir ($\mathbf{k}_{\parallel}^{\mathrm{LPB}} \gg 0$).

3. **Radiative dissociation of a cavity biexciton into a photon and an upper polariton.** Similarly to the previous case one finds $E_{\mathrm{XX}}^{\mathrm{PL}} = 2E_{\mathrm{X}} - E_{\mathrm{XX}}^{\mathrm{b}} - E_{\mathrm{UPB}}\left(\mathbf{k}_{\parallel}^{\mathrm{UPB}}\right)$, where $\mathbf{k}_{\parallel}^{\mathrm{UPB}}$ is the in-plane wave vector of the remaining upper polariton. Note that the observed biexciton emission lies at much too high energy to be ascribed to this recombination channel.

[27] Note that the thermalization time is longer than the pulse duration of our Nd:YAG laser, which explains why the quadratic increase of the biexciton photoluminescence with power is not observed.

[28] Note that the equality sign might not hold exactly as the microcavity biexciton binding energy was shown to be slightly modified by the light-matter interaction [198].

Considering the energy of the three relaxation channels listed above and the distribution of excitons and biexcitons in the momentum space compared to the limited extension of the energy trap formed by the lower polariton branch, the most probable channels for the recombination of cavity biexcitons are those leaving either an exciton or a lower polariton in the reservoir. Furthermore, as shown by the transfer matrix simulations displayed in Fig. 3.12(b), the quantity $1-R$ at zero angle does not strictly go to zero at the emission energy of excitons and biexcitons, meaning that photons with an energy comprised between the lower and upper polariton ones are allowed to leak out from the cavity. In addition, considering the finite broadening of the exciton and polariton modes, the probability of radiative decay is increased compared to the ideal and restrictive case discussed in Ref. [123]. After the radiative dissociation of one cavity biexciton, an exciton or a lower polariton is left in the cavity. Uncoupled excitons then rapidly localize and recombine whereas lower polaritons accumulate in the reservoir. In the low excitation density regime, lower polaritons relax their excess of kinetic energy *via* multiple scattering events with the surrounding electronic population or with acoustic phonons. If the relaxation time exceeds the polariton lifetime, the particles can eventually reach the ground state and escape from the cavity with a decay time of the order of the picosecond, otherwise emission occurs along the dispersion curve giving rise to the so-called bottleneck effect [199]. The role of biexcitons in the polariton relaxation dynamics in the present full microcavity is discussed in details in Section 3.3.2.

3.3 Formation of the polariton condensate

As already discussed in Section 1.4, polaritons behave as bosons in the low density limit and can therefore undergo a BEC-like thermodynamic phase transition when the carrier density is shifted beyond some critical value, similarly to what was observed in dilute atomic gases [4]. The major difference with atoms is the dual light-matter nature of polaritons. From their photonic component, they inherit an extremely short lifetime and from their excitonic one, they inherit the possibility of interacting between each other. These features significantly alter the ideal BEC picture and the way the condensate is formed.

The main limitation to achieve polariton condensation is the efficiency of the polariton relaxation from the excitonic reservoir to the bottom of the lower polariton branch [199]. To realize such a condensate under nonresonant excitation, the relaxation rate of polaritons from the exciton reservoir to the center of the Brillouin zone must indeed exceed their radiative decay rate [103, 200]. In parallel, increasing the polariton density may jointly lead to exciton screening and phase space filling. Consequently, in GaAs microcavities, the strong coupling regime might be lost before reaching the nonlinear regime [201], and great care must be taken when designing the microcavity sample so as to increase either the polariton lifetime [202, 203], the stability of polaritons by increasing N_{QW} [204] or the inter-particle interaction, e.g. by favoring exciton-electron scattering [205].

3.3.1 Formation and thermalization of polaritons: the classical picture

As all the experiments reported in this work are performed under nonresonant excitation, the electronic population first consists of a hot electron-hole plasma with a very high excess kinetic energy, typically 1 eV. Despite the high temperature of the electronic gas ($T_e > 7'000$ K), relaxation *via* LO phonons is very efficient in GaN and lasts a few hundreds of femtoseconds [206]. This high efficiency is attributed to both the high LO phonon energy ($E_{\mathrm{LO}} = 92$ meV) and the intrinsic polarization field in the wurtzite crystal along the c-direction, which enhances the Frölich interaction. As a consequence, the fast generation of a Boltzmann distribution of excitons with a temperature given by the LO-phonon energy can be

reasonably assumed. Once this initial population is formed, it further thermalizes *via* interactions with acoustic phonons and the surrounding electronic population. This process is rather slow compared to the previous one (~ 10 ps [76]) and does not allow the exchange of a significant amount of energy, the latter typically amounting to 1 meV. However, the main limitation preventing thermalization of the polariton population is the decrease in the polariton lifetime when getting close to the center of the Brillouin zone. In addition to the lifetime limitation in the formation of the polariton condensate, the increasing photonic content of lower polaritons will progressively inhibit those interactions and further promote a non-thermal lower polariton branch occupancy characterized by the presence of a relaxation bottleneck [199]. The only way to overcome this relaxation bottleneck is to favor polariton-polariton interactions in the system by all possible means. Doing so, the system progressively transits from a strongly non-thermal distribution to a thermalized one. For a given system at fixed detuning and lattice temperature, the interactions can only be enhanced by increasing the polariton carrier density, which limits the threshold for the observation of polariton condensation.[29]

Another common way to enhance the interactions in the system is to probe the sample where the exciton-cavity photon δ is more positive, i.e., when the polaritons are more exciton-like [203], as the total scattering rate of polaritons scales with the fraction of excitonic character in their wave function. In Fig. 3.19, the occupancy of the lower polariton branch is displayed for a wide range of detunings evidencing that when going from slightly positive to very negative δ-values, the occupancy of the bottom of the lower polariton branch decreases. For negative δ-values, the energy relaxation of lower polaritons is indeed hindered, due to their more pronounced photon-like character, and their distribution in momentum space is far from thermal equilibrium. This relaxation bottleneck is directly evidenced by the fact that the most salient contribution to the emission arises from the high-$\mathbf{k}_\parallel$ states forming the so-called exciton reservoir [199]. It is also seen that the system only reaches a quasi-thermal distribution for positive detunings at the considered temperature, i.e., $T = 10$ K.

[29] A detailed analysis of the polariton condensation phase diagram for the present structure is presented in Chapter 4.

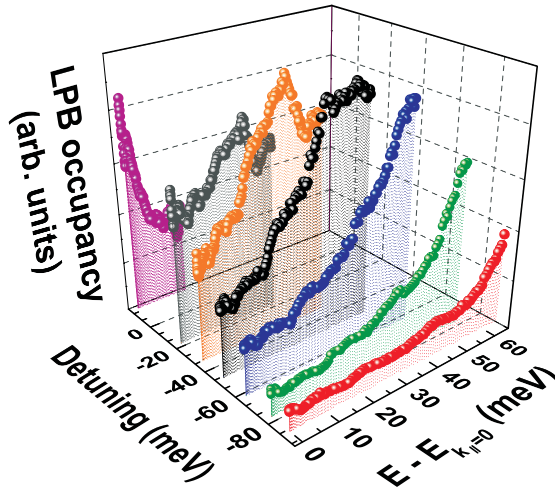

Fig. 3.19: Lower polariton branch (LPB) occupancy evolution as a function of detuning at low temperature (10 K), calculated at each angle as the intensity of the LPB signal, divided by the photon fraction, and corrected for the geometrical collection factor cos(θ). The energy $E_{k_\parallel=0}$ corresponds to the polariton ground state. Adapted from Ref. [186].

3.3.2 Biexciton-assisted relaxation

So far, we have described the properties of biexcitons in the bare active medium and in the full microcavity, as well as the available recombination channels for excitons, biexcitons and polaritons. In the present Section, we are interested in the efficiency of the various relaxations paths and determine, which one is limiting the feeding of the polariton ground state. In particular, we are interested in the role played by cavity biexcitons in the formation of the polariton condensate. To this end, we first analyze the evolution of the emission energy and intensity at $k_\parallel = 0$ (Figs. 3.20(a)-3.20(c)) and decay times (Figs. 3.21(a)-3.21(c)) for the different δ-values ranging from -40 to -160 meV. In agreement with the discussion developed in Section 3.2.4 for $\delta = -61$ meV, we observe that for all δ-values, the temporal decay of the biexciton emission quadratically follows that of the exciton emission after $\sim 700-900$ ps (see Figs. 3.21(a)-3.21(c)). In addition to the emission lines from excitons, biexcitons and lower polaritons, other lines are observed, which are reported in Fig. 3.20(a). The weak and broad emission line centered at ~ 3.82 eV is attributed to the $Al_{0.2}Ga_{0.8}N$ barrier. The two transitions falling exactly 91 meV below the exciton and biexciton emission lines (for all δ-values) are identified with exciton and biexciton first LO-phonon replicas, respectively. Finally, the multiple lines occurring

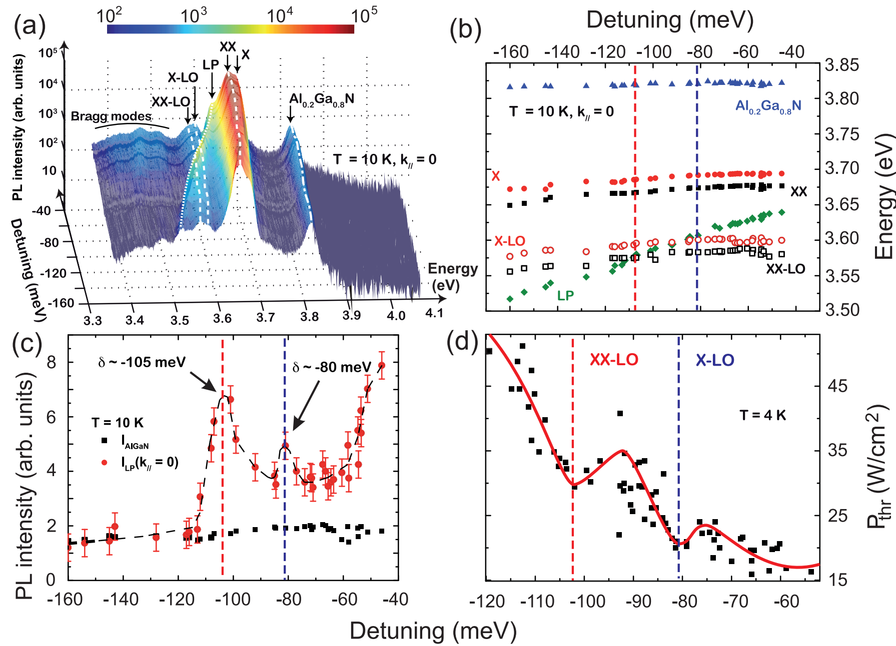

Fig. 3.20: (a) Time-integrated photoluminescence spectra of the full microcavity measured under nonresonant excitation, at normal incidence at 10 K for various δ-values. The whites lines are guides to the eye showing the δ-dependence of biexciton (XX), exciton and biexciton first LO-phonon replicas (X-LO and XX-LO, respectively), bottom of the lower polariton branch (LP) and $Al_{0.2}Ga_{0.8}N$ layer emission energies. (b) Corresponding emission energies vs. δ. (c) Emission intensity from the $Al_{0.2}Ga_{0.8}N$ barrier (squares) and the LP at $k_\parallel = 0$ (circles) vs. δ. (d) Average polariton lasing threshold power density (P_{thr}) at 4 K vs. δ. Local minima are observed for $\delta = -105$ meV and $\delta = -80$ meV corresponding to the case where LP is resonant to XX-LO (vertical red dashed line) and X-LO (vertical blue dashed line), respectively. In (c,d), lines are guides to the eye. Adapted from Ref. [186].

between 3.3 and 3.5 eV are attributed to leakage through Bragg modes due to their characteristic energy dispersions (not shown here). When collecting the emission at normal incidence for δ-values ranging from −40 to −160 meV under constant excitation power density, the emission intensity from the $Al_{0.2}Ga_{0.8}N$ barrier remains constant (black squares in Fig. 3.20(c)), indicating that the injected carrier density was kept nearly constant for all spectra displayed in Fig. 3.20(a).[30] Note that the emission energy of excitons and biexcitons increases by about 40 meV when δ is tuned between −40 and −160 meV (see Fig. 3.20(b)), which is likely due to strain variations along the wedge of the sample. However, their energy separation is kept equal to $E_X - E_{XX} = 19 \pm 1$ meV.

Contrary to exciton and biexciton emission lines, lower polaritons at $k_\parallel = 0$ feature strong intensity variations depending on δ (see Fig. 3.20(c)). One should distinguish different regions: for δ ranging between −40 and −70 meV and for $\delta < -110$ meV, the emission intensity decreases, when δ is reduced. This overall decrease goes along with a reduction in the scattering rate of lower polaritons for negative δ-values due to their increasing photonic character within the light cone [199] and usually results in the formation of a relaxation bottleneck (see Fig 3.19). Interestingly, two local maxima for the emission intensity of lower polaritons are observed. The first one occurs when $\delta \approx -80$ meV, which corresponds to the situation where the energy of lower polaritons at $k_\parallel = 0$ matches that of the first LO-phonon replica of the exciton (vertical blue dashed line in Figs. 3.20(b)-3.20(d)) and corresponds to the process $X \to LP(k_\parallel = 0) + 1LO$. Such an enhancement of the polariton relaxation when the ground state is separated from the exciton reservoir by one LO-phonon was first reported by Bœuf and coworkers for CdTe microcavities and was evidenced by a local reduction in the polariton lasing threshold [207]. In our case, the increased efficiency in the polariton relaxation due to the LO-phonon assisted transfer of uncoupled excitons and/or high-$k_\parallel$ lower polaritons to the bottom of the branch is visible *via* the local increase in the photoluminescence intensity at $k_\parallel = 0$. The second local intensity maximum occurs at $\delta \approx -105$ meV, when the bottom of the lower polariton branch is resonant with the first LO-phonon replica of the biexciton (vertical red dashed line in Figs. 3.20(b)-3.20(d)). By analogy with the previous process, we thus attribute this local enhancement in the photoluminescence intensity to the direct feeding of the lower polariton ground state by the radiative dissociation of cavity

[30] The emission intensity from lower polaritons and $Al_{0.2}Ga_{0.8}N$ in Fig. 3.20(c) has been obtained after a careful deconvolution of the time-integrated PL spectra displayed in Fig. 3.20(a).

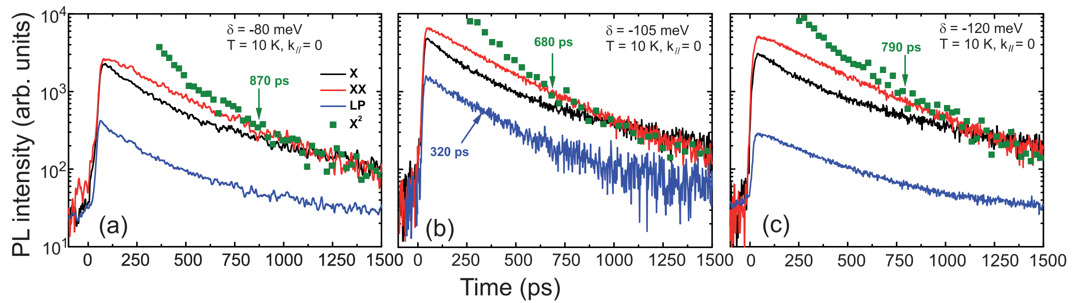

Fig. 3.21: Low-temperature photoluminescence decays for the exciton (black line), biexciton (red line) and lower polariton (blue line) emissions at $k_\parallel = 0$, for: (a) $\delta = -80$ meV, (b) −105 meV and (c) −120 meV. In (a) and (c), the lower polariton emission follows the same dynamics as the exciton. On the contrary, when $\delta = -105$ meV (b), both the biexciton and the lower polariton emissions exponentially decay with a decay time of 320 ps. For all detunings, the biexciton emission intensity follows the square of that of the exciton (green squares) after 700 – 900 ps, evidencing the full thermalization between exciton and biexciton states. Adapted from Ref. [186].

biexcitons assisted by one LO-phonon corresponding to the processes $XX \rightarrow LP(k_\parallel = 0) + 1LO + X$ and $XX \rightarrow LP(k_\parallel = 0) + 1LO + LP(k_\parallel \gg 0)$. The increased efficiency of these two relaxation channels is further supported by the dependence of the average polariton condensation threshold density (P_{thr}) with δ under nonresonant optical pumping at 4 K shown in Fig. 3.20(d): we observe two local minima for $\delta \approx -80$ meV and $\delta \approx -105$ meV (see Section 4.7 for more details).

Finally the decay of the luminescence from lower polaritons at $k_\parallel = 0$ is displayed in Figs. 3.21(a)-3.21(c) for three characteristic δ-values. For δ-values different from $\delta = -105$ meV, the lower polariton emission at normal incidence follows at all times the non-exponential decay of the excitons (see Figs. 3.21(a) and 3.21(c)). This observation demonstrates the thermal equilibrium between dark excitons and the lower polariton reservoir and the fact that the polariton relaxation is limited by the reservoir decay *via* acoustic phonon scattering and polariton-polariton interactions in agreement with the usual relaxation scheme [199, 208]. Conversely, for δ-values in the range $\delta = -105 \pm 10$ meV, the lower polaritons follow at all times the monoexponential decay of the biexciton photoluminescence (see Fig. 3.21(b)). In the latter situation, the relaxation of lower polaritons toward the center of the Brillouin zone is not limited by the scattering of high-$k_\parallel$ lower polaritons but by the radiative dissociation of cavity biexcitons.

3.4 Renormalization of the polariton branches

In this Section, the effect of the injected carrier density on the polariton dispersion in the presently investigated microcavity is addressed. First, the standard model is presented and discussed and is then compared to experimental results.

3.4.1 The standard picture

One of the most striking features of polaritons is their ability to interact *via* their matter component, which allows an efficient thermalization and the formation of a condensate in the center of the Brillouin zone. However, when increasing the carrier density, polariton properties can be significantly altered due to the renormalization of the exciton transition. In particular, as discussed in Section 1.1.5, both exciton energy and oscillator strength are affected due to the combined effects of Coulomb interaction and phase space filling resulting in a blueshift of the exciton line $\delta E_{\text{X}}(n)$ and a decrease in the light-matter coupling constant $g(n)$ [101, 103]:

$$\delta E_{\text{X}}\left(n_{\text{pol}}\right) = E_{\text{X}}^{\text{b}} \frac{n_{\text{pol}}}{n_{\text{sat}}}, \tag{3.12}$$

$$g\left(n_{\text{pol}}\right) = g_0 \left(1 - \frac{n_{\text{pol}}}{n'_{\text{sat}}}\right), \tag{3.13}$$

where g_0 is the intrinsic light-matter interaction constant[31] (see equation 1.50) and n_{pol} is the total number of injected polaritons. Note that the interaction with the reservoir is neglected in this model, i.e., the exciton renormalization only depends on the polariton density. This assumption is valid as long as the spatial overlap between the reservoir and the polariton wave function is negligible. n_{sat} and n'_{sat} are the polariton saturation densities per quantum well and per unit area corresponding to these two nonlinear processes and amount for our microcavity to [23]:

[31] For our microcavity, $g_0 \approx 30$ meV.

$$n_{\text{sat}}(\delta) = \frac{1}{2.2\pi\left(a_{\text{B}}^{\text{2D}}\right)^2 |X_0(\delta)|^2} \approx \frac{5\times10^{12}\text{cm}^{-2}}{|X_0(\delta)|^2},$$
$$n'_{\text{sat}}(\delta) = \frac{1}{4\pi\left(a_{\text{B}}^{\text{2D}}\right)^2 |X_0(\delta)|^2} \approx \frac{2.8\times10^{12}\text{cm}^{-2}}{|X_0(\delta)|^2}. \tag{3.14}$$

Note that the polariton saturation densities, which depend on the detuning *via* the excitonic fraction at zero in-plane momentum $|X_0(\delta)|^2$ can become significantly large for very negative δ-values. Another important aspect is that the polariton density is spread over the effectively coupled quantum wells ($N_{\text{QW}}^{\text{eff}} = 33.5$). As a consequence, the total saturation density is increased at least by the factor $N_{\text{QW}}^{\text{eff}}$ assuming that the carriers are homogeneously redistributed when the sample operates in the strong coupling regime [209].[32] The modification of the excitonic properties induced by relations 3.12 and 3.13 will in turn directly affect the shape of the lower and upper polariton branches given by equations 1.54. The branches are thus renormalized when the carrier density is increased according to:

$$\tilde{E}_{\text{LPB/UPB}}\left(k_\parallel,\delta,n_{\text{pol}}\right) = \frac{1}{2}\left[E_{\text{C}}\left(k_\parallel\right)+E_{\text{X}}\left(k_\parallel\right)+\delta E_{\text{X}}\left(n_{\text{pol}}\right)\right],$$
$$-\frac{1}{2}\sqrt{\left(E_{\text{C}}\left(k_\parallel\right)-E_{\text{X}}\left(k_\parallel\right)-\delta E_{\text{X}}\left(n_{\text{pol}}\right)\right)^2+4g\left(n_{\text{pol}}\right)^2}. \tag{3.15}$$

In Figs. 3.22(a)-3.22(d), the evolution of the polariton branches is displayed to show the impact of the exciton blueshift due to interactions and oscillator strength saturation. Figure 3.22(a) shows the

[32] Note that the main part of the reservoir excitons are distributed according to the laser absorption profile. Only the radiative excitons can potentially populate the other quantum wells.

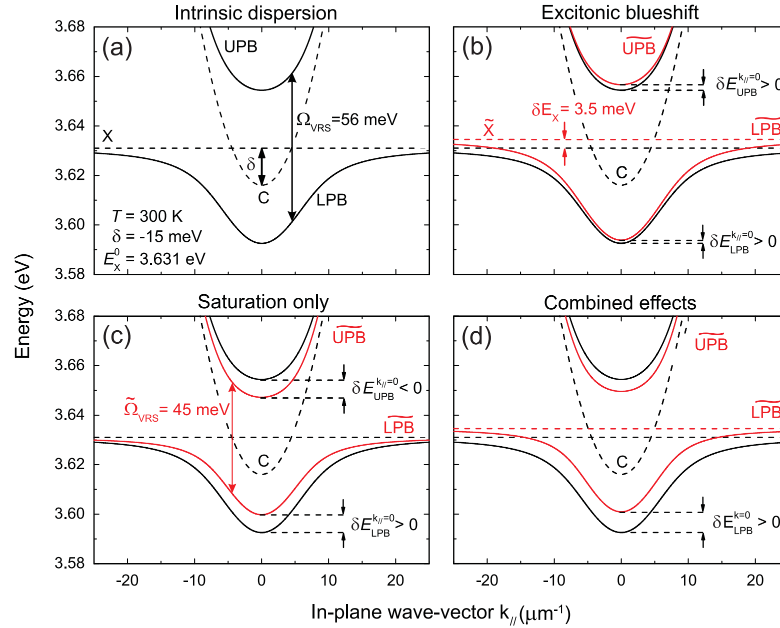

Fig. 3.22: (a) Intrinsic polariton dispersions (black lines) corresponding to the multiple quantum well microcavity investigated in this chapter for $\delta = -15\,\text{meV}$ at room temperature. Renormalized polariton dispersions (red lines) due to (b) exciton-exciton interactions (exciton blueshift), (c) oscillator strength saturation and (d) combined effects. The bare modes (excitons and cavity photons) are shown with dashed lines.

intrinsic properties of our microcavity at room temperature for $\delta = -15$ meV: a vacuum Rabi splitting of ~ 56 meV, an exciton energy of 3.631 eV corresponding to the quantum well exciton emission at room temperature. Figures 3.22(a) and 3.22(b) show separately the impact of the exciton blueshift and the oscillator strength saturation. In both cases, the energy of the lower polariton ground state is blueshifted with respect to the intrinsic case but the upper polariton branch has a different behavior: it undergoes a blueshift due to the Coulomb interaction term but a redshift due to the saturation one. The evolution of the upper polariton branch will thus depend on the relative strength of each effect.[33]

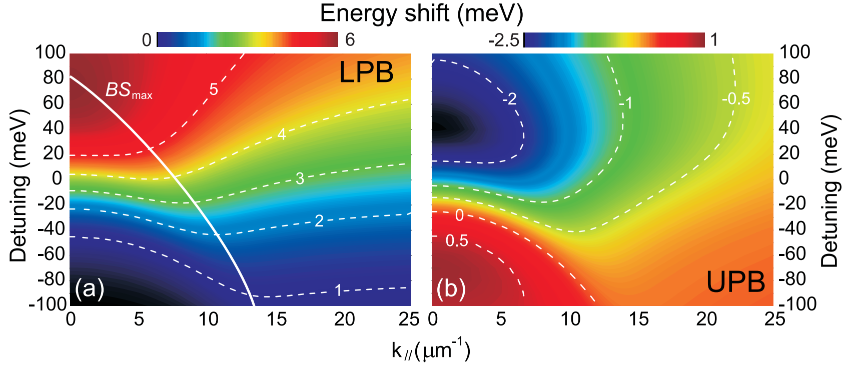

Fig. 3.23: Polariton energy renormalization based on the standard picture for the (a) lower and (b) upper polariton branches as a function of in-plane momentum and detuning for a total carrier density of $5 \cdot 10^{11}$ cm^{-2}. The thick white line indicates the evolution of the maximum blueshift (BS_{max}) for the lower polariton branch.

In Fig. 3.22(d), the impact of both effects is shown. Interestingly, the energy shift of the lower polariton branch looks quasi-rigid, i.e., for all k-vectors, the summed contribution of interaction and saturation provides a similar energy renormalization. This is however not strictly correct and strongly depends on the light-matter content of the polaritons. In Figs. 3.23(a)-3.23(b), the energy shift is displayed as a function of the in-plane k-vector and detuning for a constant polariton density of 5×10^{11} cm^{-2} in the case of the lower and upper polariton branch, respectively. It appears that the shape of the renormalized dispersion is non-trivial and critically depends on the relative weight of the saturation and the interaction terms. When interactions dominate, the polaritons branches are mainly affected at large k-vectors, whereas the impact of saturation is more visible for small wave vectors. A direct way to discriminate between these two effects experimentally is thus to monitor the renormalization of the lower polariton branch at normal incidence (main contribution of the saturation term) and at high angle (main contribution of the interaction term).[34] Note the separation between this two effects is optimum only when the blueshift for the lower polariton branch (thick white line shown in Fig. 3.23(a)) does not occur at $k_{\parallel} = 0$. The case of the upper branch is more unpredictable as the system can exhibit either a red- or a blueshift depending on $k_{\parallel}$ and δ.

[33] Note that the situation depicted in Fig. 3.22 corresponds to typical experimental values at the condensation threshold and they do not necessarily match the values given by relations 3.12 and 3.13.

[34] Such an experiment is not possible in the present microcavity due the to the contribution of the Bragg modes at angles higher than 40°.

In Figs. 3.24(a)-3.24(b), the renormalization of the lower and upper polariton branches at $k_{\parallel} = 0$ is shown for different detunings and polariton densities highlighting the impact of the excitonic fraction[35] and injected carrier density on the polariton ground state energy. In particular, in Fig. 3.24(b), it appears that for detuning values higher than -25 meV, the upper polariton branch energy shift changes its sign and becomes negative, indicating a crossover in the respective weight played by Coulomb interaction and saturation. As expected, the renormalization becomes more pronounced when the matter-content of polaritons becomes large.

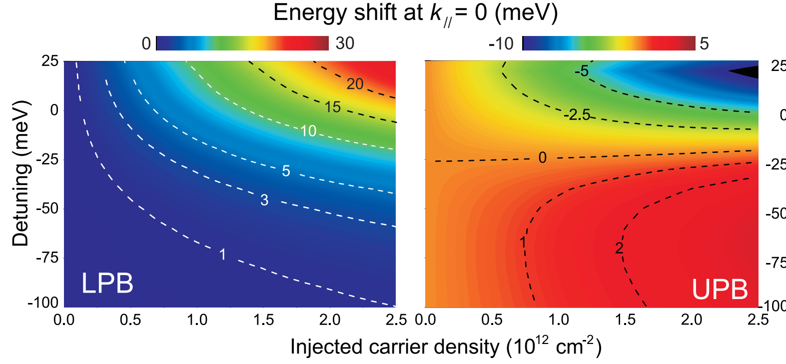

Fig. 3.24: Renormalization of the (a) lower and (b) upper polariton branches at $k_{\parallel} = 0$ for different detunings and polariton densities.

In the present model, the energy shift of the polariton ground state energy $\delta E^{0}_{\mathrm{LPB}} = \tilde{E}_{\mathrm{LPB}}(k_{\parallel} = 0) - E_{\mathrm{LPB}}(k_{\parallel} = 0)$ contains two contributions, one stemming from the saturation of the oscillator strength ($\delta E^{\mathrm{sat},0}_{\mathrm{LPB}}$) and the other one from the Coulomb interaction ($\delta E^{\mathrm{int},0}_{\mathrm{LPB}}$). Considering the parameters of our system, a linear expansion of equation 3.15 is justified and one can write:[210]

$$\delta E^{\mathrm{int},0}_{\mathrm{LPB}}\left(n_{\mathrm{pol}}\right) \approx \delta E_{\mathrm{X}}\left(n_{\mathrm{pol}}\right)|X_0|^2 = \beta_1(\delta)\, n_{\mathrm{pol}}\,, \tag{3.16}$$

$$\delta E^{\mathrm{sat},0}_{\mathrm{LPB}}\left(n_{\mathrm{pol}}\right) \approx \delta\Omega_{\mathrm{VRS}}\left(n_{\mathrm{pol}}\right) \frac{\Omega_{\mathrm{VRS},0}}{2\sqrt{\delta^2 + \Omega^2_{\mathrm{VRS},0}}} \approx \beta_2(\delta)\, n_{\mathrm{pol}}\,, \tag{3.17}$$

where $\delta\Omega_{\mathrm{VRS}}$ is the reduction in the vacuum Rabi splitting due to the saturation of the oscillator strength, $\Omega_{\mathrm{VRS},0}$ is its intrinsic value and $\beta_{1,2}$ are proportionality constants, which obviously depend on δ. These relations suggest that the link between the injected carrier density and the ground state polariton energy is linear. Even if this seems to be verified in GaAs-based microcavities below the polariton condensation threshold [211] or in CdTe ones [18], the situation becomes more complex when the carrier density crosses the threshold. In particular, for GaAs-based microcavities the energy blueshift was found to switch from a linear to a logarithmic power dependence [211, 212]. These observations disagree with the theory, which also predicts a linear behavior of the blueshift above threshold but with a larger slope due to the contribution of the thermal population [213].

It was shown by Huynh and coworkers by means of resonant pump-probe experiments that in a CdTe microcavity, the system is first dominated by Coulomb interaction in the low density regime

[35] In the following, we will mainly focus our attention on the renormalization of the lower polariton branch at $k_{\parallel} = 0$, as the ground state behavior is of major interest to achieve a comprehensive understanding of the polariton condensate properties.

whereas close to the condensation threshold, the saturation-term becomes dominant and rules the renormalization of the polariton branches [214]. The dominant role of the saturation in CdTe was also evidenced by photoluminescence experiments performed under nonresonant excitation with the monitoring of the redshift of the upper polariton branch when the carrier density is increased (see on-line supplementary material of Ref. [18]). Conversely, for GaAs-based microcavities, the impact of the renormalization term is usually found to be negligible compared to the interaction one [211, 215]. This can be understood by estimating the relative contribution of each effect. In the calculation of the polariton scattering rates, the saturation term gives a contribution of the order of $\left(\Omega_{\text{VRS}}/4\,E_{\text{X}}^{\text{b}}\right)^2$ compared to the exciton-exciton scattering term [101]. As both Ω_{VRS} and E_{X}^{b} quantities strongly depend on the sample design, the contribution of saturation is not specific to a given material and changes from one sample to another and a ratio of 0.2 is found for the state of the art GaAs multiple quantum well microcavity described in Ref. [202], 0.067 for the CdTe one studied in Ref. [18] and 0.1 for the GaN one investigated in this thesis [34, 53].

3.4.2 Impact of the lattice temperature, detuning and disorder

According to the model presented in the previous section, the renormalization of the polariton condensate energy should strongly depend on the detuning as exciton nonlinearities scale with the excitonic fraction. In Fig. 3.25(a), the evolution of the blueshift at threshold in our GaN multiple quantum well-based microcavity is reported as a function of the lattice temperature and detuning. The microcavity was probed with a spot size of about 5 μm (using the high N.A. microscope objective). Despite a large scattering in the data, a correlation is visible between the blueshift of the condensate at $k_\parallel = 0$ and the two parameters (δ, T): the blueshift increases for high temperatures and negative detuning (see projection planes in Fig. 3.25(a) represented with plus and cross signs for T and δ, respectively). This trend is due to the increase of the condensation threshold density, which results in large carrier concentrations (see Chapter 4 for a detailed discussion of the polariton phase diagram).

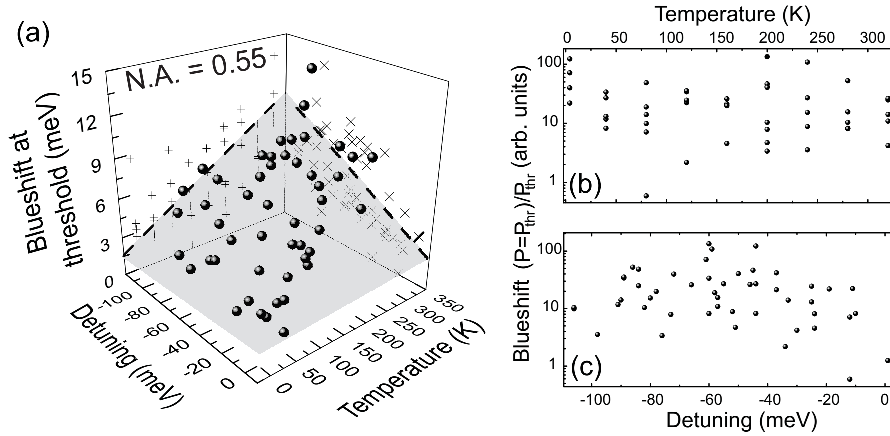

Fig. 3.25: (a) Blueshift of the lower polariton ground state for different detunings and lattice temperatures at the condensation threshold ($P = P_{\text{thr}}$). Evolution of the lower polariton blueshift normalized to P_{thr} as a function of (b) temperature and (c) detuning. All measurements were performed with the high numerical aperture microscope objective.

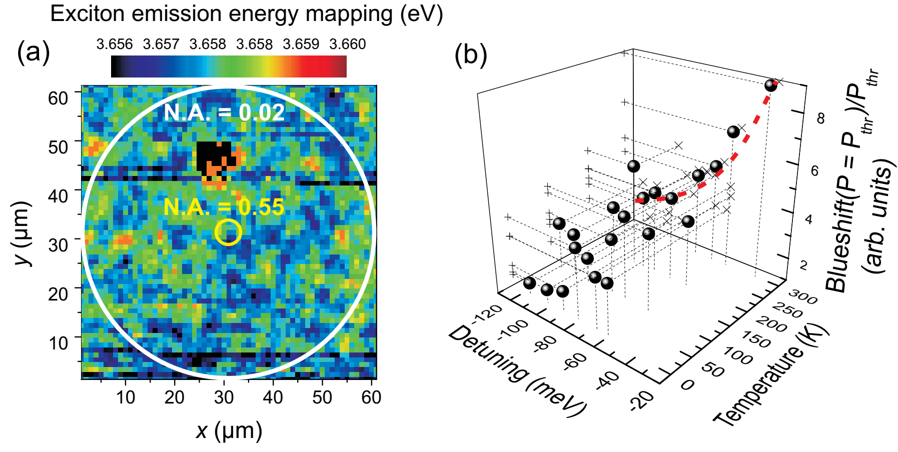

Fig. 3.26: (a) Exciton emission energy mapping. The yellow and white circles represent the approximative excitation spot size when either the microscope objective (N.A. = 0.55) or a conventional lens (N. A. = 0.02) is used. (b) Measured energy renormalization of the lower polariton at $k_{\|} = 0$ for different detunings and lattice temperatures at the condensation threshold (N.A. = 0.02). The red dashed line is a guide-to-the-eye of the projected data in the δ-plane.

As $\delta E^0_{\mathrm{LPB}}$ directly scales with the polariton density according to relations 3.16 and 3.17, eventual correlations between the renormalized ground state energy at threshold and the two parameters would be revealed by rescaling the measured blueshift with the threshold power density (see Figs. 3.25(b)-3.25(c)). The quantity $\delta E^0_{\mathrm{LPB}}/P_{\mathrm{thr}}$ is then expected to be proportional to $\beta_1 + \beta_2$, which accounts for the combined effect of Coulomb interaction and saturation. Considering that exciton-exciton interactions are affected by both detuning and the lattice temperature, $\beta_1 + \beta_2$ is thus expected to increase for exciton-like polaritons and for elevated temperatures. However, no obvious correlation is visible in Figs. 3.25(b)-3.25(c).

The main difficulty when extracting correlations between $\delta E^0_{\mathrm{LPB}}$ and the system parameters affecting the polariton relaxation, i.e., the lattice temperature and the detuning, likely comes from exciton and cavity-photon in-plane disorder. In Fig. 3.26(a), the variation in the exciton energy measured on the bare active medium under nonresonant cw excitation is reported over a spatial region of $60 \times 60\,\mu\mathrm{m}^2$ with a spatial resolution of $0.2 \times 0.2\,\mu\mathrm{m}^2$ together with the areas probed with the microscope objective (yellow circle, N.A. = 0.55) and with a lens with a focal length of 7.5 cm (white circle, N.A. ≈ 0.02).[36] It is seen that the quantum well emission is homogeneous over regions comparable with the spot size used in Figs. 3.25(a)-3.25(c). The same consideration is true for the photonic disorder: it was shown that the cavity mode is homogeneous over regions not larger than $10 \times 10\,\mu\mathrm{m}^2$ in similar microcavities [65]. As a consequence, the scattering in the data shown in Figs. 3.25(a)-3.25(c) is likely due to the impact of disorder on the polariton condensate formation, which bleaches the contribution of exciton nonlinearities. Note also that in the successive measurements the spot size (and therefore the threshold power density) was changing from one measurement to another due to slight imprecisions in the focusing affecting the spot size.[37]

In order to get rid of the unpredictable contribution of the in-plane static disorder, the same measurements were repeated with a smaller numerical aperture (N.A.≈ 0.02, white circle in Fig. 3.26(a))

[36] N.A. is defined here using the laser spot size on the focusing lens.

[37] This effect is likely inherited from the small depth of focus (DOF≈ 1 μm) of our high numerical aperture objective.

and therefore a larger spot size (see Fig. 3.26(b)). The exciton and cavity energies are now averaged over a diameter of about 50 – 60 μm, resulting in well defined values but with a more significant inhomogeneous broadening. In Fig. 3.26(b), the blueshift of the polariton condensate energy at threshold normalized by the threshold power density is reported as a function of the lattice temperature and the detuning. Interestingly, the increase in the blueshift when the detuning reaches less negative values (higher excitonic content) is now consistent with the model presented in the previous Section and highlights the increased renormalization occurring at larger δ-values. The slight increase in the blueshift with temperature can be qualitatively understood by the nonlinear dependence of the condensation threshold with temperature resulting in a more significant population in the condensate (see Chapter 4 for more details). However, at this point the impact of the exciton oscillator strength saturation and the Coulomb interactions are not separated.

3.4.3 *Impact of interactions and saturation*

3.4.3.1 Role of Coulomb interactions

Measurements performed on the bare active medium have shown that the blueshift of the exciton energy before reaching the onset of the Mott transition approximately amounts to 3.5 meV (see Fig. 3.10(c)). This value is in relatively good agreement with that predicted by equation 3.12 for the saturation density per quantum well, i.e., $n \approx 1.2 \times 10^{12}\,\text{cm}^{-2}$ (black line in Fig. 3.27(a)).[38] According to the standard model presented in Section 3.4.1, the corresponding blueshift of the lower polariton branch due to exciton-exciton interactions can be deduced and is displayed in Fig. 3.27(b) at $k_\parallel = 0$ for different δ-values.

The 3.5 meV energy shift corresponds to the renormalization of the exciton energy close to the onset of the Mott density. As already discussed in Section 3.2.4, exciton dark states can also be probed *via* photoluminescence in the full microcavity. Even if the luminescence mainly originates from the uncoupled quantum wells, it gives more information on the exciton renormalization in the full

[38] Note that we use here the criterion of Schmitt-Rink and coworkers for the saturation density (relation 1.21), which is lower than the value given by relations 3.14.

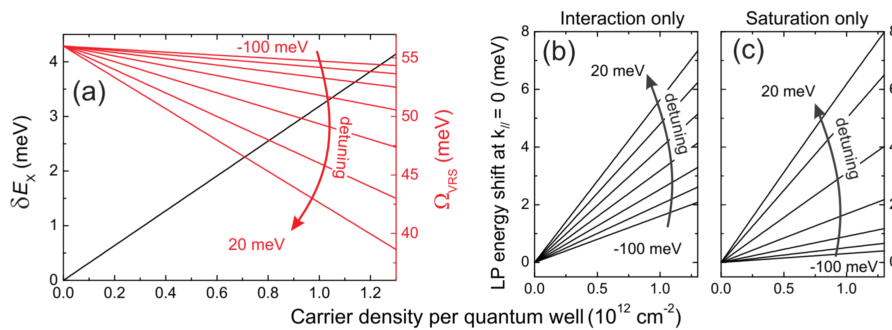

Fig. 3.27: (a) Evolution of the exciton energy shift (black line) and vacuum Rabi splitting (red lines) vs. carrier density per quantum well in the present microcavity according to the standard model. Evolution of the lower polariton energy at $k_\parallel = 0$ as a function of the injected carrier density in the case where only (b) the Coulomb interaction and (c) the saturation term is considered. The curves are displayed for various detunings ranging from −100 to 20 meV.

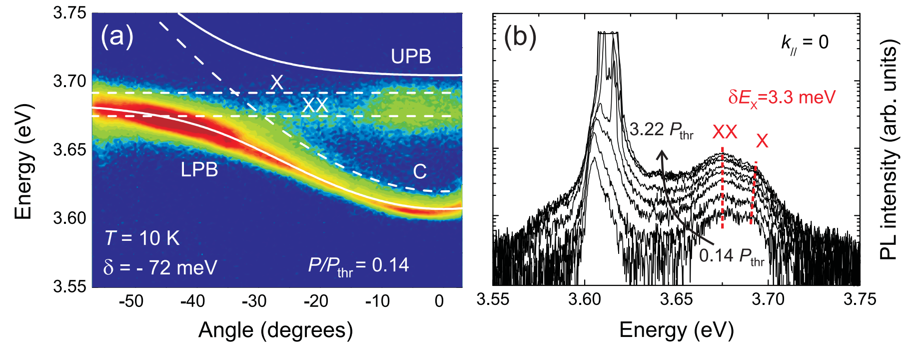

Fig. 3.28: (a) Far-field emission pattern of the full microcavity measured under nonresonant quasi-cw excitation ($\lambda = 266\,\text{nm}$) at 10 K for $\delta = -72\,\text{meV}$ below the condensation threshold. The bare modes, i.e., the free exciton (X), biexciton (XX) and cavity mode (C) are shown with white dashed lines and the polariton branches (LPB and UPB) are shown with white continuous lines. (b) Photoluminescence spectra at $k_\parallel = 0$ obtained at the same position with the same condition for various excitation power ranging from 0.14 to 3.22 P_{thr}. The evolution of X and XX lines is indicated with red dashed lines.

microcavity as radiative excitons in the strongly coupled quantum well are redistributed in the whole cavity section due to Rabi oscillations.[39] In Fig. 3.28(a), the photoluminescence of the full microcavity is displayed below the condensation threshold under pulsed nonresonant excitation at $T = 10\,\text{K}$. Assuming that the luminescence is dominated by free excitons due to the relatively high peak power per pulse, the power series displayed in Fig. 3.28(b) allows probing the uncoupled exciton and biexciton energy renormalization. The energy shift of the dark exciton at $k_\parallel = 0$ approximately amounts to 3.3 meV at $P/P_{\text{thr}} = 3.22$ and the high energy side does not show any exponential tail indicating that the system is still below the Mott transition [98].

3.4.3.2 Role of saturation

Let us now turn our attention to the saturation of the oscillator strength due to phase space filling and Coulomb exchange. According to the standard model described in Section 3.4.1, we can calculate the expected decrease in the vacuum Rabi splitting (see red lines in Fig. 3.27(a)) and also the corresponding blueshift of the lower polariton branch at $k_\parallel = 0$. In Fig. 3.27(c), the energy shift is reported for different detuning values in the case where only the saturation of the exciton oscillator strength is considered. This model predicts that the saturation becomes the dominant effect for positive detunings only as polariton nonlinearities linearly scale with the excitonic fraction.

In Fig. 3.29, angle-resolved photoluminescence spectra obtained with a spot size of $\sim 5\,\mu\text{m}$ at 280 K under quasi-cw nonresonant excitation for $\delta = -54\,\text{meV}$ are displayed for various excitation power densities ranging from 0.15 to P_{thr}. The exciton energy is assumed to be approximately constant over the power range investigated as the change of energy dispersion with increasing angle cannot be reproduced by shifting the quantum well resonance indicating that saturation is the dominant effect in this case. The quasi-absence of exciton renormalization can be explained by the relatively large negative detuning and the small power-range investigated. The vacuum Rabi splitting Ω_{VRS} is deduced

[39] Note that nonradiative excitons with $k_\parallel > k_{\text{rad}}$ do not directly participate to the light-matter interaction and are distributed according to the pump absorption profile. An estimation following Lambert-Beer law indicates that only the first 12 quantum wells are pumped.

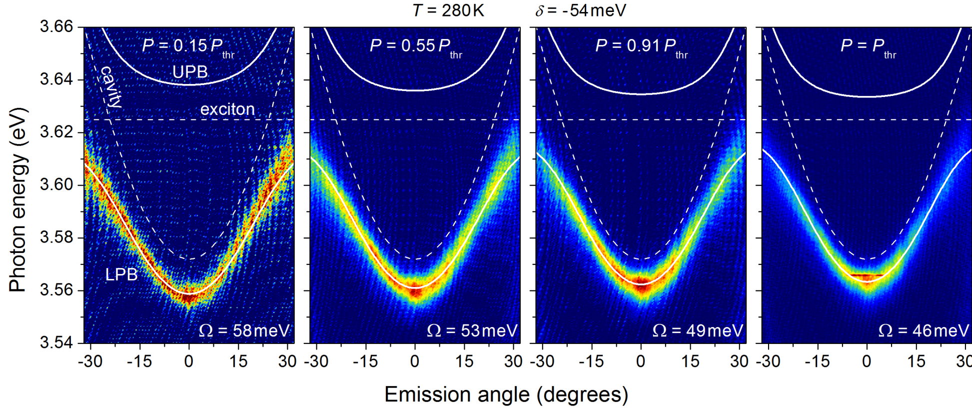

Fig. 3.29: Far-field emission pattern of the full microcavity under nonresonant quasi-cw excitation at 280 K for $\delta = -54$ meV for various excitation power densities ranging from 0.15 to P_{thr}. The bare modes, i.e., the free exciton (X), biexciton (XX) and cavity mode (C) are shown with white dashed lines and the polariton branches (LPB and UPB) with white continuous lines. The vacuum Rabi splitting (Ω) is strongly decreased between the lowest and highest powers used.

by fitting the lower polariton branch with a two level model keeping exciton and cavity photon energies constant. Interestingly, Ω_{VRS} is decreased by $\sim 20\%$ between $0.15P_{\text{thr}}$ and P_{thr}. Note that the polariton energy at $k_{\parallel} = 0$ remains below the cavity energy over the whole power range investigated, ensuring that the strong coupling regime is preserved.

We repeated these measurements for different detunings and temperatures (see Figs. 3.30(a)-3.30(b)) and surprisingly, the impact of saturation seems to decrease when the detuning is increased, independently from the temperature in contradiction with the expected behavior. This observation is in total disagreement with the behavior expected from the standard model (see Fig. 3.27(a)). This result can be qualitatively understood by considering the power-evolution of the homogeneous broadening of the lower polariton γ^0_{lpb} at $k_{\parallel} = 0$ (see red lines in Fig. 3.30). For the larger negative detuning ($\delta = -86$ meV), γ^0_{lpb} increases from 8 to 12 meV and from 14 to 18 meV for $\delta = -24$ meV. In both cases the lower polariton induced broadening is $\Delta\gamma^0_{\text{lpb}} \approx 4$ meV. Neglecting the dependence of the cavity mode linewidth and the excitonic fraction $|X_0(\delta)|^2$ on the carrier density n, the lower polariton broadening is directly related to the exciton collisional broadening term $\Delta\gamma^{\text{coll}}_{\text{X}}(n)$. The relation 1.65 leads to: $\Delta\gamma^0_{\text{lpb}} \approx \Delta\gamma^{\text{coll}}_{\text{X}}(n)\,|X_0(\delta)|^2$. As $|X_0(\delta = -86\,\text{meV})|^2 \approx 0.1$ and $|X_0(\delta = -24\,\text{meV})|^2 \approx 0.3$ and assuming that the collisional term linearly depends on the carrier density, i.e., $\Delta\gamma^{\text{coll}}_{\text{X}}(n) \propto n$, the ratio between the injected carrier densities can be roughly estimated: $n(\delta = -86\,\text{meV}) / n(\delta = -24\,\text{meV}) \approx 3$. The large difference between the carrier densities needed to reach the condensation threshold inevitably leads to different saturation values of the oscillator strength.

In Fig. 3.30(b), the impact of temperature on the vacuum Rabi splitting is shown for comparable detunings at 40 and 300 K, featuring different behaviors. At low temperature (black squares), the decrease in Ω_{VRS} is less pronounced and seems to slow down once the condensation threshold is crossed. This behavior is very interesting as it seems to indicate that the renormalization is governed by the exciton reservoir whose density is clamped above the condensation threshold [216]. The situation looks a bit different at room temperature (black dots), where a rapid decrease in Ω_{VRS} is seen with increasing carrier density. Again, this behavior can be qualitatively understood by the different

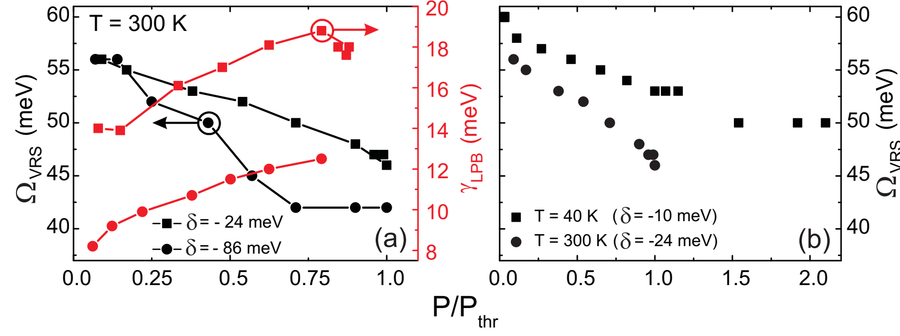

Fig. 3.30: Evolution of the vacuum Rabi splitting (Ω_{VRS}) vs. excitation power (a) at room temperature for different δ-values (black curves) with the corresponding polariton homogeneous broadening γ_{lpb} (red curves) and (b) for different temperatures for two close δ-values.

threshold densities required to reach the condensation threshold. In conclusion, a comprehensive description of saturation effects in III-nitride microcavities is closely related to the evolution of the critical density for polariton condensation. A theoretical and experimental description of the polariton phase diagram is thus of paramount importance and is treated separately in Chapter 4.

3.4.4 Nonlinear renormalization of the polariton condensate: possible contribution of biexcitons

Usually it is assumed that the blueshift of the condensate is attributed to the saturation and interaction terms only. In this model, the blueshift is modeled by a single constant (α), which corresponds to the slope of $\delta E^0_{\text{LPB}}(n_0)$, i.e., $\alpha = \frac{dE^0_{\text{LPB}}(n_0)}{dn_0}$, where n_0 is the polariton density in the ground state.[40] This approach suggests that the evolution of the condensate energy linearly scales with the injected carrier density. However, this behavior is rarely observed. In GaAs pillar microcavities for instance, Brichkin and coworkers observed a sublinear increase in the polariton energy with carrier density for small spot sizes [210]. They attribute this behavior to an enhancement of the escape of lower polaritons from the condensate caused by the blueshift, which acts as a repulsive force and results in an increase in the condensation area as particles are ballistically expelled toward potential minima away from the excitation spot. In another work, Ferrier and coworkers investigate in more details the effect of the spatial overlap between the pump and the condensate on the polariton renormalization in GaAs pillar microcavities [217]. They show that the blueshift of the polariton ground state has two main contributions: (i) the interactions occurring between the polaritons in the condensate and the excitons from the reservoir whose distribution is given by the excitation pump profile and (ii) the interactions between polaritons within the reservoir. These two effects linearly scale with the pump intensity but the impact of polariton-polariton interactions in the condensate is found to become the dominant effect when the lateral extension of the system increases. However, contrary to Brichkin and coworkers, they do not observe a sublinear behavior of the polariton condensate energy with increasing carrier density.

In Figs. 3.31(a)-3.31(d), the blueshift of the lower polariton branch at $k_\parallel = 0$ is displayed as a function of the normalized pump power for a constant detuning of about $-60\,$meV. Measurements are performed

[40] For GaAs microcavities, a value of $7 \pm 0.8\,\text{meV/cm}^2$ is found [210].

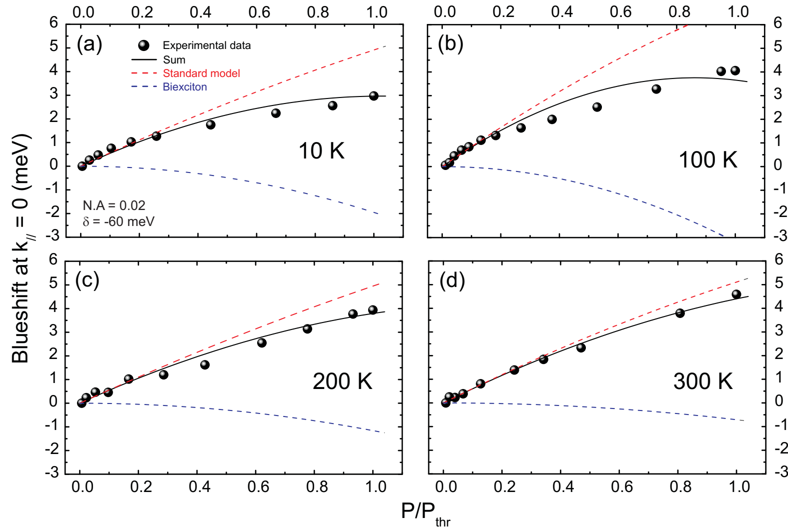

Fig. 3.31: Blueshift of the lower polariton at $k_\parallel = 0$ as a function of the normalized pump power for $\delta \approx -60$ meV. Measurements are performed under nonresonant excitation with a spot size of about 50 μm diameter at (a) $T = 10$ K, (b) $T = 100$ K, (c) $T = 200$ K and (d) $T = 300$ K. The data are shown with the fit (black lines), which is the sum of the standard model prediction (red dashed lines) and the biexciton contribution (blue dashed lines) according to Ref. [218].

under nonresonant excitation with a spot size of 50 – 60 μm diameter for 4 different lattice temperatures between 10 K and room temperature. According to Ref. [210], the blueshift is expected to be linear under these conditions as the spot size is rather big and the measurements are performed below the condensation threshold. However, a clear deviation from linearity is observed for temperatures lower than 200 K. This transition from a sublinear to a linear transition cannot be attributed to a repulsive force imprinted by the excitation spot as this effect is not expected to strongly depend on temperature.

The main weakness of the standard model is that it only accounts for the exciton-exciton interactions and phase space filling. In a recent work, Vladimirova and coworkers have presented an extended model accounting for the spinor nature of the polariton condensate [218]. In this framework, the renormalization is no longer described by one, but two interactions constants: $\alpha_1 > 0$ describing the repulsive interaction between polaritons with the same spin and $\alpha_2 < 0$ the attractive interaction between polaritons with opposite spins [219].[41] Usually $|\alpha_2| \ll |\alpha_1|$, due to the dominating contribution of the exchange interaction term in two-dimensional systems [102]. The shift of the condensate energy will thus depend on the polarization of the emitted light, circular ($\delta E_{\mathrm{LPB}}^{\mathrm{circ},0}$) or linear ($\delta E_{\mathrm{LPB}}^{\mathrm{lin},0}$):

$$\begin{aligned} \delta E_{\mathrm{LPB}}^{\mathrm{lin},0}(n_0) &= \frac{\alpha_1 + \alpha_2}{2} n_0 , \\ \delta E_{\mathrm{LPB}}^{\mathrm{circ},0}(n_0) &= \alpha_1 n_0 . \end{aligned} \tag{3.18}$$

Note that relations 3.18 only account for the renormalization due to polariton-polariton interactions in the condensate and neglect the contribution of the exciton reservoir. In addition to the interaction terms, Vladimirova and coworkers also include in their model the contribution of the mean-field electrostatic energy, the Van der Waals dipole-dipole interaction of polaritons, the contribution of dark

[41] The spin anisotropic interaction constants are discussed in more details in Chapter 5.

excitons and that of the biexcitons to both α_1 and α_2. To account for the nonlinear blueshift observed in our microcavity, an important contribution from α_2 is needed. In addition, this contribution is expected to nonlinearly depend on the carrier density to account for the strong deviation from the quasi-linear behavior predicted by the standard model (red dashed lines in Figs. 3.31(a)-3.31(d)). The biexciton-mediated interaction results in an effective polariton-polariton attraction [220] and exclusively contributes to α_2 (i.e. negative energy shift). The corresponding renormalization of the lower polariton energy is given by [218]:

$$\delta E_{\mathrm{LPB}}^{\mathrm{XX},0}(n_0) = f\frac{\Delta_{\mathrm{XX}}}{2}\left(\sqrt{1-\frac{\left(1-|X_0|^2\right)|X_0|^2\left(\hbar\Omega_{\mathrm{VRS}}\pi a_{\mathrm{B}}^2 n_0\right)^2}{\Delta_{\mathrm{XX}}^2}}-1\right), \tag{3.19}$$

where f is a numerical factor close to unity and Δ_{XX} is the energy splitting between the biexciton state and the polariton ground state, i.e., $\Delta_{\mathrm{XX}} = \frac{1}{2}(E_{\mathrm{X}} + E_{\mathrm{XX}}) - E_{\mathrm{LPB}}^0$. Note that relation 3.19 does not strictly apply to our microcavity as it is only valid for systems where the impact of the saturation term is negligible compared to the Coulomb interaction one, like the GaAs microcavity investigated in Ref. [221], but it can be reasonably used below and close to the condensation threshold. It is interesting to note that in equation 3.19 the strength of the biexciton contribution to the renormalization of the condensate energy nonlinearly depends on the polariton density in the ground state n_0. In Figs. 3.31(a)-3.31(d), the experimental data are fitted by adding the biexciton contribution given by relation 3.19 (blue dashed lines) to the standard renormalization model (red dashed lines).[42] Interestingly, for 10 and 100 K the deviation from linearity is important and it becomes more and more negligible above 200 K. Note that this behavior could be linked to the thermal dissociation of biexcitons as it is expected around 200 K in our system.[43] The qualitative agreement between fits and experimental data suggests that the biexciton-mediated interaction is a probable candidate for the nonlinear renormalization behavior of the lower polariton energy in our system.

3.5 The nonlinear regime

All the measurements presented so far in this chapter were obtained below or close to the condensation threshold, i.e., $P/P_{\mathrm{thr}} \approx 1$, to describe the formation of the polariton condensate. We now focus our attention on the behavior of the system above P_{thr}.

3.5.1 Condensation in real and momentum spaces

One of the main features of III-nitride planar microcavities is the relatively important excitonic ($\gamma_{\mathrm{inh}}^{\mathrm{X}} \approx$ 12 meV) and photonic disorder ($\gamma_{\mathrm{inh}}^{\mathrm{C}} \approx 10-15$ meV [65]), which directly impact on the system properties. Despite a significant in-plane disorder landscape for polaritons, polariton condensation has been observed in bulk III-nitride [33] and multiple quantum well based planar microcavities [65].

In Figs. 3.32(a)-3.32(c), the far-field emission pattern of the present microcavity at room temperature for $\delta \approx -100$ meV is displayed for three different pumping regimes $P/P_{\mathrm{thr}} = 0.89$, 1, and 1.5, respectively. In Figs. 3.32(d)-3.32(f), the corresponding real space images are displayed. This power series shows the quasi-Gaussian polariton distribution below the condensation threshold imprinted by the excitation

[42] The critical density is taken into account in the estimation of n_0 used for the evaluation of relation 3.19. The critical density is deduced from the polariton phase diagram established in Chapter 4 and we assume here that $n_{\mathrm{crit}} \propto P_{\mathrm{thr}}$.

[43] Note that the biexciton transition is considered as a virtual state in Ref. [218] and its contribution to α_2 should not be significantly altered by temperature.

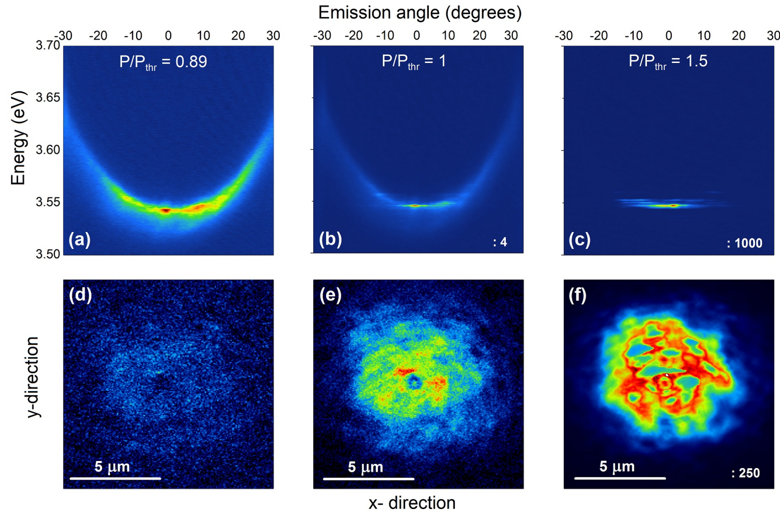

Fig. 3.32: (a)-(c) Far-field emission pattern of the present microcavity at room temperature under nonresonant excitation for $\delta \approx -100$ meV displayed for three different pumping regimes $P/P_{\mathrm{thr}} = 0.89$, 1, and 1.5, respectively. (d)-(f) Corresponding real space images.

spot. As the system operates at room temperature, the polariton distribution is quasi-thermal with an effective temperature of $T_{\mathrm{eff}} \approx 900 \pm 50$ K for $P/P_{\mathrm{thr}} = 0.89$ (see Fig. 3.32(a)). This relatively high temperature is attributed to the relatively large negative detuning, which prevents an efficient relaxation despite the high lattice temperature. At the condensation threshold, a sharp emission occurs at zero in-plane momentum. Similarly to what was reported in CdTe planar microcavities, condensation takes place in both real and reciprocal spaces as the exciton polariton wave function is peaked at structural imperfections [222]. The reciprocal space condensation is visible in Fig. 3.32(b) *via* the sharp emission centered at $k_{\parallel} = 0$ and the real space condensation *via* the patterned shape of the nonlinear emission in Figs. 3.32(e)-3.32(f).

The dispersionless character of the emission around $k_{\parallel} = 0$ originating from the polariton condensate extends over an angular range $\Delta\theta \approx 10 \pm 2°$ (to which corresponds an in-plane wave-vector spread $\Delta k_{\parallel}$). A similar feature was reported for CdTe microcavities [223] and is consistent with localization effects induced by photonic disorder. In this latter case, the polariton localization radius $r_{\mathrm{loc}} \approx \Delta k_{\parallel}^{-1} \approx 1.5\,\mu$m is larger than the 0.3$\mu$m deduced from the present measurements [55]. This is consistent with the larger in-plane photonic disorder characteristic of III-nitride-based microcavities [65] compared with CdTe structures [223] and GaAs ones [215] where such an effect has not been reported. The condensate localization is supported by the observation of fragmented spots above the condensation threshold with a typical size smaller than 1 μm. When increasing the injection power density, the pattern changes and the number of intense spots increases in agreement with the observations of Richard and coworkers [222]. However, it should be pointed out that contrary to their measurements, the spots seem to be interconnected above a given power (see Fig. 3.32(f)) but no conclusion can be drawn on eventual mutual coherence between the emitting spots on the basis of these measurements.

Another striking feature above the condensation threshold is the multimode character of the emission. In Fig. 3.33(a), photoluminescence spectra measured at $k_{\parallel} = 0$ are reported for various power densities. The emission becomes multimode for $P > 1.2P_{\mathrm{thr}}$ and the number of modes continuously increases then. It is difficult to identify the nature of these modes as they can originate either from independent

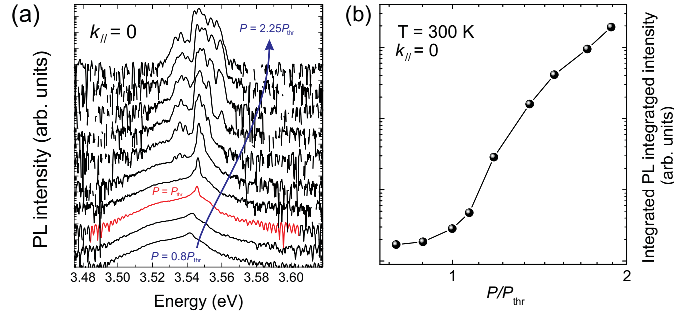

Fig. 3.33: Power-series at $k_\parallel = 0$ of the present microcavity at room temperature for $\delta \approx -100$ meV under nonresonant excitation: (a) Photoluminescence spectra for different power densities ranging from 0.8 to $2.25P_{\text{thr}}$. The red curve corresponds to $P = P_{\text{thr}}$. (b) Energy-integrated intensity vs. normalized power density.

spots or from the excited states of the same condensate. In 2008, Baas and coworkers have shown that localized condensates can synchronize above threshold allowing for the build-up of a single ground state extended over the excitation spot [224]. They also showed that if the disorder is too large the correlations between the spots can be destroyed resulting in independent condensates. Considering the larger photonic disorder in GaN microcavities compared to CdTe-ones, it is reasonable to assume that the nonlinear emission likely arises from independent condensates. Finally, in Fig. 3.33(b), the power evolution of the integrated intensity at $k_\parallel = 0$ is shown featuring the characteristic exponential increase in the output power with power density. However, for $P > 1.2P_{\text{thr}}$, this curve should be considered with caution as several modes take part to the emission process.

3.5.2 Output power efficiency

One of the main interests of planar microcavities is the possibility of controlling the emission properties of the embedded active material. The figure of merit to quantify the efficiency of such lasing device with a small active volume is the fraction of spontaneous emission coupled to the cavity mode (β). However, the requirements to reach the nonlinear threshold are different depending whether the structure operates in the strong (polariton laser) coupling regime or not (VCSEL).

In VCSELs only the cavity mode lies within the emission bandwidth. In such a case, the number of photons leaking through the cavity mode starts to increase only when stimulated emission is triggered. In the pathologic case where $\beta = 1$, i.e., all the photons spontaneously leak out through the cavity mode, the laser becomes thresholdless and the input-output emission curve does not show any threshold behavior [109, 225] (dashed line in Fig. 3.34(a)). The fraction of light coupled to the cavity mode in a planar microcavity is usually obtained by fitting the output integrated intensity as a function of the pump power $I_{\text{output}}(r)$ given by the solution of the standard rate equation model [226]:

$$I_{\text{output}}(r) \propto r - \sqrt{(r-1)^2 + 4\beta r}, \tag{3.20}$$

where $r = I_{\text{input}}/I_{\text{thr}}$ and I_{thr} is the pump density at threshold.

Let us now turn our attention to the specific case of polariton lasers. Equation 3.20 does not exactly hold due to the different nature of the amplification process, which results from the stimulated scattering of

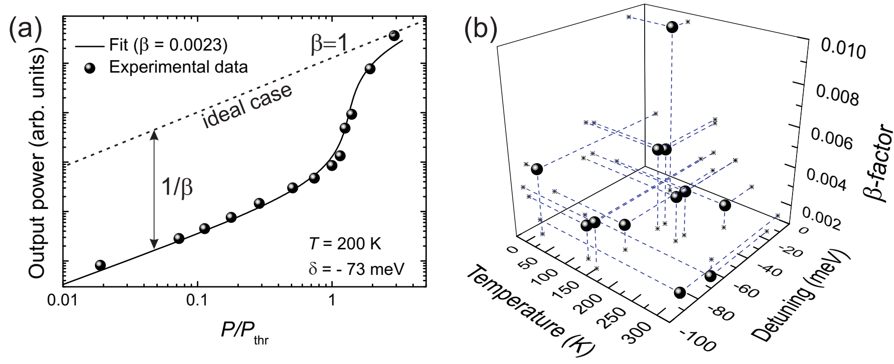

Fig. 3.34: (a) Output vs. input optical power measured for $\delta = -73\,\text{meV}$ and $T = 200\,\text{K}$ featuring a β-value equal to 0.0023. The continuous dashed line corresponds to the ideal case $\beta = 1$. (b) Evolution of the β-factor for different temperatures and detunings in the present microcavity.

polaritons from the exciton reservoir to the bottom of the lower polariton branch and the subsequent spontaneous radiative decay of the polariton condensate. Far below the condensation threshold, the polariton relaxation is mainly governed by acoustic phonon emission and the output power linearly scales with the injected carrier density. When further increasing the excitation power density, the relaxation becomes dominated by pair scattering, which quadratically scales with the input power. For $P \approx P_{\text{thr}}$, the polariton relaxation suddenly switches from the spontaneous to the stimulated scattering regime resulting in an exponential increase in the output power. Far above the condensation threshold, the system relaxation is ruled by stimulated scattering only and the output power P_{out} linearly scales with the pump density. Even if VCSELs and polariton lasers are driven by different physical processes, they share very similar rate equations [14] and equation 3.20 can also be used to extract the β-factor [227]. Note that the interpretation is slightly different in the case of polariton lasers as it corresponds to the probability, that spontaneously emitted polaritons emerge in the mode which undergoes stimulated scattering [33].

In Fig. 3.34(a), a typical output power curve is shown for the present multiple quantum well GaN-based microcavity under quasi-cw nonresonant optical pumping for $\delta = -73\,\text{meV}$ and $T = 200\,\text{K}$. Such measurements were repeated for different values of the detuning and lattice temperature in order to analyze the evolution of β. From Fig. 3.34(b), it appears that the highest β-factors are obtained for low-temperature operation for the less negative detuning values. The maximum value $\beta_{\text{max}} \approx 0.1$ is obtained for $T = 80\,\text{K}$ and $\delta = -13\,\text{meV}$. The temperature dependence is likely related to the higher quantum efficiency of the quantum well exciton at low temperature and also to the fact that the thermodynamic threshold is lower at low temperatures [228]. The detuning dependence is more difficult to understand and is likely related to the decrease in the polariton condensation threshold for exciton-like polaritons.[44] Further characterization and a convenient modeling are therefore required to get a better understanding of the behavior of β with detuning and lattice temperature. The relation between β and the threshold power density P_{thr} can be modeled by the expression [76]:

$$P_{\text{thr}} \approx E_{\text{LPB}}(k_{\parallel} = 0) V \Gamma_{\text{nrad}} \frac{\Gamma_0}{c}, \tag{3.21}$$

[44] See Chapter 4 for a detailed analysis of the relation between P_{thr} and both detuning and temperature.

where V is the mode volume, Γ_0 is the radiative decay rate of the polariton condensate and $\Gamma_{nrad} = \frac{1}{\tau_X^{NR}} + (1-\beta)\Gamma_{sp}$ is the non radiative decay rate and Γ_{sp} is the spontaneous emission rate. Expression 3.21 shows that the threshold is minimum for large β values. Even in the limit case where $\beta = 1$, it appears that the threshold is still limited by the non-radiative lifetime of the excitonic transition. As a consequence, polariton lasers could be thresholdless only in the limit $\tau_X^{NR} \to \infty$ and $\beta \to 1$.

3.5.3 Kinetically driven polariton condensation

In Figs. 3.32(a)-3.32(f) polariton condensation in real and momentum spaces was shown at ambient conditions. Due to the important interactions with optical and acoustic phonons, the polariton gas reaches quasi-thermal equilibrium even for large negative δ-values and the condensate is formed at the bottom of the lower polariton branch. When the interactions between polaritons and their environment is too weak, the system is not able to reach a well defined effective temperature and the polariton condensate formation is governed by the relaxation kinetics [56, 229] (see Chapter 4 for more details). In Fig. 3.35, a power series performed at 4 K under quasi-cw nonresonant excitation is shown for different pump powers on a sample region with $\delta \approx -75$ meV at 4 K.

In these conditions, the low photonic content associated with the low lattice temperature prevents the system from reaching a thermal distribution. The non-equilibrium nature of the polariton gas is clearly visible through the luminescence from the bottleneck region, which is dominating the far field up to $P = P_{thr} \approx 5\text{W/cm}^2$ (see Fig. 3.35(a)) and is still visible for the highest pump powers used. The steady state does not correspond to a thermal state but is the result of the imbalance between the incoming rate from the exciton reservoir and the various losses in the system for each $k_\parallel$-states [216]. Even when the power density is increased up to $67P_{thr}$, the nonlinear emission occurs below the uncoupled cavity mode ensuring that the system still operates in the strong coupling regime. It is also worth pointing out that the change in the cavity mode position due to Kerr-effect is negligible, i.e., $\Delta n_{cav}/n_{cav} \approx 10^{-8}$ for a power-density of 1000W/cm^2 [230].[45] Note that the exciton energy is indicated at a constant position on the graphs even if it is expected to blueshift when increasing the injected carrier density. The reason is that at such large negative detunings, it only marginally impacts on the polariton ground state energy.

[45] Even when considering the peak power density when using the quasi-cw Nd:YAG laser with the UV microscope objective, $\Delta n_{cav}/n_{cav}$ does not induce cavity mode energy shift is not larger than $0.1-1$ meV.

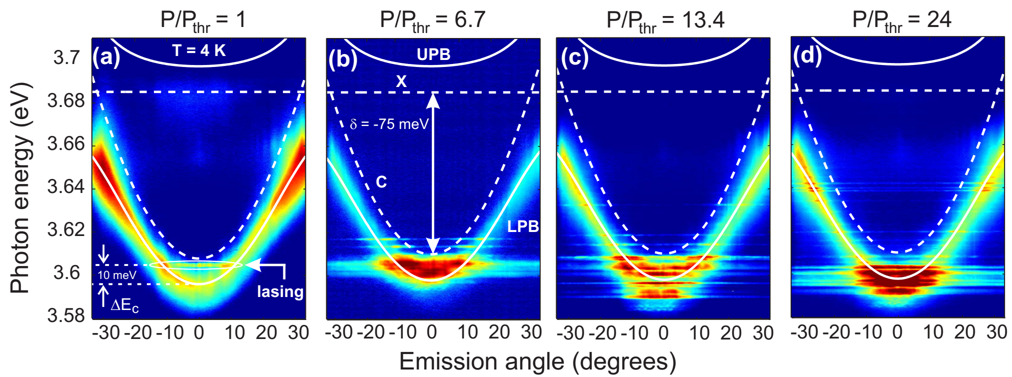

Fig. 3.35: Far-field emission pattern measured at 4 K under quasi-cw nonresonant excitation for $\delta \approx -75$ meV for different pump powers: (a) $P/P_{thr} = 1$ (b) $P/P_{thr} = 6.7$ (c) $P/P_{thr} = 13.4$ and (d) $P/P_{thr} = 24$.

More interesting is the absence of decrease in the Rabi splitting, which is likely due to the clamping of the reservoir density above the condensation threshold (see Section 3.4.3).

Polariton condensation does not occur at the system ground state energy at $P = P_{\text{thr}}$ (see Fig. 3.35(a)), but with an excess of kinetic energy $\Delta E_c = E_c - E^0_{\text{LPB}} \approx 10\,\text{meV}$, where E_c is the energy of the condensate. This singular behavior might come from the fact that the occupation factor first becomes larger than unity in excited states, which triggers stimulated scattering for states with $k_\parallel \neq 0$. Even if this assertion can look surprising in the frame of the thermodynamical phase transition originally proposed by Einstein, the generalization of BEC for open systems and in particular for the out-of-equilibrium polariton ensemble is compatible with polariton condensation occuring in excited states [231]. This behavior is thus not necessarily attributed to disorder and it is also observed in GaAs-based planar microcavities where the in-plane potential landscape is smooth compared to III-nitrides [202, 211].

The dispersion curves displayed in Figs. 3.35(a)-3.35(d) present several interesting features: (i) a non-linear emission for $k_\parallel \neq 0$ and $E_c > E^0_{\text{LPB}}$, (ii) the appearance of extra lasing modes along the lower polariton dispersion with increasing power densities and (iii) the appearance of lasing modes with $E_c < E^0_{\text{LPB}}$. These effects can be understood by considering the out-of-equilibrium nature of the condensates, the interactions occurring in the condensates revealed by the slight blueshift of the emission energy, the finite size of the excitation spot and finally the important static disorder. Let us now have a look at the impact of each of these effects by starting with the description of a homogeneous system and adding successively the impact of each contribution on the polariton dynamics, following the theory described in Ref. [216].

3.5.3.1 Polariton condensation in a homogeneous system under homogeneous excitation

In a spatially homogeneous system pumped with a uniform nonresonant excitation spot, the polariton condensate wave function is found to be zero for $P < P_{\text{thr}}$ while the exciton density in the reservoir grows linearly, i.e., $n_X = P/\gamma_X$, where γ_X is the effective relaxation decay rate of the excitons. For $P = P_{\text{thr}}$, the stimulated incoming rate from the reservoir into the polariton condensate balances the system losses and for $P > P_{\text{thr}}$, n_X is clamped at its threshold value while the condensate density linearly grows with the pump density, i.e., $n_0 = (P - P_{\text{thr}})/\gamma_C$ [216]. In this simplified case, the direction of the condensate wave vector $\mathbf{k}_c$ is undefined as it is defined by the pumping conditions and interactions, but its norm is fixed by the kinetic energy excess ΔE_c *via*:

$$\Delta E_c = \frac{\hbar^2 k_c^2}{2m_{\text{LPB}}} + \hbar\alpha n_0 + \hbar\alpha_X n_X + \hbar g P, \tag{3.22}$$

where m_{LPB} is the lower polariton effective mass, $n_0 = |\psi_0|^2$ is the polariton condensate density, $\frac{\hbar^2 k_c^2}{2m_{\text{LPB}}}$ is the condensate kinetic energy, $\Delta E_c = \hbar\alpha_X n_X$ is the renormalization of the condensate energy due to interactions with the excitonic reservoir and $\hbar g P$ is the renormalization of the condensate energy induced by the homogeneous pump power density P and characterized by the constant g. Expression 3.22 indicates that the excess energy given to the polariton ground state is transformed into kinetic energy, which results in a non-zero condensate wave vector $\mathbf{k}_c$. In principle this theory does not strictly apply for real structures where disorder-induced localization and short polariton lifetimes prevent the observation of long-range spatial coherence. However, the recent observation of expansion of polariton condensates governed by the repulsive potential induced by photogenerated excitons over the excitation spot has been reported in a one-dimensional GaAs microwires [232].

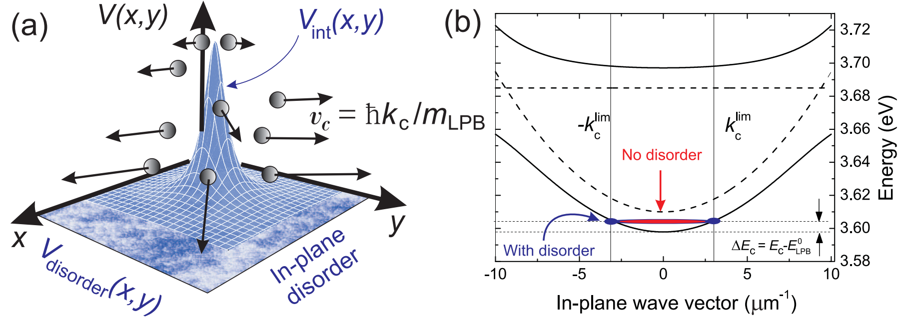

Fig. 3.36: (a) In-plane potential profile seen by the polariton $V(x,y)$, which is the sum of the in-plane static disorder $V_{\mathrm{disorder}}(x,y)$ and pump-induced blueshift acting as a repulsive potential $V_{\mathrm{int}}(x,y)$. Polaritons are ballistically expelled from the high density area with a velocity $v_{\mathrm{c}} = \hbar / k_{\mathrm{c}} m_{\mathrm{LPB}}$. (b) Representation of the polariton condensate energy and wave vector with and without disorder.

3.5.3.2 Polariton condensation in a homogeneous system with an inhomogeneous excitation

The previous model cannot apply to our measurements due to the inhomogeneous spot profile used in our experiments. In the case of an excitation spot with a finite size and a Gaussian profile, the pump term P, the polariton condensate and reservoir densities in equation 3.22 will now depend on the in-plane position $\mathbf{r}$ while the condensate energy remains constant in space. Assuming that the spot size is much smaller than the lateral extension of disorder, an analytical solution is found for $\mathbf{k}_{\mathrm{c}}$ in the case of a Gaussian beam. The important repulsive interactions create in fact an antitrapping potential $V_{\mathrm{int}}(\mathbf{r})$ for the polaritons [216] (see Fig. 3.36(a)):

$$V_{\mathrm{int}}(\mathbf{r}) = \hbar\alpha n_0(\mathbf{r}) + \hbar\alpha_{\mathrm{X}} n_{\mathrm{X}}(\mathbf{r}) + \hbar g P(\mathbf{r}) \,. \tag{3.23}$$

The blueshift of the condensate thus acts as a quantum pressure: polaritons convert the resulting potential energy $V_{\mathrm{int}}(\mathbf{r})$ into kinetic energy. As a result, polaritons are accelerated up to a velocity $v_{\mathrm{c}} = \hbar / k_{\mathrm{c}} m_{\mathrm{LPB}}$. This ballistic propagation induced by the pump is traduced in the dispersion curve by the appearance of nonlinear emission occurring at non-zero in-plane momenta for $-k_{\mathrm{c}}^{\mathrm{lim}} < k_{\parallel} < k_{\mathrm{c}}^{\mathrm{lim}}$ (see red shape in Fig. 3.36(b)), where $k_{\mathrm{c}}^{\mathrm{lim}} \neq 0$ corresponds to the free particle dispersion.

3.5.3.3 Polariton condensation in a disordered system with an inhomogeneous excitation and a finite spot size

Even if the model presented before accounts for the observation of condensation at energies higher than the ground state for $k_{\parallel}$-vectors comprised between $-k_{\mathrm{c}}^{\mathrm{lim}}$ and $k_{\mathrm{c}}^{\mathrm{lim}}$, the emission is centered at $k_{\parallel} = 0$, which does not correspond to our observations (see Figs. 3.35(a)-3.35(d)). Wouters and coworkers have shown that when introducing a disordered in-plane potential profile $V_{\mathrm{disorder}}(\mathbf{r})$ in the generalized Gross-Pitaevskii equation, weak narrow peaks with $k \neq 0$ appear on top of the regular background [216] (blue dots in Fig. 3.36(b)). They explain this behavior in terms of constructive interferences arising from localized and mutually coherent condensates. However, in our microcavity, we collect nearly no luminescence around $k_{\parallel} = 0$ and the condensate emission is peaked at $(E,k) = (E_{\mathrm{c}}, \pm k_{\mathrm{c}}^{\mathrm{lim}})$. In addition, the important static disorder present in III-nitride based microcavities is not consistent with the appearance of mutual coherence between localized condensates. The impact of the finite spot size should be included to explain our observations. In our measurements, we use a microscope

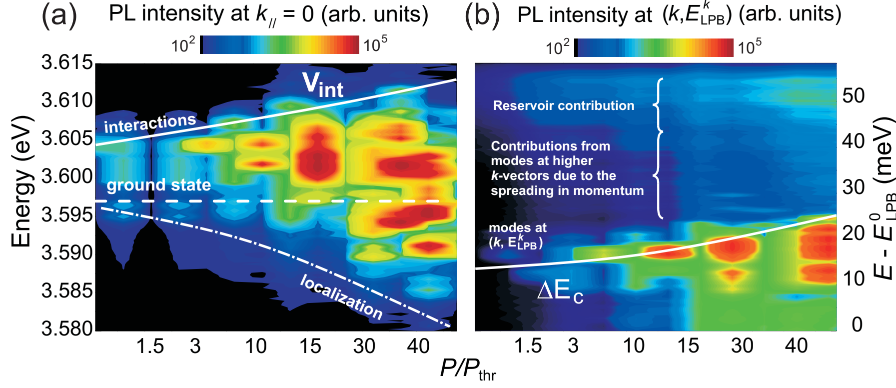

Fig. 3.37: Evolution of the polariton condensate photoluminescence intensity at 4 K under quasi-cw nonresonant excitation for $\delta \approx -75$ meV for normalized pump power densities ranging from 1 to $67P_{\mathrm{thr}}$ (a) at $k_{\parallel} = 0$ and (b) along the dispersion curve, i.e., at $(k_{\parallel}, E_{\mathrm{LPB}}(k_{\parallel}))$. For both figures the color scale is logarithmic.

objective with a high numerical aperture (N.A. = 0.55), which implies a small spot size of the order of 5 μm. The propagation length of polaritons might become smaller than the pumped area and most of the polaritons ballistically expelled due to the strong antitrapping potential are found outside the excitation area. In this case the far-field emission pattern in k-space concentrates on a ring of radius $k_{\mathrm{c}}^{\mathrm{lim}}$. The resulting energy dispersion is thus sharply peaked at $(E, k) = (E_{\mathrm{c}}, k_{\mathrm{c}}^{\mathrm{lim}})$ as in our measurements. Richard and coworkers have shown that when increasing the pump spot, the formation of the polariton condensate at $k_{\parallel} = 0$ is recovered [222].

In Fig. 3.37(a), the energy profile at $k_{\parallel} = 0$ is displayed for normalized pump power densities ranging from P_{thr} to $67P_{\mathrm{thr}}$. The position of the polariton ground state at $P = P_{\mathrm{thr}}$ is indicated by a horizontal dashed line. In addition to the multi-mode emission, other striking features are visible. First, when the injected carrier density is increased, the condensate energy globally shifts to higher energies by approximately 10 – 15 meV (continuous line in Fig. 3.37(a)) due to polariton-polariton interactions occurring in the condensates. This pump-induced blueshift can be identified with the antitrapping potential V_{int}. In Fig. 3.37(b), the photoluminescence intensity along the lower polariton branch is reported as a function of the energy relative to the ground state ($\Delta E = E^{\mathrm{k}}_{\mathrm{LPB}} - E^{0}_{\mathrm{LPB}}$) for different pump powers extracted from the same data as for Figs. 3.35(a)-3.35(d) and 3.37(b). The continuous line corresponds thus to the excess of kinetic energy of the polariton condensate ΔE_{c} vs. excitation power and increases from 11.5 to 24 meV over the investigated power range. This increase in ΔE_{c} corresponds to a variation of the critical wave vector $k_{\mathrm{c}}^{\mathrm{lim}}$ from 4 to 5.8 μm^{-1}. Interestingly, the increase in kinetic energy of the polariton condensate corresponds to an increase in V_{int} over the same power range (continuous line shown in Fig. 3.37(a)), indicating the conversion of the pump-induced blueshift into kinetic energy. Such ballistic propagation of polariton condensates was recently claimed in a ZnO-based bulk microcavity presenting an important static disorder [233].

We can thus reasonably assume that the polariton motion is ballistic and deduce the radial velocity of polaritons $v_{\mathrm{c}} = \hbar k_{\mathrm{c}}^{\mathrm{lim}} / m_{\mathrm{pol}}$, which varies from 9.3×10^{6} to 1.3×10^{7} m/s between the lowest and the highest pump power density. The corresponding propagation length L_{prop} out of the pump area is directly given by the polariton condensate decay rate γ_{pol} according to the relation $L_{\mathrm{prop}} = 2v_{\mathrm{c}}/\gamma_{\mathrm{pol}}$. Considering the very negative value of the detuning ($\delta = -75$ meV), γ_{pol} is approximately given by the inverse of the cavity photon lifetime, i.e., $\gamma_{\mathrm{pol}} \approx 1/\tau_{\mathrm{C}} \approx 5.5 \times 10^{12}$ ps^{-1}. At the condensation threshold,

the propagation length amounts thus to 3.4 μm and increases up to 5 μm at the highest power used. The radius of the condensate is thus increased by 1.6 μm over the power range investigated. Another interesting feature visible in Fig. 3.37(a) is the redshift of the nonlinear emission at low energy (dash-dotted line shown). This redshift, $\Delta E \approx -12$ meV, can be qualitatively understood by considering the increase in the penetration length in the radial direction. Polaritons propagate further and further when the excitation power is increased and can probe a wider sample area before getting localized in regions with a lower potential energy. As the scale of disorder in our sample roughly corresponds to the spot area, polaritons will experience regions with energy fluctuations mainly given by the photonic disorder. This point is consistent with the fact that the redshift is comparable with the photonic inhomogeneous broadening ($\Gamma_C^{inh} \approx 15$ meV) and indicates that the polariton condensates localize in potential minima set by the in-plane disorder profile.

4 Polariton condensation phase diagram

As polaritons are half-light, half-matter particles, the mechanisms leading to the nonlinear threshold are totally different from those of a conventional semiconductor laser. In particular, the possibility to tune the interactions in the system by changing the photonic fraction of the polaritons or the lattice temperature allows discriminating between different relaxation regimes. The condensation can be governed either by the kinetics or by the thermodynamics depending on the strength of the interactions. In this chapter, a comprehensive picture of the polariton phase diagram is presented for the c-plane GaN microcavity investigated so far and the optimum condition to achieve polariton lasing is derived.

4.1 Introduction

Contrary to the bulk case, polaritons in quantum well-based microcavities have a well defined energy minimum at $k_{\|} = 0$, suggesting the possibility of achieving a BEC-like phase transition (see Section 1.4). Furthermore, the extremely low effective mass of lower polaritons in the center of the Brillouin zone should lead to pretty high condensation temperatures according to relation 1.77. However, the bidimensional character of microcavity polaritons prevents the observation of a true BEC phase transition at any non-zero temperature [128]. Instead, local condensation or a Berezinsky-Kosterlitz-Thouless (BKT) phase transition is allowed [234–236].

In Fig. 4.1, the polariton phase diagram is displayed for a CdTe-based microcavity containing 16 quantum wells at zero exciton-cavity photon detuning [237]. Four different regions are visible, depending on the lattice temperature and the polariton density in the system. The critical temperature T_X^{diss} and the density $n_{\mathrm{pol}}^{\mathrm{sat}}$ represented by vertical and horizontal dashed lines indicate the loss of the polariton character due to exciton thermal dissociation and exciton bleaching, respectively. Above these values, the electronic population is dominated by a degenerate electron-hole plasma and the laser phase transition is ruled by the Bernard-Durrafourg condition [238]. Note that this description considers an abrupt Mott transition and not a continuous one. A more correct description should thus account for the progressive loss of the excitonic behavior. In addition, the strong coupling regime is likely lost before the excitonic dissociation due to the progressive saturation of the exciton transition. The origin of the phase transition in a system operating in the weak coupling regime with $T < T_X^{\mathrm{diss}}$ and density $n_{\mathrm{pol}} < n_{\mathrm{pol}}^{\mathrm{sat}}$ should therefore be addressed (see Section 4.1.1).

The lower continuous line in Fig. 4.1 shows the evolution of the polariton critical density n_c as a function of temperature for the transition between an incoherent polariton phase and a coherent condensed

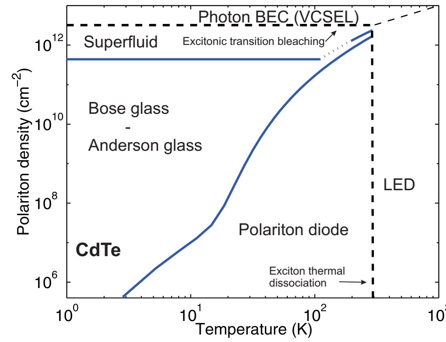

Fig. 4.1: Phase diagram of a CdTe-based microcavity containing 16 quantum wells at zero detuning derived from the thermodynamic model. The lower and upper solid lines show the critical polariton density n_c as a function of temperature for the transition from an incoherent population to a condensed phase and from a condensed to a superfluid phase, respectively. The term LED should refer to an electrical injection scheme but the present phase diagram is also valid in the case of optical pumping. Vertical and horizontal dashed lines set an upper limit for the loss of the strong coupling regime defined by the exciton thermal dissociation and screening, respectively. Adapted from Ref. [237].

one. Despite the short radiative lifetime of cavity polaritons, stimulated scattering as well as quasi-thermal equilibrium have been demonstrated in various semiconductor systems [18, 33, 215]. Under such conditions, the system is expected to exhibit a BKT transition toward a superfluid phase [234–236] with critical temperatures exceeding ambient ones for wide band gap semiconductor materials [239]. However, experimental observations indicate that the in-plane disorder induces a localization of the condensate in the minima of the disorder potential instead [222]. Depending on the interplay between hopping, nonlinear interactions and disorder, this insulating phase is called a Bose-glass (strong-interaction regime) or an Anderson-glass (weak interaction regime) [240]. It is usually assumed that an ensemble of polaritons behaves as a weakly interacting Bose gas as it operates in the low density regime. The associated phase transition thus corresponds to an Anderson-glass where interactions compete with disorder and can lead to delocalization and percolation of the localized condensates toward a superfluid phase (upper continuous line in Fig. 4.1) [237, 240]. Such a situation cannot be presently avoided in III-nitride based samples, which exhibit strong in-plane spatial photonic disorder [65].

4.1.1 Phase transition in the weak coupling regime

When the system switches from the nonperturbative to the perturbative regime, the excitonic transition is not necessarily bleached. One should thus consider two distinct cases. First, when the carrier density exceeds the saturation concentration n_X^{sat}, the system is properly described in terms of uncorrelated electrons and holes and the physics of conventional semiconductor lasers applies. In the case of planar microcavities, the system exactly behaves like a VCSEL, once the modal gain compensates for the system losses. Below the Mott transition, the situation is more complicated and one should account for the possibility of observing gain of excitonic origin.

4.1.1.1 Lasing from a degenerate electron-hole plasma in a 2D-system

In a conventional semiconductor laser, the material gain reads:

$$g(E) = \alpha_{2D}\left(f_c(E) - f_v(E)\right), \tag{4.1}$$

where α_{2D} is the quantum well absorption at thermal equilibrium. The gain expressed by relation 4.1 becomes positive only when the difference between the electron and hole distributions becomes positive. This condition is equivalent to the population inversion condition in an atomic laser and is usually formulated *via* the so-called Bernard-Durrafourg condition transposed to the 2D-case[238]:

$$E_1 + HH_1 \leq \hbar\omega \leq E_{F_c} - E_{F_v}, \tag{4.2}$$

where E_1 and HH_1 correspond to the energies of the first electron and heavy hole subbands, respectively.[46] This condition expresses that only photons with an energy comprised between the confined levels and the energy difference between the quasi Fermi-levels for the electrons and the holes (E_{F_c} and E_{F_v}, respectively) can be amplified. It is fulfilled only above a given concentration n_{tr}, which corresponds to the transparency threshold where the active material no longer absorbs photons with $E \leq E_1 + HH_1$. n_{tr} is thus given by the condition $E_{F_c}(n_{tr}, T) - E_{F_v}(n_{tr}, T) = E_1 + HH_1$. The position of the quasi-Fermi levels depends on the carrier density n and on the temperature *via* the relations:

$$E_{F_c}(n, T) = E_G + E_1 + k_B T \ln\left(\exp\left(\frac{n}{\rho_c^{2D} k_B T}\right) - 1\right), \tag{4.3}$$

$$E_{F_v}(p, T) = -HH_1 - k_B T \ln\left(\exp\left(\frac{n}{\rho_v^{2D} k_B T}\right) - 1\right), \tag{4.4}$$

where $\rho_{c,v}^{2D} = \frac{m_{c,v}^*}{\pi\hbar^2}$ is the 2D-density of states of the conduction and valence bands and m_c^* and m_v^* are the effective masses of the electron and the hole, respectively. For a GaAs and a GaN-based laser structure operating at room temperature, the calculated transparency carrier densities are $1.14 \times 10^{12}\,\text{cm}^{-2}$ and $3.15 \times 10^{12}\,\text{cm}^{-2}$, respectively. The difference between these two systems is due to the large effective masses of wide band gap semiconductors, which intrinsically limits the threshold of short wavelength laser diodes. Note that the obtained transparency concentrations are higher than the Mott density in the considered systems indicating that conventional lasing from a degenerate electron-hole plasma can only occur above the Mott transition.

The lasing oscillation only occurs when the modal gain Γg exceeds the system losses, which necessarily occurs for carrier densities higher than n_{tr}. In a semiconductor laser, the losses can be accounted for by two contributions: the mirror, whose contribution is given by relation 1.36 and the cavity, which is usually described by a constant value α_c (including absorption, scattering, etc.). The lasing condition finally reads:

$$\Gamma g > \alpha_c + \frac{1}{2L_{eff}} \ln\left(\frac{1}{R_1 R_2}\right). \tag{4.5}$$

Note that contrary to the bulk case, the gain is reduced by the confinement factor Γ, which corresponds to the overlap between the electric field along the growth direction and the gain medium [15].

[46] Note that the energies E_1 and HH_1 are measured from the top of the valence band.

4.1.1.2 Lasing below the Mott density in the weak coupling regime

Below the Mott density, the electronic population is dominated by excitons for $T < T_X^{diss}$. However, in a homogeneously broadened excitonic system, population inversion cannot be achieved without bleaching the resonance as it consists of a two-level system [85]. As a consequence, excitonic lasing is only possible if another mechanism is involved such as a biexcitonic [241] or phonon-assisted transition [242], bosonic condensation of excitons [243], inelastic exciton-exciton scattering [244] or the presence of exciton localized states [245]. Considering the relatively important disorder present in III-nitride systems, the physical mechanism for gain involving localized excitons is the most probable.

A simplified model consists in assimilating the inhomogeneously broadened transition with a multilevel system where the initially excited free excitons having a 2D-density of states efficiently relax toward more localized states [246] (see Fig. 4.2(b)). Gain is then possible by the induced emission between X_{loc} and the crystal ground state and is triggered when the transparency condition is reached, i.e., when the absorption of the localized states is saturated. Such lasing mechanism is expected to exhibit a lower threshold compared to a conventional laser as it relies on a reduced density of localized states and is expected to strongly depend on the local potential disorder profile. Assuming that a given localization site can be occupied by one exciton only, the population inversion condition reads [246]:

$$f_X - (1 - f_X) = 2f_X - 1 > 0, \tag{4.6}$$

where f_X is the probability for a localized state to be occupied and correspond to the Fermi-Dirac statistics, i.e. one exciton per localization center. Note that the assumption of a single exciton per site implies an infinitely large repulsive exchange interaction between two localized excitons. A better description should include the spin degree of freedom and the possibility of biexciton formation [241]. In this simplified model, the gain coefficient can then be expressed as:

$$g(E) = \int_{-\infty}^{+\infty} L_{inh}(E') L_h(E - E') \left(\frac{2}{e^{(E'-\mu)/k_B T} + 1} - 1 \right) dE', \tag{4.7}$$

where $L_h(E)$ and $L_{inh}(E)$ are the homogeneous and inhomogeneous line shape function, respectively. $L_{inh}(E)$ characterizes the in-plane disorder potential and reflects the nature of the localized states.

In Figs. 4.2(a) and (b), schematic representations of conventional lasing and excitonic lasing relying on localized states are shown, highlighting the different nature of the energy levels. In Fig. 4.2 (c), the

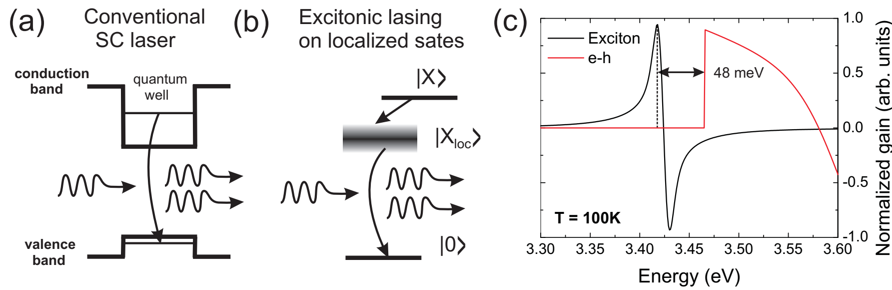

Fig. 4.2: Schematic representation of (a) conventional lasing and (b) excitonic lasing relying on localized states in a nonpolar GaN quantum well. (c) Calculated normalized gain at 100 K for a GaN quantum well in the case where the gain is provided either by an inverted electron-hole plasma (red curve) or localized excitons (black curve).

normalized gain at 100 K using relations 4.1 and 4.7 in the case of a GaN quantum well in the case where the gain is provided either by an inverted electron-hole plasma (red curve) or localized excitons (black curve). The considered confinement energy for electrons and holes are 20 and 5 meV. In the case of conventional lasing, a carrier density of $10^{13}\,\mathrm{cm}^{-2}$ is assumed for the calculation of the quasi Fermi-levels and in the case of excitonic lasing, a binding energy of 40 meV, a homogeneous linewidth of 15 meV and an inhomogeneous one of 20 meV are assumed. Interestingly, the maximum of gain in the excitonic case occurs approximately 50 meV below the maximum gain in the conventional case. For larger inhomogeneous broadenings, this value further increases as lasing originates from deeper levels.

4.1.2 Phase transition in the strong coupling regime

The nature of the transition from the incoherent uncondensed phase (incoherent polariton emission or polariton LED) to the condensed one (Anderson-glass) strongly depends on how far the system is from thermodynamic equilibrium. In the thermodynamic limit, i.e. assuming an infinite polariton lifetime, the system can reach thermal equilibrium with the lattice with $T_{\mathrm{eff}} = T_{\mathrm{latt}}$, where T_{eff} is the effective polariton temperature and T_{latt} is the lattice temperature. In this situation, the transition is conveniently described by the Bose-Einstein theory and the associated phase transition is referred to as *polariton BEC*. Conversely, when the short lifetime of polaritons is considered, the polariton kinetics might not be sufficient to bring the polariton population to thermal equilibrium with the lattice. In this case, two situations should be distinguished. First, if the kinetics is fast enough, the polariton distribution might still reach a quasi-equilibrium situation defined by an effective temperature higher than that of the lattice, i.e. $T_{\mathrm{eff}} > T_{\mathrm{latt}}$ [229]. In this case, an effective temperature is found both below and above the condensation threshold and the thermodynamic theory is still valid. The second situation occurs when the kinetics is not sufficient to bring the polariton gas to a quasi-equilibrium state. In this situation, no effective temperature can be defined (neither below nor above the condensation threshold) and the condensate formation is governed by the system kinetics only. In both cases, the transition is indifferently called a *polariton condensate* or a *polariton laser*.[47] The term polariton BEC exclusively applies to the thermodynamic limit.

The nature of the phase transition in a weakly interacting polariton system depends on (i) the efficiency of the relaxation channels, which allows for the thermalization of the polariton ensemble and on (ii) the polariton lifetime, which sets the limit to reach thermal equilibrium. A clear and complete description of these phenomena thus requires a careful study of these two quantities, which critically depend on the temperature and on the detuning. In the forthcoming chapter the phase diagram, i.e., the evolution of the polariton condensation threshold power density P_{thr} as a function of the independently tunable parameters δ and T will be presented and discussed for the multiple quantum well GaN-based microcavity introduced in the previous chapter. P_{thr} will be shown to be either governed by the carrier relaxation kinetics or by the thermodynamics depending on the set of δ and T values investigated. At this stage it is worth pointing out that a polariton BEC does not correspond to a BEC in the classical sense: polaritons rely on the strong coupling between photons and electronic excitations in the solid state and are thus short-lived quasi-particles. This means that the condensate has to be continuously pumped to compensate for losses and as such it represents an intrinsically open system. Nevertheless, both phenomena share numerous essential characteristics leading to the denomination *non-equilibrium BEC* for exciton-polaritons [247].

[47] The term polariton laser was first introduced in 1996 by Imamoğlu and coworkers [5], who suggested the use of stimulated scattering in a polariton gas and its subsequent radiative decay as a mechanism for novel coherent light emitters.

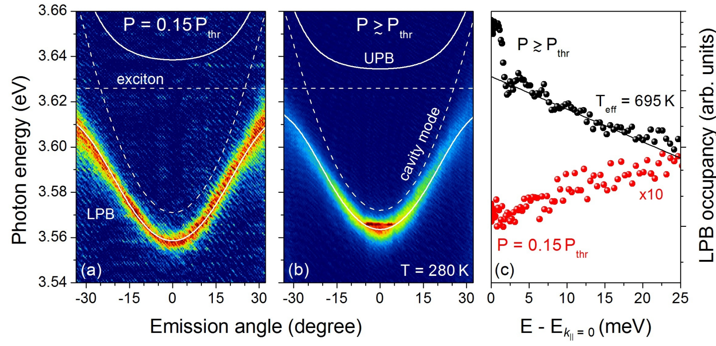

Fig. 4.3: Polariton far-field emission spectra measured at 280 K (a) far below and (b) slightly above the threshold pumping power (P_{thr}), respectively. The macroscopic occupancy of the ground state is clearly seen at threshold and is associated with a blueshift of about 4.8 meV ($\delta \approx -56$ meV). (c) The deduced LPB occupancy shows the transition from a non-thermal distribution below threshold, i.e., a relaxation bottleneck is present [101], to a thermal one above.

Typical far-field emission spectra of the present microcavity measured at 280 K are shown in Fig. 4.3. Far below the condensation threshold the lower polariton branch occupancy clearly appears non-thermal. With increasing polariton density relaxation toward the ground state becomes more efficient resulting in a thermal carrier distribution when approaching P_{thr}. Note that for the transition region between both regimes the effective polariton temperature T_{eff} does not necessarily have to coincide with the lattice one and commonly exceeds the latter. In this specific case, i.e. $\delta = -56$ meV and $T_{\text{latt}} = 280$ K, the relaxation processes are efficient enough to bring the polariton population in a thermalized state below and above the condensation threshold indicating that the Bose-Einstein description applies. However, this situation critically depends on the relaxation efficiency *via* δ and T_{latt}. One of the goals of the present chapter will therefore consist in quantifying the thermalization process to check for which system configuration a thermodynamic picture could apply to the polariton condensate.

4.2 Specificities of GaN-based microcavities

The first demonstration of polariton lasing [33] and BEC of exciton-polaritons [52] at room temperature was achieved in a bulk GaN-based microcavity. However, since the device operating temperatures are often exceeding the ambient one, a structure relying on a bulk GaN layer looks hardly probable considering the bulk exciton binding energy $E_X^b \approx 25$ meV. This intrinsic limitation can be effectively overcome by switching to appropriate multiple quantum well-based active regions. Quantum confinement enhances the exciton oscillator strength and the robustness of excitons: E_b^X values of up to 50 meV have been obtained [53]. This approach also induces a reduction in the critical density for condensation n_c by at least one order of magnitude [54] and the observation of polariton condensation over a wider range of detunings δ and temperatures T [55, 56]. In the present sample, polariton condensation was observed for detunings spanning from −150 meV to 0 meV in the 4 − 340 K temperature range [55, 56]. The large tunability of the detuning is made possible by the local fluctuations of the effective cavity length. By moving the characterization spot along this wedge, the cavity mode position can be changed. Note that the range of accessible δ-values directly scales with Ω_{VRS} and corresponds to polariton states with a non-negligible excitonic or photonic fraction, i.e., $|\delta| < \Omega_{\text{VRS}}$,[48] which explains why wide band

[48] Note that this criterion sets an arbitrary frontier and the excitonic fraction at $k_\parallel = 0$ corresponds to 15% for $\delta/\Omega_{\text{VRS}} = -1$ and 85% for $\delta/\Omega_{\text{VRS}} = 1$. For $|\delta|/\Omega_{\text{VRS}} = 2$, these ratios still amount to 5 and 95%, respectively.

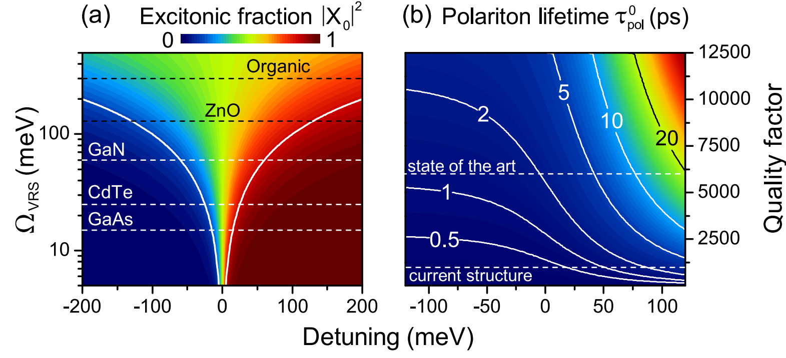

Fig. 4.4: (a) Excitonic fraction at $k_\parallel = 0$ as a function of δ and vacuum Rabi splitting Ω_{VRS}. The horizontal dashed lines represent the state-of-the art for different planar microcavities. The continuous white lines are defined by the condition $\delta = \pm\Omega_{\text{VRS}}$ and set the range where the polaritons significantly depart from the bare modes. (b) Polariton lifetime at $k_\parallel = 0$ as a function of the microcavity quality factor and the exciton cavity-photon detuning δ calculated for a GaN quantum well-based planar semiconductor microcavity operating in the strong coupling regime with an exciton transition at 3.65 eV at room temperature and $\Omega_{\text{VRS}} = 60$ meV. The horizontal dashed lines illustrate the state of the art for hybrid microcavities [248] and the sample investigated here, respectively.

gap semiconductors cover such a wide range of detunings. The situation is illustrated in Fig. 4.4(a) for the case of GaAs, CdTe and GaN quantum well-based structures (white dashed lines) together with bulk ZnO and organic microcavities (black dashed lines). The main limitation preventing the thermalization of the polariton population is the decrease in the lower polariton lifetime $\tau_{\text{LPB}} \sim \hbar/\gamma_{\text{LPB}}$ close to the center of the Brillouin zone. For the achievement of a thermal carrier distribution and thus to minimize P_{thr} the relaxation bottleneck has to be overcome, which directly implies a relaxation timescale τ_{rel} smaller or at least comparable to the mean lifetime of the polariton ensemble $\langle\tau_{\text{pol}}\rangle$:

$$\frac{1}{\langle\tau_{\text{pol}}\rangle} = \left\langle \frac{1}{\tau_{\text{pol}}(k_\parallel)} \right\rangle_{n_{tot}} = \frac{1}{n_{\text{tot}}} \sum_{k_\parallel} \frac{n_{k_\parallel}}{\tau_{\text{pol}}(k_\parallel)}, \tag{4.8}$$

where $n_{\text{tot}} = \sum_{k_\parallel} n_{k_\parallel}$ is the total number of particles in the system and $n_{k_\parallel}$ is the occupancy number of a polariton state with in-plane momentum $k_\parallel$ and $\tau_{\text{pol}}(k_\parallel)$. The value of $n_{k_\parallel}$ can be deduced either from the Bose distribution function (see Section 4.4.1) or from kinetic simulations (see Section 4.4.2), depending whether the system is driven by the thermodynamics or the kinetics, respectively. In the center of the Brillouin zone, the excitonic contribution to τ_{pol} is almost negligible, whereas it sets the tone for wave vectors beyond the light cone. In this region the lower polariton dispersion is governed by a high excitonic fraction and the lifetime is set by the nonradiative exciton decay time τ_X^{NR} and $\tau_{\text{pol}}(k_\parallel)$ reads:

$$\frac{1}{\tau_{\text{pol}}(k_\parallel)} = \frac{|C_{k_\parallel}|^2}{\tau_{\text{C}}} + \frac{|X_{k_\parallel}|^2}{\tau_X^{\text{NR}}}. \tag{4.9}$$

Since the exciton lifetime in equation 4.9 significantly exceeds the photonic one, the lifetime of the polariton condensate, i.e., the lifetime at zero in-plane momentum $\tau_{\text{pol}}(k_\parallel = 0) = \tau^0_{\text{pol}}$, appears to be clearly limited by the photonic component and is well approximated by $\tau^0_{\text{pol}} \approx \tau_C/|C_0|^2$. As a consequence, the microcavity quality factor $Q = E_C\tau_C/\hbar$, which mainly depends on the structural quality [65], is a key parameter to improve the relaxation efficiency as it directly sets the number

of scattering events before polariton decay. The hybrid multiple quantum well-based microcavity structure investigated in the present chapter exhibits a Q-factor of ~ 1000, but values in excess of 6000 have been demonstrated in similar nitride-based microcavities [248]. Figure 4.4(b) illustrates the evolution of the polariton condensate lifetime as a function of detuning and quality factor. In the Q-factor range displayed, it is particularly visible that lifetimes longer than 5 ps are restricted to positive values of δ, even for full dielectric microcavities that are expected to exhibit significantly larger Q-factors.

4.3 A pedestrian approach to the phase diagram: kinetic vs. thermodynamic regimes

The polariton lasing threshold behavior crucially depends on how far the polariton gas is from thermal equilibrium, which in turn depends on the characteristic timescales involved in the system: the polariton ensemble lifetime $\langle\tau_{\text{pol}}\rangle$ and the relaxation time τ_{rel}, i.e., the time required for the polaritons to thermalize with the lattice. As a consequence, a good figure of merit to understand the behavior of P_{thr} is the ratio $R_{\text{th/kin}} = \langle\tau_{\text{pol}}\rangle/\tau_{\text{rel}}$ that can be naively understood as the ratio between the respective roles played by the thermodynamics and the kinetics. Intuitively, when $R_{\text{th/kin}}$ tends to zero, the polariton distribution cannot reach a thermal distribution and the final state of the system is fully governed by the relaxation kinetics. By contrast, when this ratio tends to large values, the polariton distribution approaches equilibrium and the threshold can be reasonably described within the BEC thermodynamic theory framework. The case $R_{\text{th/kin}} \approx 1$ defines an intermediate regime where both theories cannot be applied independently. The following sections will focus on the influence of the cavity-exciton detuning δ and the temperature T on the different timescales. As a result separate regions where the polariton relaxation is governed either by the thermodynamics ($R_{\text{th/kin}} \to \infty$) or by the carrier kinetics ($R_{\text{th/kin}} \to 0$) emerge in the (δ, T)-plane.

4.3.1 Effect of detuning and temperature on the polariton relaxation time

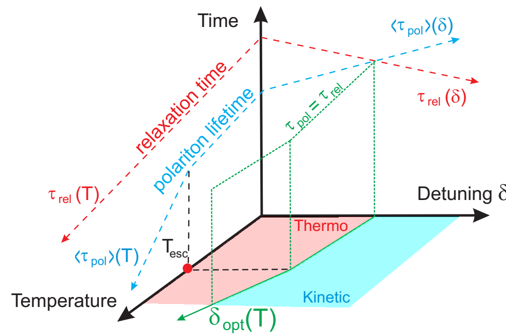

Fig. 4.5: Schematic representation the evolution of the characteristic times, $\langle\tau_{\text{pol}}\rangle$ and τ_{rel} as a function of δ and T (see text for details). Adapted from Ref. [56].

The role played by δ in semiconductor microcavities operating in the strong coupling regime is essential as it allows to adjust the light-matter content of polaritons. According to relation 1.56 and Fig. 4.4(a), when δ is negative lower polaritons become photon-like and conversely exciton-like for positive detunings. More precisely, polaritons mimic the behavior of the closest bare mode and can be tuned

from quasi non-interacting particles for $|X(0)|^2 \rightarrow 0$ to strongly interacting ones when $|X(0)|^2 \rightarrow 1$. As a consequence τ_{rel} is a monotonically decreasing function of δ for a given temperature (cf. Fig. 4.5):[49]

$$\left.\frac{\partial \tau_{\mathrm{rel}}(\delta, T)}{\partial \delta}\right|_{\mathrm{T=cst}} < 0 . \tag{4.10}$$

Hence, a higher excitonic content has been shown to favor relaxation processes bringing the system closer to the thermodynamic limit (see Ref. [203] and Fig. 3.19). On the other hand increasing the temperature also affects the particles behavior. Even if polariton-polariton and polariton-acoustic phonon scattering rates decrease when the carrier temperature is increased [101], the overal dynamics is faster since the imbalance between income and escape rates for a given state with wave vector $k_{\parallel}$ increases with temperature. In particular, Porras and coworkers have shown that there is an approximately linear relation between the exciton reservoir temperature and the maximum energy loss in the relaxation process, i.e., the higher the temperature, the faster the relaxation dynamics [249]. The relaxation dynamics is further accelerated by the progressive apparition of free thermal electrons according to Saha's law (see Section 4.6) inducing additional polariton-electron scattering events. Consequently, a rising temperature promotes the relaxation efficiency (cf. Fig. 4.5):

$$\left.\frac{\partial \tau_{\mathrm{rel}}(\delta, T)}{\partial T}\right|_{\delta=\mathrm{cst}} < 0 . \tag{4.11}$$

This effect becomes more pronounced for positive detunings as the total scattering rate $W^{\mathrm{tot}}_{\mathrm{k}_{\parallel}\rightarrow \mathrm{k}'_{\parallel}}$ between initial and final states $k_{\parallel}$ and $k'_{\parallel}$ is proportional to the product of the excitonic fraction of the initial and final states. It is worth mentioning that the temperature also affects the exciton reservoir lifetime $\tau_{\mathrm{res}} = \tau_{\mathrm{X}}^{\mathrm{NR}}$. The latter decreases with rising lattice temperature resulting in an additional increase in P_{thr}. However, this effect is neglected in the present situation as it only occurs at high temperatures where the system is in the thermodynamic regime and thermal depopulation is the predominantly limiting contribution affecting P_{thr}.

4.3.2 Impact of the thermodynamics on the threshold power density

4.3.2.1 Role of temperature

In the previous section, the evolution of τ_{rel} has been qualitatively deduced depending on the weights of interactions for different regions in the phase diagram (δ, T)-plane (cf. Fig. 4.5). However, so far the discussion has only accounted for the carrier kinetics. In order to get a complete picture of the P_{thr} evolution the role of thermodynamics has to be considered. Figure 4.6 displays the calculated critical density $n_{\mathrm{c}}^{\mathrm{th}}(\delta, T)$ of polaritons following the formalism presented later on in Section 4.4.1, which corresponds to the total density of polaritons in the system at $P = P_{\mathrm{thr}}$. Even if this treatment is only valid for a perfect 2D non-interacting Bose gas, it provides a basic understanding of the system behavior. For instance, it appears that for a given δ-value $n_{\mathrm{c}}^{\mathrm{th}}$ continuously increases with temperature due to the progressive population of the higher energy states:

$$\left.\frac{\partial n_{\mathrm{c}}^{\mathrm{th}}(\delta, T)}{\partial T}\right|_{\delta=\mathrm{cst}} > 0 . \tag{4.12}$$

Note that for temperatures higher than a certain value T_{esc}, the increase in $n_{\mathrm{c}}^{\mathrm{th}}$ is faster due to the onset of thermal detrapping as described hereafter.

[49] This is true if one discards extra relaxation channels such as the LO-phonon assisted one [207].

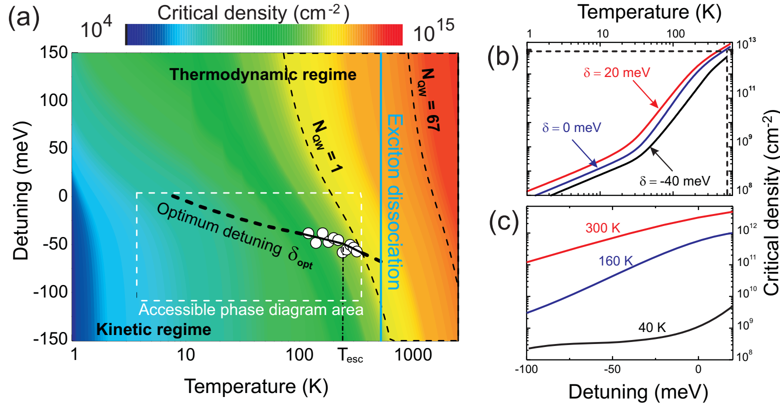

Fig. 4.6: (a) Critical density for polariton BEC in the thermodynamic limit n_c^{th} as a function of δ and T. The saturation density for a GaN-based microcavity with 1 and 67 thin GaN quantum wells (corresponding to the investigated structure) is symbolized by the thin black dashed lines. The vertical blue line marks the dissociation temperature for quantum well excitons in the present structure. The filled white circles represent the experimental data for the optimum detuning corresponding to the minimum threshold power density required for condensation. This line separates the kinetic and thermodynamic regimes and the thick black dashed line represents the expected trend. The dashed white rectangle displays the experimentally accessible detunings and temperatures in the present microcavity; (b) n_c^{th} as a function of temperature for different δ values and (c) as a function of δ for different temperatures. The dashed lines in (b) indicate the limits of the strong coupling regime fixed by the exciton/polariton screening density (horizontal) and the exciton dissociation (vertical line).

4.3.2.2 Role of detuning

To have a complete picture of the mechanisms ruling P_{thr}, the evolution of n_c^{th} with δ should also be considered. From Fig. 4.6 it appears that n_c^{th} increases with δ for the whole temperature range:

$$\left.\frac{\partial n_c^{th}(\delta, T)}{\partial \delta}\right|_{T=cst} > 0. \tag{4.13}$$

This can be intuitively understood when considering that for more positive detunings the density of states at zero in-plane momentum increases due to the rising matter-like character of polaritons. Thus, more particles have to be brought to the bottom of the lower polariton branch to reach the degeneracy condition. Interestingly, at the same time τ_{rel} undergoes a significant decrease due to the enhancement of interactions. The system is therefore facing simultaneously two opposite constraints: the thermodynamic threshold is low in the region where $R_{th/kin}$ is small and the relaxation efficiency is comparably low (kinetic regime) while it increases where $R_{th/kin}$ is large (thermodynamic regime) but τ_{rel} is short. As a consequence, for each temperature an optimum situation occurs where both kinetic and thermodynamic regimes are competing with each other and $\langle\tau_{pol}\rangle$ and τ_{rel} become comparable. In this region, a minimum value for P_{thr} is expected and an optimum detuning δ_{opt} can be estimated by:

$$\tau_{pol}\left(\delta_{opt}, T\right) = \tau_{rel}\left(\delta_{opt}, T\right) \rightarrow R_{th/kin}\left(\delta_{opt}, T\right) = 1, \tag{4.14}$$

while satisfying:

$$\left.\frac{\partial P_{thr}(\delta, T)}{\partial \delta}\right|_{T=cst} = 0. \tag{4.15}$$

$\delta_{opt}(T)$ follows from equation 4.14 based on the knowledge of the averaged polariton lifetime $\langle\tau_{pol}\rangle$ corresponding to equation 4.8. The derivation of τ_{rel}, which requires a modeling of the polariton relaxation kinetics by solving semi-classical Boltzmann equations, is presented in the following section.

4.3.2.3 High temperature regime: role of thermal depopulation

We are interested here in the evolution of the polariton condensation threshold power density as a function of δ at various lattice temperatures in the region of the phase diagram dominated by the thermodynamics, i.e. for temperatures ranging from 180 to 340 K (see Fig. 4.7(a)). From the investigation of the phase diagram it appears that above a given temperature, the threshold power density increases at a faster rate. To account for this behavior, we performed a phenomenological analysis. At first sight, one could think that the evolution of P_{thr} with δ is closely linked to that of the polariton effective mass of the lower polariton ground state as in a perfect two-dimensional system the 2D-density of states is proportional to the mass of the carriers. However, the latter is not varying significantly in the range of δ values of interest. Besides, we do not expect the 2D-density of states to be a strongly temperature-dependent parameter. Instead our approach is based on the deviation of the lower polariton branch from a true parabolic dispersion. We phenomenologically introduce the thermal in-plane wavevector k_{cross} where polaritons at $k_\parallel = 0$ are preferentially scattered at a given thermal

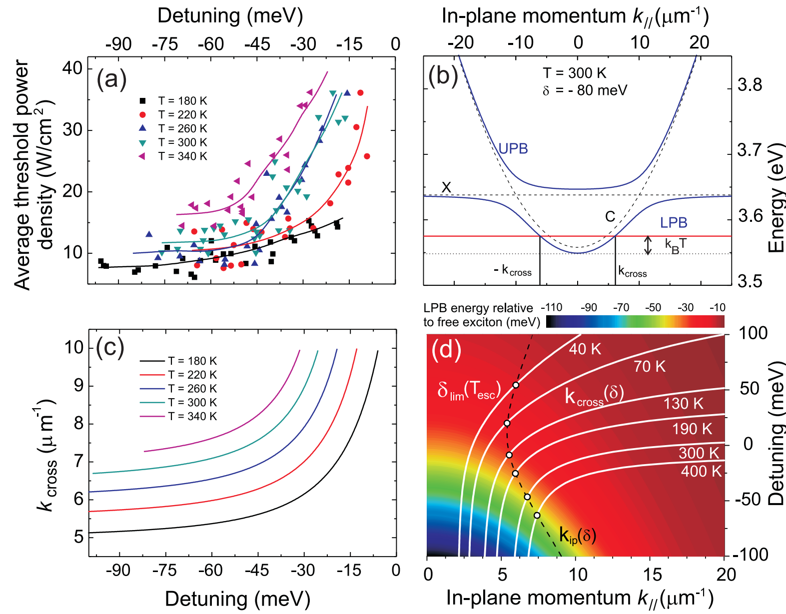

Fig. 4.7: (a) P_{thr} vs. δ for various T in the 180−340 K range. (b) Dispersion of the LPB and UPB (blue lines) at $\delta = -80$ meV and corresponding bare modes (black dashed lines). The red line is upshifted by $k_B T$ from the bottom of the trap and defines k_{cross}. (c) Evolution of k_{cross} vs. δ for various T deduced from computed dispersions accounting for the LPB renormalization. (d) Color map of the LPB relative to the free exciton line vs. $k_\parallel$ for different δ-values and $\Omega_{VRS} = 60$ meV. For a more accurate description, the renormalized vacuum Rabi splitting at $P = P_{thr}$ should be used for each δ. The continuous white lines $k_{cross}(\delta)$ define the maximum $k_\parallel$ where scattering from $k_\parallel = 0$ occurs for different temperatures. The black dashed line $k_{i.p}(\delta)$ corresponds to the position of the inflection point in the LPB. The transition detuning δ_{lim} is found when these two curves cross each other. T_{esc} sets the onset of thermal detrapping for each detuning δ_{lim}. Adapted from Ref. [250].

energy $k_B T$ (see Fig. 4.7(b)):

$$E_{LPB}\left(k_\parallel = 0, \delta\right) + k_B T_{latt} = E_{LPB}\left(k_{cross}, \delta\right) . \tag{4.16}$$

A good agreement is observed between the evolution of $P_{thr}(\delta)$ (Fig. 4.7(a)) and that of $k_{cross}(\delta)$ (Fig. 4.7(c)) highlighting the strong correlation between the critical density and the condensate depletion. The sudden increase in k_{cross} at a given temperature thus coincides with the thermal escape of polaritons from the bottom of the trap toward lower polariton states beyond the inflection point. Once it occurs, polaritons are scattered much further away from the center of the Brillouin zone. Consequently, more scattering steps through acoustic phonon interactions are required for those polaritons to relax to the bottom of the trap. In order to counterbalance the $k_\parallel = 0$ state depopulation with T an additional increase in the pump power is therefore needed to reach the condensation threshold.

In Fig. 4.7(d) the lower polariton branch energy is shown for detunings ranging from −100 to 100 meV as a function of the in-plane momentum $k_\parallel$. The position of the inflection point $k_{i.p}(\delta)$ is indicated and shown together with $k_{cross}(\delta)$. The intersection of $k_{cross}(\delta)$ and $k_{i.p}(\delta)$ defines, for a given lattice temperature T_{esc}, the critical detuning δ_{lim} above which thermal depopulation becomes the dominant effect (cf. Fig. 4.7(a)). In conclusion, thermal depopulation is triggered for regions of the phase diagram where $\delta > \delta_{lim}$ and $T > T_{esc}$. This simple picture is in agreement with the experimental behavior (see Figs. 4.5 to 4.12, [250]) and explains why the optimum threshold is seen to be shifted toward more negative detunings at elevated temperatures (see hereafter).

4.4 Theoretical description of polariton relaxation

The establishment of the phase diagram requires the use of the correct formalism to calculate the polariton occupancy factor for each state depending on the dominant regime, the kinetic or the thermodynamic one. Even if the kinetic approach can be applied to the whole phase diagram, it is of major importance to define the domain of validity of the thermodynamic one.

4.4.1 The thermodynamic limit

Here, quantum well excitons are assimilated to weakly interacting bosons in the low to medium carrier density range so that in turn cavity polaritons also behave as weakly interacting bosons in the same density range. Polaritons are considered to interact with a phonon bath characterized by a lattice temperature T_{latt}. Furthermore, we assume in this section that the polariton lifetime is much longer than their typical relaxation time thus implying that $R_{th/kin}$ tends toward infinity. This is indeed a prerequisite condition in order to reach an equilibrium with the lattice and thus the thermodynamic limit.[50] Thermalization means that the polariton gas can be described by the Bose-Einstein distribution with a well-defined temperature $f_{BE}\left(E_{LPB}\left(k_\parallel\right), T, \mu\right)$ [228]. Due to the strong in-plane spatial photonic disorder in III-nitride microcavities, the polariton gas first undergoes a phase transition toward an Anderson glass [237]. The critical density for this phase transition to take place is defined as the total number of polaritons, which can occupy all energy levels apart from the ground state. Considering that the sample is probed over a typical spot size r and calling $n^{th}(\delta, T, \mu)$ the total polariton density, the critical density for polariton condensation is reached when the chemical potential μ vanishes. Beyond this point, every particle newly added to the system will accumulate in the ground state. Thereby, the

[50] Note that in the present experiments this thermodynamic limit represented by T_{latt} cannot be fully reached by photocreated carriers.

critical density can be derived *via* [239]:

$$n_c^{th}(\delta, T) = \lim_{\mu \to 0} n^{th}(\delta, T, \mu) = \frac{1}{2\pi} \int_{k_\parallel > 2\pi/r} f_{BE}\left(E_{LPB}\left(k_\parallel\right), T, \mu = 0\right) k_\parallel \, dk_\parallel \,. \tag{4.17}$$

Figure 4.6 displays the calculated values for $n_c^{th}(\delta, T)$ over a wide range of detunings and temperatures for the investigated microcavity containing 67 thin GaN-quantum wells ($L_{QW} = 1.2$ nm, $E_X^b \approx 46$ meV) in the active region, which theoretically allows the observation of the strong coupling regime up to ~ 540 K. Note that a characteristic of the current system, namely the intrinsic interacting nature of polaritons and the non-equilibrium character arising from their finite lifetime, restrict the validity of the thermodynamic description to regions of the phase diagram where the ratio $R_{th/kin}(\delta, T)$ is significantly larger than unity. Since polariton condensation occurs far from thermodynamic equilibrium, it is important to keep in mind that the above-mentioned analysis can be considered as valid because a *quasi*-thermodynamic approximation is adopted.

4.4.2 The kinetic limit

The polariton relaxation kinetics, i.e., the time-evolution of the occupancy number $n_{k_\parallel}(t)$, can be numerically solved through a semi-classical Boltzmann approach by using the following set of equations for $n_{k_\parallel}(t)$ for discrete values of $k_\parallel$:

$$\frac{\mathrm{d}n_{k_\parallel}}{\mathrm{d}t} = I_{k_\parallel} - \Gamma_{k_\parallel} n_{k_\parallel} - n_{k_\parallel} \sum_{k_\parallel} W_{k_\parallel \to k'_\parallel} \left(n_{k'_\parallel} + 1\right) + \left(n_{k_\parallel} + 1\right) \sum_{k'_\parallel} W_{k'_\parallel \to k_\parallel} n_{k'_\parallel} \,, \tag{4.18}$$

where $I_{k_\parallel}$ and $\Gamma_{k_\parallel}$ account for the pumping and decay rates (both of radiative and nonradiative origin) of the particles and $W_{k_\parallel \to k'_\parallel}$ is the total scattering rate between the initial state $k_\parallel$ and the final state $k'_\parallel$. The scattering rates are treated perturbatively and encompass all the interactions polaritons can undergo with their environment, namely exciton-phonon, exciton-exciton and exciton-electron interactions. Owing to strong piezoelectric effects and large deformation potentials in GaN-based systems attention has to be paid in particular to the treatment of the exciton-phonon interaction.

From the ensemble of solutions $n_{k_\parallel}$ various information can be deduced such as the polariton relaxation time τ_{rel} or the critical density n_c for polariton condensation for each temperature and detuning of the phase diagram accounting correctly for the system specificities *via* the total scattering rates. Note that the critical density calculated within the polariton kinetics approach is always larger compared to the ideal thermodynamic one n_c^{th}. However, $R_{th/kin}$ monotonically increases with δ and T bringing the system closer to the thermodynamic limit and the gap between n_c^{th} and n_c can eventually vanish [54]. It is also worth mentioning that the Boltzmann approach in the current form neglects the spin state of polaritons since all the experiments have been performed without polarization selection. This approximation is expected to be correct under nonresonant excitation where the various processes of decoherence induce fast random changes of the phase of polaritons, which then nearly behave as classical particles. At and above the polariton condensation threshold, where the phase of the condensate is stabilized and amplified by the stimulated scattering process, the spin state has to be properly taken into account *via* the introduction of the two-component order parameter of the condensate (see Chapter 5).

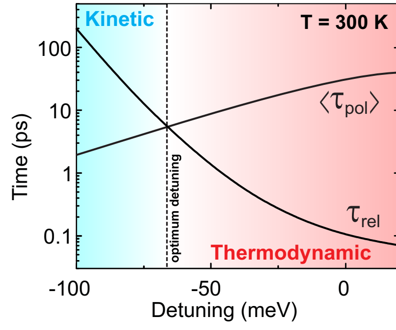

Fig. 4.8: Calculated relaxation time (τ_{rel}) and mean polariton lifetime (τ_{pol}) at $T = 300\,\text{K}$ vs. δ. At $\delta \approx -65\,\text{meV}$, the crossing of τ_{rel} and τ_{pol} corresponds to the critical value δ_{opt} where P_{thr} is minimized (vertical dashed line). For $\delta \gg \delta_{\text{opt}}$, the system is dominated by the thermodynamics (red region) and for $\delta \ll \delta_{\text{opt}}$, by the kinetics (blue region). Adapted from Ref. [56].

Figure 4.8 shows a typical example of information, which can be extracted from Boltzmann simulations of polariton relaxation. Here, a nonresonant pumping scheme is assumed inducing a thermalized exciton gas with an effective temperature given by the LO-phonon energy, i.e., $T = 1070\,\text{K}$. In order to calculate the relaxation time τ_{rel} of the exciton-polariton gas, a pulsed excitation is considered with an infinite polariton lifetime. τ_{rel} is then defined as the characteristic time of the temperature decrease: it can be linked to the signal rise time of the cavity emission in pulsed experiments carried out with short picosecond pulses. Figure 4.8 shows the evolution of τ_{pol} and τ_{rel} vs. δ at 300 K. As expected, the relaxation time is much longer than the mean polariton lifetime at large negative δ-values. The system is therefore expected to be strongly out of equilibrium, i.e., in the kinetic regime (blue area). The two curves cross at $\delta = -65\,\text{meV}$ and the lifetime becomes much longer than the cooling time when approaching positive detunings, which means that the system is in the thermodynamic regime in this detuning range (red area).

Figure 4.9(a) shows the calculated occupancy of the ground state $n_0(t)$ for two different pumping powers, below and above threshold at a detuning of $-30\,\text{meV}$ at $T = 220\,\text{K}$.[51] Below threshold, the rise time is quite long and a real steady state regime is only achieved at the end of the 500 ps of the pulse duration. Above threshold, the dynamics becomes much faster and the rise time becomes shorter and shorter when increasing the pumping power. After the end of the exciting pulse, $n_0(t)$ decays with a decay time given by the mean particle lifetime defined as in equation 4.8 and in the low pumping regime (dashed red curve), the distribution function is Boltzmann type (see Fig. 4.9). In the high pumping regime, the distribution function becomes Bose-like, with a large occupancy of the ground state. The mean lifetime is therefore shorter until the ground-state occupancy reaches unity where the system recovers its low pumping-regime characteristics.

Figure 4.9(b) shows the plot of the kinetic distribution function after 50 ps for the same system parameters, when the emission from the cavity is still rising, and at 500 ps, when a steady-state regime is achieved below (solid) and above (dashed) threshold. The effective temperature of the gas in the range of excess energy 20 – 100 meV is about 260 K as shown by the blue dashed curve. Closer to the ground state, the distribution function is weakly depleted. Using only the 0 – 15 meV range of excess energy, we can deduce an effective temperature of 350 K for the polariton gas. It is also interesting to notice that

[51] For this set of detuning and temperature, the system was demonstrated to be in the thermodynamic regime [56].

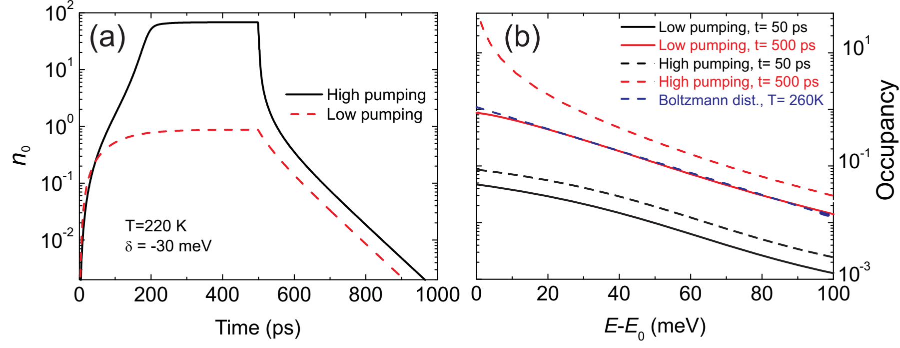

Fig. 4.9: Boltzmann semi-classical equation simulations for $T = 220$ K and $\delta = -30$ meV: (a) Dynamics of the occupancy of the ground state $n_0(t)$ below and above threshold. (b) Occupancy of the polariton states below (solid) and above (dashed) threshold at two different times (50 ps, black and 500 ps, red) under quasi-cw excitation (500 ps long pulses). The blue dashed curve is a Boltzmann fit of the red curve with an effective temperature found equal to 260 K. E_0 corresponds to the lowest-energy state of the system. Adapted from Ref. [56].

polaritons close to $k_{\parallel} = 0$ are warmer in the transient regime $t = 50$ ps with an effective temperature close to 500 K.

4.5 Phase diagram: experimental results vs. theory

Figure 4.10(a) displays experimental values for the polariton condensation average threshold power density for a wide range of detunings and temperatures and Figs. 4.10(b) and 4.10(c) show cross-sections of the phase diagram ($T_{\text{latt}}, P_{\text{thr}}$) and ($\delta, P_{\text{thr}}$), respectively. The accessible δ and T values are restricted by the sample geometry and the experimental setup.

For the available detuning range, a nonlinear decrease in P_{thr} is observed at low temperatures when going toward positive detunings. This is a direct manifestation of the kinetic regime, the radiative polariton lifetime being shorter than the relaxation time due to the dominant photonic fraction of lower polaritons at $k_{\parallel} = 0$. For intermediate temperatures ($T_{\text{latt}} \sim 150 - 300$ K), P_{thr} first decreases and then starts increasing again when going toward positive values (see Fig. 4.10(b)). In this temperature range, the threshold power can be minimized, i.e., an optimum detuning δ_{opt} corresponding to a balance between polariton relaxation time and radiative lifetime is found. For $\delta > \delta_{\text{opt}}$, polaritons are thermalized and the threshold is controlled by the thermodynamic properties (region II in Figs. 4.10(b)-4.10(c)) of the system whereas for $\delta < \delta_{\text{opt}}$, polaritons are not thermalized and the threshold is controlled by the kinetics (region I in Figs. 4.10(b)-4.10(c)). For even higher temperatures, the optimum detuning goes out of the range of experimental measurements and in the whole (δ, T_{latt}) range we observe the thermodynamic regime, with the threshold power density increasing with detuning because of the joint increase in the effective mass and the thermal escape of polaritons from the bottom of the trap toward lower polariton states located beyond the inflection point.

When the detuning tends toward the most negative values at a given temperature, an increase in P_{thr} is observed. This is the opposite behavior with respect to the prediction for a system operating in the exact thermodynamic limit, which can certainly be ascribed to relaxation kinetic effects. Furthermore, the shape of the curves $P_{\text{thr}}(T)$ in Fig. 4.10(c) is fully consistent with the kinetic phase diagram calculated in Ref. [54] for a GaN-based multiple quantum well based microcavity under pulsed excitation: (i) the

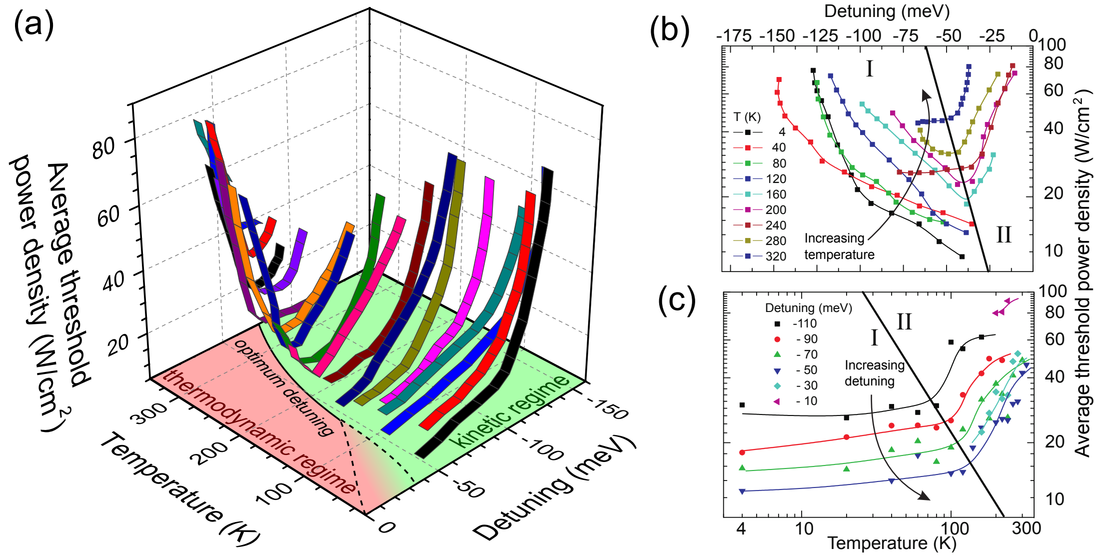

Fig. 4.10: (a) Experimental 3D polariton lasing phase diagram. Adapted from Ref. [55]. Evolution of P_{thr} as a function of (b) the lattice temperature at various detunings (lines are a guide to the eyes) and (c) detuning at various temperatures. Region (I) corresponds to a kinetically driven system whereas region (II) corresponds to a thermodynamic-like behavior. Adapted from Ref. [56].

threshold density is expected to be considerably increased with respect to the ideal thermodynamic case at low temperatures because of the slow kinetics and (ii) the critical density should be nearly independent on temperature due the disorder-induced broadening until the system transits into the thermodynamic regime. These two features are clearly visible in Fig. 4.10(c), confirming the transition between the kinetic and thermodynamic regimes, i.e., regions I and II.

These experimental results are well reproduced by theoretical simulations performed using semi-classical Boltzmann equations. Contrary to the conditions for the calculation of the relaxation time shown in Fig. 4.8, the same pumping scheme as in the experiment is adopted, i.e., a long quasi-cw pulse of 500 ps. Figure 4.11 displays the calculated threshold power density as a function of detuning for different temperatures. An important feature of these curves is that they cross each other. To be more precise, the higher the temperature, the larger the threshold in the thermodynamic regime region

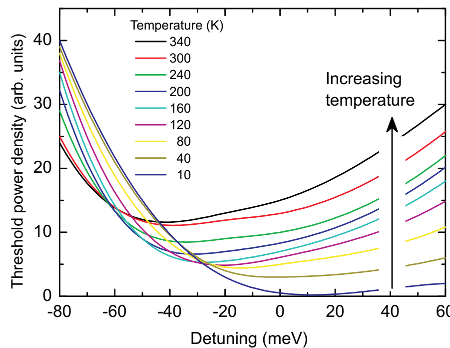

Fig. 4.11: Theoretical dependence of the threshold power density as a function of detuning at various temperatures. Adapted from Ref. [56].

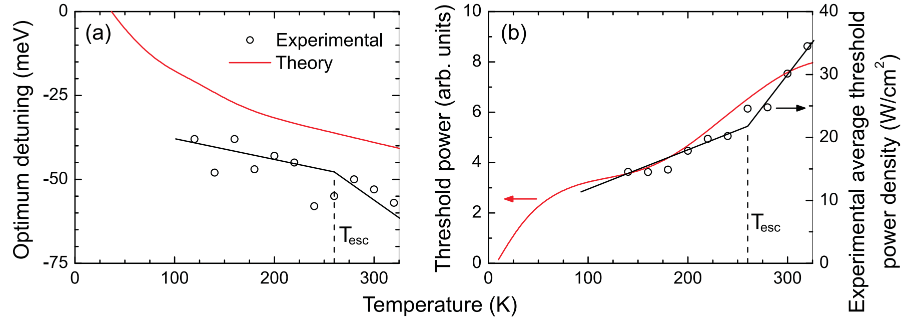

Fig. 4.12: (a) Optimum detuning $\delta_{\text{opt}}(T)$ as a function of the lattice temperature. (b) Evolution of P_{thr} at $\delta_{\text{opt}}(T)$. The black solid lines in (a) and (b) act as a guide to the eyes for the experimental values emphasizing T_{esc}. Adapted from Ref. [56].

corresponding to slightly negative and positive detunings whereas the higher the temperature, the lower the threshold in the kinetic regime. Therefore those curves will cross as it was recently reported for CdTe- and GaAs-based microcavity samples on a much narrower temperature range (see Refs. [202, 229] and Figs. 4.13(a)-4.13(d)). Such a crossing is however not systematically observed in the present experiment. We believe that in addition to thermal escape mechanisms this is due to the temperature dependence of the nonradiative exciton lifetime, which is presently neglected in the theory. The nonradiative lifetime decreases versus T, which should therefore result in a slight rise of the threshold versus T.

In the theoretical calculations, a wider range of detunings is accessible, which allows plotting δ_{opt} for a large range of temperatures. In Fig. 4.12(a), $\delta_{\text{opt}}(T)$ deduced from experimental measurements is thus compared to theoretical calculations. The general trend is a shift of the optimum detuning toward more negative δ-values with increasing temperature. The solid black line is the experimental analog of the green line $\delta_{\text{opt}}(T)$ sketched in Fig. 4.5. Based on the analysis of Fig. 4.5, we can extract from this line a critical escape temperature $T_{\text{esc}} = 258 \pm 10\,\text{K}$ associated with an optimum detuning of $-40\,\text{meV}$ beyond which the optimum polariton condensation threshold power strongly increases due to a large thermal depletion of the fundamental lower polariton state. Interestingly, the corresponding thermal energy $E_{\text{esc}} = 22\,\text{meV}$ does indeed coincide with the minimum energy required to scatter polaritons from the bottom of the trap to lower polariton states located beyond the inflection point for a renormalized normal-mode splitting of 40 meV [55, 250]. The difference observed between theory (solid red line) and experiment (open circles) might stem from the fact that the renormalization of the polariton dispersion curve is not taken into account when using the Boltzmann approach. At 300 K, the optimum detuning is about $-55\,\text{meV}$.

Another quantity, which can be advantageously plotted is the evolution of the threshold power density at δ_{opt} vs. temperature (see Fig. 4.12(b)). Interestingly, as for the evolution of $\delta_{\text{opt}}(T)$ we can define two slopes for the evolution of the optimum condensation threshold power as a function of T (black line in Fig. 4.12(b)) with the kink occurring at the same critical temperature $T_{\text{esc}} = 258 \pm 10\,\text{K}$, which would coincide with the appearance of significant depletion effects of the fundamental lower polariton state. P_{thr} increases with temperature in both theory and experiment, which is likely originating from the increase in the thermodynamic threshold with temperature. The latter will slightly prime over the threshold given by the kinetics in this intermediate region. Note however that the situation might be different in other systems, where the enhancement of kinetics with temperature, e.g., at cryogenic temperatures, might play a stronger role.

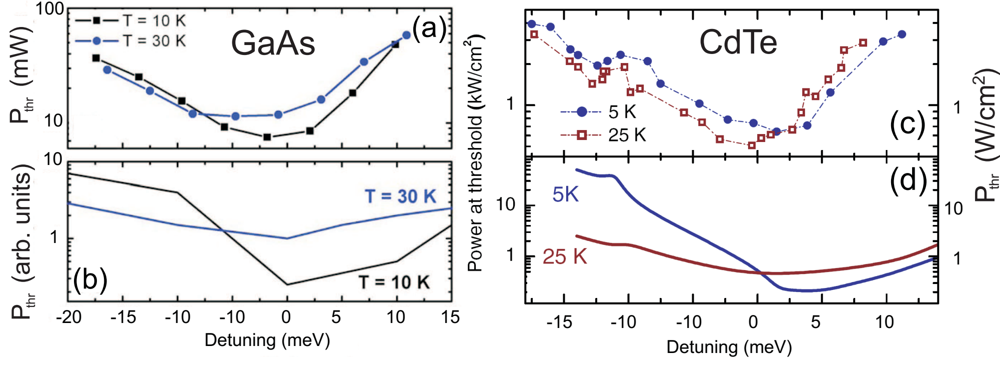

Fig. 4.13: Measured and calculated P_{thr} as a function of δ for (a)-(b) GaAs at $T_{\mathrm{latt}} = 10\,\mathrm{K}$ (black squares) and 30 K (blue circles). Adapted from Ref. [202] ; (c)-(d) CdTe at $T_{\mathrm{latt}} = 5\,\mathrm{K}$ (solid blue circles) and 25 K (open brown squares). Adapted from Ref. [229].

The position of δ_{opt}, at a given temperature, also sets the frontier between kinetics and thermodynamics and its absolute value is characteristic of the system and fixed by the relative weights of these two regimes.[52] For the sake of comparison, the condensation threshold for GaAs and CdTe-based microcavities are reported in Figs. 4.13(a)-4.13(b) as a function of detuning for two different lattice temperatures. Comparing these data with the GaN ones in Fig. 4.10(b), it appears that GaAs and CdTe are less dominated by the kinetics leading to δ_{opt} values much closer to zero compared to GaN-based microcavities at low temperatures: $\delta_{\mathrm{opt}}^{\mathrm{GaAs}}(10\,\mathrm{K}) \approx -3 \pm 1\mathrm{meV}$ [202] and $\delta_{\mathrm{opt}}^{\mathrm{CdTe}}(4\,\mathrm{K}) \approx 3 \pm 1\mathrm{meV}$ [229]. However, a shift toward more negative δ values with increasing temperatures due to enhanced thermodynamics is also observed in these two systems.

4.6 Impact of temperature on the electronic populations

As already detailed in Sections 3.2.2 and 3.2.3, the carrier population is composed of free and localized excitons and biexcitons. At thermal equilibrium, these populations are distributed according to the following mass action laws [107, 186, 251]:

$$e + h \xleftrightarrow{K_{\mathrm{X}}} X \quad \rightarrow \quad \frac{n_{\mathrm{e}} n_{\mathrm{h}}}{n_{\mathrm{X}}} = K_{\mathrm{X}}(T) = \frac{\mu k_{\mathrm{B}} T}{2\pi\hbar^2} \exp\left(-\frac{E_{\mathrm{X}}^{\mathrm{b}}}{k_{\mathrm{B}} T}\right), \tag{4.19}$$

$$X + X \xleftrightarrow{K_{\mathrm{XX}}} XX \quad \rightarrow \quad \frac{n_{\mathrm{X}}^2}{n_{\mathrm{X}}} = K_{\mathrm{XX}}(T) = \frac{M_{\mathrm{X}} k_{\mathrm{B}} T}{\pi\hbar^2} \exp\left(-\frac{E_{\mathrm{XX}}^{\mathrm{b}}}{k_{\mathrm{B}} T}\right), \tag{4.20}$$

$$X \xleftrightarrow{K_{\mathrm{X}}^{\mathrm{loc}}} X_{\mathrm{loc}} \quad \rightarrow \quad \frac{n_{\mathrm{X}}}{n_{\mathrm{X}}^{\mathrm{loc}}} = K_{\mathrm{X}}^{\mathrm{loc}}(T) = \frac{2 M_{\mathrm{X}} k_{\mathrm{B}} T}{\pi\hbar^2 N_{\mathrm{D}}} \exp\left(-\frac{\delta E_{\mathrm{X}}^{\mathrm{loc}}}{k_{\mathrm{B}} T}\right), \tag{4.21}$$

$$XX \xleftrightarrow{K_{\mathrm{XX}}^{\mathrm{loc}}} XX_{\mathrm{loc}} \quad \rightarrow \quad \frac{n_{\mathrm{XX}}}{n_{\mathrm{XX}}^{\mathrm{loc}}} = K_{\mathrm{XX}}^{\mathrm{loc}}(T) = \frac{4 M_{\mathrm{X}} k_{\mathrm{B}} T}{\pi\hbar^2 N_{\mathrm{D}}} \exp\left(-\frac{\delta E_{\mathrm{XX}}^{\mathrm{loc}}}{k_{\mathrm{B}} T}\right), \tag{4.22}$$

where N_{D} is the localization center density, which was estimated to $\sim 3 \times 10^{12}\,\mathrm{cm}^{-2}$ in a previous study performed on GaN-based quantum wells grown on an a-plane bulk GaN substrate [252]. As we consider undoped quantum wells, charge conservation implies that $n_{\mathrm{e}} = n_{\mathrm{h}} = n_{\mathrm{free}}$, where n_{free} is the

[52] Note that extrinsic material properties such as doping, strain or defects might significantly alter the transition between thermodynamically and kinetically driven regimes.

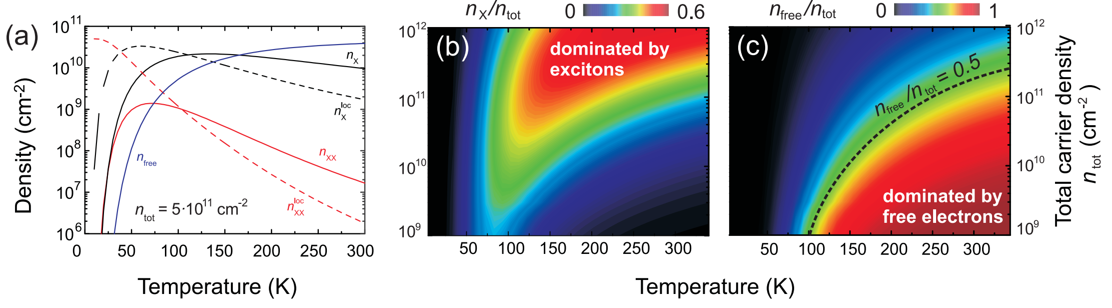

Fig. 4.14: (a) Calculated free (solid lines) and localized (dashed lines) densities of excitons, biexcitons and free electrons (black, red and blue lines, respectively) confined in a 1.2 nm thick GaN/$Al_{0.2}Ga_{0.8}N$ quantum well for a photogenerated pair density $n_{tot} = 5 \times 10^{11}$ cm^{-2}. Adaptated from Ref. [186]. Evolution of the (b) free exciton (n_X/n_{tot}) and (c) free electron (n_{free}/n_{tot}) to total carrier density ratios vs. lattice temperature and n_{tot}.

thermal free electron density. Assuming that all photons absorbed in the quantum wells are converted into electron-hole pairs (with density n_{tot}), one can write:

$$n_X + n_X^{loc} + n_{XX} + n_{XX}^{loc} + n_{free} = n_{tot}\,. \tag{4.23}$$

Solving equations 4.19 to 4.23 for different values of n_{tot} and temperatures, one can calculate the relative contribution of each population depending on the experimental configuration. In Fig. 4.14(a), the evolution of each population is displayed as a function of the lattice temperature for $n_{tot} = 5 \times 10^{10}$ cm^{-2}. At low temperature, i.e., in the 4 – 50 K range, the electronic population is dominated by localized excitons and biexcitons (black and red dashed lines in Fig. 4.14(a)).[53] However, in this temperature range, polariton thermalization is not achieved for the presently available detunings and the condensation dynamics is governed by the relaxation kinetics. In the 50 – 125 K range, the electronic population is dominated by free excitons (see Fig. 4.14(b)). Finally, for temperatures higher than 150 K, the free electron population becomes comparable to the excitonic one (see Figs. 4.14(a)-4.14(c)), opening an extra relaxation channel for the polariton relaxation *via* electron-exciton scattering. The presence of electrons was shown to efficiently accelerate the relaxation dynamics of the whole system, not only close to the center of the Brillouin zone but also in the exciton reservoir [205, 253].

Recently, Tsotsis and coworkers have shown that the increase in the carrier densities due to the presence of thermal electrons induces a crossover from strong to weak coupling regime in a planar GaAs-based microcavity [254]. They also present a simple model that takes into account the rise in the reservoir lifetime due to thermalization of carriers to high wave vector states when the temperature is increased, which in turn increases the steady-state carrier density. In our microcavity, the situation is different. First, the high exciton binding energy makes the exciton stable up to room temperature (see Fig. 4.14(b)) and the relatively important in-plane disorder prevents the increase in the reservoir lifetime with temperature, which is seen to exponentially decrease with temperature (see Fig. 3.8(b)).

[53] Note that even the electronic population is dominated by localized excitons, the strong light-matter interaction occurs on a time-scale given by the Rabi period, which is faster than the localization time.

4.7 LO-phonon mediated relaxation

Now that we have addressed the general trend of the polariton phase diagram, let us turn our attention to the role of the additional relaxation channels involving the emission of one LO-phonon. Contrary to the other relaxation mechanisms, LO-phonons take part to the condensate formation only when the polariton ground-state energy plus one LO-phonon is resonant with the particle reservoir of energy E_{res}, i.e., for a detuning δ_{res} satisfying $E_{\text{LPB}}(\delta_{\text{res}}, k_{\parallel}) + E_{\text{LO}} = E_{\text{res}}$.

In Figs. 4.15(a)-4.15(c), the evolution of the threshold power P_{thr} is reported as a function of the detuning at low temperature for a CdTe-, a GaAs- and a GaN-based multiple quantum well microcavity, respectively. For the CdTe microcavity, a local minimum of P_{thr} occurs for $\delta = -15$ meV, where the exciton reservoir and the polariton ground-state are separated in energy by $E_{\text{LO}}^{\text{CdTe}} = 21.5$meV [207] (mechanism labeled as $X - LO$ in Figs. 4.15(a) and 4.15(c)-4.15(d)).[54] The case of GaAs is shown in Fig. 4.15(b) and the reservoir is provided by the medium polariton branch (mechanism labeled as $MP - LO$ in Fig. 4.15(b)): a polariton bottleneck is formed at high momentum along the MP-branch, which efficiently feeds the polariton ground-state when the cavity detuning is tuned to -4 meV [80]. As already discussed in details in Section 3.3.2, dark excitons efficiently bind into biexcitons in the present microcavity forming an extra reservoir with an energy equal to $E_{\text{XX}} = 2E_{\text{X}} - E_{\text{XX}}^{\text{b}}$. The radiative dissociation of cavity biexcitons can directly feed the polariton ground state according to the relaxation channels $XX \rightarrow LP(k_{\parallel} = 0) + LO + X$ or $XX \rightarrow LP(k_{\parallel} = 0) + LO + LP(k_{\parallel} \gg 0)$ (labeled as $XX - LO$ in Figs. 4.15(c)-4.15(d)). In conclusion, in addition to the $X - LO$ mechanism, which occurs for $\delta_{\text{res},1} \approx -80$ meV, a second minimum of P_{thr} is observed for $\delta_{\text{res},2} \approx -105$ meV for the $XX - LO$ channel, evidencing the presence of an extra particle reservoir in GaN-based microcavities.

[54] Note that the mechanism $X - LO$ was also recently reported in a bulk ZnO microcavity leading to an efficient formation of the polariton condensate [256].

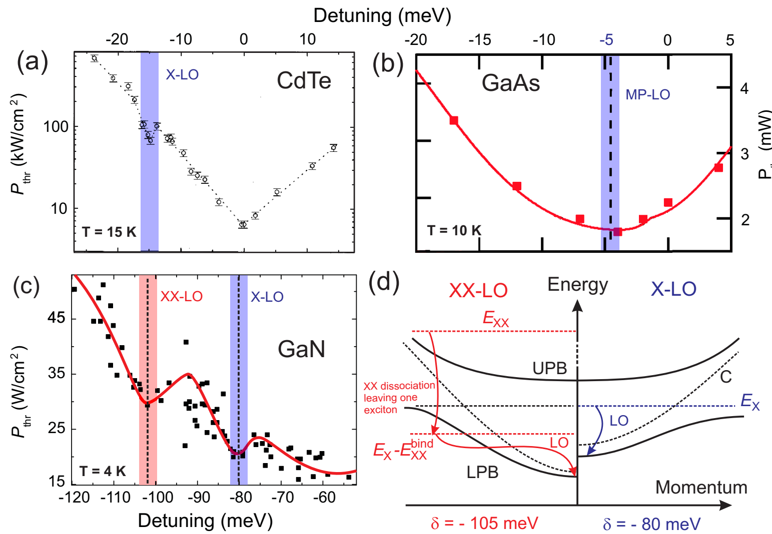

Fig. 4.15: Evolution of P_{thr} as a function of δ for (a) a CdTe-based microcavity containing 16 quantum wells (adapted from Ref. [207]); (b) a GaAs-based microcavity containing 12 quantum wells (adapted from Ref. [255]) and (c) the present GaN-based microcavity containing 67 quantum wells (adapted from Ref. [186]). (d) Schematic representation of the LO-phonon assisted relaxation involving a biexciton (XX-LO, left) and the exciton reservoir (X-LO, right).

4.8 Polariton laser vs. VCSEL: evidence of the matter-like character of polaritons

To complete our analysis, we also investigated the evolution of the average lasing threshold power density measured on an InGaN/GaN multiple quantum well vertical cavity surface emitting laser (VCSEL) similar to that of Ref. [61] under nonresonant excitation as a function of δ at room temperature (see Fig. 4.16(a)). Lasing is achieved over a broad spectral bandwidth, slightly in excess of 50 nm. The corresponding curve at room temperature for the present sample is displayed below for the sake of comparison (Fig. 4.16(b)).

The strong difference between these two samples arises from the different physics, which is involved. In the VCSEL case, the driving force responsible for the coherent emission is population inversion of free carriers and the key parameter governing the threshold value is the spectral overlap between the bare modes (Fig. 4.16(c)). The minimum in P_{thr} is thus expected to occur close to zero detuning, i.e., when the overlap between the cavity resonance and the gain band of the lasing medium is maximum [257]. This behavior is common to all semiconductor lasers and does not significantly depend on the lattice temperature. In the case of the polariton laser, the threshold is driven by the efficiency of carrier relaxation toward the ground state (Fig. 4.16(d)) and the thermal escape mechanisms that depend on both δ and T. The relaxation kinetics of carriers and the thermodynamic processes are competing against each other and the minimum of P_{thr} is found when the constraints acting on the system are minimized. In the present sample, this occurs at $\delta \approx -55$ meV (Fig. 4.16(b)). This singular behavior is fully incompatible with a conventional photon laser picture and is a clear signature of the matter-like character of polaritons.

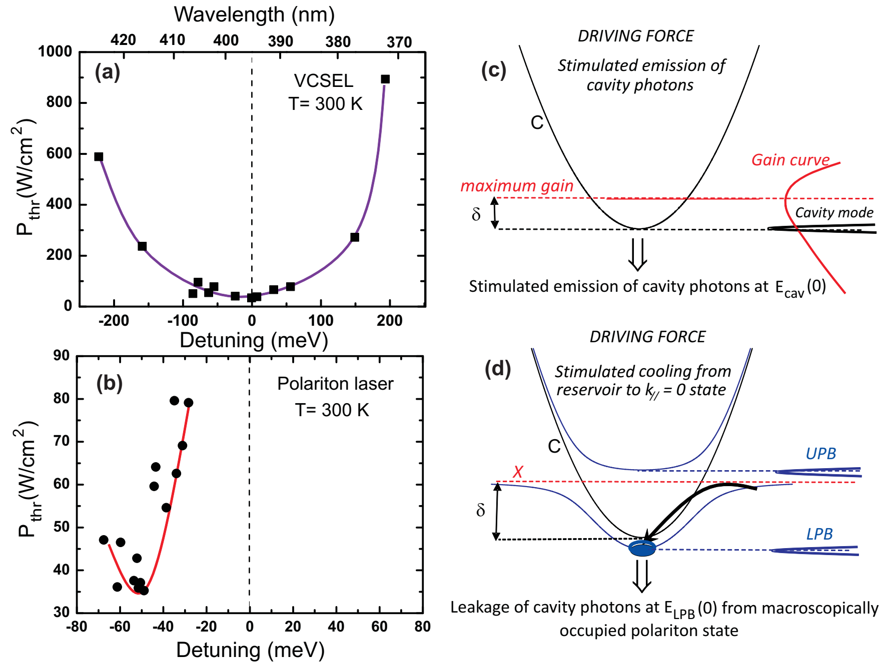

Fig. 4.16: Evolution of the average nonlinear emission threshold at room temperature versus δ in the case of (a) a VCSEL, and (b) a polariton laser. (c) Sketch of the working principle of a semiconductor laser (here a VCSEL). (d) Same as (c) for a polariton laser. Adapted from Ref. [250].

5 Polariton polarization properties: evolution of the order parameter

5.1 Introduction

The formation dynamics of polariton condensates is still subject to intensive research. A deeper understanding of the build-up and the evolution of the condensate order parameter is thus of major interest. Due to the efficient polariton relaxation and the possibility of performing measurements up to room temperature, III-nitride based microcavities appear as the system of choice to probe polariton condensation close to the thermodynamic limit. In the previous chapter, it has been clearly established under which conditions the system can be conveniently described by a thermodynamic description. In this chapter, the polarization properties of light emitted by a room temperature polariton condensates are investigated.

5.1.1 Representation of the polariton spin state

In a simplified picture, exciton-polaritons formed by the coupling of heavy hole excitons ($J_z^{\mathrm{hh}} = \pm 1, \pm 2$) and photons in semiconductor microcavities with embedded quantum wells have two possible spin projections on the structure growth axis corresponding to the right- ($J_{\mathrm{z}} = +1$) and left-circular ($J_{\mathrm{z}} = -1$) polarizations of the emitted photons, respectively.[55] It is reflected in the spinor nature of the order parameter of polariton BECs, whose components define the weights and phases of the spin $+1$ and -1 components of the condensate. By extension, a coherent superposition of$+1$ and -1 states corresponds to elliptical polarization of the light emitted by the condensate.

Referring to quantum well excitons, the dominant free-carrier relaxation channel is given by the Bir-Aronov-Pikus mechanism, which exclusively involves transitions between optically active states ensuring that the contribution of dark excitons for carrier relaxation can be neglected here [258]. As there are only two possible spin projections, polaritons form a classical two-level system[56] whose spinor wave function $|\psi\rangle$ is expressed in the basis $\{|\psi_\downarrow\rangle, |\psi_\uparrow\rangle\}$ corresponding to the total angular momentum $J_z = -1$ and $+1$, respectively. Despite this natural geometric representation of $|\psi\rangle$ in the *Bloch sphere*, it is convenient to make use of the one-to-one correspondence between the polarization of the emitted photons and the components of $|\psi\rangle$ to directly relate the polariton pseudospin **S**, which is a complex

[55] Excitons with $J_z = 0$ or $J_z = \pm 2$ cannot couple to the vacuum field as the photon carries a momentum $J_z^{\mathrm{C}} = \pm 1$. They are called dark states.

[56] This discussion is generally valid for any in-plane momentum $k_\parallel$. However, throughout the following discussion we only consider the pseudospin of the condensate.

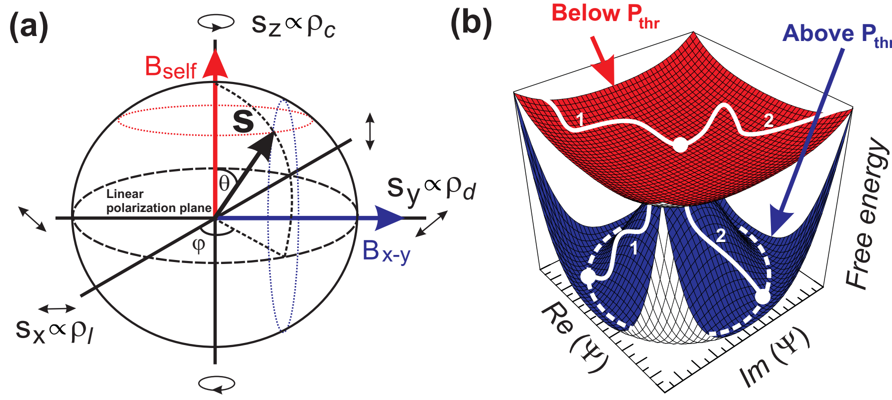

Fig. 5.1: In the Poincaré sphere, the pseudospin vector **S** describes the spin state of the polariton. The equatorial plane corresponds to a linear polarization while the poles correspond to circular polarization of the emitted light. B_{x-y} and B_{self} are the effective magnetic fields created by the static disorder splitting ΔE_{x-y} and polariton-polariton interactions ΔE_{self}, respectively. (b) Schematic representation of the polariton free energy as a function of the real and imaginary parts of the polariton wave function x_1 and x_2, respectively (see text for details). Below threshold, the symmetric solution $\psi = 0$ is stable while above threshold, the condensate spontaneously acquires a different phase for each realization (e.g., paths 1 and 2).

vector describing the quantum state of this 2-level system, to the Stokes-vector parameters [259, 260]. Thus, the linear (ρ_{l}), diagonal (ρ_{d}) and circular (ρ_{c}) polarization degrees of the emitted light and the polariton pseudospin components $S_{\text{x,y,z}}$ are directly linked *via* the relations $\rho_{\text{l,c,d}} = 2S_{\text{x,y,z}}/n_0$ where n_0 denotes the occupation number of the polariton condensate. As a consequence, the pseudospin **S** can be represented in the *Poincaré sphere* (see Fig. 5.1(a)) and is directly obtained from the polariton wave function components *via* the relations:

$$\begin{aligned} S_{\text{x}} &= \frac{1}{2}\left(\psi_\downarrow^* \psi_\uparrow + \psi_\uparrow^* \psi_\downarrow\right), \\ S_{\text{y}} &= \frac{i}{2}\left(\psi_\downarrow^* \psi_\uparrow - \psi_\uparrow^* \psi_\downarrow\right), \\ S_{\text{z}} &= \frac{1}{2}\left(|\psi_\uparrow|^2 - |\psi_\downarrow|^2\right). \end{aligned} \tag{5.1}$$

Note finally that the norm of the pseudovector $|\mathbf{S}|$ is related to the degree of spin coherence: If $|\mathbf{S}|/2n_0 < 1$ the polarization state contains a certain degree of incoherence whose limit $|\mathbf{S}| \to 0$ corresponds to a fully incoherent system, exhibiting totally unpolarized emitted light.

5.1.2 Spontaneous symmetry breaking and polariton BEC

In a thermodynamic phase transition an order parameter x can be defined whose value is zero below the transition point, i.e., the condensation threshold, and acquires a finite value above. In the Landau functional theory - providing a phenomenological description of the phase transition - the system free energy F is expanded in powers of x, which is small close to the transition point:

$$F[x] = F_0 + F_1 x + F_2 x^2 + F_3 x^3 + F_4 x^4 + O\left(x^5\right), \tag{5.2}$$

where F_0 is a constant and can be ignored as it has no influence on the treatment and F_1 and F_3 vanish due to symmetry arguments. For a given temperature the value of x is determined by minimizing $F[x]$. Owing to the spinor nature of the order parameter for exciton-polaritons physically associated with the macroscopic wave function of the polariton condensate ψ, x has the form $\mathbf{x} = \{x_1, x_2\} = \{\mathrm{Re}(\psi), \mathrm{Im}(\psi)\}$ [261]. Once the expression of F is known, the state of the polariton condensate is defined by the minimum of $F[\psi]$. The situation is illustrated in Fig. 5.1(b). At the transition point the symmetric solution $x = 0$ is no longer stable and the whole system chooses a certain phase spontaneously. This remarkable effect is referred to as *spontaneous symmetry breaking*.

On the basis of the in-plane translation invariance and the 2D character of cavity-polaritons considered here, it is convenient to express the free energy in the microcavity (x, y)-plane with $\psi_{\downarrow,\uparrow} = \frac{1}{\sqrt{2}}(\psi_x \pm i\psi_y)$. The free energy then reads [76]:

$$F[S_z, n_0] = -\mu n_0 + \frac{1}{4}(\alpha_1 + \alpha_2)\, n_0^2 + (\alpha_1 - \alpha_2)\, S_z^2, \tag{5.3}$$

where the occupation number of the polaritons in the condensate is given by $n_0 = \psi \cdot \psi^* = |\psi_\mathrm{x}|^2 + |\psi_\mathrm{y}|^2 = 4S^2$ (with $S^2 = S_x^2 + S_y^2 + S_z^2$). The nonlinear terms in F account for the polariton-polariton interactions including a repulsion of polaritons with the same spin ($\alpha_1 > 0$) and a weak attraction of polaritons with opposite spins ($\alpha_2 < 0$). This spin anisotropy arises from the dominant role of the exchange term in the polariton-polariton interaction [262]. The chemical potential μ, i.e., the energy needed to add a particle in the system, is fixed by the imbalance between the escape rate $W_\mathrm{out} \sim 1/\tau_\mathrm{pol}(0)$ of polaritons limited by their short radiative lifetime and the income rate W_in into the condensate from the higher energy states. In this framework, μ is simply given by the minimum of the free energy with respect to the total particle number in the condensate: $\delta F[S_\mathrm{z}, n_0]/\delta n_0 = 0$, which directly leads to:

$$\mu = \frac{(\alpha_1 + \alpha_2)}{2} n_0 \,. \tag{5.4}$$

This expression shows that the injection-dependent blueshift observed in photoluminescence experiments depends on the interaction constants and allows an estimation of n_0 above threshold.[57] Similarly, minimizing F with respect to S_z leads to the polarization state at the condensation threshold $S_z = 0$, i.e., the pseudospin $\mathbf{S}$ of the light emitted by the condensate lies in the equatorial plane of the Poincaré sphere, which corresponds to linearly polarized light. Note that the minimum of F is not unique and each realization of the condensate should result in a randomly-oriented linearly polarized state (see Fig. 5.1(b)). Thus, a true BEC requires the build-up of the order parameter, which in turn can be considered as a necessary feature for its existence [52, 263].

Note that the presence of an optical in-plane anisotropy for the cavity mode and/or the exciton will cancel the observation of spontaneous symmetry breaking. In this case F contains an extra term $-\Delta E_{x-y} S_x$, where ΔE_{x-y} is the energy splitting between the two in-plane polarizations x and y [223]. Without loss of generality the lowest energy is assumed to lie along the x-axis in the following. In this case, the minimum of F is reached for $S_y = S_z = 0$. As a consequence, in presence of an optical anisotropy the order parameter is pinned to the x-direction and the same polarization is adopted by the condensate for each experimental realization. However, these considerations are only valid in the thermodynamic limit. Even if this situation is hardly realized in a polariton condensate, this thermodynamic approach gives a qualitative trend, at least in the region of the phase diagram where

[57] Note that the exciton renormalization is neglected here. However, this relation is commonly used to evaluate the energy shift of the polariton ground state observed in photoluminescence experiments, which results in an overestimation of the condensate population.

$R_{th/kin}(\delta, T) > 1$ (see Chapter 4). For this reason the measurements presented hereafter are performed at room temperature, i.e., at a temperature where quasi-thermal equilibrium is reached [264].

5.1.3 Pseudospin dynamics

Due to the one-to-one correspondence between the Stokes vector and the polariton pseudospin components, polaritons with a given momentum $k_\parallel$ can be selectively excited[58] (or observed) in a specific state represented by $\mathbf{S}_{k_\parallel}$ accounting for both spin and dipole moment orientation. The time-evolution of this pseudospin is very complex as it continuously changes under the various influences of effective magnetic fields and due to scattering with phonons, defects and other polaritons. The role of magnetic fields, both internal and external will mix the polarization components, causing the precession of the vector $\mathbf{S}_{k_\parallel}$ and scattering events will tend to destroy the system coherence. In this chapter, only the polariton condensate pseudospin evolution $\mathbf{S} = \mathbf{S}_{k_\parallel=0}$ will be considered.

5.1.3.1 Impact of interactions

In absence of any magnetic fields, the polariton pseudospin randomly evolves in the Poincaré sphere on a time scale given by the coherence time of the condensate τ_{coh} [52, 265]:

$$\frac{1}{\tau_{coh}} \approx \frac{W_{in}}{n_0 + 1} + \frac{1}{\tau_{deph}}, \tag{5.5}$$

where W_{in} is the income rate of polaritons from the exciton reservoir and τ_{deph} is the dephasing time of the condensate. Interestingly, τ_{coh} is affected by two contributions. The first one is driven by the relaxation efficiency toward to polariton ground-state, indicating that the noise in the reservoir significantly impacts on the coherence of the polariton condensate. Note that this term becomes small for large condensate occupation numbers and strongly depends on the pumping scheme, i.e. pulsed or cw [266]. The second term corresponds to the probability for the pseudospin to change its direction and depends on polariton-polariton interactions *via* the interparticle interaction constant V and on the mean particle number in the system $\langle N \rangle$ with a dephasing time $\tau_{deph} = \frac{\hbar\sqrt{2}}{V\sqrt{\langle N \rangle}}$. The critical dependence of the condensate coherence on these two parameters was demonstrated by Love and coworkers [267] who could lengthen τ_{coh} up to ~ 150 ps, a value 30 times longer than that reported in previous experiments [18, 215] thanks to the use of a laser diode being noise-free over the condensate lifetime.

Note finally that the spin state of polaritons is governed by that of electrons and holes. Multiple scattering events with surrounding carriers and the lattice inevitably leads to spin and dipole moment relaxation over a characteristic time scale called *spin relaxation time* τ_{spin}. For GaN at room temperature, τ_{spin} was estimated to ≈ 100 ps for electrons [268]. For excitons this timescale might be even shorter as holes usually relax their spins much faster than electrons in quantum wells. However τ_{spin} is certainly not shorter than 10 ps [221]. In the forthcoming simulations, we assume $\tau_{spin} \approx 30$ ps, which is long compared to the polariton condensate lifetime $\tau^0_{pol} < 1$ ps.

[58] This can be only achieved under resonant excitation.

5.1.3.2 Impact of effective magnetic fields

In the presence of an effective magnetic field $\mathbf{B}_{\text{eff}}$, the pseudospin of each polariton state evolves according to [269]:

$$\frac{\partial \mathbf{S}}{\partial t} = \frac{g_{\text{p}}\mu_{\text{B}}}{\hbar}\mathbf{S} \times \mathbf{B}_{\text{eff}}, \tag{5.6}$$

where $\mu_{\text{B}} = \frac{e\hbar}{2m_0}$ is the Bohr magneton and g_{p} is the effective polariton g-factor (or dimensionless magnetic moment). The effective magnetic field can have different contributions and only act on the radiatively active polariton states, i.e., it does not mix active and dark states. The mathematical form of equation 5.6 indicates that the pseudospin precesses around the effective magnetic field in the Poincaré sphere with a pulsation Ω_{eff} given by:

$$\Omega_{\text{eff}} = \frac{g_{\text{p}}\mu_{\text{B}}}{\hbar} |\mathbf{B}_{\text{eff}}| . \tag{5.7}$$

All effective magnetic fields result from an energy anisotropy ΔE between two poles of the Poincaré sphere. The precession frequency is directly given by the energy splitting *via* $\Delta E = \hbar\Omega_{\text{eff}}$. In Fig. 5.1(a), the situation is schematically depicted in presence of two magnetic fields, i.e. $\mathbf{B}_{\text{self}}$ (splitting between circularly polarized components) and $\mathbf{B}_{x-y}$ (splitting between linearly polarized components).

5.2 Polarization properties of III-nitride-based microcavities

5.2.1 The bulk microcavity: spontaneous build-up of the order parameter

Bulk microcavities are characterized by the absence of a spin quantization axis. As a consequence, polariton-polariton interactions are expected to be isotropic [52] and the polariton effective potential is similar to the one displayed in Fig. 5.1(b). The orientation of the polarization plane is thus sponta-

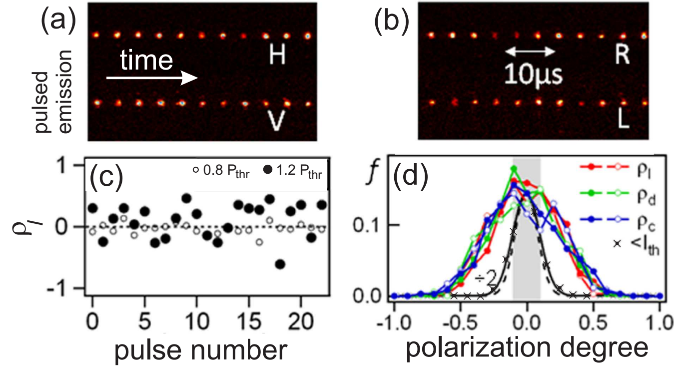

Fig. 5.2: Above-threshold polarization-resolved emission when analyzing along (a) horizontal or vertical and (b) right or left circular bases. (c) Extracted linear polarization degree ρ_{l} showing stochastic variation from pulse to pulse above and below threshold. (d) Histogram of the fraction of each polarization state f along linear, diagonal, and circular bases of nearly 2000 polariton condensates. Open and closed circles show repeated measurements with reversed polarization split (e.g., H=V and V=H), while crosses show below-threshold unpolarized emission statistics (curve divided by 2 to fit on scale, within detection sensitivity shaded gray and scaled dashed line). Adapted from Ref. [52].

neously chosen by the system and the observed polarization degree is changing stochastically from one experiment to another.

In 2008, Baumberg and coworkers have investigated a bulk GaN-based microcavity excited nonresonantly by short optical pulses (150 fs) at room temperature. With the optical setup used, they were able to record for each separate pulse the horizontal, vertical, right- and left-circular polarization degree for each realization of the polariton condensate (see Figs. 5.2(a)-5.2(b)). In Fig. 5.2(c), the linear polarization degree ρ_l is shown for each pulse individually below and above threshold. Interestingly, below threshold, ρ_l is close to zero and acquires a random finite value above. By measuring the polarization degrees for a high number of realizations of the polariton condensate, a polarization histogram is obtained for each basis (Fig. 5.2(d)) showing that linear, circular and diagonal polarization degrees spontaneously build up with comparable magnitudes (≈ 25%). The resulting mean polarization degree $\rho = \sqrt{\rho_c^2 + \rho_l^2 + \rho_d^2} \approx 43\%$ above threshold is reduced compared to the fully coherent case due to the finite condensate coherence time (see Section 5.1.3).

5.2.2 *The multiple quantum well microcavity: pinning of the order parameter*

5.2.2.1 General frame

Contrary to the bulk case, the current GaN quantum well-based microcavity presents a pinning of the order parameter at threshold: $\langle \rho_l \rangle$ does not average to zero. This pinning is commonly observed in all quantum well-based microcavities investigated so far, i.e, in CdTe [18] and GaAs ones [215], and originates from the optical in-plane anisotropy ΔE_{x-y} at $k_\parallel = 0$ of either the excitonic (ΔE^X_{x-y}) or the photonic component (ΔE^C_{x-y}), or from both of them, assuming a linear dependence on the excitonic and photonic fractions:

$$\Delta E_{x-y} = |X_0|^2 \Delta E^X_{x-y} + |C_0|^2 \Delta E^C_{x-y}. \tag{5.8}$$

Since all the above-mentioned material systems are expected to exhibit isotropic optical properties,[59] ΔE^X_{x-y} likely originates from structural non-idealities such as a reduced symmetry of the quantum wells (in or out of plane) as the exciton ground state splitting is forbidden in a perfectly symmetric quantum well [270]. Indeed, due to the vicinal growth of the III-nitride based microcavity on sapphire substrates with a slight miscut, the in-plane crystalline directions are not completely equivalent possibly resulting in a $x - y$ splitting of the excitonic state. In polar quantum well-based microcavities, the presence of a built-in electric field enhances this effect as it separates electrons and holes toward opposite sides of the quantum well, making the exciton more sensitive to interface and alloy disorder [271]. Note that ΔE^C_{x-y} is non-zero only if at least one of the microcavity building blocks exhibits some birefringence (see relation 2.21). However so far no experimental evidence allowed to firmly assess the origin of the mechanism involved in the pinning of the order parameter. The role of ΔE_{x-y} on the polariton population is important since it acts as an effective magnetic field $\mathbf{B}_{x-y}$ in the plane of the structure around which the pseudospin $\mathbf{S}$ can precess according to equation 5.6 [260] (see Fig. 5.1(a)). The relation between the TE-TM energy splitting of the bare modes and the effective magnetic field is given by relation 5.7. Under resonant pumping, ΔE_{x-y} can lead to time beats between circularly-polarized components of the photoemission [272], or to a conversion between linear and circular light polarization [41]. However, in the nonresonant injection scheme, the polariton condensate is formed spontaneously and ΔE_{x-y} causes the pinning of the order parameter as expected from the

[59] Note that GaN is a uniaxial anisotropic material. However, for the c-plane structure investigated here the optical axis coincides with the surface normal and therefore no in-plane anisotropy is expected for $k_\parallel = 0$.

thermodynamic picture, where the energy relaxation brings the system to its lowest energy state, which is a linearly polarized one.

5.2.2.2 Experimental observations

In the experiments presented below the structure already investigated in Chapters 3 and 4 is pumped nonresonantly (~ 1 eV above the condensate emission energy) in order to guarantee the memory loss of the laser polarization. Time-integrated polarization-resolved photoluminescence measurements are performed at room temperature under quasi-cw excitation (τ_{pulse} = 500 ps, repetition rate 8.52 kHz) and give access to the average linear polarization degree $\langle \rho_l \rangle$ of the emitted light.[60] The laser beam was focused down to a 50 μm diameter spot on a sample region and within a power density range where the emission spectrum was unaltered by competing modes. In Figs. 5.3(a) and 5.3(b), the far field emission pattern of the present multiple quantum well based GaN microcavity is displayed at room temperature for $\delta \approx -15$ meV together with the polar intensity plot slightly below and slightly above the polariton condensation threshold, respectively. The system transits from a totally unpolarized state to a highly polarized one with $\langle \rho_l \rangle = 80\%$. Note that this pinning behavior is commonly observed for all sample positions and is independent of temperature and detuning.

It is usually assumed that for quantum-well based microcavities the plane of polarization is pinned along one of the crystalline axes regardless of the semiconductor investigated [18, 211, 215]. In Fig. 5.4(a), the direction of the polarization plane of the emitted light at the condensation threshold is displayed for various sample positions at room temperature (black lines) together with the crystalline orientation a- and m-axes (red arrows). Despite the significant scattering of the reported data, a clear trend is visible: the light is preferentially polarized along the a- and m-axes. However, this observation does not allow to conclude on the mechanism responsible for the pinning of the polarization plane (excitonic or photonic one) as there are two other equivalent a- and m-axes (dashed lines) due to the sixfold symmetry of the wurtzite cell.

[60] The experimentally measured linear polarization degree is averaged over about 200 pulses.

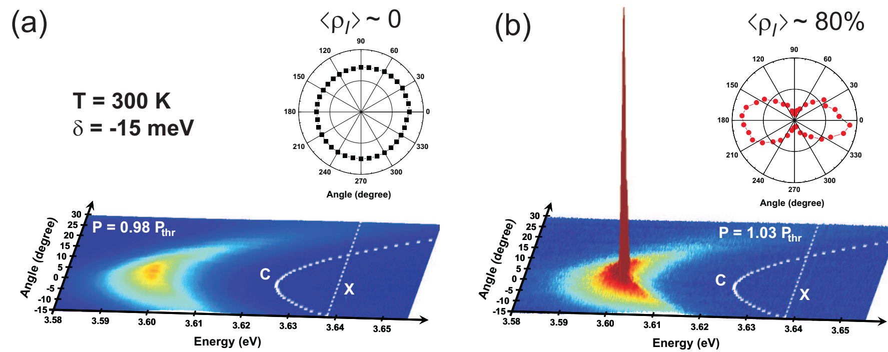

Fig. 5.3: Three-dimensional representation of the far-field emission pattern with the intensity displayed along the vertical axis (linear scale) (a) below and (b) above threshold together with the emission intensity as a function of the linear polarizer angle featuring an average linear polarization degree $< \rho_l >$ of 0 and 80%, respectively. C and X are also reported as white dashed lines. Adapted from Ref. [65].

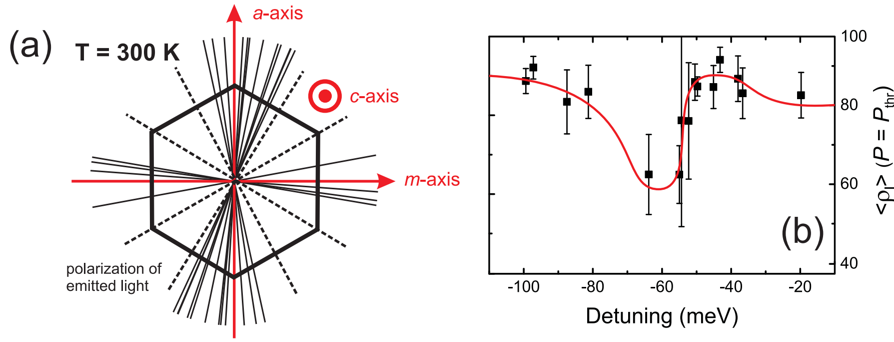

Fig. 5.4: (a) Direction of the polarization plane of the emitted light at room temperature at the condensation threshold for various sample positions (black lines). The crystalline orientation a- and m-axes are also indicated (red arrows). The black dashed lines indicate the two other equivalent a and m-planes. (b) Dependence of the average linear polarization degree as a function of detuning corresponding to the measurements shown in (a). Adapted from Ref. [264].

In principle, one could think to experimentally distinguish between excitonic and photonic mechanisms for the polarization splitting by investigating the dependence of the linear polarization degree at $P = P_{\text{thr}}$ as a function of δ [40]. If the polarization is large at positive detunings, then the mechanism is likely attributed to excitons and *vice versa* for negative detunings. The corresponding measurements are reported in Fig. 5.4(b) for the presently available detunings in our sample at room temperature. The non-monotonous behavior of $\langle\rho_l\rangle(\delta)$ seems to indicate that both mechanisms play some role in the pinning process. However, no conclusion can be drawn on the basis of those measurements only, as the density of carriers in the condensate also significantly changes with δ according to the phase diagram established in the previous chapter. In order to get a deeper understanding of the pinning dynamics and the impact of the carrier density on the order parameter behavior, the power-evolution of $\langle\rho_l\rangle(\delta)$ is investigated in the next section.

5.3 Evolution of the order parameter with carrier density

For the present GaN-based microcavity the ideal thermodynamic picture does not hold above the polariton condensation threshold, where a rapid decrease in $\langle\rho_l\rangle$ with injected carrier density is observed at room temperature for $\delta \approx -40$ meV (see Fig. 5.6(e)). This behavior deviates from the one observed in CdTe-based microcavities at low temperatures [223]. In this latter case, a fast increase in $\langle\rho_l\rangle$ is followed by a saturation with no evidence for a decrease up to $5\,P_{\text{thr}}$. The goal of the present section is to describe both experimentally and theoretically the behavior of the polarization properties above the condensation threshold, accounting for the system specificities.

5.3.1 *Theoretical description*

For a reasonable description of the depinning behavior the stochastic formation of the polariton condensate in the time-domain has to be considered, while accounting for the relative weights of two antagonistic effects: the in-plane static polarization anisotropy that pins the order parameter and the spin dependent polariton-polariton interactions that tend to destroy it as demonstrated hereafter. The polarization behavior of the polariton condensate and its formation is described using a stochastic

approach accounting for the spinor nature or the order parameter $\psi_\sigma(t)$ with $\sigma \in \{\downarrow, \uparrow\}$ [263]. An important role is played by the incoming flux of polaritons from the incoherent reservoir with random phases and polarizations, which is responsible for the stochastic nature of the condensate formation. The order parameter thus evolves following the Langevin-type equation [263]:

$$\begin{aligned} \frac{d\psi_\sigma}{dt} &= \frac{1}{2}\left[W_{\text{in}}(t) - W_{\text{out}}(t)\right]\psi_\sigma + \frac{1}{2}\left[\frac{1}{\tau_{\text{spin}}} + \frac{i}{\hbar}\Delta E_{x-y}\right]\psi_{-\sigma} \\ &- \frac{i}{\hbar}\left[\alpha_1\left|\psi_\sigma\right|^2 + \alpha_2\left|\psi_{-\sigma}\right|^2\right]\psi_\sigma + \theta_\sigma(t)\,. \end{aligned} \tag{5.9}$$

This equation consists of four terms: The first one describes the evolution of the order parameter due to a changing polariton condensate population, which is caused by the imbalance between the income rate from the reservoir $W_{\text{in}}(t)$ and the depletion rate of polaritons at the Brillouin zone center $W_{\text{out}}(t) \sim 1/\tau^0_{\text{pol}}$, which is set by the short radiative lifetime. $W_{\text{in}}(t)$ is usually obtained by solving the set of semi-classical Boltzmann equations (Eqs. 4.18) for a two-level system formed by the condensate and the incoherent reservoir. The second term accounts for the spin relaxation time $\tau_{\text{spin}} \ll \tau^0_{\text{pol}}$ and the in-plane polarization splitting ΔE_{x-y} that is responsible for the pinning of the order parameter. The third term includes the effect of the anisotropic polariton-polariton interactions between polaritons with parallel ($\alpha_1 > 0$) and antiparallel spin orientations ($\alpha_2 < 0$). Its impact rises when the carrier density increases. The last term $\theta_\sigma(t)$ accounts for the shot noise originating from spontaneous scattering of polaritons out of the incoherent excitonic reservoir into the polariton condensate. It is a complex function with correlators $\left\langle\theta_\sigma(t)\theta_{\sigma'}(t')\right\rangle = 0$ and $\left\langle\theta_\sigma(t)\theta^*_{\sigma'}(t')\right\rangle = \frac{1}{2}W_{\text{in}}(t)\delta_{\sigma\sigma'}\delta(t-t')$. The description of the noise is the central point in the stochastic description of the formation dynamics as it is responsible for the fluctuations of phase and polarization in the condensate. It depends on the pumping regime *via* the polariton income rate.

Formally, without $\theta_\sigma(t)$ and without the pinning term ΔE_{x-y}, equation 5.9 is perfectly isotropic and cannot explain the build-up of any preferential polarization. Due to spontaneous scattering modeled by the noise term, some random polarization appears that quickly vanishes below P_{thr} but is amplified above it due to the onset of stimulated scattering. Without energy relaxation pinning is inhibited, since **S** would just precess around the effective in-plane magnetic field $\mathbf{B}_{x-y}$ (see Fig. 5.1(a)) and any polarization would occur with the same probability. Taking into account energy relaxation, the system shifts toward the minimum of free energy resulting in a linearly-polarized state with random orientation. This behavior has been observed in the experiments of Baumberg *et al.* on a bulk GaN microcavity [52] (see Fig. 5.2). The polarization is large for each experimental realization but as it has no preferential orientation, it averages to zero over many pulses. In presence of a ΔE_{x-y} value distinct from zero but without interactions (i.e. when the third term in equation 5.9 is omitted), the lowest energy state would always be pinned along the same direction corresponding to that of $\mathbf{B}_{x-y}$ ($x-$polarized in our case).

The role of interactions is of paramount importance as their contribution to the order parameter evolution increases together with the pump power density. As already mentioned the interactions between polaritons with equal and opposite spin are not equivalent. In the mean-field approximation the anisotropic interaction term reduces to an equation of precession of **S** along an effective magnetic field $\mathbf{B}_{\text{self}}$ oriented in the z-direction with a norm given by [76]:

$$B_{\text{self}} \propto (\alpha_1 - \alpha_2)\left(n_0^\downarrow - n_0^\uparrow\right), \tag{5.10}$$

where $\left(n_0^\downarrow - n_0^\uparrow\right)$ represents the population imbalance between the polariton populations with spin up and down. In the case of a spin-isotropic interaction, i.e., $\alpha_1 = \alpha_2$, B_{self} vanishes. Similarly, in the case

where populations with opposite spins are balanced, B_{self} is also reduced to zero. This corresponds to the general case when θ_σ is neglected in equation 5.9 emphasizing the important role of statistical fluctuations in the process of the polariton condensate formation. Thus, the polariton ensemble experiences the contribution of two magnetic fields: one caused by the static disorder $\mathbf{B}_{x-y}$ being completely power independent and that of $\mathbf{B}_{\mathrm{self}}$, which strongly depends on the injection regime. $\mathbf{B}_{\mathrm{self}}$ is responsible for the precession of the polariton pseudospin around the z-axis and tends to lift any asymmetry in the equatorial plane of the Poincaré sphere. This effect is referred to as self-induced Larmor precession [269, 273]. As a consequence, in the presence of interactions but without pinning, the phase of each condensate realization would exhibit a random polarization state, so that $\langle \rho_l \rangle$ would average to zero as for the bulk case. With $\Delta E_{x-y} \neq 0$ both pinning and interactions compete with each other and the polarization degree continuously changes when the pump increases: the higher the injection the stronger the effect of depolarization due to the pseudospin precession.

5.3.2 Theory vs. experiments

Polarization-resolved photoluminescence studies allow to probe the components of the Stokes vector, which is directly related to the condensate pseudospin $\mathbf{S}$. The polarization degree of the emitted light can be traced out time-dependently [266] with high experimental effort. However, in the present case, it is integrated over several experimental realizations of the condensate (pulsed excitation in the quasi-cw regime, ~ 200 condensate realizations per measurement). For a given realization, i.e., one specific value of θ_σ, the observed polarization corresponds to the normalized time-integrated components s_i with $i \in \{x, y, z\}$:

$$s_i = \frac{\int S_{\mathrm{i}}(t)\, dt}{\int |\mathbf{S}(t)|\, dt} = 2\frac{\int S_i(t)\, dt}{\int n_0(t)\, dt}, \tag{5.11}$$

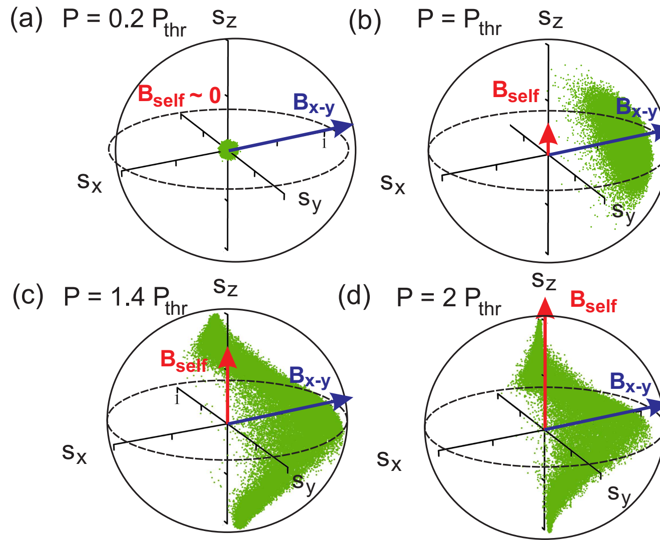

Fig. 5.5: All the figures correspond to room temperature conditions with a detuning of −40 meV. (a-d) Time-integrated simulation of the pseudospin components for different pumping regimes, equal to 0.2, 1, 1.4 and $2\,P/P_{\mathrm{thr}}$, respectively. The increasing role of the self-induced Larmor precession is indicated by the effective magnetic field B_{self} and that of the static influence of pinning by B_{x-y}. Adapted from Ref. [264].

where $n_0(t)$ is the instantaneous condensate occupation number and the time-integration is performed over the whole condensate lifetime. The obtained value of s_i gives precious information about the order parameter ψ as the role of fluctuations is directly reflected by the build-up of the linear polarization degree. As the experimental data displayed in Fig. 5.6(a) represent an average over multiple pulses, it is necessary to average s_i over many realizations of the noise term $\theta_\sigma(t)$. This procedure is repeated for each pump power density of the investigated experimental range between 0 and $2P_{\text{thr}}$ and the obtained normalized pseudospin values are reported in the Poincaré sphere illustrated in Figs. 5.5(a)-5.5(d) [264]. After this averaging procedure, it turns out that $\langle s_y \rangle \sim \langle s_z \rangle \sim 0$, which is consistent with the system symmetry, so that the only remaining contribution comes from $\langle s_x \rangle$. Thus, the experimentally determined degree of linear polarization directly corresponds to $\langle \rho_l \rangle = \langle s_x \rangle$. In Figs. 5.5(a-d) four representative situations are displayed corresponding to:

- $P \ll P_{\text{thr}}$: Far below threshold, when the condensate occupation is low, the effect of pinning is not pronounced. ψ corresponds to an incoherent state and $\langle \rho_l \rangle = 0$.
- $P = P_{\text{thr}}$: At threshold, the condensate formation is fully dominated by the effect of static disorder and $\langle \rho_l \rangle$ is maximum.
- $P_{\text{thr}} < P < P_{\text{max}}$: Both pinning and self-induced Larmor precession compete to be the dominant effect. The resulting $\langle \rho_l \rangle$ is decreased with respect to the threshold case.
- $P = P_{\text{max}}$: For the highest injection regime the Larmor precession sets the tone and lifts any remaining asymmetry in the equatorial plane leading to a value of $\langle \rho_l \rangle$ approaching zero.

From Fig. 5.6(a), it is seen that the behavior of the theoretical curve (black line) closely follows that of experimental data (filled black circles). $\langle \rho_l \rangle$ shows a maximum at $P = P_{\text{thr}}$ followed by a subsequent decrease. The maximum of $\langle \rho_l \rangle$ occurs at a given macroscopic occupation of the condensate, which can be deduced from the blueshift of the emission line at threshold compared to the weak excitation case.[61] The interaction constant α_1 is a fitting parameter of the performed calculation. The best agreement with the data is obtained for $\alpha_1 = 5.7 \times 10^{-5}$ meV. The other parameters used in the calculations are $\tau^0_{\text{pol}} = 0.24$ ps, $\tau_{\text{spin}} = 33$ ps and $\alpha_2/\alpha_1 = -0.1$. The in-plane anisotropy energy between x and

[61] Note that the deduced population might be slightly overestimated as the contribution of the oscillator strength saturation to the total LPB blueshift is neglected here.

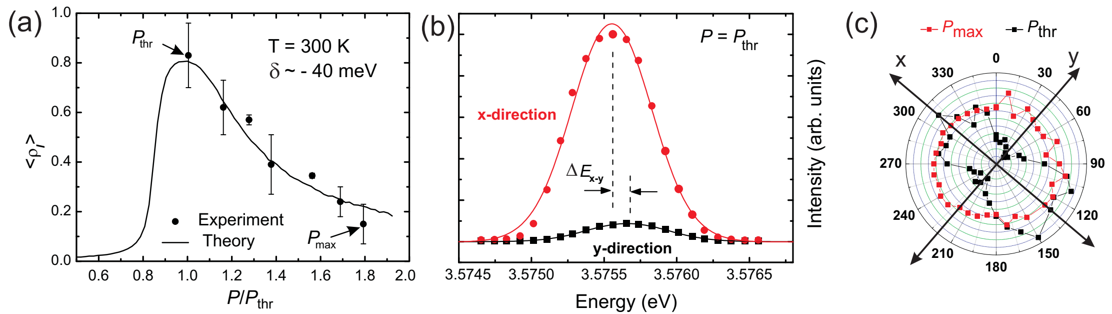

Fig. 5.6: (a) Evolution of the average linear polarization degree $\langle \rho_l \rangle$ as a function of P/P_{thr}. (b) Emission spectra at $P = P_{\text{thr}}$ for the two orthogonal emission directions, corresponding to $x-$ (red circles) and y-polarizations (black squares). (c) Polar plots for the minimum (black squares) and the maximum power regimes (red squares) from threshold. Adapted from Ref. [264].

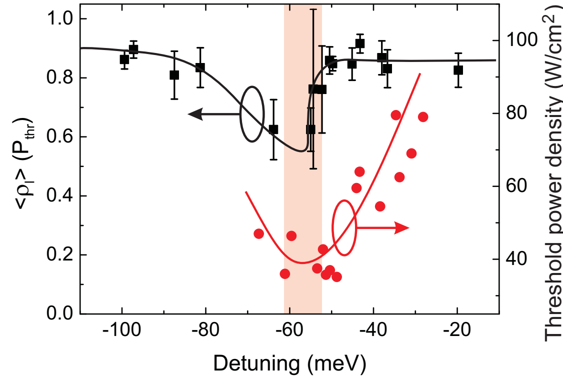

Fig. 5.7: Respective evolution of the average linear polarization degree $\langle \rho_l \rangle$ at the condensation threshold power density P_{thr} (left axis) and P_{thr} (right axis) as a function of δ at room temperature. The coincidence in the minima in terms of detuning highlights the role of the relaxation dynamics in the polariton condensate formation. The continuous lines are guide to the eyes. Adapted from Refs. [264] and [56].

y-direction is estimated to be $\Delta E_{x-y} = 150\,\mu$eV at $P \approx P_{thr}$ (see Fig. 5.6(b)).[62] As expected polariton-polariton interactions do not affect the kinetics of the condensate formation at threshold and the polarization buildup is governed by the static anisotropy in the microcavity plane. Here the polarization degree is large but less than unity due to the presence of fluctuations (see Fig. 5.6(c)). A subsequent increase in the carrier density results in a rapid growth of the condensate occupation and the nonlinear interaction terms in equation 5.9 become more and more important. These terms lead to self-induced Larmor precession, which destroys the polarization pinning so that above threshold polariton-polariton interactions dominate and overwhelm the pinning effect resulting in a nearly unpolarized emission (see Fig. 5.6(c)). In conclusion, the progressive depinning observed experimentally is well described by the competition between the static disorder anisotropy, which dominates in the low density regime, and the Larmor precession at high excitation density, which successively breaks up the degree of linear polarization [264].

The efficiency of the pinning at threshold depends on δ in a non-monotonous way. Intuitively, one would expect that the pinning follows the behavior of equation 5.8, meaning that depending on the polariton character (light or matter-like), $\langle \rho_l \rangle$ reproduces the behavior of ΔE_{x-y} that changes with δ according to the excitonic and photonic fraction of the $k_\parallel = 0$ state. Experimentally, the situation looks more intricate and a minimum of $\langle \rho_l \rangle$ is observed at $\delta \approx -60$ meV (see Fig. 5.7). This peculiar feature can be qualitatively understood from the present model by comparing the evolution of $\langle \rho_l \rangle$ as a function of δ to that of the phase diagram, i.e., the evolution of $P_{thr}\,(\delta, T = 300\,\mathrm{K})$ (see Fig. 5.7). What matters in the present theoretical description is the timescale of polariton relaxation from the reservoir to the condensate. As detailed in Chapter 4, both T and δ govern P_{thr}, an effect directly related to τ_{rel}. In the optimum case $\delta = \delta_{opt}$ the condensate builds-up quickly and the polariton relaxation time is short ($R_{th/kin} = \tau_{pol}/\tau_{rel} = 1$) implying that there is no time for polaritons to relax to the lowest energy state, which would be linearly polarized. This results in an apparent decrease in $\langle \rho_l \rangle$ at $\delta = \delta_{opt}$.

[62] Note that the resolution of the monochromator is comparable with $\Delta E_{x-y} = 150\,\mu$eV, which prevents a clear determination of the LT-splitting.

5.3.3 *Some polarization features in other semiconductor systems: comparison and perspectives*

It is clear from the previous analysis that the suppression of linear polarization holds as long as some circular component of the pseudospin is present due to the shot noise induced by the reservoir. However, in the thermodynamic limit where the polariton lifetime becomes infinitely long, the energy relaxation would bring the system to its lowest energy state and $\langle \rho_l \rangle$ would approach unity at threshold. In addition, $\langle \rho_l \rangle$ is expected to increase with the chemical potential which scales linearly with the polariton condensate occupation according to relation 5.4 [223], contrary to our observations. This behavior was observed by Kasprzak and coworkers in a multiple quantum well CdTe-based microcavity (see Fig. 5.8(a)) for $T_{latt} = T_{eff} = 20\,K$, indicating that the system is thermalized and operates in the thermodynamic regime [223]. In GaN microcavities the build-up of $\langle \rho_l \rangle$ is limited by the kinetics due to the short lifetime of polaritons and the fact that experiments are performed at elevated temperatures. Thus, the difference between GaN [264] and CdTe-based microcavities [223] can be explained by the difference between τ_{pol}^{CdTe} and τ_{pol}^{GaN}. In CdTe-based microcavities the energy relaxation prevents the impact of self-induced Larmor precession. Hence, the free energy approaches its minimum and the polarization vector of the condensate lies in the equatorial plane of the Poincaré sphere along a preferential crystalline direction. In addition, in the experiment from Ref. [223], the condensate was excited by means of a cw laser and therefore did not decay within the characteristic spin relaxation time of polaritons contrary to the present experiment.[63]

In the present study, the polarization properties of a polariton condensate above the condensation threshold have been investigated for a given detuning, i.e. for specific values of the anisotropic interaction constants. Recently, Vladimirova and coworkers have studied both theoretically and experimentally the detuning dependence of α_1 and α_2 in a GaAs-based microcavity (see Fig. 5.8(b)). The respective values of these parameters do not only affect the relaxation of the polaritons driving the depinning of the order parameter but they also critically impact on the nature of the polariton condensation. The universal phase diagram shown in Fig. 5.8(b) indicates for which values of the interaction constants the system could condense in real space (collapse) rather than forming a polariton BEC. The key-ingredient

[63] Here the laser pulse length is comparable to the typical coherence times measured in polariton condensates [267].

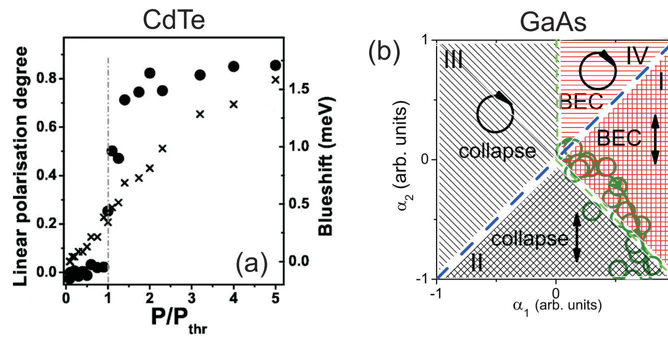

Fig. 5.8: (a) Evolution of the average linear polarization degree vs. P/P_{thr} in a CdTe multiple quantum well based microcavity. Adapted from Ref. [223]. (b) Phase diagram of an interacting polariton gas in the parameter space (α_1, α_2): regions corresponding to the real (reciprocal) space condensation are shown by black (red) color. The polarization of the polariton gas is shown by hatching. A dense hatch stands for a linearly while a rare hatch stands for a circularly polarized state. Adapted from Ref. [218].

to bring the system to critical configurations is to act on α_2, which is usually negative and negligible compared to α_1. For given δ-values α_2 can be enhanced significantly so that the ratio α_2/α_1 can eventually go below -1. In this limit, the polariton-polariton interaction becomes attractive rather than repulsive producing the real space collapse of the BEC. Large values of α_2 can be obtained for instance *via* the attractive biexciton-mediated polariton-polariton interaction. Considering the important role of biexcitons in the presently investigated microcavity (see Section 3.2.4) and the wide range of available detunings leading to polariton condensation, a detailed study of the polariton phase diagram in the parameter space (α_1, α_2) featuring the impact of detuning and temperature on the relaxation dynamics is of high interest.

6 Polariton condensation in anisotropic nonpolar GaN-based microcavities

6.1 Introduction

In the present chapter, the optical properties of GaN multiple quantum well-based microcavities grown along the nonpolar m-plane orientation on bulk GaN substrate are investigated. Contrary to the structure investigated so far, the intrinsic in-plane anisotropy has to be considered as it significantly impacts on the light-matter coupling regime. The results presented here have been obtained during the last year of the present PhD thesis and the described samples are still under investigation at the moment of the writing. In particular, the results presented in the last section - *Possible origin for the lasing mechanism in the weak coupling regime* - are still preliminary and await further experimental observations and theoretical modeling.

6.1.1 Motivation: why going for nonpolar?

In the case of III-nitride heterostructures grown along the [0001]-direction, the polarization mismatch between quantum well and barriers leads to the apparition of a built-in electric field $\mathbf{F}_{bi}$ in the active region, which experiences the so-called quantum confined Stark effect: electron and hole wave functions are separated toward opposite edges of the well, resulting in a decrease in the exciton oscillator strength. This effect is highly undesirable for the design of microcavities operating in the strong coupling regime as it directly reduces the vacuum Rabi splitting compared to the flat band potential configuration. For this reason growth along nonpolar surface orientation - $(10\bar{1}0)/m$-plane or $(11\bar{2}0)$/a-plane - is of large interest as it suppresses $\mathbf{F}_{bi}$ [141, 142], even if the achievement of a high crystal quality is still challenging.

The absence of quantum confined Stark effect reinforces not only the exciton transition but it also allows more freedom in the sample design. In the case of the c-plane multiple quantum well microcavity discussed in Chapters 3-5, the quantum wells are homogeneously distributed in the cavity to avoid the broadening induced by built-in electric field fluctuations. Even if such a design considerably simplifies the growth of the active region, it strongly affects the strong coupling regime by introducing undesirable absorption from uncoupled quantum wells. In nonpolar microcavities, we can envisage a more traditional design where quantum wells are located at the antinodes of the electric field standing wave. This design is the one usually considered in other semiconductor systems, such as GaAs [202] or CdTe [18].

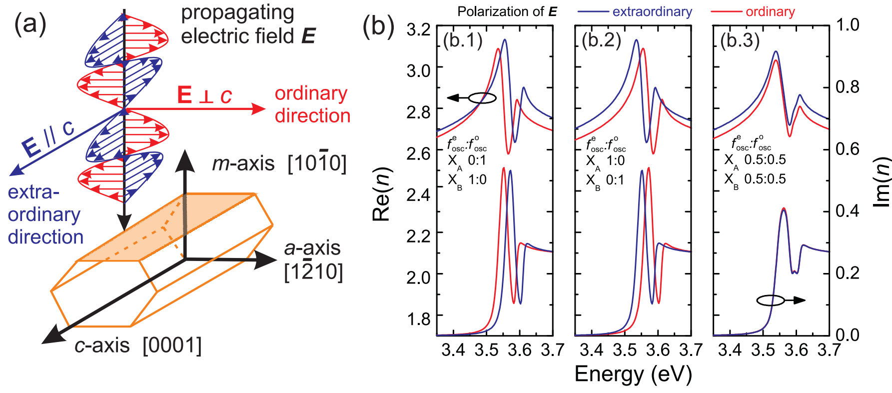

Fig. 6.1: (a) In III-nitride compounds grown along the m-axis, the optical electric field **E** experiences a different optical response along the a- and c-axes (ordinary and extraordinary axes, respectively). (b.1)-(b.3) Real and imaginary parts of the refractive index vs. energy of a nonpolar GaN quantum well for light propagating along the ordinary (red lines) and extraordinary (blue lines) directions calculated in the Drude-Lorentz approximation accounting for the inhomogeneous broadening and the electron-hole continuum absorption. The curves are displayed for different relative oscillator strengths between A and B excitons.

6.1.2 *Optical anisotropy, a fair price to pay*

Switching from the high symmetry axis corresponding to the polar orientation to a nonpolar one by rotating the crystal by 90° inevitably affects the optical properties. In particular, the new in-plane optical axes are no longer equivalent. This optical anisotropy is twofold as it affects both real and imaginary parts of the complex dielectric constant tensor (see relation 2.19) and is traduced by the presence of *birefringence* and *dichroism*, respectively. Birefringence occurs when light propagating with the electric field vector **E** polarized perpendicular (ordinary direction) and parallel to the optical c-axis (extraordinary direction) experiences different refractive indices n_o and n_e, respectively (see Fig. 6.1(a)). The birefringence magnitude is defined as the difference $\Delta n = n_e - n_o$ and is usually positive in III-nitrides below the band gap [172]. In a microcavity, birefringence will inevitably lead to anisotropic cavity modes with the lowest energy mode oriented along the extraordinary direction as $n_e > n_o$. Dichroism is related to the imaginary part of the dielectric tensor and is manifested by a polarization-dependent absorption profile, i.e., the active medium will exhibit a different oscillator strength (f_{osc}) for light polarized along the two orthogonal directions.

In Figs. 6.1(b.1)-6.1(b.3), the real and imaginary parts of the refractive index are shown as a function of energy for a GaN layer for light propagating along the ordinary (a-axis) and extraordinary (c-axis) directions. The refractive index is calculated in the Drude-Lorentz approximation accounting for the inhomogeneous broadening and the electron-hole continuum (see relations 1.29-1.32). The dispersions are shown in the case where only A and B excitons,[64] termed X_A and X_B with respective energy equal to 3.55 and 3.57 eV, are considered for different distributions of the relative oscillator strength between the two orthogonal directions. The distribution between the different excitons relies on the symmetry of each band. As the response of the conduction band has an almost isotropic response with symmetry Γ_7^c, the selection rules for the different transitions are determined by the symmetry of the three valence bands with symmetry Γ_9^v, Γ_7^c and Γ_7^c, for X_A, X_B and X_C, respectively. In the specific case of unstrained

[64] The contribution of the C exciton is usually negligible in GaN compressively strained on nonpolar (Al,Ga)N epilayers [175, 274]. This point is discussed in more details in Section 6.4.2.

GaN, the lowest energy transitions X_A and X_B dominate the optical response for the ordinary direction, while C rules the extraordinary one (see Tab. 2.6). In strained layers, the selection rules are altered and the total oscillator strength is redistributed between the optically active excitons according to the Thomas-Reiche-Kuhn sum rule [15]. Neglecting the contribution of the C exciton, X_A and X_B radiate with complementary weights along the two directions. In Fig. 6.1(b1), X_A only radiates in the e-direction and X_B in the o-direction. The situation is reversed in Fig. 6.1(b2) and finally in Fig. 6.1(b3), the isotropic case is shown, i.e., X_A and X_B have the same oscillator strength. The effect of strain on the selection rules will thus considerably affect the nature of the coupling regime between excitons and cavity modes along the two orthogonal directions [275](see Section 6.4.2). Indeed, according to relation 1.50, the anisotropy of the oscillator strength will result in an anisotropy of the light-matter interaction constant g. Anisotropic microcavities are thus a fascinating playground to investigate either birefringence effects or the impact of the exciton oscillator strength anisotropy on the emission properties. Among the possible coupling regimes, which can arise from the bare mode anisotropy, one might obviously expect to observe light emission either in the weak or in the strong coupling regime for both directions [35, 275]. In 2010, Kéna-Cohen and Forrest reported on room temperature polariton lasing in an anisotropic organic microcavity where orthogonal linearly polarized polariton branches were observed with lasing occurring at the bottom of the lowest energy mode [35].

6.1.3 State of the art before this work

The first realization of a passive nonpolar III-nitride microcavity (without active region) was obtained in 2008 by Zhu and coworkers at EPFL [174]. A microcavity grown on an a-plane template with a bulk GaN λ-spacer layer using the so-called epitaxial lateral overgrowth (ELO) technique was achieved. The ELO approach allowed to considerably improve the surface morphology in the wing regions [276, 277]. A stopband width of the 13 pair AlN/GaN bottom DBR of ~ 250 meV and a quality factor $Q \approx 100$ was reported. Finally, the impact of birefringence was clearly observed *via* the shift of the cavity mode energy ($\Delta E \approx 47$ meV) between ordinary ($\mathbf{E} \parallel m$-axis) and extraordinary directions ($\mathbf{E} \parallel c$-axis).

The first demonstration of strong coupling regime in a nonpolar based microcavity followed one year later with the work of Mastro and coworkers on a nonpolar a-plane $\lambda/2$ microcavity with 3 embedded GaN/$Al_{0.8}Ga_{0.2}N$ quantum wells positioned at the antinode of the electric field [278]. The sample was grown by metalorganic chemical vapor deposition on r-plane sapphire substrate yielding a relatively rough surface. They observed the signature of anticrossing between cavity and exciton modes in reflectivity measurements featuring a vacuum Rabi splitting of about 40 meV for both ordinary and extraordinary directions at room temperature, but no transition toward the nonlinear regime.

6.2 Growth and structural properties

In the present chapter, we will discuss the properties of nonpolar based microcavities *via* the presentation of two successive sample generations, all grown on nonpolar $(10\bar{1}0)$ m-plane bulk GaN substrates by molecular beam epitaxy using ammonia as a nitrogen source. The choice of the m-plane orientation was motivated by unsuccessful trials of microcavity growth along the nonpolar a-orientation and also by the availability of m-plane bulk GaN substrates provided by UNIPRESS. The samples described in the present chapter are all grown on a 100 μm thick m-plane bulk GaN substrate to minimize the lattice mismatch and differences in the thermal expansion coefficients preventing the formation of cracks during the growth of the microcavity. To obtain these m-plane GaN substrates a procedure of subsequent growth runs by hydride vapor phase epitaxy method was used [279]. The surface roughness

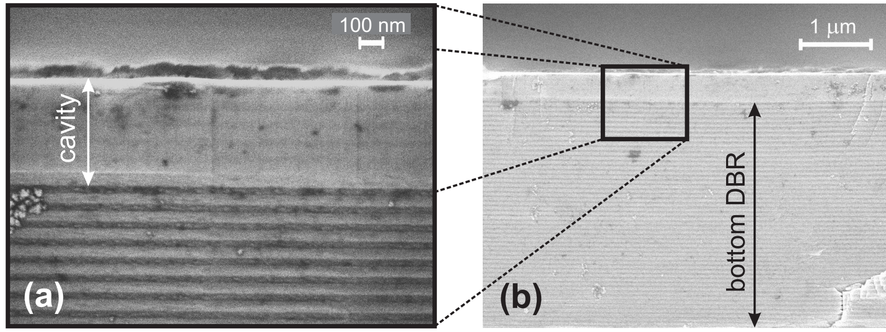

Fig. 6.2: (a) Enlarged cross-section SEM image of the cavity section deposited on top of a 50-pair (Al,Ga)N-based DBR. (b) Cross-section SEM view of the whole structure (without top DBR).

measured by atomic force microscopy (AFM) is 1.4 nm over an area of $10 \times 10\,\mu\text{m}^2$. The etch pit density on the $(10\bar{1}0)$ plane varies from 5×10^5 to $2 \times 10^6\,\text{cm}^{-2}$.

In the following, we will term the investigated samples by *generation 1* (G1) and *generation 2* (G2), respectively. The term *generation* encompasses a set of samples grown on the same bulk GaN substrate and consists of different microcavity building blocks, the half-microcavity (active medium grown on top of the bottom DBR) and the full microcavity after deposition of the top dielectric DBR. Cross-section scanning electron microscopy images of the G2 half-microcavity are shown in Figs. 6.2(a)-6.2(b) for two different magnification levels. Note that the present images correspond to the G2-sample but both generations present similar structural qualities and share the same bottom DBR design, i.e. 50 pairs of $Al_{0.15}Ga_{0.85}N/Al_{0.35}Ga_{0.65}N$ quarter wave layers. The pairs are nicely visible due to atomic mass contrast between the bilayer components, evidencing smooth interfaces. On top of the DBR the cavity region containing the five sets of GaN quantum wells is well resolved.

Figure 6.3(a) shows a $10 \times 10\,\mu\text{m}^2$ AFM-scan of the sample surface. Again, the image is shown only for the G2-sample but it looks similar for the G1 generation. The different growth rates along the *a* and *c*-directions lead to an anisotropic surface morphology featuring grooves aligned along the *c*-axis. The line scan along the *a*-axis displayed in Fig. 6.3(a) (corresponding to the white arrow in Fig. 6.3(b))

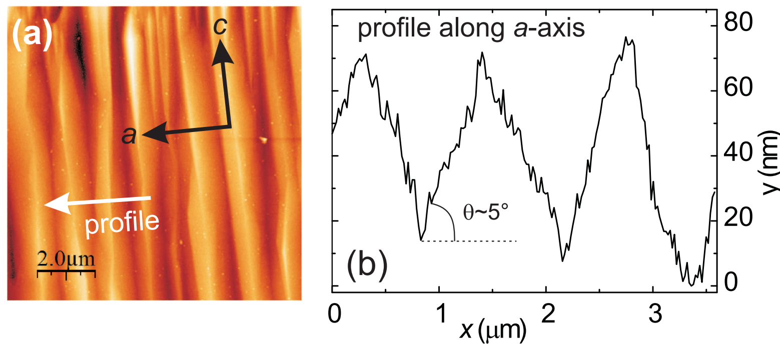

Fig. 6.3: (a) $10 \times 10\,\mu\text{m}^2$ AFM scan with indication of the crystal orientations. (b) Profile of the surface taken along the *a*-axis. The mean angle formed by the facets with respect to the surface plane approximately amounts to 5°.

shows a saw tooth profile of alternating valleys and peaks. The mean distance between two successive maxima approximately amounts to 1 μm, whereas the mean height difference does not exceed 70 nm yielding a rms surface roughness of ~ 25 nm. In comparison, the facets are much smoother exhibiting a rms surface roughness reduced by about one order of magnitude. Note finally that despite the angle between the facets and the plane of the sample ($\theta \approx 5°$), the projection of the polarization field along the growth direction remains zero as the c-axis is parallel to the grooves.

6.3 Samples of first generation: Bragg polaritons

6.3.1 Sample design

The first sample generation represented in Fig. 6.4 is grown on an m-plane bulk GaN substrate homoepitaxially overgrown with 400 nm of GaN by molecular beam epitaxy (ammonia source MBE). Subsequently, a 50 pair $Al_{0.15}Ga_{0.85}N/Al_{0.35}Ga_{0.65}N$ DBR with nominal layer thicknesses of 34.3 nm and 36.8 nm, respectively, was deposited. The active region consists of five sets of three GaN quantum wells separated by 25.9 nm of $Al_{0.13}Ga_{0.87}N$. Each section is formed by three 8 nm thick GaN quantum wells separated by 8 nm thick $Al_{0.13}Ga_{0.87}N$ barriers. They are located at the antinodes of the 3λ-cavity. The active region is surrounded by two $Al_{0.13}Ga_{0.87}N$ spacer layers with a thickness of 45.9 nm. Finally the top dielectric DBR consisting of eight SiO_2/ZrO_2 pairs was grown by electron beam evaporation with nominal layer thicknesses of 61.5 nm and 51.9 nm, respectively.

The design of the bottom $Al_{x_1}Ga_{1-x_1}N/Al_{x_2}Ga_{1-x_2}N$ DBR was dictated by several contradictory constraints. First of all, a high refractive index contrast between the two bilayer components is mandatory to have a low pair numbers to achieve a high reflectivity and a small penetration length of the electric field into the DBR. This condition is optimum when the ratio x_2/x_1 is maximized, i.e. for a GaN/AlN DBR. Such a choice raises two issues. The first one is the absorption of the light emitted by the quantum wells, which imposes to keep x_1 as high as possible. The second issue is the strain accumulation occurring in the DBR, which should be minimized in order to prevent the formation of cracks and dislocations yielding the second constraint that $|x_2 - x_1|$ should be minimized. Considering transfer-matrix simulations, strain estimations and residual absorption in the low aluminum content layer, the best compromise was found for $x_1 \approx 0.15$ and $x_2 \approx 0.35$.

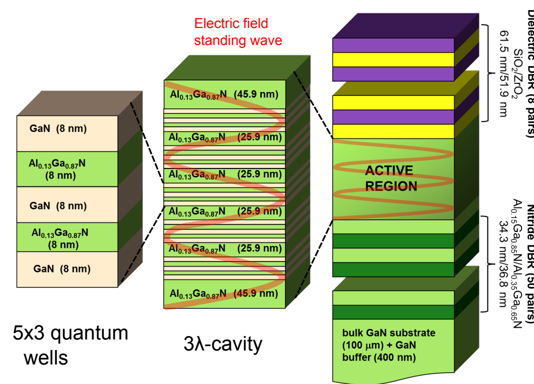

Fig. 6.4: Schematic representation of the first generation samples. The active region is zoomed in for the sake of clarity.

The active medium consists of five sets of three GaN/$Al_{0.13}Ga_{0.87}N$ quantum wells located at the antinode of the electric field. The choice of the layer thickness was dictated by a previous study on single GaN/(Al,Ga)N quantum wells grown on *a*- and *m*-plane bulk GaN substrates also provided by UNIPRESS (Poland). In particular, it was shown that the highest optical quality was achieved for a thickness of 8 nm [280]. The evolution of the exciton inhomogeneous broadening at T = 10 K is shown in Fig. 6.6(a) as a function of the quantum well thickness for a series of single GaN/(Al,Ga)N quantum wells with different aluminum contents grown along the *a*-plane orientation. The reason for the decrease in the inhomogeneous broadening of wide quantum wells is the small leakage of the exciton wave function in the barrier, minimizing the impact of alloy disorder on exciton localization.

6.3.2 Half-microcavity

As the bottom nitride DBR and the active medium were grown during the same run, the optical properties of these two building blocks are investigated simultaneously. In Fig. 6.5(a), room temperature micro-photoluminescence spectra performed under nonresonant cw excitation (λ = 244 nm) with an excitation power density of 2 kW/cm^2 are reported for random positions over the sample surface, featuring a mean quantum well exciton energy of 3.480 ± 0.01 eV with a linewidth of 56 ± 4 meV. Here, the excitonic properties suffer from relatively large in-plane fluctuations revealed by a pronounced luminescence from defects at some sample positions.

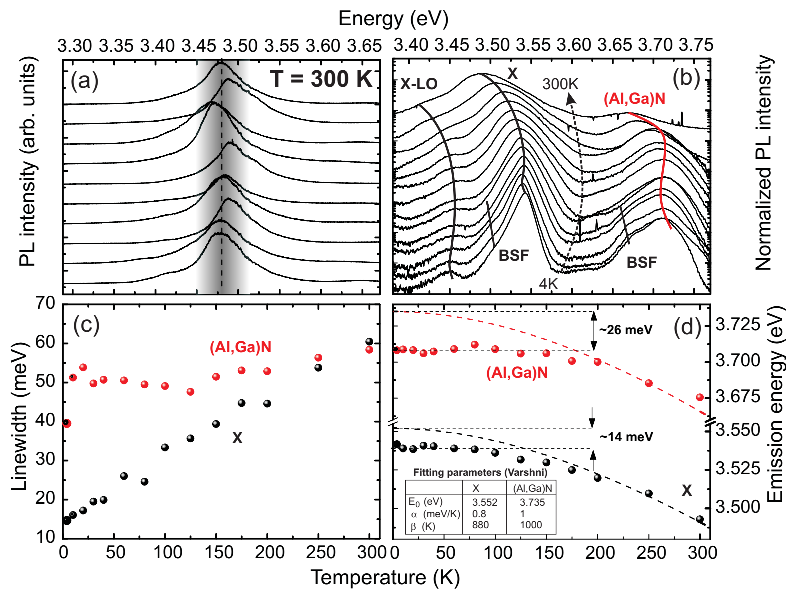

	X	(Al,Ga)N
E_0 (eV)	3.552	3.735
α (meV/K)	0.8	1
β (K)	880	1000

Fig. 6.5: (a) Normalized micro-photoluminescence spectra measured at room temperature for various random positions on the sample surface. (b) Temperature-dependent micro-photoluminescence spectra obtained under nonresonant cw excitation. The spectra are normalized and vertically shifted for the sake of clarity. The quantum well emission is labeled with X, the barrier with (Al,Ga)N. The exciton first LO-phonon replica (X-LO) and the BSF emission lines are also shown. (c) Linewidth and (d) peak energy of the barrier (red dots) and the quantum well emission (black dots) as a function of temperature.

Figure 6.5(b) shows temperature-dependent micro-photoluminescence spectra measured under non-resonant cw excitation ($\lambda = 244$ nm) without polarization selection. Both quantum well and barrier emission are clearly visible from 4 to 300 K. Between 4 and 30 K (first four spectra), an additional emission line stemming from defect states occurring approximately 45 meV below the X-transition is visible and can likely be attributed to basal stacking faults (BSFs), a feature commonly observed in nonpolar GaN-based quantum well structures [281]. Finally, the first longitudinal-optical phonon replica of the quantum well ($X - LO$) is visible for all temperatures. In Fig. 6.5(c), the peak energy of the barrier (red) and the quantum well emission (black) are displayed as a function of the lattice temperature. Assuming that the carriers are delocalized at room temperature, a fit using the semi-empirical Varshni's law (see equation 2.17) provides the temperature evolution of the free exciton for the quantum well and barrier excitons. The fitting procedure yields for the energies at zero temperature 3.552 and 3.735 eV for the quantum well exciton and the (Al,Ga)N barrier, respectively. Comparing the fits with the experimental data, localization energies of 14 and 26 meV are deduced for the excitons in the quantum wells and in the barriers, respectively.

In Fig. 6.6(b), the wave function of the electron and the hole is calculated for one quantum well using the envelope function formalism within the Numerov approximation (see Appendix A). It appears that the penetration length of the electronic wave functions is sufficiently small to prevent the formation of minibands in the active region. All quantum wells can thus be treated as independent emitters. Repeating this calculation for different quantum well thicknesses leads to the evolution of the exciton binding and confinement energies (Fig. 6.6(c)).[65] For the specific case of the G1 sample (black and red dashed lines), we find a confinement energy E_X^{conf} of about 21 meV and an exciton binding energy of 35 meV. Even if this choice does not look optimal from the point of view of the exciton stability, thick quantum wells provide the best optical quality in terms of optical linewidth. From Fig. 6.5(d), it appears that the exciton linewidth does not exceed 60 meV at room temperature and the inhomogeneous broadening is of the order of 15 meV, making possible the observation of the strong coupling regime nearly up to room temperature. This point is supported by previous studies where it was shown that an inhomogeneous broadening comparable to the value of the vacuum Rabi splitting inevitably leads to

[65] The exciton binding energy was calculated with a different program already available in our laboratory and using the transfer matrix formalism.

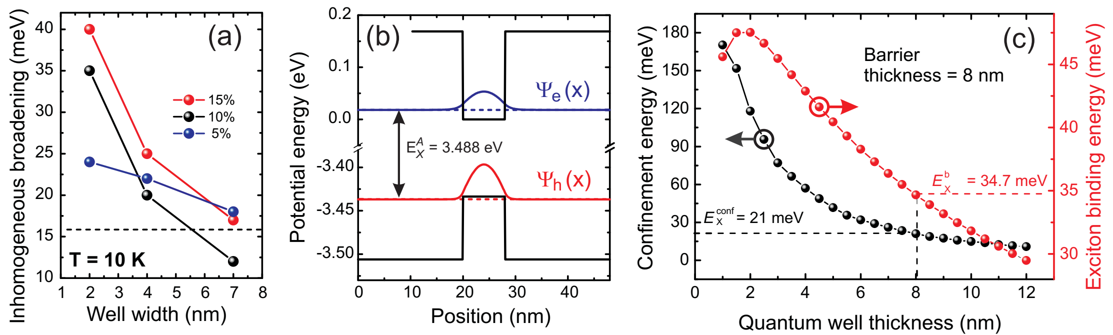

Fig. 6.6: (a) Evolution of the exciton inhomogeneous broadening at $T = 10$ K as a function of quantum well thickness for a series of single GaN/(Al,Ga)N quantum wells with different aluminum contents grown along the a-plane orientation. Adapted from Ref. [280]. (b) Envelope function simulation of the G1-sample active region in the Numerov approximation. (c) Evolution of the confinement and exciton binding energies vs. quantum well thickness. The presently envisaged design is highlighted with dashed lines.

the loss of the strong coupling regime [66]. The condition $\Omega_{VRS} > 15$ meV is easily fulfilled for wide band gap semiconductors such as GaN [53, 175]. Note that the homogeneous broadening of the multiple quantum well structure compares well with the value expected from a previous analysis on single GaN/(Al,Ga)N quantum wells grown along the nonpolar a-plane orientation (see horizontal dashed line in Fig. 6.6(a)).

The growth along a nonpolar orientation cancels the detrimental impact of the quantum confined Stark effect on the excitonic transition. However, assuming that the quantum wells are pseudomorphically grown, one should account for the compressive strain inherited from the underlying (Al,Ga)N layers.[66] The energy shift due to strain δE_{strain} can be estimated from the photoluminescence emission energy E_X^{PL} by:

$$\delta E_{\text{strain}} = E_X^{\text{PL}} + \delta E_X^{\text{loc}} - E_G + E_X^{\text{b}} - E_X^{\text{conf}}. \tag{6.1}$$

At $T = 4$ K, the band gap edge energy amounts to 3.502 eV, which leads to $\delta E_{\text{strain}} \approx 68$ meV. The positive energy shift is consistent with the expected compressive strain inherited from the (Al,Ga)N underlying layers. In order to evaluate δE_{strain}, we performed $k \cdot p$ calculations following the approach of Chuang and Chang [167] with material constants taken from Refs. [153] and [282] assuming that the structure is pseudomorphically grown with an average lattice constant corresponding to an equivalent $\text{Al}_{\bar{x}}\text{Ga}_{1-\bar{x}}\text{N}$ layer (see Fig. 6.7(a)). Considering the thick stack of layers forming the bottom DBR (see Fig. 6.7(a)), one can reasonably assume that it is relaxed to an intermediate lattice constant $\bar{x}$ intermediate between that of the bottom DBR bilayer components, $x_1 = 15\%$ and $x_2 = 35\%$ (see Fig. 6.7(a)). Using a geometrical argument, we can estimate $\bar{x}$ as:

$$\bar{x}_{\text{geom}} = \frac{d_1 x_1 + d_2 x_2}{d_1 + d_2}, \tag{6.2}$$

where d_1 and d_2 are the thicknesses of the bottom DBR (Al,Ga)N bilayer components with low and high aluminum content, respectively. For the present structure ($d_1 = 34.3$ nm and $d_2 = 36.8$ nm), we find $\bar{x}_{\text{geom}} \approx 25.4\%$. The assumption that the bottom DBR is relaxed with a mean lattice constant is confirmed by complementary X-ray diffraction (XRD) measurements performed at UNIPRESS revealing

[66] Note that the effective hole mass along the growth direction is increased by the strain experienced by the GaN layer, while the effective electron mass is almost unaffected. As a result, the hole confinement energy is decreased and the reduced effective mass is mainly governed by the effective electron mass $m_e^* \approx 0.2 m_0$.

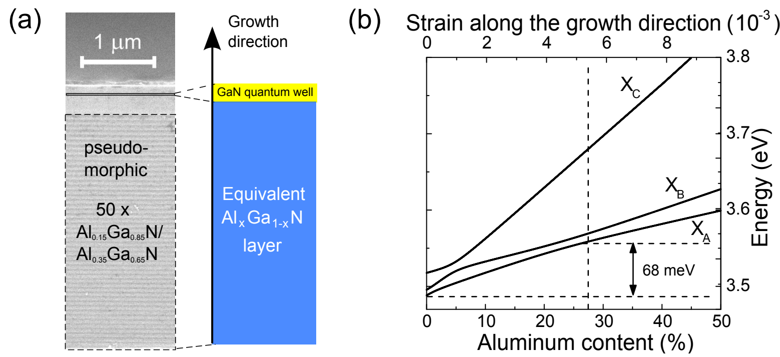

Fig. 6.7: (a) Model for the $k \cdot p$ simulations: the active region (yellow) is pseudomorphically grown on the thick bottom DBR represented by a mean lattice constant corresponding to an equivalent $\text{Al}_x\text{Ga}_{1-x}\text{N}$ layer (blue). (b) Evolution the A, B and C exciton energies vs. mean aluminum content x (bottom) and strain along the growth direction (top). The values corresponding to the presently investigated sample are highlighted with dashed lines.

that the strain is relaxed within the first pairs of the DBR, which results in intermediate lattice constants corresponding to $\bar{x}_{XRD} \approx 28\%$, which is in relatively good agreement with the value estimated by the previous geometrical argument. The same lattice constant is then kept over the whole structure, including the cavity section and the quantum wells.

In Fig. 6.7(b), the energy of A, B and C excitons is calculated for different strain states corresponding to different average aluminum contents $\bar{x}$.[67] The case $\bar{x} = 0$ corresponds to the unstrained case, i.e. GaN grown on GaN. Increasing the aluminum content, the compressive strain is also rising resulting in a blueshift of the transition energies. Interestingly, the aluminum content at which the A exciton transition is shifted by $\delta E_{strain} = 68$ meV corresponds to $\bar{x} = 27.5\%$, which is in perfect agreement with $\bar{x}_{geom}$ and $\bar{x}_{XRD}$. For the present strain state, only A and B excitons are considered as they are close in energy, whereas the C exciton will not significantly contribute to the optical response due to its high energy. Note finally that this $k \cdot p$ treatment is only valid for band-to-band transitions in bulk layers where quantum confinement and excitonic contributions are neglected. Nevertheless, it was shown that excitons nearly behave as the bands they belong to in bulk GaN [163] and that the influence of confinement is marginal even for GaN quantum wells thinner that the ones investigated in the present study [283].

6.3.3 *Full microcavity*

The main concerns when designing a microcavity aiming to operate in the strong coupling regime are on the one side a high structural and optical quality of the active medium and on the other side a good spectral matching between the various building blocks, i.e. the bottom DBR, the active region and the top DBR. In Fig. 6.8(a), room-temperature micro-photoluminescence and micro-reflectivity spectra taken on the half-microcavity for polarization parallel to the c-axis (extraordinary direction) are shown. This figure highlights the narrow stopband of the bottom DBR due to the low refractive index contrast between the bilayer components and also the important detuning between the center of the stopband and the quantum well emission line ($\Delta E = 127$ meV). This shift is reduced to 60 meV at

[67] The exciton energies are calculated from the band-to-band transition considering the confinement and exciton binding energies of the present structure.

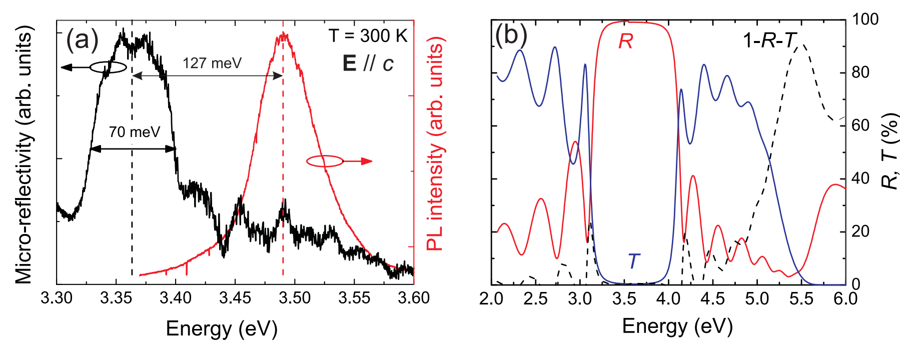

Fig. 6.8: (a) Room-temperature micro-photoluminescence and micro-reflectivity spectra taken on the half-microcavity for light polarization parallel to the c-axis (extraordinary direction). (b) Reflectivity (red line) and transmission (blue line) of the 8 pair SiO_2/ZrO_2 top DBR featuring a peak reflectivity of 98.5% and a stopband width of approximately 1 eV. The quantity $1 - R - T$ is plotted with a black dashed line.

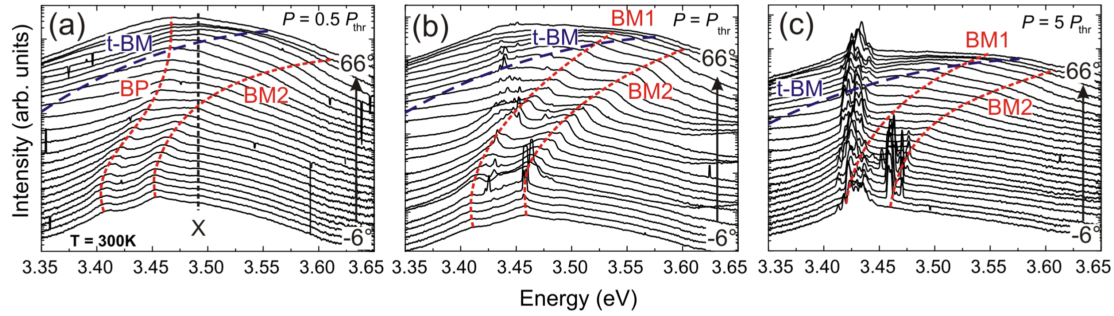

Fig. 6.9: Room temperature photoluminescence spectra of the full microcavity G1 for angles ranging between 6 and 66° with steps of 3° and an angular selection $\Delta\theta \approx 1°$ for three different pump powers: (a) $P/P_{thr} = 0.5$, (b) $P/P_{thr} = 1$ and (c) $P/P_{thr} = 5$, where $P_{thr} \approx 75\,W/cm^2$ is the average threshold power density.

$T = 4\,K$, but nevertheless the strong coupling regime between the cavity mode and the quantum well exciton is seriously compromised. The half-microcavity is finally completed with a 8 pair SiO_2/ZrO_2 top DBR. In Fig. 6.8(b), reflectivity (red line) and transmission (blue line) spectra of the top DBR are shown featuring a peak reflectivity of 98.5% and a stopband width of approximately 1 eV. Assuming that scattering is negligible, the quantity $1 - R - T$ (black dashed line) provides a reliable signature of the absorption in the DBR (black dashed line), which becomes large above 5 eV only.[68]

The full microcavity was then investigated at room temperature by means of angle-resolved photoluminescence for angles ranging between −6 and 66° with steps of 3° and an angular selection $\Delta\theta \approx 1°$ for three different pump powers, i.e. for $P/P_{thr} = 0.5$, 1 and 5, where $P_{thr} \approx 75\,W/cm^2$ is the average threshold power density (see Figs. 6.9(a)-6.9(c)). The measurements were performed without polarization selection so that both ordinary and extraordinary components of the electric field are detected. Below P_{thr}, two modes are clearly visible with strongly pronounced dispersions, labeled as BP and $BM2$[69] in Fig. 6.9(a). The BP mode converges to the free exciton line (labeled X, black dashed line) for high angles resulting in a non-parabolic dispersion whereas $BM2$ has a regular quadratic dispersion. Due to the strong mismatch between the bottom DBR stopband and the quantum well emission energy, the BP mode cannot result from the strong coupling between the exciton and the cavity mode but rather with the first Bragg mode ($BM1$) located on the high energy side of the bottom DBR stopband (see Fig. 6.8(a)). The first Bragg mode arising from the top DBR ($t - BM$) is also visible on the photoluminescence spectra and is indicated with a blue dashed line.

At $P = P_{thr}$, two interesting features occur. First, the BP mode does no longer follow a non-parabolic dispersion but it also presents a parabolic dispersion similar to that of $BM2$, indicating the loss of the strong coupling regime between X and $BM1$. Second, the nonlinear emission comes from both $BM1$ and $BM2$ modes with a much higher intensity for $BM2$. This feature can be explained by the higher spectral overlap between the emission line shape and $BM2$ and is not compatible with the polariton lasing picture as the strongest emission intensity would then be expected from the lowest energy mode. These two observations confirm that the system is in the weak coupling regime with appearance of a nonlinear emission originating from the two nearest modes coupled to the vacuum field, namely $BM1$ and $BM2$. Note also that lasing is also visible at higher angles. This surprising feature could be due to

[68] The energy position of the absorption edge allows to use a Nd:YAG laser ($\lambda = 266\,nm$) as an excitation source without causing significant damage to the top DBR.

[69] BP and BM stand for Bragg polariton and Bragg mode, respectively.

scattering on the sample surface, which presents a saw tooth profile (see Fig. 6.3(a)) and becomes more pronounced at higher pump power densities. For $P = 5\,P_{\text{thr}}$ for instance, the nonlinear emission is very intense for all angles with a maximum centered at $\theta = 0°$.

The situation is even made more complicated by the intrinsic in-plane anisotropy between the c- and a-axes. In Figs. 6.10(a) and 6.10(b), micro-reflectivity performed on the half-microcavity for various collection angles are shown for the electric field polarized along the two polarization planes, i.e. $\mathbf{E} \parallel c$ (extraordinary direction) and $\mathbf{E} \perp c$ (ordinary direction), respectively. Interestingly, the optical properties drastically differ for the two configurations, i.e. the energy position and the spectral width of the stopband do not coincide due to the intrinsic birefringence of III-nitrides ($n_{\text{o}} < n_{\text{e}}$). Considering the energy position of the first two Bragg modes along the two directions, it appears that the modes labeled $BM1$ and $BM2$ in Figs. 6.9(a)-6.9(c) likely correspond to the first Bragg mode along the extraordinary and ordinary direction, i.e. $BM1 = BM1_{\text{e}}$ and $BM2 = BM1_{\text{o}}$. In addition to birefringence, which is mainly affecting the position of the cavity and Bragg modes, the anisotropic distribution of the quantum well oscillator strength of the excitonic transition(s) should also be accounted for. The complexity of the G1 sample generation due to the presence of multiple Bragg modes along each direction and the strong in-plane anisotropy makes the study of the system far too complex. For this reason, a second sample generation was designed in order to correct the detuning between the different microcavity building blocks.

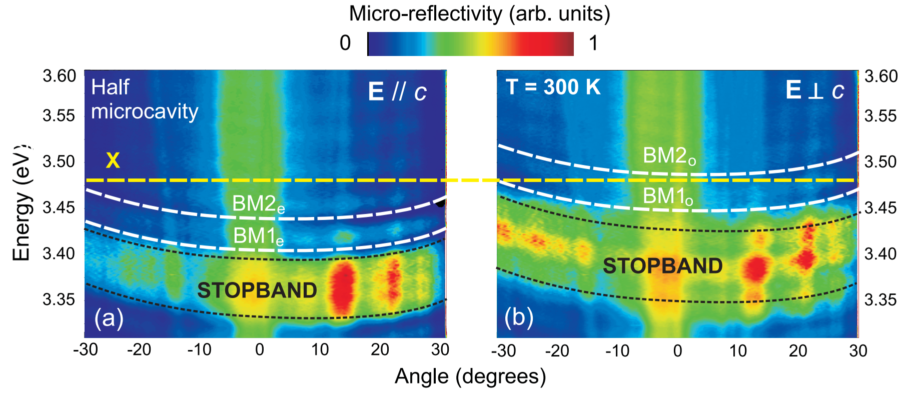

Fig. 6.10: Angle-resolved micro-reflectivity performed at room temperature on the G1 half-microcavity sample along the: (a) extraordinary direction ($\mathbf{E} \parallel c$) and (b) ordinary direction ($\mathbf{E} \perp c$).

6.4 Samples of second generation: Anisotropic polariton lasing

6.4.1 Sample design

As for the G1 sample, the growth started with a 400 nm-thick homoepitaxial GaN layer by molecular beam epitaxy (ammonia source MBE). Then a 50 pair $\text{Al}_{0.15}\text{Ga}_{0.85}\text{N}/\text{Al}_{0.35}\text{Ga}_{0.65}\text{N}$ DBR with nominal layer thicknesses of 31.8 and 34.8 nm, respectively, was deposited. The overgrown active region consists of five sets of GaN quantum wells located at the antinodes of the 3λ cavity, each being separated by 30.8 nm of $\text{Al}_{0.13}\text{Ga}_{0.87}\text{N}$ interlayers. Each set is formed by four 5 nm-thick GaN quantum wells with 5 nm-thick $\text{Al}_{0.13}\text{Ga}_{0.87}\text{N}$ barriers. This region is surrounded by two $\text{Al}_{0.13}\text{Ga}_{0.87}\text{N}$ spacer layers with a

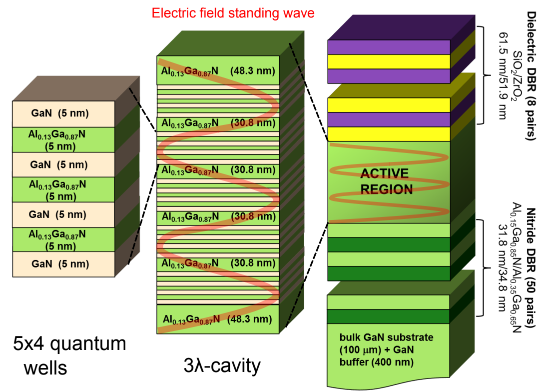

Fig. 6.11: Schematic representation of the generation 2 samples. The active region is zoomed in for the sake of clarity.

thickness of 48.3 nm. Finally the microcavity was completed by an 8-pair SiO_2/ZrO_2 top dielectric DBR deposited by the electron beam evaporation technique.

The design of the second sample generation was inspired by the encouraging results of the first one and the high quality of the active region. Regarding the bottom DBR, the design was left unchanged (same aluminum contents $x_1 = 0.15$ and $x_2 = 0.35$), but the layer thicknesses have been slightly decreased to shift the stopband to higher energy in order to obtain a good matching with the quantum well emission. The active region is still a 3λ-cavity but the quantum well thickness has been modified in order to strengthen the strong coupling regime and maximize the chances of observing polaritonic effects at room temperature: their thickness has been reduced from 8 to 5 nm and their number was increased from 15 to 20. The barrier thickness has also been reduced from 8 to 5 nm, which is still enough to prevent the coupling between adjacent quantum wells and the formation of mini-bands. As a consequence, the simulations performed in the previous section (see Fig. 6.6(b)) still apply to the present structure and the quantum well exciton is expected to present a confinement energy $E_X^{conf} \approx 40$ meV and an exciton binding energy $E_X^b \approx 41$ meV.

6.4.2 Half-microcavity: investigation of the optical in-plane anisotropy

6.4.2.1 Quantum well homogeneity and temperature study

The half-microcavity was first investigated by means of nonresonant photoluminescence under cw excitation ($\lambda = 244$ nm) with an excitation power density of 2 kW/cm^2. A cw line scan was performed at room temperature along the c-axis from one sample extremity to the other (see Fig. 6.12(a)) revealing a mean exciton energy of 3.494±0.01 eV and a linewidth of 55.7±5 meV. Spectra obtained *via* temperature-dependent photoluminescence taken under cw excitation without polarization resolution are displayed in Figs. 6.12(b)-6.12(d). As for the previous sample generation the emission from the quantum wells and the $Al_{0.13}Ga_{0.87}N$-barrier occurring around 3.55 eV and 3.72 eV at 4 K are clearly visible up to room temperature. Also, at low temperatures both features show an additional emission from defect states about 40 meV below the main transition line, while the longitudinal-optical phonon-replica of the quantum wells are well resolved for all temperatures. The evolution of the quantum well emission peak energy in Fig. 6.12(b) shows a redshift of 55 meV from 4 to 300 K. Fitting the temperature evolution

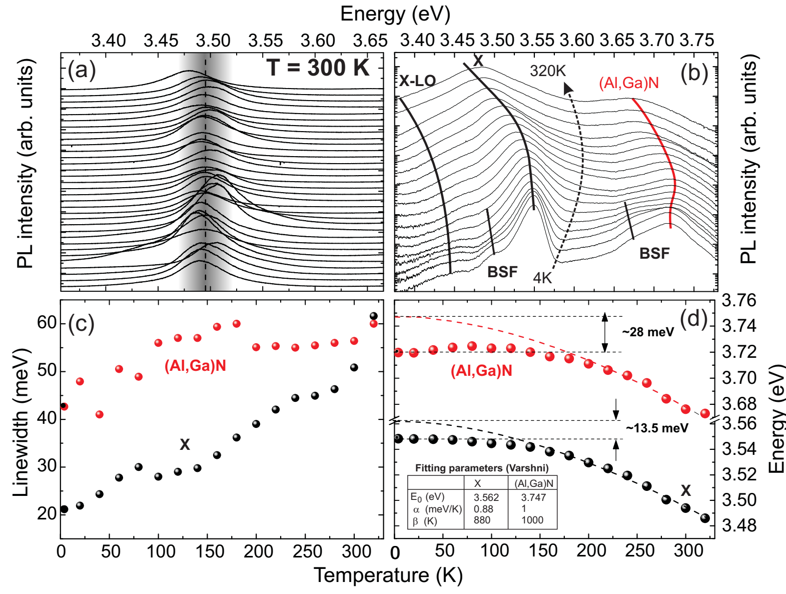

Fig. 6.12: (a) Normalized micro-photoluminescence spectra taken at room temperature for various random positions on the sample surface. (b) Temperature-dependent micro-photoluminescence spectra obtained under nonresonant cw excitation. The spectra are normalized and vertically shifted for the sake of clarity. The quantum well emission is labeled with X, the barrier with (Al,Ga)N. The exciton first LO-phonon replica (X-LO) and the BSF emission lines are also shown. (c) Linewidth and (d) peak energy of barrier (red dots) and quantum well emission (black dots) as a function of temperature.

of the peak energy with the semi-empirical Varshni's law (see equation 2.17) with the same fitting parameters than those used for the G1 sample(s), a localization energy of about 13.5 meV is extracted. This value is similar to that of the G1 sample whereas a higher value would have been expected, due to the smaller thickness of the quantum wells leading to a higher sensitivity to alloy disorder from the (Al, Ga)N barriers [280]. Note that photoluminescence sets a lower limit to δE_X^{loc} as the position of the emission energy strongly depends on the ratio between injected carrier and defect densities due to the progressive filling of localized states.

The linewidth evolution displayed in Fig. 6.12(d) shows an increase from 21 to 51 meV between 4 K and room temperature featuring the high quality of the quantum wells, which compares well with the previous sample generation. Note also that part of the broadening increase is likely caused by carrier delocalization and thermal occupancy of the B exciton transition, situated approximately 15 meV above the A one.[70] The relatively small inhomogeneous broadening ($\gamma_X^{inh} \approx 20$ meV) is again suitable for the achievement of the strong coupling regime at elevated temperatures.

Considering equation 6.1 for the present design with the correct values for the confinement and exciton binding energies, we find that the energy shift induced by the compressive strain in the quantum wells amounts to $E_{strain} \approx 61$meV. The proximity between this value and that obtained for the G1 half-microcavity sample (see Section 6.3.2) confirms our assumption that the compressive strain is inherited from the thick bottom DBR and is given by the mean lattice constant. As the two DBR generations have the same aluminum composition and comparable thicknesses, relation 6.2 leads to similar values in both cases, i.e., $\bar{x}_{geom}^{G1} \approx 25.4\%$ and $\bar{x}_{geom}^{G2} \approx 25.5\%$ and consequently the same strain state is expected.

[70] This value is deduced from the $k \cdot p$ simulations displayed in Fig. 6.7.

6.4.2.2 Impact of anisotropic oscillator strength on the excitonic transitions

In order to correctly describe the anisotropic radiative properties of the active medium, polarization-resoled optical measurements are required. In Fig. 6.13(a), room temperature photoluminescence spectra performed under nonresonant quasi-cw excitation are displayed as a function of the polarizer angle set in the collection line. It appears that the emission is dominated by the quantum well emission, featuring a marked polarization dependence, both in intensity and peak energy, as evidenced in Fig. 6.13(b). Considering the exciton localization energy in this structure $\delta E_X^{loc} \approx 10-15$ meV and the high lattice temperature, one can reasonably assume that the luminescence is dominated by free excitons. The most surprising feature of the present quantum well emission is the clear anticorrelation between intensity and peak energy of the emission line for $\mathbf{E} \parallel c$ and $\mathbf{E} \perp c$ (see Fig. 6.13(b)). The photoluminescence intensity is higher for the lowest peak energy for $\mathbf{E} \parallel c$ and is conversely weaker for $\mathbf{E} \perp c$. Simultaneously, the peak energy is shifted by $\Delta E \approx 10-11$ meV, revealing the contribution of at least two excitonic transitions orthogonally polarized and separated in energy by at least ΔE. Considering the electronic properties of m-plane GaN layers [284] and the previous $k \cdot p$ calculations, we can identify these two levels with A and B excitons, respectively. Finally, from the $k \cdot p$ simulations shown in Fig. 6.7, one can discard the influence of the C exciton, which lies at too high energy.

The intensity of each transition is affected by the oscillator strength distribution but also by the thermal occupancy of the higher energy states. However, considering the energy separation between X_A and X_B (≈ 12 meV), one can give a lower limit to the exciton linear polarization degree:

$$\rho_{\text{lin}} = \frac{I_{\mathbf{E}\parallel\text{c}} - I_{\mathbf{E}\perp\text{c}}}{I_{\mathbf{E}\parallel\text{c}} + I_{\mathbf{E}\perp\text{c}}}, \tag{6.3}$$

where $I_{\mathbf{E}\parallel\text{c}}$ and $I_{\mathbf{E}\perp\text{c}}$ are the integrated intensity after deconvolution of the exciton luminescence along the extraordinary and ordinary directions, respectively. For the A exciton transition, we find $\rho_{\text{lin}}^{A} \approx 0.39$. This value strongly deviates from the expected one for relaxed GaN ($\varepsilon \approx 0$), i.e. an almost fully polarized transition along the ordinary direction. This reversed polarization behavior is due to the compressive strain experienced by the quantum wells. To evaluate the impact of strain on the emission properties, $k \cdot p$ calculations are needed (see Fig. 6.14).[71]

[71] Note that the present $k \cdot p$ simulations correspond to the transition energy calculations reported in Fig. 6.7.

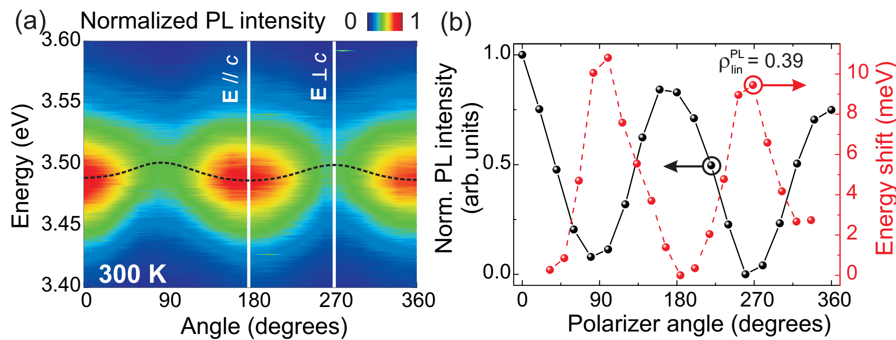

Fig. 6.13: (a) Room temperature photoluminescence (PL) spectra measured under nonresonant quasi-cw excitation as a function of the linear polarizer angle ranging from 0 to 360°: the extraordinary and ordinary directions correspond to 0 and 90°, respectively. (b) Relative evolution of the peak energy (red) and intensity (black).

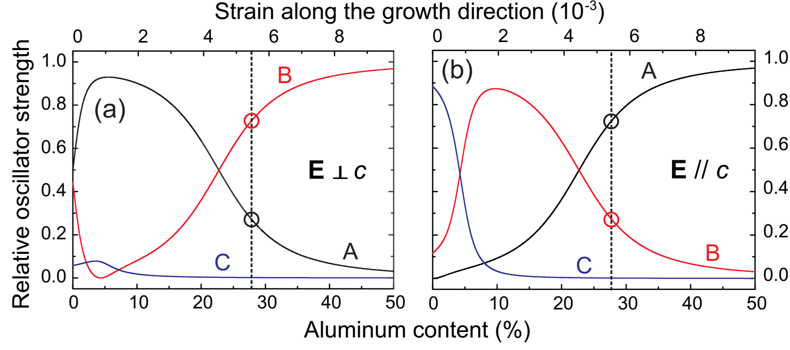

Fig. 6.14: Polarization-dependent relative oscillator strength f_{osc} at the Γ-point for the interband transitions A, B, and C deduced from $k \cdot p$ calculations for: (a) $\mathbf{E} \perp c$ and (b) $\mathbf{E} \parallel c$. The strain state of the quantum wells deduced from XRD measurements is indicated by the vertical dashed lines.

Again, the approach of Chuang and Chang [167] is used with the material constants taken from Refs. [153, 282] to calculate the relative oscillator strength $f_{\text{osc}}^{\text{rel}}$ of A, B and C transitions (see Fig. 6.14(b)). Increasing the aluminum content, the compressive in-plane strain also increases causing a redistribution of $f_{\text{osc}}^{\text{rel}}$ between ordinary and extraordinary directions for the optically active transitions. For $x \approx 5\%$, B and C bands exchange their relative oscillator strength and the same happens between A and B bands for $x \approx 22\%$.[72] Interestingly, we see that for aluminum contents higher than 5%, the in-plane contribution of X_{C} vanishes and only X_{A} and X_{B} have to be considered. The vertical dashed line in Figs. 6.14(a)-6.14(b) corresponds to the mean aluminum content in the bottom DBR measured by XRD ($\bar{x}_{\text{XRD}} \approx 28\%$) and defines the strain in the active medium. For this strain state, X_{A} and X_{B} share complementary oscillator strengths along the two in-plane directions: $f_{\text{osc,o}}^{\text{rel,A}} : f_{\text{osc,e}}^{\text{rel,A}} = 0.26 : 0.74$ and $f_{\text{osc,o}}^{\text{rel,B}} : f_{\text{osc,e}}^{\text{rel,B}} = 0.74 : 0.26$. The resulting value for the linear polarization degree for the X_{A} line is $\rho_{\text{lin}}^{\text{A}} = 0.48$, which is in relatively good agreement with the values extracted from photoluminescence measurements, i.e. $\rho_{\text{lin}}^{\text{PL,A}} = 0.39$, which corresponds to $f_{\text{osc,o}}^{\text{rel,B}} : f_{\text{osc,e}}^{\text{rel,B}} = 0.7 : 0.3$.

6.4.2.3 Impact of birefringence on the cavity mode

In parallel to the anisotropic distribution of the oscillator strength, which is related to the imaginary part of the dielectric tensor and which mainly affects the exciton mode, one should also consider the impact of birefringence. In an anisotropic microcavity, light polarized along ordinary and extraordinary directions experiences different refractive indices n_{o} and n_{e}, respectively. In III-nitrides, $n_{\text{o}} < n_{\text{e}}$ below the band gap [172], which results in a shorter optical path length and thus a higher cavity mode energy for $\mathbf{E} \perp c$. As both the bottom DBR and the active region exhibit birefringence, both will impact on the formation of the cavity mode. In Figs. 6.15(a) and 6.15(c), the bottom DBR reflectivity is simulated within the 4×4 transfer matrix formalism (see Appendix C.2) as a function of the incident angle for the components of the electric field polarized along $\mathbf{E} \perp c$ and $\mathbf{E} \parallel c$, respectively. As expected, the stopband along the extraordinary direction appears at lower energy ($E_{\text{DBR,e}} \approx 3.553\,\text{eV}$) compared to the ordinary one ($E_{\text{DBR,o}} \approx 3.613\,\text{eV}$). For $\mathbf{E} \parallel c$, the refractive index contrast is slightly decreased yielding a reduced stopband width: $\Delta E_{\text{SB,e}} \approx 112\,\text{meV}$ vs. $\Delta E_{\text{SB,o}} \approx 121\,\text{meV}$. The energy detuning of about

[72] Note that the oscillator strengths displayed in Figs. 6.14(a)-6.14(b) correspond to relative values $f_{\text{osc}}^{\text{rel}}$. The real value used in the transfer matrix simulations is obtained by considering the specific material constant F related to the Kane's parameter *via* $f_{\text{osc}} = F \times f_{\text{osc}}^{\text{rel}}$. In the following, we consider the value reported for c-plane narrow GaN quantum wells, i.e., $F = 5.1 \times 10^{13}\,\text{cm}^{-2}$ [53].

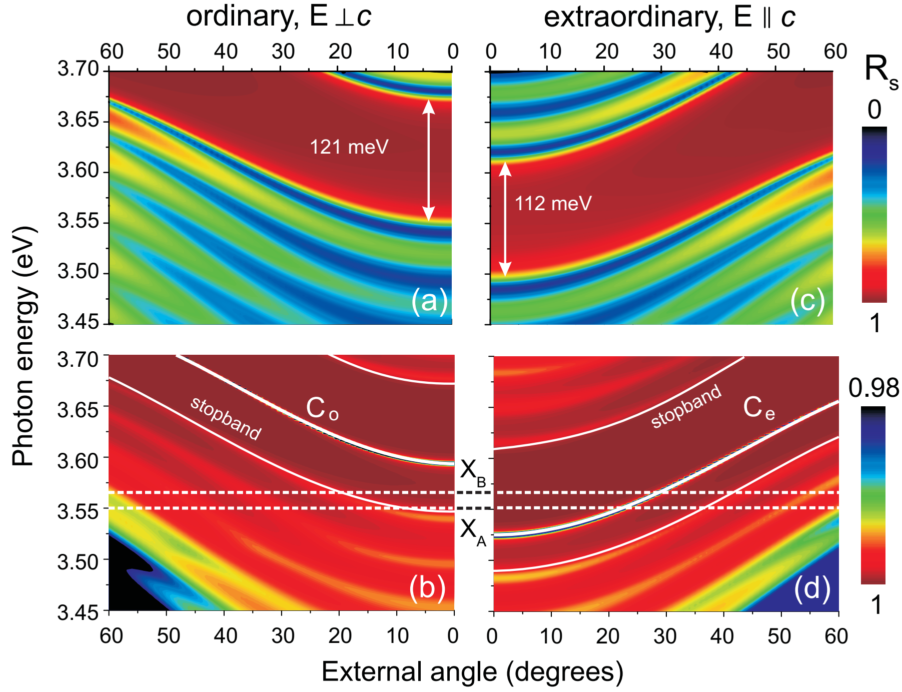

Fig. 6.15: Bottom DBR reflectivity simulated with the 4 × 4 transfer matrix formalism as a function of the external angle for: (a) $\mathbf{E}\perp c$ and (c) $\mathbf{E}\parallel c$. Simulation of the bare cavity structure for (b) $\mathbf{E}\perp c$ and (d) $\mathbf{E}\parallel c$: the quantum well absorption is set to zero in order to track the cavity mode energy along each direction, i.e., C_o and C_e, respectively.

60 meV between the two directions will likely result in a comparable shift of the cavity mode energy. To evaluate this shift, the full microcavity structure is simulated in Figs. 6.15(b) and 6.15(d) for the two directions with the quantum well absorption set to zero in order to access the cavity mode energy. From the simulation the energy shift is deduced, $E_{C,o}(0) - E_{C,e}(0) = 69$ meV, which compares well with the bottom DBR stopband shift. For each polarization, the bottom DBR stopband is indicated with thin white continuous lines and the cavity modes C_o and C_e by thick white continuous lines. The energy position of the two optically active excitons X_A and X_B is also shown (white dashed lines) in order to highlight the matching between the quantum well emission and the cavity mode for each polarization.

In Fig. 6.16, reflectivity spectra obtained at low temperature ($T = 4$ K) on the half-microcavity at an angle of ~ 11° are shown as a function of the polarizer angle in the collection line. These measurements confirm the impact of the birefringence on the stopband behavior: along the ordinary direction, the stopband is slightly broader ($\Delta E_{SB,o} \approx 100$ meV) and lies at higher energy ($E_{DBR,o} \approx 3.582$ eV) compared to the extraordinary direction ($\Delta E_{SB,e} \approx 90$ meV and $E_{DBR,e} \approx 3.542$ eV). Even if this behavior is in qualitative agreement with the transfer matrix simulations shown in Figs. 6.15(a) and 6.15(c), the observed energy shift between orthogonal directions and the stopband widths are approximately 80% lower than the calculated values. This discrepancy likely arises from the uncertainty in the anisotropic refractive index constants used for the simulations. Indeed so far, no systematic study on the refractive index of nonpolar (Al,Ga)N alloys has been performed as it is the case for polar ones [173]. To compensate for this lack of information, we linearly interpolated the complex dielectric constants of the (Al,Ga)N alloys between the anisotropic values of AlN and GaN reported in Ref. [172]. This approximation is reasonable only for low aluminum contents and becomes problematic for the

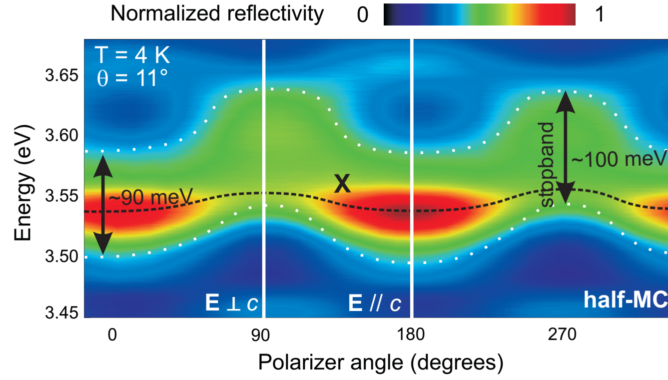

Fig. 6.16: Reflectivity spectra measured at 4 K on the half-microcavity at an angle of ~ 11° as a function of the polarizer angle. The black dashed line marks the position of the excitonic response and the white dotted lines the limits of the stopband.

bottom DBR, especially for the $Al_{0.35}Ga_{0.65}N$ layers. Note finally that the relatively small stopband observed experimentally could also be due an average effect, considering the relatively large spot size (~ 100 μm) used compared to the photonic disorder (< 5 μm).

As the measurements are performed on the half-microcavity structure, the response of the active region is also visible. In particular, the signature of the exciton transition indicated by a black dashed line in Fig. 6.16 is seen to shift to higher energy when the polarizer angle is aligned along the ordinary direction. This behavior further confirms our assumption that the optical response is dominated by two excitons separated in energy by approximately 15 meV with an anisotropic oscillator strength distribution.

6.4.3 Full microcavity: the linear regime

After investigating the half-microcavity, the structure was completed with an 8-pair ZrO_2 / SiO_2 dielectric DBR, which exhibits fully isotropic in-plane optical properties. The goal of the present section is to analyze the impact of the bare mode anisotropy on the full microcavity.

6.4.3.1 Anisotropic light-matter coupling

The light-matter interaction constant g_0 given by relation 1.50 is affected by the birefringence and the anisotropic oscillator strength distribution of each optically active exciton, i.e., X_A and X_B. In particular, it will have a different value for each transition $\mathrm{t} \in \{A, B\}$ depending on the electric field polarization $y \in \{e, o\}$ according to:[73]

$$g_{\mathrm{y}}^{\mathrm{t}} = \hbar \sqrt{\frac{e^2}{2\varepsilon_0 m_0} \frac{N_{\mathrm{QW}}^{\mathrm{eff}}}{n_{\mathrm{cav,y}} L_{\mathrm{eff}}} f_{\mathrm{osc,y}}^{\mathrm{t}}}, \tag{6.4}$$

where $N_{\mathrm{QW}}^{\mathrm{eff}}$ is the effective number of quantum wells coupled to the cavity mode. Considering relation 1.71 for the present structure, we find $N_{\mathrm{QW}}^{\mathrm{eff}} \approx 16.3$, meaning that 3 to 4 quantum wells over the 20 do not take part to the light-matter interaction but act as an extra source of loss. Even if the birefringence affects both $n_{\mathrm{cav,y}}$ and L_{eff}, its impact on g_0 is small compared to that of the oscillator strength anisotropy $f_{\mathrm{osc,y}}^{\mathrm{t}}$

[73] Note that the subscript y indifferently refers to the light polarization or to the crystal orientation.

Table 6.1: Summary of the optical anisotropy in the G2 sample

	$n_{Al_{0.15}Ga_{0.85}N}$ (E = 3.5 eV)	$f_{osc}^{rel,A}$	$f_{osc}^{rel,B}$	E_{DBR} (eV)	ΔE_{SB} (meV)
$\mathbf{E} \parallel c$	2.625	0.73	0.27	3.542	90
$\mathbf{E} \perp c$	2.566	0.27	0.73	3.582	100

as shown by the values reported in Tab. 6.1: the relative variation in the refractive index along the two directions $(n_e - n_o)/n_e \approx 2\%$ at 3.5 eV for an $Al_{0.15}Ga_{0.85}N$ layer is negligible compared to the relative variation in the oscillator strength of X_A, i.e., $(f_{osc,e}^{rel,A} - f_{osc,o}^{rel,A})/f_{osc,e}^{rel,A} \approx 64\%$. This property suggests the use of strain-engineering as a powerful tool to tune the light-matter interaction in nonpolar microcavities *via* the manipulation of the exciton oscillator strength [175]. If the strong coupling regime is reached for a given direction y between the cavity mode C_y and a transition X_t, the corresponding vacuum Rabi splitting $\Omega_{VRS,y}^{t}$ reads:

$$\Omega_{VRS,y}^{t} = 2 \cdot Re\left\{ \sqrt{(g_y^t)^2 - \frac{\gamma_{X_t}^2 + \gamma_{C,y}^2}{2}} \right\}, \tag{6.5}$$

where γ_{X_t} is the homogeneous broadening of the X_t exciton and $\gamma_{C,y}$ is the homogeneous broadening of the cavity mode in the y-direction.[74]

6.4.3.2 Anisotropic response of the full microcavity: coexistence of the weak and strong coupling regimes

The detuning between the active medium and the bottom DBR stopband is known from the optical characterization performed on the half-microcavity and is summarized in Figs. 6.15(b) and 6.15(d) and Tab. 6.1 at $T = 50$ K.[75] Note that the cavity modes along the ordinary and extraordinary directions, C_o and C_e, respectively, depend on the local photonic disorder and might change from one sample position to another. The first striking feature is the excellent matching between X_A and the bottom DBR for $\mathbf{E} \parallel c$. In addition, X_A has a maximum oscillator strength along this direction favoring the appearance of the strong coupling regime, contrary to X_B. Using the sample parameters and relations 6.4 and 6.5, we can estimate the expected vacuum Rabi splitting of both transitions in this direction, i.e, $\Omega_{VRS,e}^{A} \approx 45$ meV and $\Omega_{VRS,e}^{B} \approx 20$ meV. Considering the inhomogeneous broadening of the excitonic transition $\gamma_X^{inh} \approx 20$ meV and the fact that a non-perturbative regime is usually not sustained for $\gamma_X^{inh} > \Omega_{VRS}$, only X_A is expected to be in the strong coupling regime for $\mathbf{E} \parallel c$. For $\mathbf{E} \perp c$, the situation is more complicate. While X_A lies out of the bottom DBR stopband, the position of X_B is only partly overlapping it and this situation might change from spot to spot on the sample due to excitonic and photonic disorder. Considering the relative oscillator strength of each transition, the strong coupling is definitively not expected for X_A but no direct conclusion can be drawn for X_B.

[74] As for the measurements presented hereafter we do not have a direct access to the homogeneous broadening along the extraordinary direction, we assume that $\gamma_{C,e} = \gamma_{C,o}$, which is equivalent to consider comparable DBR reflectivities (bottom and top ones) at the cavity mode energy.

[75] Note that above 50 K, the overlap between X_A and the bottom DBR stopband is strongly reduced resulting in the loss of the strong coupling regime. In addition, the stopband widths calculated from transfer matrix simulations shown in Figs. 6.15(b) and 6.15(d) are approximately 20% larger than the experimental ones.

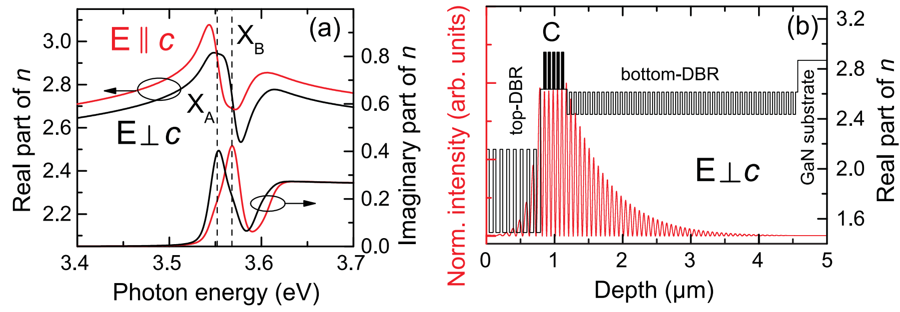

Fig. 6.17: (a) Real and imaginary parts of the quantum well refractive index vs. energy. (b) Electric field intensity profile in the full microcavity structure. The spatial refractive index profile is shown to feature the appropriate tuning between the quantum well sets and the electric field antinodes.

In order to understand the nature of the coupling regime for each polarization direction, transfer matrix simulations have been performed considering the sample parameters extracted from the optical measurements and $k \cdot p$ simulations. In Fig. 6.17(a), the calculated real and imaginary parts of the optical refractive index of the quantum wells are shown for the two orthogonal directions, assuming an inhomogeneous broadening of 15 meV and a homogeneous one of 7 meV and an exciton binding energy of 40 meV for X_A and X_B.[76] The Urbach tail and the absorption from the electron-hole continuum are also considered assuming a sigmoid profile (equation 1.12). The electric field intensity distribution in the whole structure is displayed in Fig. 6.17(b) for $\mathbf{E} \perp c$, featuring the different penetration lengths in the dielectric and in the nitride DBR as well as the overlap between the quantum well sets and the cavity mode.

In Figs. 6.18(a)-6.18(d), the calculated reflectivity and absorption spectra are displayed for each polarization direction as a function of the external angle for s-polarization. As expected, for $\mathbf{E} \parallel c$ a non-ambiguous signature of the strong coupling regime is observed between X_A and the cavity mode C_e (LPB$_e$ and UPB$_e$, white continuous lines) and for $\theta \approx 35°$ X_A weakly anticrosses the first Bragg mode. Regarding X_B no clear anticrossing is observed, neither with C_e nor with the Bragg modes, confirming our assumption that its oscillator strength is not sufficient to bring the transition into the non-perturbative regime. Nevertheless, its presence is manifested by the large smearing of the UPB close to $\theta = 0$ and the overall damping of the latter in in reflectivity spectra, an effect, which is additionally enhanced by the proximity of the band-to-band absorption. For $\mathbf{E} \perp c$, the situation looks more complicated due to the presence of multiple Bragg modes located in the vicinity of X_A and X_B. However, no obvious anticrossing feature between X_A and these modes is visible in agreement with its low oscillator strength and its poor overlap with the bottom DBR stopband. In Fig. 6.18(b), absorption is clearly visible at the energy of X_B, which seems to indicate that no transition toward the strong coupling regime occurs between X_B and C_o. Note that the large positive detuning between C_o and X_B would result in a large linewidth and a fuzzy dispersion for LPB$_o$. As a conclusion no obvious conclusion can be drawn for X_B along the ordinary direction. Another interesting feature is the excellent matching between X_A and the first Bragg mode, below the stopband suggesting that X_A or its localized states can radiate out of the microcavity.

[76] Note that we consider a slightly lower value for the inhomogeneous broadening in order to enhance the visibility of the simulations without affecting the nature of the coupling regime. Regarding the homogeneous broadening, the considered value corresponds to the low injection case.

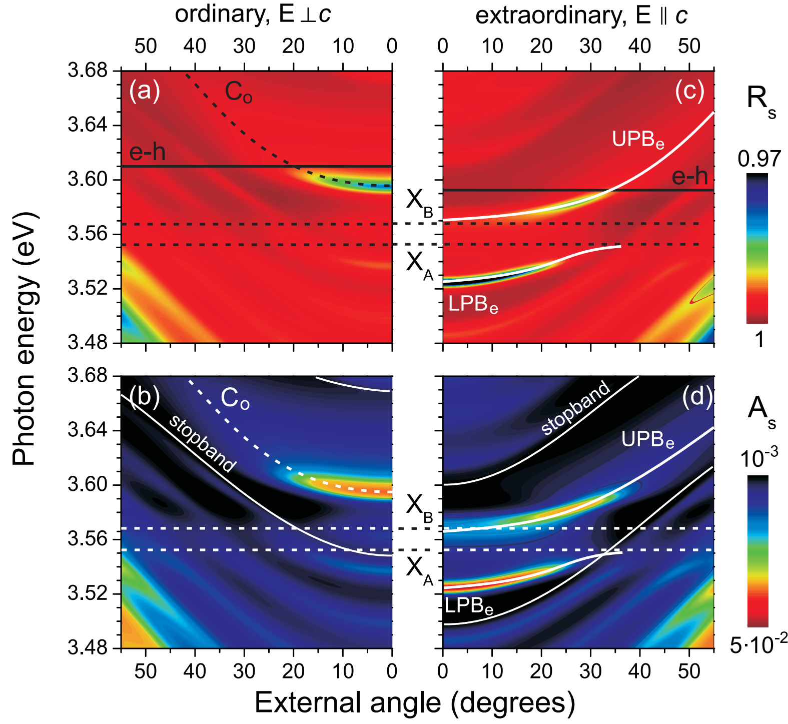

Fig. 6.18: Simulated reflectivity (linear scale) and absorption (logarithmic scale) spectra vs. external angle for: (a)-(b) $\mathbf{E} \perp c$, and (c)-(d) $\mathbf{E} \parallel c$. The index s in R_s and A_s corresponds to the TE-polarization configuration. The onset of the continuum electron-hole (e-h) absorption is indicated with a black continuous line and the two optically active excitons with dashed lines. The bottom DBR stobpand as well as the polariton branches are indicated with white continuous lines.

Let us now turn our attention to the experimental data. In Figs. 6.19(a)-6.19(b), the far-field emission pattern of the full microcavity measured at 50 K under nonresonant quasi-cw excitation is shown for the extraordinary and ordinary directions, respectively. For $\mathbf{E} \parallel c$, the photoluminescence is dominated by a dispersive mode converging toward X_A at high angles. In agreement with transfer matrix simulations, we attribute this mode to the lower polariton branch $\mathrm{LPB_e}$ arising from the strong coupling between X_A and C_e. Fitting the dispersion with a two-level coupled oscillator model, we find $\Omega^{A}_{\mathrm{VRS,e}} = 45\,\mathrm{meV}$ under low injection, in perfect agreement with our transfer matrix calculations. The detuning approximately amounts to $-20\,\mathrm{meV}$ which leads to a C_e energy at $k_\parallel = 0$ of 3.352 eV.

The polaritonic origin of the observed mode in the extraordinary direction is further confirmed by low temperature reflectivity and photoluminescence measurements performed in tilted configuration to have access to higher angles. In the reflectivity spectra shown in Fig. 6.20(a), only the lower polariton branch is visible. This feature is in agreement with transfer matrix simulations where the minimum of reflectivity for the upper branch amounts to 0.985 around 27°, whereas the lower branch goes down to 0.936 at normal incidence. In addition, the relatively large spot size ($\sim 100\,\mu$m) used for the measurements is considerably exceeding the photonic disorder, which causes a decrease of the overall sensitivity. In the photoluminescence spectra shown in Fig. 6.20(b) the non-thermal occupancy of the lower polariton branch originates from the relaxation bottleneck due to the slight photon-like character of the polaritons for the observed detuning ($\delta \approx -20\,\mathrm{meV}$) and the relatively low lattice temperature, which likely drives the system in the kinetically driven regime. No luminescence is observed from the

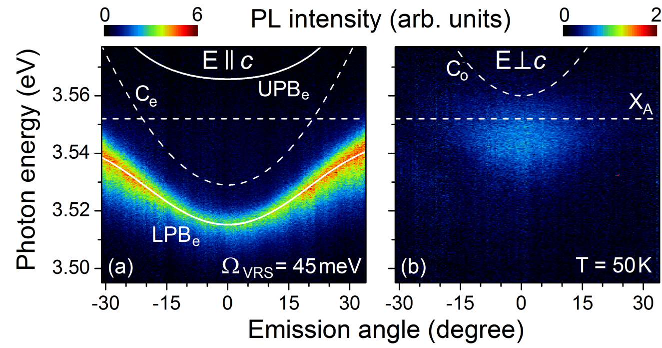

Fig. 6.19: Far-field angle-resolved photoluminescence spectra of the complete microcavity obtained at 50 K along (a) the extraordinary and (b) the ordinary polarization directions.

upper polariton branch because of the low thermal occupation factor, residual damping and efficient relaxation toward LPB_e.

For $\mathbf{E} \perp c$, no signal from LPB_e is collected and the far-field emission pattern is dominated by a weak emission originating from the X_A localized states X_A^{loc} (see Fig. 6.19(b)). This interpretation is supported by the slightly redshifted energy with respect to the free exciton line, the occupation of localized states at such low temperatures and low excitation densities, and also by the fact that the emission is slightly dispersive in complete agreement with the proximity of the first Bragg mode calculated by transfer matrix simulations. This behavior confirms that X_A is in the weak coupling regime with C_o. Note that the low occupation factor of X_B at the present lattice temperature prevents its observation in photoluminescence measurements. In order to have a better understanding of the role played by X_B, the design and the bottom DBR should be adjusted in order to have a broader stopband and a better overlap with all optically active excitons.

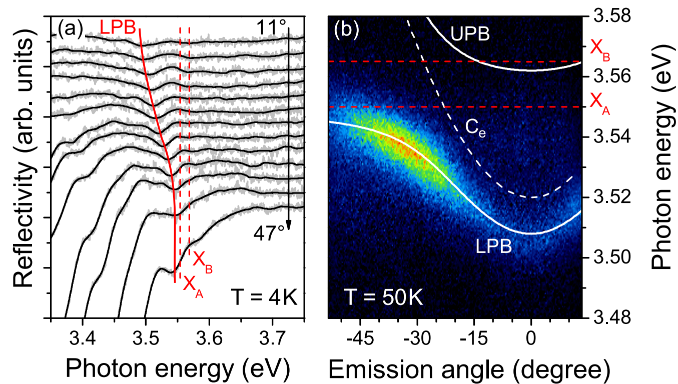

Fig. 6.20: (a) Angle-resolved reflectivity spectra of the full microcavity measured at 4 K with $\mathbf{E} \parallel c$: The red solid line acts as a guide to the eye for the lower polariton branch (LPB) converging toward X_A at high angles. (b) Polarization-resolved Fourier-PL image acquired below threshold for $\mathbf{E} \parallel c$ at 50 K showing the clear anticrossing behavior of the LPB with X_A and a signature of the relaxation bottleneck.

6.4.4 *Full microcavity: the nonlinear regime*

In this section, the nonlinear emission properties of the present microcavity featuring the coexistence of the strongly and weakly coupled modes along orthogonal polarization planes are studied under nonresonant optical pumping. Lasing is observed for both directions well below the exciton saturation density with different threshold power densities $P_{\text{thr},1}$ and $P_{\text{thr},2}$ along extraordinary and ordinary directions, respectively. The goal of the present section is to identify the mechanisms involved along each direction considering the optical anisotropy.

6.4.4.1 Far-field emission pattern evolution with power density: identification of the modes

In Fig. 6.21, the evolution of the mode dispersion is reported for three different average pump power densities at $T = 50$ K. No polarization selection was set in the collection line so that both polarization components $\mathbf{E} \parallel c$ and $\mathbf{E} \perp c$ are detected. Again, the spectra in the low injection regime are dominated by the $X_{\text{A}}^{\text{loc}}$ emission at 3.535 eV and the lower polariton branch LPB_{e}. For $P = P_{\text{thr},1} \approx 15\,\text{W/cm}^2$, the LPB_{e} intensity nonlinearly increases at $\theta = 0$ and a third mode at higher energy ($E \approx 3.552$ eV) becomes visible. This mode also exhibits a transition toward a the nonlinear regime but for a higher average pump power density $P_{\text{thr},2} \approx 1.3 P_{\text{thr},1}$. The polarization-resolved photoluminescence measurements shown in Fig. 6.22(a) performed at normal incidence for an average power density higher than $P_{\text{thr},1}$ and $P_{\text{thr},2}$ reveal that this mode is counter-polarized with respect to LPB_e and co-polarized with $X_{\text{A}}^{\text{loc}}$. Due to its energetic position ~ 30 meV above the cavity mode in the e-direction C_e this emission likely originates from photons leaking through the uncoupled cavity mode C_o. The energy position of C_o is supported by the shift of the bottom DBR stopband by ~ 35 meV between extraordinary and ordinary directions (see Fig. 6.16), which should approximately correspond to the energy shift between the corresponding cavity modes C_{e} and C_{o}.

In Fig. 6.22(b), photoluminescence spectra measured along the ordinary (black) and extraordinary directions (red) at normal incidence for $T = 50$ K are displayed for excitation power densities ranging from 0.07 to 2.14 $P_{\text{thr},1}$. Interestingly, along the ordinary direction, the excitonic emission is governed by $X_{\text{A}}^{\text{loc}}$ whereas along the extraordinary one, an emission occurring at slightly higher energy is also visible and likely corresponds to $X_{\text{B}}^{\text{loc}}$. In addition to the correct expected energy position, this interpretation

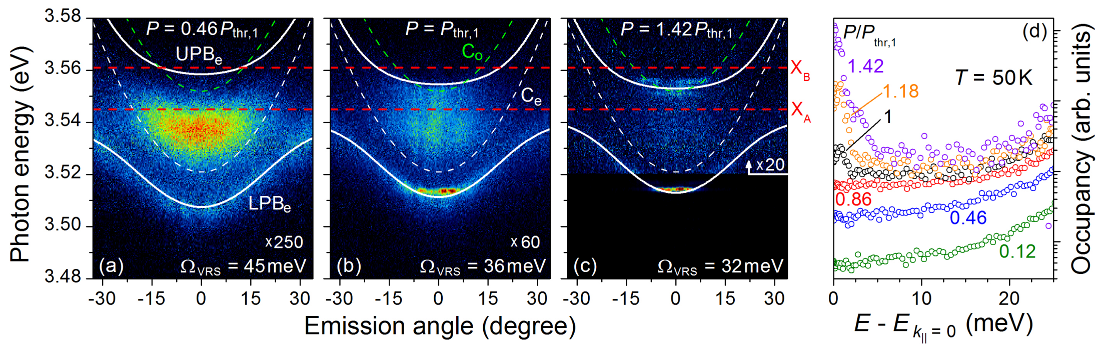

Fig. 6.21: (a)-(c) Fourier space images measured at various excitation power densities below and above the polariton lasing threshold ($P_{\text{thr},1}$) without polarization selection ($T = 50$ K). Fitted coupled modes (solid lines) are displayed for $\mathbf{E} \parallel c$ (white line) only. The green color is used for $\mathbf{E} \perp c$ and the two free exciton lines (red) are active in both directions. (d) LPB occupancy as a function of excitation.

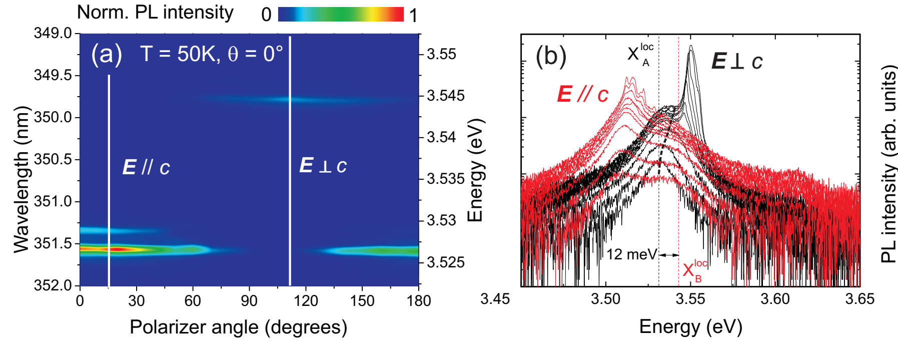

Fig. 6.22: Polarization-resolved photoluminescence measurements performed at normal incidence at 50 K above $P_{\mathrm{thr},1}$ and $P_{\mathrm{thr},2}$: (a) as a function of the polarizer angle and (b) as a function of the average excitation power density for $\mathbf{E} \parallel c$ (red) and $\mathbf{E} \perp c$ (black).

is supported by the different nature of the coupling of each transition along the two directions. As X_{A} is in the strong coupling regime with C_{e} for $\mathbf{E} \parallel c$, it has nearly no optical signature in the far field explaining why only a weak emission arising from $X_{\mathrm{B}}^{\mathrm{loc}}$ is visible.[77] For $\mathbf{E} \perp c$, the situation is different as the system is in the weak coupling regime and the excitonic states (free and localized ones) are therefore distributed according to a thermal distribution so that the main contribution arises from $X_{\mathrm{A}}^{\mathrm{loc}}$. Note that the high energy tail extends to higher energies when the carrier density is increased because of the progressive filling of $X_{\mathrm{B}}^{\mathrm{loc}}$ (black dashed line in Fig. 6.22(b)). The energy separation between $X_{\mathrm{A}}^{\mathrm{loc}}$ and $X_{\mathrm{B}}^{\mathrm{loc}}$ is in agreement with $k \cdot p$ simulations for X_{A} and X_{B} assuming comparable localization energies for the two excitonic populations. The measurements finally show a transition toward a nonlinear emission in both directions with respective linewidths of 1 and 2.5 meV at threshold for $\mathbf{E} \parallel c$ and $\mathbf{E} \perp c$. These values are significantly lower than the bare cavity mode linewidth (~ 10 meV), which is a signature of temporal coherence.

Switching from polariton emission along the e-direction to weakly coupled modes ($X_{\mathrm{A}}^{\mathrm{loc}}$ and C_o) in the orthogonal one illustrates that both strong and weak coupling regimes coexist at the same spot position under identical excitation conditions for orthogonal polarizations. The fact that C_o is only visible under high injection is explained by the delocalization of excitons, an increase in the homogeneous excitonic linewidth due to collisional broadening and the rise of the carrier temperature with increasing injection as visible from the linewidth evolution of $X_{\mathrm{A}}^{\mathrm{loc}}$ in Fig. 6.23(b).

6.4.4.2 Lasing in the strong coupling regime for E ∥ *c*

From the measurements shown in Fig. 6.21 and the injection-dependent analysis displayed in Fig. 6.23, it is obvious that the nonlinear emission first occurs slightly above the bottom of LPB$_e$ but well below C_{e} and then on C_{o} for a slightly higher average power density $P_{\mathrm{thr},2} = 1.3\, P_{\mathrm{thr},1}$. The first one displays typical features of polariton lasing that are a nonlinear increase in the intensity at $k_{\parallel} = 0$ due to final state stimulation, a blueshift of the emission due to polariton-polariton interactions and oscillator strength saturation [103], and the narrowing of the emission line from 15 down to 1 meV (Figs. 6.23(a)

[77] The localized states of X_{A} are also not visible likely because the localization time of excitons in the quantum well τ_{loc} is short compared to the Rabi period $\tau_{\mathrm{Rabi}} = \frac{2\pi\hbar}{\Omega_{\mathrm{VRS}}} < 100$ fs. For high quality nonpolar bulk GaN layers with a carrier density of $10^{16}\,\mathrm{cm}^{-3}$, τ_{loc} amounts to ~ 25 ps for X_{A} and X_{B} at 8 K [117]. For quantum wells, this time is likely shorter due to in-plane disorder but a value larger than 100 fs is expected [118].

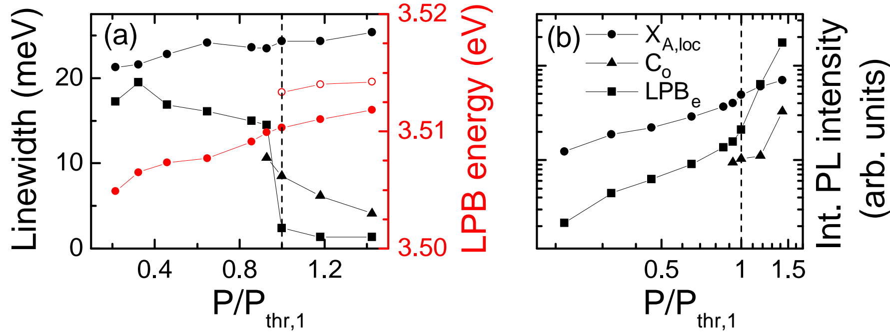

Fig. 6.23: Analysis of the excitation power-dependent eigenmode profiles at $k_{\parallel} = 0$ for $T = 50\,\mathrm{K}$: (a) linewidth evolution (black) of the LPB$_e$ (squares), $X_{\mathrm{A}}^{\mathrm{loc}}$ (circles), and C_o (triangles) and the photon energy of the linear (red solid circles) and nonlinear (red open circles) LPB$_e$ emissions. (b) Evolution of the corresponding integrated photoluminescence intensities.

and 6.23(b)), which reflects the increase in the coherence time following the spontaneous build-up of a polariton condensate.

Similarly to the measurements reported in Section 3.4.3 for c-plane GaN multiple quantum well based microcavities, the vacuum Rabi splitting is reduced from 45 down to 32 meV over the investigated power range likely due to saturation of the exciton oscillator strength. However, the polariton emission remains below the cavity mode energy for all excitation powers applied ensuring that the system remains in the strong coupling regime. Finally, it is worth pointing out that the non-thermal occupancy of LPB$_e$ shown in Fig. 6.21(d), likely arises from the limited quality factor $Q \approx 350$ and the reduced polariton relaxation efficiency for negative detunings in combination with the low temperature [55, 56]. In order to firmly assess the polaritonic nature of the observed transition, one still needs to demonstrate that the system operates far below the Mott transition by estimating the injected carrier density.

6.4.4.3 Estimation of the carrier density

To validate the assumption that the electronic population is dominated by excitons, we still need to demonstrate that our system operates below the exciton saturation density n_X^{sat} for all power densities explored. Usually relation 3.5 is used to estimate the total carrier density n_X. However, such an approach is a bit hazardous as it requires several assumptions on barely known system parameters such as the quantum well absorption, losses in the barriers and carrier lifetimes. In a strongly coupled system, it is commonly accepted to relate the LPB blueshift to n_X *via* the relationship $\Delta E_{\mathrm{LPB}} = 6 n_X a_B^2 E_X^B |X_0|^2$ [103]. However, as already discussed in Section 3.4.3, this treatment is only valid if the LPB renormalization can be exclusively attributed to exciton-exciton interactions, which is not the case for GaN-based systems where the role of the oscillator strength saturation cannot be neglected, even below $P_{\mathrm{thr},1}$ [55]. This leads to a significant overestimate of n_X resulting for the present structure in an injection density approximately twice the saturation level deduced in Ref. [53]. Indeed, the impact of saturation effects is revealed by the observation of an Ω_{VRS} reduction ~ 30% for the injection range investigated (see Fig. 6.21). In addition, the renormalization analysis is made more complex since the lasing mode is slightly blueshifted with respect to the bottom of the lower polariton branch (see Figs. 6.21(b) and 6.23(a)), likely due to the local photonic disorder.

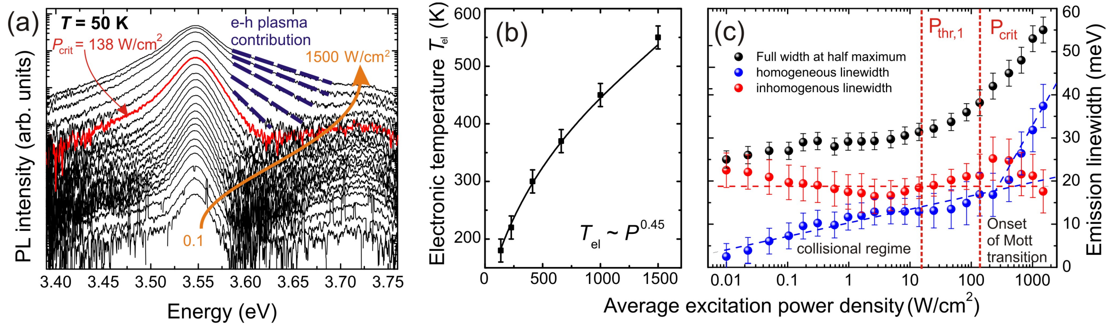

Fig. 6.24: (a) Excitation power-dependent emission spectra of the half-microcavity. Evolution of (b) the electron-hole plasma effective temperature (T_{el}) and (c) the quantum well emission linewidth deduced from a Voigt-profile analysis.

A more reliable way to compare n_X with n_X^{sat} first consists in investigating the optical response of the bare active medium as a function of the injected carrier density. From the power-dependent photoluminescence series performed on the half-microcavity at the same temperature, $T = 50\,\mathrm{K}$ (see Fig. 6.24(a)), it is seen that the quantum well emission linewidth decomposed into homogeneous and inhomogeneous contributions (Fig. 6.24(b)) shows a singular behavior at $P_{\mathrm{crit},1} \approx 140\,\mathrm{W/cm}^2$ where the rise of the homogeneous broadening becomes much faster.[78] For $P < P_{\mathrm{crit},1}$ the moderate increase in the homogeneous linewidth can be ascribed to carrier heating induced by collisions, whereas the fast rise in the carrier temperature and the transition to an exponentially decaying slope for the high energy tail when $P > P_{\mathrm{crit},1}$ can be attributed to a progressive loss of the excitonic character - the Mott transition, according to Ref. [98]. This behavior is in perfect agreement with the one observed for polar GaN-based quantum wells in Fig. 3.10(a) (blue dashed lines in Fig. 6.24(a)). Note that the Mott transition continuously occurring above $P_{\mathrm{crit},1}$ should be accompanied with an emission energy redshift due to band gap renormalization. This effect is hardly observable in GaN-based microcavities (polar and nonpolar ones), which might be related to a partial compensation due to exciton screening (blueshift) and band gap renormalization (redshift). Note that the increase in the free carrier temperature with excitation power density shown in Fig. 6.24(b) compares well with the polar multiple quantum well sample investigated in Chapter 3 (see Fig. 3.10) as it follows approximately the same power law, i.e., $T_{\mathrm{el}} \approx P^{0.45}$.

To transpose this discussion to the full microcavity case the average power density of the polariton lasing threshold $P_{\mathrm{thr},1}$ is also reported in Fig. 6.24(c) by a vertical red dashed line lying about one order of magnitude below $P_{\mathrm{crit},1}$. Note that this position with respect to the Mott transition only states an upper limit. In the full microcavity the different surface reflectivity, the transmission of the top DBR at the pump wavelength (~65%) and the redistribution of the radiative excitons inside the cavity section have to be considered. Indeed, whereas in the half-microcavity only the first set of four quantum wells is significantly populated due to the strong absorption at the pumping wavelength, the optical feedback in the full microcavity leads to a fast redistribution of the carriers coupled to the cavity light field by emission and reabsorption processes (Rabi-oscillations) and thus to a lower

[78] In the deconvolution procedure, only the contribution of X_{A} is considered due to the smaller contribution of X_{B} at such low lattice temperature. However, the progressive filling of X_{B} will likely result in an assymetric lineshape, which is blurred by the electron-hole contribution at large power densities.

exciton density per quantum well.[79] According to experiments, where no significant changes in the emission characteristics of the full microcavity are observed (cf. exciton linewidth evolution shown in Fig. 6.23(a)), and in complete agreement with the present quasi-cw excitation regime, the preservation of a sub-saturation carrier density and thus the strong coupling regime for the injection regimes investigated is ensured.

6.4.4.4 Possible origin for the lasing mechanism in the weak coupling regime for **E** ⊥ *c*

Let us now have a look at the nonlinear emission occurring for **E** ⊥ *c* where the light-matter interaction strength is not sufficient to bring X_A in the non-perturbative regime with C_o [175]. Interestingly the energy position of the lasing mode is above the X_A line and on the low energy side of the X_B transition (see Figs. 6.21(c) and 6.22(a)-6.22(b)). The estimation of the carrier density indicates that the system operates well below the Mott density. Considering the relatively low lattice temperature and the high exciton binding energy, excitons dominate the optical response of the quantum wells and the contribution of thermal free electrons deduced from Saha's law is negligible (see Section 4.6). The fact that the excitonic transition is not bleached is further confirmed by the coexistence of polaritonic features for **E** ∥ *c* at the same sample position. Our main concern is how such a system dominated by excitons can then provide gain. As already discussed in Section 4.1.1, excitonic lasing cannot be achieved without bleaching the resonance as it consists of a two-level system and it is only possible if another mechanism is involved such as a biexcitonic or phonon-assisted transition, bosonic condensation of excitons, or the presence of exciton localization [85]. Considering the high exciton binding energy and the important disorder of III-nitride compounds compared, e.g. to GaAs, it strongly suggests that gain occurring *via* localized excitonic states is the most probable mechanism. The potential landscape is set by alloy concentration disorder [81] and atomic monolayer well width fluctuations [178], which introduce low-energy states in the band tail. At low temperature, exciton localization induces a quantum dot-like behavior with a zero-dimensional density of states as the carriers are not free to propagate in the quantum well plane. In the present structure, the presence of localized states is evidenced by the quantum well inhomogeneous linewidth of ~ 20 meV.

A determination of the excitonic gain curve using relation 4.7 is prevented by the large uncertainties on the homogeneous and inhomogeneous line shapes, the localization center and the injected carrier densities. However, considering the sample parameters, one can estimate that the maximum of gain for excitonic lasing is expected approximately 40 – 50 meV below the maximum of gain for an inverted electron-hole plasma (situation corresponding to Fig. 4.2(c)), i.e. 10 – 20 meV below the free exciton line. In order to validate the applicability of this model in our system and to firmly assess the excitonic origin of the observed nonlinearities for **E** ⊥ *c*, extra measurements are required. In particular, optical gain measurements should be performed and the presence of a second threshold when the system transits toward a degenerate electron-hole plasma must be observed above n_X^{sat}. It is worth mentioning that excitonic gain relying on localized states has already been demonstrated for ZnSe-based quantum wells featuring an inhomogeneous linewidth of 9 meV [245] and in a GaAs-based microcavity operating in the nonperturbative regime by tuning the cavity resonance to the low-energy side of the inhomogeneous distribution [285]. In both cases, the system was shown to operate below the Mott density, as in our microcavity.

The interpretation of nonlinear emission for **E** ⊥ *c* in terms of lasing occurring in the weak coupling regime on localized states is further supported by the polarization-dependent real space emission

[79] Note that the excitonic reservoir does not take directly part to the light-matter interaction and decays with the excitonic nonradiative lifetime τ_X^{NR}.

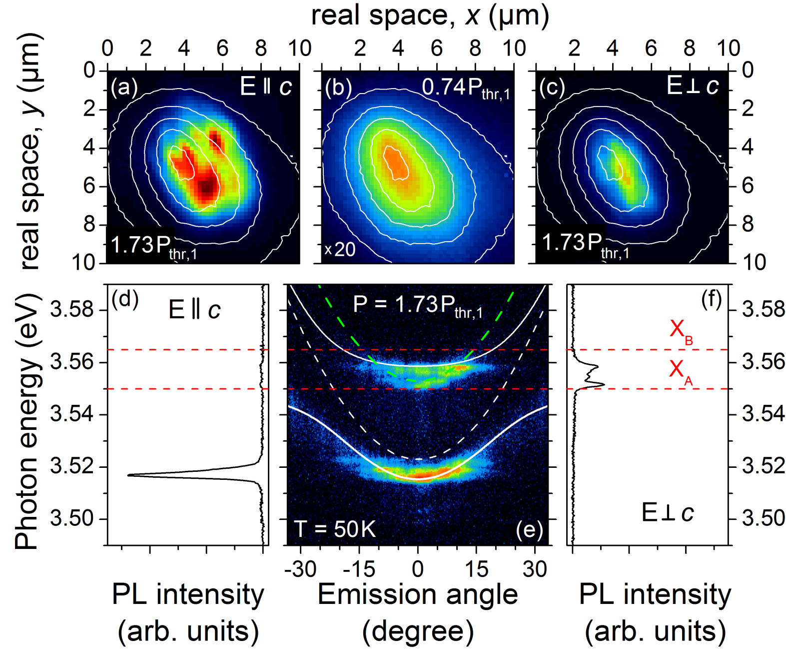

Fig. 6.25: (e) Fourier space-image measured above the two lasing thresholds without polarization selection (logarithmic scale, $T = 50\,\mathrm{K}$). Cavity modes along ordinary and extraordinary directions are represented with green and white dashed lines, respectively, the upper and lower polariton branches with white continuous lines and A and B excitons with red dashed lines. (d), (f) Corresponding polarization-resolved spectral profiles at $k_{\parallel} = 0$. (a), (c) Color maps of the corresponding polarization-resolved near-field images. The superimposed white solid lines represent the near-field emission pattern measured below threshold without polarization selection displayed in (b).

patterns shown in Figs. 6.25(a)-6.25(f). Whereas the emission profile below $P_{\mathrm{thr},1}$ is unstructured and corresponds to that of the pump spot, the profiles measured above $P_{\mathrm{thr},2}$ reveal the different nature of the lasing mechanisms. For light emitted along $\mathbf{E} \parallel c$ the nonlinear increase in intensity occurs at the bottom of LPB_e (Fig. 6.25(d)) and the near-field emission pattern exhibits randomly distributed emission hot spots even apart from the center of the pump spot. They likely correspond to polariton traps induced by photonic disorder in agreement with the broadening observed in momentum space [55, 222]. Conversely, for $\mathbf{E} \perp c$ in Fig. 6.25(c), the nonlinear emission exclusively arises from a small region close to the maximum pump power density as expected for lasing action occurring in the weak coupling regime. Note that the threshold for this lasing mechanism is also affected by photonic disorder, i.e., by the local quality factor. It is worth recalling that despite their distinct nature both nonlinear emissions emerge from the same spot and thus coexist and share the same exciton reservoir.

Since the emission energetically occurs between X_{A} and X_{B} we believe that the gain is likely originating from localized states of X_{B} supported by their optimum overlap with C_o (see Figs. 6.25(e)-6.25(f) and 6.22(b)). This interpretation is further supported by the luminescence spectra measured at $k_{\parallel} = 0$ shown in Fig. 6.22(b) where lasing is seen to occur on the low energy tail of X_{B} for $\mathbf{E} \perp c$. The energy position of the lasing mode E_{lasing} is imposed by the total losses in the system $\alpha_{\mathrm{tot}} = \alpha_{\mathrm{m}} + \alpha_{\mathrm{c}}$, where α_{m} and α_{c} correspond to the mirror and internal cavity losses, respectively. Stimulated emission is triggered when the modal gain exceeds the losses at the lasing energy (relation 4.5). Note that the

condition for nonlinear emission strongly depends on the local quality of the active region and the mirrors *via* the losses coefficient α_{m} and α_{c}, respectively.

Before concluding, note that $P_{\mathrm{thr},1} < P_{\mathrm{thr},2}$ seems consistent with a polariton laser picture where the threshold is expected to be lower than for its weak coupling regime counterpart owing to the light effective mass and the bosonic nature of polaritons. The observed proximity between the two thresholds might look surprising as polariton lasing is often claimed to be a thresholdless mechanism owing to the release of the Bernard-Duraffourg condition. Nevertheless the threshold is limited by the carrier relaxation kinetics and the finite lifetime of the exciton reservoir resulting in a significantly increased threshold with respect to the optimum case set by the thermodynamics [56]. The out-of-equilibrium nature of the presently observed polariton condensation is confirmed by the non-thermal occupancy of LPB_e in Fig. 6.21(d). Another important aspect, which could explain the proximity between the two thresholds, is that the lasing mechanism on localized states depends on a zero- and not a two-dimensional density of states resulting in a lower threshold to reach the transparency condition on $X_{\mathrm{B}}^{\mathrm{loc}}$. In 1996, Fan and coworkers have shown that the threshold for lasing on localized exciton states is significantly lower than for an inverted electron-hole plasma population [285]. Finally the observation of a randomly distributed $P_{\mathrm{thr},2}/P_{\mathrm{thr},1}$ ratio, which ranges between 0.8 and 5 all over the sample indicates that the lasing mechanism involved for $\mathbf{E}\perp c$ strongly depends on the local excitonic and photonic disorder landscapes, which both affect the system losses. In any case, at this stage a quantitative comparison between the two thresholds remains rather elusive and a detailed understanding of the lasing mode in the ordinary direction still awaits further theoretical developments and experimental evidences.

7 Conclusion and perspectives

7.1 Summary of the experimental results

The goal of this thesis was to investigate the properties of GaN-based planar microcavities below and above the polariton condensation threshold, to describe the mechanisms leading to the formation of polariton condensates and to give the key elements for the optimization of devices relying on polariton nonlinearities. To reach this purpose, a Fourier-imaging spectroscopy setup allowing for the simultaneous monitoring of real space and far-field energy dispersions including polarization selection was carefully designed to probe the sample emission at various temperatures in the UV spectral range.

In Chapter 3, a detailed analysis of the active region allowed to clearly identify the role of biexcitons at low temperature evidencing their localization on potential fluctuations due to alloy disorder as well as the thermalization between both localized and free excitonic and biexcitonic populations. Then, the role of biexcitons was considered in the full microcavity: in particular, for specific detunings the bottom of the lower polariton branch was seen to be directly fed by the radiative dissociation of either cavity biexcitons or excitons mediated by one LO-phonon. Accordingly, a minimum polariton lasing threshold has been observed, when the bottom of the lower-polariton branch corresponds in energy to exciton and cavity biexciton first LO-phonon replicas. This singular observation highlights the role of excitonic molecules in the polariton condensate formation process as being a more efficient relaxation channel, when compared to the usually assumed acoustical phonon emission one. This mechanism had never been observed so far in other semiconductor systems and highlights both the high quality of the investigated sample and the impact of biexcitons in III-nitride based structures and potentially in other wide band gap semiconductors presenting large biexciton binding energies. Then the impact of the injected carrier density on the polariton branch renormalization was investigated, evidencing the important role played by phase space filling in GaN-based systems compared to other material systems such as II-tellurides or III-arsenides. In the last section, the impact of disorder on the polariton condensate formation was studied. Similarly to CdTe-based microcavities, condensation in real space due to in-plane disorder was observed. At higher injection power densities, the far-field emission pattern exhibited multimode nonlinear features for wave vectors $k_{\parallel} \neq 0$, which was ascribed to the ballistic propagation of polaritons induced by the large local blueshift imprinted by the pump.

In Chapter 4, the evolution of the polariton condensation threshold P_{thr} was investigated under incoherent optical pumping both theoretically and experimentally over a wide range of temperatures and exciton-cavity photon detunings in the multiple quantum well-based microcavity presented in the previous chapter. The condensation phase diagram of these bosonic quasiparticles was first

theoretically described within the framework of Bose-Einstein condensation of polaritons in the thermodynamic limit. Then a qualitative picture of cavity polariton relaxation kinetics including the impact of detuning and temperature was given before introducing a modeling of cavity polariton relaxation kinetics with semiclassical Boltzmann equations. The results of the theoretical modeling were finally compared with systematic measurements of P_{thr}. At low temperature and negative detunings, the polariton gas is far from thermal equilibrium and the condensation threshold is governed by the efficiency of the relaxation kinetics of the particles. Conversely, at high temperature and for less negative detunings, the relaxation kinetics is efficient enough to allow the achievement of a thermal polariton distribution function with a critical density for condensation given by the thermodynamic theory of Bose-Einstein condensation. For temperatures ranging between 140 and 340 K, an optimum detuning is found experimentally, where the condensation threshold power density is minimized. In this temperature range, polariton detrapping effects from the bottom of the trap formed in k-space by the lower polariton branch are found to play a supplementary role among the processes governing P_{thr}.

In Chapter 5, the polarization properties of the light emitted by the polariton condensates has been investigated at room temperature. Similarly to the behavior reported in other quantum well-based planar microcavities, the light emission is linearly polarized at threshold with the plane of polarization preferentially pinned to one of the crystallographic axes. With increasing pumping power, a depinning of the polarization is observed resulting in a progressive decrease in the polarization degree of the emitted light. This depinning is understood in terms of polariton-polariton repulsion competing with the static disorder potential. The polarization behavior differs from that of conventional lasers where the polarization degree usually increases as a function of pumping power. The detuning-dependence of the pinning efficiency was also investigated at threshold, featuring a non-monotonous behavior. This behavior was qualitatively understood from our model by taking into account the evolution of the polariton relaxation rate between the reservoir and the condensate with the detuning.

In the last chapter, the behavior of non-polar m-plane GaN based microcavities was addressed through two successive sample generations. Due to the important detuning between the quantum well emission and the bottom DBR stopband in the first sample generation, the strong coupling regime was observed between the quantum well exciton and the Bragg modes only. In the second sample generation, the good matching between the microcavity building-blocks has allowed the unambiguous observation of the strong light-matter coupling between the A exciton and the cavity mode along the extraordinary polarization direction, whereas only weakly coupled modes have been observed in the orthogonal direction. This singular behavior was attributed to the intrinsic twofold anisotropy: the birefringence is responsible for the polarization dependence of the cavity mode and the distribution of the exciton oscillator strength causes different coupling constants between light and matter along the two orthogonal directions. In the presently investigated structure, the different selection rules and optical constants for light polarization perpendicular and parallel to the optical axis leads to the coexistence of weak and strong coupling regimes. This point was further supported by transfer matrix simulations. Finally, a transition toward the nonlinear regime is observed in both directions. Whereas the emission could be attributed to polariton lasing in the extraordinary direction, the interpretation was more prospective in the ordinary one. As the system operates below the Mott density, gain on localized states of the excitonic transition was suggested as a possible mechanism but further theoretical and experimental developments are required.

7.2 Perspectives

7.2.1 Room temperature polariton condensation

The observations reported in other semiconductor systems at cryogenic temperatures, including integer [19] and half-integer quantum vortices [20], superfluidity [21–23] or solitons in polariton fluids [24] could be transposed to room temperature owing to the stability of exciton-polaritons in III-nitrides. Presently, the main experimental limitations to observe these effects come from the difficulty of achieving a high laser stability under cw condition in the UV range. Beside GaN, other systems, including ZnO and organic-based microcavities, are serious candidates for the observation of polariton nonlinearities at elevated temperatures (see Tab. 7.1). Their relative advantages and drawbacks compared to GaN are briefly discussed hereafter.

Table 7.1: Relevant physical properties for the different systems exhibiting high temperature polariton condensation.

	GaN (bulk)	GaN (QW)	ZnO (bulk)	Organic (bulk)
E_X^b (meV)	26 [50]	~ 45 [34]	~ 60 [286]	~ 1000 [35]
Ω_{VRS} (meV)	30 [33]	~ 56 [34]	~ 130 [287]	~ 256 [35]

7.2.1.1 ZnO-based microcavities

On the basis of its high exciton binding energy (~ 60 meV for bulk material [286]) and oscillator strength, ZnO has already been proposed in 2002 as a candidate of choice for high temperature polariton condensation [288]. Indeed, the strong coupling regime for a bulk active zone was achieved in several realization geometries: in monolithic cavities grown on top of a III-nitride bottom DBR [287, 289, 290], in fully-hybrid microcrystalline ZnO structures relying on two dielectric DBRs [291, 292], and it was even claimed in ZnO nanorods with a vacuum Rabi-splitting $\Omega_{VRS} \approx 280$ meV [293]. Although the strong coupling regime has been shown to be maintained up to 410 K [294], nonlinear emission in the strong coupling regime corresponding to polariton lasing has only been found very recently [233, 287, 295]. Despite a substantial research activity, the limited material quality prevented more sophisticated studies on ZnO-based microcavities until now and the lack of a reproducible and stable p-type doping might hamper the way toward devices.

7.2.1.2 Organic microcavities

Optical excitations in organic semiconductors are preferentially described in the framework of Frenkel excitons [296], i.e., strongly bound and localized electron-hole pairs (E_X^b up to 1 eV) exhibiting a high oscillator strength and commonly a transition energy in the visible spectral range. In combination with the ability of doping, organic microcavities present serious advantages over the inorganic ones and the potentially low cost of device fabrication promotes this research activity in the scientific community. Until now the strong coupling regime has been obtained for various planar sample geometries and active media [297–303] up to room temperature. Nevertheless, polariton condensation has only been demonstrated in an anthracene-based microcavity under optical excitation by Kéna-Cohen and Forrest

[35]. Despite obvious advantages, the limited thermal, physical and chemical stability of the most common active organic media constitutes the major drawback of organic microcavities.

7.2.2 Polariton lasing in systems with lower dimensions

Even if most of the achievements observed in strongly coupled atomic systems have been reproduced with planar semiconductor microcavities, the latter are far from being an ideal two-level system due to the complexity of the band structure. However, semiconductors offer serious advantages in terms of integration and scalability and a more exact analog of the atomic system can be achieved when considering quantum dots instead of quantum wells as the elementary excitations are fully quantized. Assuming that a single quantum dot is located at the antinode of the cavity electromagnetic field, the light-matter interaction constant reads [304]:

$$g_{\mathrm{QD}} = \sqrt{\frac{1}{4\pi\epsilon_{\mathrm{r}}\epsilon_0}\frac{\pi e^2 f_{\mathrm{osc}}^{\mathrm{QD}}}{m_0 V}}, \tag{7.1}$$

where $f_{\mathrm{osc}}^{\mathrm{QD}}$ is the quantum dot oscillator strength and V is the mode volume. The coupling scales thus with the quantity $\sqrt{f_{\mathrm{osc}}^{\mathrm{QD}}/V}$. Considering the small linewidth of single quantum dots, the achievement of the strong coupling regime is mainly limited by the cavity quality factor Q and the threshold for strong coupling might be overcome when the product $Q\sqrt{f_{\mathrm{osc}}^{\mathrm{QD}}/V}$ is maximized. This can be achieved by confining the cavity mode in a very small volume of space. The first demonstrations of strong coupling regime between a single quantum dot and the cavity field were obtained quasi-simultaneously in photonic crystal nanocavities ($Q = 13300$) [305] and in micropillars ($Q = 8000-9000$) [306]. The onset of lasing in a single InAs quantum dot strongly coupled to a high quality photonic crystal nanocavity ($Q = 20000$) was obtained only very recently by Nomura and coworkers [307].

Even if the strong coupling regime with single quantum dot has not been observed in III-nitrides, recent developments in photonic crystal nanocavities have revealed quality factors in excess of 5000 [308, 309]. Such high quality resonators should allow the observation of 0D-polaritonic effects in the forthcoming years. Beside 0D-structures and quantum well-based microcavities, the strong coupling regime and polariton lasing with ultra-low threshold has been reported recently in a single GaN nanowire coupled to a large area dielectric microcavity at room temperature [310, 311].

7.2.3 Toward electrically injected polariton lasers

The practical realization of polariton laser diodes based on III-nitride materials is sustained by the encouraging report of polariton lasing under nonresonant optical pumping at room temperature for both bulk GaN and GaN/(Al,Ga)N multiple quantum well microcavity structures [33, 34]. In order to transpose these observations in an electrically injected structure, excitons must be created in the active region by external contacts. The stability of the exciton complex under such conditions was demonstrated by Bajoni and coworkers in 2007 in an electrically pumped p-i-n diode with an embedded InGaAs quantum well [312]. One year after, Tsintzos and coworkers demonstrated the first polariton LED operating up to room-temperature in a monolithic GaAs-based microcavity [313, 314]. Despite the fact that the strong coupling regime is preserved at high temperatures under electrical injection, the cut-off temperature leading to the observation of optical nonlinearities is likely limited by the exciton binding energy [29] and polariton laser diodes based on III-arsenides would be restricted to cryogenic

conditions only. However, so far no clear evidence for polariton nonlinearities have been reported under electrical injection.[80]

Considering the realization of an electrically injected polariton-based device made of III-nitrides the choice of the active region is not obvious. From the point of view of the optical quality, GaN/(Al,Ga)N multiple quantum wells represents the most appropriate choice but an efficient p-type doping is extremely challenging. The problem of doping can be solved by switching to an (In,Ga)N/GaN quantum well-based structure instead. However, such quantum wells suffer from relatively large in-plane fluctuations, which detrimentally impact on the observation of the strong coupling regime [66]. Despite numerous constraints, (In,Ga)N quantum wells still remain the most promising system and different designs have been proposed for the realization of a polariton laser diode [11, 14]. Up to date, the main limitation remains the quality of the active region. Recently, Glauser and coworkers have worked on the optimization of the active region for such structures. They have shown that the number of (In,Ga)N/GaN quantum wells with an indium content ~ 12 – 15% and thicknesses of 1.5 – 2 nm/3 nm for the wells and the barriers, respectively, should not exceed 30 for microcavity structures grown on free standing-GaN substrate in order to keep an excitonic linewidth below 50 meV at room temperature [316]. Note that an electrically pumped InGaN-based exciton-polariton LED operating at room temperature was recently claimed [317].

7.2.4 Applications in biology

The possibility of achieving low-threshold lasing from the UV to the blue spectral range by switching from GaN to (In,Ga)N-based microcavities, the chemical inertness and the non-toxicity of these compounds make the III-nitride polariton laser an optoelectronic device of choice for medical and biological purposes. The majority of medical diagnostics relying on fluorescence sensing, which is a widely applied technique in biotechnology, usually require cumbersome, slow and expensive laboratory techniques. During the past years, a lot of effort has been dedicated to the development of integrated sensors on biochips including micro-channels, able to perform many parallel tasks *in vivo*. Such systems embedding VCSELs as a laser source have already been demonstrated [318]. However, even if this technology is well established in the near-infrared spectral range *via* the use of GaAs-based microcavities, moving to shorter wavelengths is a real issue as VCSELs become more and more difficult to fabricate. In this respect, switching from GaAs-based VCSELs to GaN-based polariton lasers would allow to incorporate low-power consumption and robust UV coherent emitters on biochips extending the possibilities for fluorescence analysis.

[80] Note that Bhattacharya and coworkers have claimed very recently the observation of nonlinearities in an $In_{0.1}Ga_{0.9}As$/GaAs multiple quantum well microcavity diode operating in the strong coupling regime at low temperature. However, the interpretation is still unclear [315].

Bibliography

[1] A. Einstein, *Quantentheorie des einatomigen idealen Gases. Zweite Abhandlung.*, Sitzber. Preuss. Akad. **1**, 3 (1925)

[2] A. Einstein, *Zur Quantentheorie des idealen Gases*, Sitzber. Preuss. Akad. **3**, 18 (1925)

[3] K. B. Davis, M. O. Mewes, M. R. Andrews, N. J. van Druten, D. S. Durfee, D. M. Kurn, W. Ketterle, *Bose-Einstein condensation in a gas of sodium atoms*, Phys. Rev. Lett. **75**, 3969 (1995)

[4] M. H. Anderson, J. R. Ensher, M. R. Matthews, C. E. Wieman, E. A. Cornell, *Observation of Bose-Einstein condensation in a dilute atomic vapor*, Science **269**, 198 (1995)

[5] A. Imamoğlu, R. J. Ram, S. Pau, Y. Yamamoto, *Nonequilibrium condensates and lasers without inversion: Exciton-polariton lasers*, Phys. Rev. A **53**, 4250 (1996)

[6] S. Nakamura, N. Iwasa, T. Yamada, T. Matsushita, H. Kiyoku, M. Senoh, S.-I. Nagahama, Y. Sugimoto, *InGaN-based multi-quantum-well-structure laser diodes*, Jpn. J. Appl. Phys. **35**, L74 (1996)

[7] S. Nakamura, M. Senoh, S. Nagahama, N. Iwasa, T. Yamada, T. Matsushita, H. Kiyoku, Y. Sugimoto, T. Kozaki, H. Umemoto, M. Sano, K. Chocho, *InGaN/GaN/AlGaN-based laser diodes with modulation-doped strained-layer superlattices*, Jpn. J. Appl. Phys. **36**, L1568 (1997)

[8] S. Nagahama, T. Yanamoto, M. Sano, T. Mukai, *Wavelength dependence of InGaN laser diode characteristics*, Jpn. J. Appl. Phys. **40**, 3075 (2001)

[9] H. Y. Ryu, K. H. Ha, J. K. Son, S. N. Lee, H. S. Paek, T. Jang, Y. J. Sung, K. S. Kim, H. K. Kim, Y. Park, O. H. Nam, *Determination of internal parameters in blue InGaN laser diodes by the measurement of cavity-length dependent characteristics*, Appl. Phys. Lett. **93**, 011105 (2008)

[10] D. Kasahara, D. Morita, T. Kosugi, K. Nakagawa, J. Kawamata, Y. Higuchi, H. Matsumura, T. Mukai, *Demonstration of blue and green GaN-based vertical-cavity surface-emitting lasers by current injection at room temperature*, Appl. Phys. Express **4**, 072103 (2011)

[11] R. Butté, N. Grandjean, *A novel class of coherent light emitters: polariton lasers*, Semicond. Sci. Technol. **26**, 014030 (2011)

[12] T.-C. Lu, C.-C. Kao, H.-C. Kuo, G.-S. Huang, S.-C. Wang, *CW lasing of current injection blue GaN-based vertical cavity surface emitting laser*, Appl. Phys. Lett. **82**, 141102 (2008)

[13] Y. Higuchi K. Omae, H. Matsumura, T. Mukai, *Room-temperature cw lasing of a GaN-based vertical-cavity surface-emitting laser by current injection*, Appl. Phys. Express **1**, 121102 (2008)

[14] I. Iorsh, M. Glauser, G. Rossbach, J. Levrat, M. Cobet, R. Butté, N. Grandjean, M. A. Kaliteevski, R. A. Abram, A. V. Kavokin, *Generic picture of the emission properties of III-nitride polariton laser diodes: steady-state and current modulation response*, Phys. Rev. B , submitted (2012)

[15] E. Rosencher, B. Vinter, *Optoélectronique* (Dunod, Paris, 2002)

[16] A. Castiglia, *Design and development of GaN-based electrically pumped vertical cavity surface emitting lasers*, PhD Thesis, Universita degli studi di Palermo (2007)

[17] C. Weisbuch, M. Nishioka, A. Ishikawa, Y. Arakawa, *Observation of the coupled exciton-photon mode splitting in a semiconductor quantum microcavity*, Phys. Rev. Lett. **69**, 3314 (1992)

[18] J. Kasprzak, M. Richard, S. Kundermann, A. Baas, P. Jeambrun, J. M. J. Keeling, F. M. Marchetti, M. H. Szymanska, R. André, J. L. Staehli, V. Savona, P. B. Littlewood, B. Deveaud-Plédran, Le Si Dang, *Bose-Einstein condensation of exciton polaritons*, Nature (London) **443**, 409 (2008)

[19] K. G. Lagoudakis, M. Wouters, M. Richard, A. Baas, I. Carusotto, R. André, Le Si Dang, B. Deveaud-Plédran, *Quantized vortices in an exciton-polariton condensate*, Nature Phys. **4**, 706 (2008)

[20] K. G. Lagoudakis, T. Ostatnický, A. V. Kavokin, Y. G. Rubo, R. André, B. Deveaud-Plédran, *Observation of half-quantum vortices in an exciton-polariton condensate*, Science **326**, 5955 (2009)

[21] A. Amo, D. Sanvitto, F. P. Laussy, D. Ballarini, E. del Valle, M. D. Martin, A. Lemaître, J. Bloch, D. N. Krizhanovskii, M. S. Skolnick, C. Tejedor, L. Viña, *Collective fluid dynamics of a polariton condensate in a semiconductor microcavity*, Nature (London) **457**, 291 (2008)

[22] A. Amo, J. Lefrère, S. Pigeon, C. Adrados, C. Ciuti, R. Houdré I. Carusotto, E. Giacobino, A. Bramati, *Superfluidity of polaritons in semiconductor microcavities*, Nature Phys. **5**, 805 (2009)

[23] S. Utsunomiya, L. Tian, G. Roumpos, C. W. Lai, N. Kumada, T. Fujisawa, M. Kuwata-Gonokami, A. Löffler, S. Höfling, A. Forchel, Y. Yamamoto, *Observation of Bogoliubov excitations in exciton-polariton condensates*, Nature Phys. **4**, 700 (2008)

[24] A. Amo, S. Pigeon, D. Sanvitto, V. G. Sala, R. Hivet, I. Carusotto, F. Pisanello, G. Leménager, R. Houdré, E Giacobino, C. Ciuti, A. Bramati, *Polariton superfluids reveal quantum hydrodynamic solitons*, Science **332**, 1167 (2011)

[25] S. Savasta, O. Di Stefano, V. Savona, W. Langbein, *Quantum complementarity of microcavity polaritons*, Phys. Rev. Lett. **94**, 246401 (2005)

[26] H. Oka, H. Ishihara, *Highly efficient generation of entangled photons by controlling cavity bipolariton states*, Phys. Rev. Lett. **100**, 170505 (2008)

[27] R. M. Stevenson, V. N. Astratov, M. S. Skolnick, D. M. Whittaker, E. Emam-Ismail, A. I. Tartakovskii, P. G. Savvidis, J. J. Baumberg, J. S. Roberts, *Continuous wave observation of massive polariton redistribution by stimulated scattering in semiconductor microcavities*, Phys. Rev. Lett. **85**, 3680 (2000)

[28] P. G. Savvidis, J. J. Baumberg, R. M. Stevenson, M. S. Skolnick, D. M. Whittaker, J. S. Roberts, *Angle-resonant stimulated polariton amplifier*, Phys. Rev. Lett. **84**, 1547 (2000)

[29] M. Saba, C. Ciuti, J. Bloch, V. Thierry-Mieg, R. André, Le Si Dang, S. Kundermann, A. Mura, G. Bongiovanni, J. L. Staehli, B. Deveaud-Plédran, *High-temperature ultrafast polariton parametric amplification In semiconductor microcavities*, Nature (London) **414**, 731 (2001)

[30] T. K. Paraïso, M.Wouters, Y. Léger, F. Morier-Genoud, B. Deveaud-Plédran, *Multistability of a coherent spin ensemble in a semiconductor microcavity*, Nature Mat. **9**, 655 (2010)

[31] C. Leyder, M. Romanelli, J.-Ph. Karr, E. Giacobino, T. C. H. Liew, M. M. Glazov, A. V. Kavokin, G. Malpuech, A. Bramati, *Observation of the optical spin Hall effect*, Nature Phys. **3**, 628 (2007)

[32] L. S. Dang, D. Heger, R. André, F. Bœuf, R. Romestain, *Stimulation of polariton photoluminescence in semiconductor microcavity*, Phys. Rev. Lett. **81**, 3920 (1998)

[33] S. Christopoulos, G. Baldassarri Höger von Högersthal, A. J. D. Grundy, P. G. Lagoudakis, A. V. Kavokin, J. J. Baumberg, G. Christmann, R. Butté, E. Feltin, J.-F. Carlin, N. Grandjean, *Room-temperature polariton lasing in semiconductor microcavities*, Phys. Rev. Lett. **98**, 126405 (2007)

[34] G. Christmann, R. Butté, E. Feltin, J.-F. Carlin, N. Grandjean, *Room temperature polariton lasing in a GaN/AlGaN multiple quantum well microcavity*, Appl. Phys. Lett. **93**, 051102 (2008)

[35] S. Kéna-Cohen, S. R. Forrest, *Room-temperature polariton lasing in an organic single-crystal microcavity*, Nature Phot. **4**, 371 (2010)

[36] I. A. Shelykh, G. Pavlovic, D. D. Solnyshkov, G. Malpuech, *Proposal for a mesoscopic optical Berry-phase interferometer*, Phys. Rev. Lett. **102**, 046407 (2009)

[37] L. Gu, H. Huanga, Z. Gan, *Sagnac effect of excitonic polaritons*, Phys. Rev. B **84**, 075402 (2011)
[38] F. P. Laussy, A. V. Kavokin, I. A. Shelykh, *Exciton-polariton mediated superconductivity*, Phys. Rev. Lett. **104**, 106402 (2010)
[39] C. Leyder, T. C. H Liew, A. V. Kavokin, I. A. Shelykh, M. Romanelli, J.-Ph. Karr, E. Giacobino, A. Bramati, *Interference of coherent polariton beams in microcavities: Polarization-controlled optical Gates*, Phys. Rev. Lett. **99**, 196402 (2007)
[40] I. A. Shelykh, A. V. Kavokin, Y. G. Rubo, T. C. H Liew, G. Malpuech, *Polariton polarization-sensitive phenomena in planar semiconductor microcavities*, Semicond. Sci. Technol. **25**, 013001 (2009)
[41] I. Shelykh, K. V. Kavokin, A. V. Kavokin, G. Malpuech, P. Bigenwald, H. Deng, G. Weihs, Y. Yamamoto, *Semiconductor microcavity as a spin-dependent optoelectronic device*, Phys. Rev. B **70**, 035320 (2004)
[42] A. Amo, T. C. H. Liew, C. Adrados, R. Houdré, E. Giacobino, A. V. Kavokin, A. Bramati, *Exciton-polariton spin switches*, Nature Phot. **4**, 361 (2010)
[43] T. C. H. Liew, A. V. Kavokin, I. A. Shelykh, *Optical circuits based on polariton neurons in semiconductor microcavities*, Phys. Rev. Lett. **101**, 016402 (2008)
[44] K. V. Kavokin, M. A. Kaliteevski, R. A. Abram, A. V. Kavokin, S. Sharkova, I. A. Shelykh, *Stimulated emission of terahertz radiation by exciton-polariton lasers*, Appl. Phys. Lett. **97**, 201111 (2010)
[45] A.V. Kavokin, I. A. Shelykh, T. Taylor, M. M. Glazov, *Vertical cavity surface emitting terahertz laser*, Phys. Rev. Lett. **108**, 197401 (2012)
[46] D. Bajoni, E. Semenova, A. Lemaître, S. Bouchoule, E. Wertz, P. Senellart, S. Barbay, R. Kuszelewicz, J. Bloch, *Optical bistability in a GaAs-based polariton diode*, Phys. Rev. Lett. **101**, 266402 (2008)
[47] J. Robertson, *High dielectric constant oxides*, Eur. Phys. J. Appl. Phys **28**, 265 (2004)
[48] G. Bastard, E. E. Mendez, L. L. Chang, L. Esaki, *Exciton binding energy in quantum wells*, Phys. Rev. B **26**, 1974 (1982)
[49] S. Nakamura, T. Mukai, M. Senoh, *Candela-class high brightness InGaN/AlGaN double-heterostructure blue-light-emitting diodes*, Appl. Phys. Lett. **64**, 1687 (1994)
[50] K. Kornitzer, T. Ebner, K. Thonke, R. Sauer, C. Kirchner, V. Schwegler, M. Kamp, M. Leszczynski, I. Grzegory, S. Porowski, *Photoluminescence and reflectance spectroscopy of excitonic transitions in high-quality homoepitaxial GaN films*, Phys. Rev. B **60**, 1471 (1999)
[51] A. V. Kavokin, B. Gil, *GaN microcavities: Giant Rabi splitting and optical anisotropy*, Appl. Phys. Lett. **72**, 2880 (1998)
[52] J. J. Baumberg, A. V. Kavokin, S. Christopoulos, A. J. D. Grundy, R. Butté, G. Christmann, D. D. Solnyshkov, G. Malpuech, G. Baldassarri Höger von Högersthal, E. Feltin, J.-F. Carlin, N. Grandjean, *Spontaneous polarization build-up in a room-temperature polariton laser*, Phys. Rev. Lett. **101**, 136409 (2008)
[53] G. Christmann, R. Butté, E. Feltin, A. Mouti, P. A. Stadelmann, A. Castiglia, J.-F. Carlin, N. Grandjean, *Large vacuum Rabi splitting in a multiple quantum well GaN-based microcavity in the strong-coupling regime*, Phys. Rev. B **77**, 085310 (2008)
[54] D. Solnyshkov, H. Ouerdane, G. Malpuech, *Kinetic phase diagrams of GaN-based polariton lasers*, J. Appl. Phys. **103**, 016101 (2008)
[55] R. Butté, J. Levrat, G. Christmann, E. Feltin, J.-F. Carlin, N. Grandjean, *Phase diagram of a polariton laser from cryogenic to room temperature*, Phys. Rev. B **80**, 233301 (2009)
[56] J. Levrat, R. Butté, E. Feltin, J.-F. Carlin, N. Grandjean, D. Solnyshkov, G. Malpuech, *Condensation phase diagram of cavity polaritons in GaN-based microcavities: Experiment and theory*, Phys. Rev. B **81**, 125305 (2010)
[57] N. Antoine-Vincent, F. Natali, D. Byrne, A. Vasson, P. Disseix, J. Leymarie, M. Leroux, F. Semond, J. Massies, *Observation of Rabi splitting in a bulk GaN microcavity grown on silicon*, Phys. Rev. B **68**, 153313 (2003)

[58] F. Semond, I. R. Sellers, F. Natali, D. Byrne, M. Leroux, J. Massies, N. Ollier, J. Leymarie, P. Disseix, , A. Vasson, *Strong light-matter coupling at room temperature in simple geometry GaN microcavities grown on silicon*, Appl. Phys. Lett. **87**, 021102 (2005)

[59] J.-F. Carlin, M. Ilegems, *High-quality AlInN for high index contrast Bragg mirrors lattice matched to GaN*, Appl. Phys. Lett. **83**, 668 (2003)

[60] J.-F. Carlin, J. Dorsaz, E. Feltin R. Butté, N. Grandjean, M. Ilegems, M. Laügt, *Crackfree fully epitaxial nitride microcavity using highly reflective AlInN/GaN Bragg mirrors*, Appl. Phys. Lett. **86**, 031107 (2005)

[61] E. Feltin, G. Christmann, J. Dorsaz, A. Castiglia, J.-F. Carlin, R. Butté, N. Grandjean, S. Christopoulos, G. B. H. von Högersthal, A. J. D. Grundy, P. G. Lagoudakis, J. J. Baumberg, *Blue lasing at room temperature in an optically pumped lattice-matched AlInN/GaN VCSEL structure*, Electron. Lett. **43**, 924 (2007)

[62] R. Butté, E. Feltin, J. Dorsaz, G. Christmann, J.-F. Carlin, N. Grandjean, M. Ilegems, *Recent progress in the growth of highly reflective nitride-based distributed Bragg reflectors and their use in microcavities*, Jpn. J. Appl. Phys. **44**, 7207 (2005)

[63] R. Butté, G. Christmann, E. Feltin, J.-F. Carlin, M. Mosca, M. Ilegems, N. Grandjean, *Room-temperature polariton luminescence from a bulk GaN microcavity*, Phys. Rev. B **73**, 033315 (2006)

[64] E. Feltin, G. Christmann, R. Butté, J.-F. Carlin, M. Mosca, N. Grandjean, *Room temperature polariton luminescence from a GaN/AlGaN quantum well microcavity*, Appl. Phys. Lett. **89**, 071107 (2006)

[65] G. Christmann, D. Simeonov, R. Butté, E. Feltin, J.-F. Carlin, N. Grandjean, *Impact of disorder on high quality factor III-V nitride microcavities*, Appl. Phys. Lett. **89**, 261101 (2006)

[66] G. Christmann, R. Butté, E. Feltin, J.-F. Carlin, N. Grandjean, *Impact of inhomogeneous broadening on the strong exciton-phonon coupling in quantum well nitride cavities*, Phys. Rev. B **73**, 153305 (2006)

[67] F. Stokker-Cheregi, A. Vinattieri, F. Semond, M. Leroux, R. Sellers, J. Massies, D. Solnyshkov, G. Malpuech, M. Colocci, M. Gurioli, *Polariton relaxation bottleneck and its thermal suppression in bulk GaN microcavities*, Appl. Phys. Lett. **92**, 042119 (2008)

[68] F. Réveret, P. Disseix, J. Leymarie, A. Vasson, F. Semond, M. Leroux, J. Massies, *Influence of the mirrors on the strong coupling regime in planar GaN microcavities*, Phys. Rev. B **77**, 195303 (2008)

[69] E. Grilli, M. Guzzi, R. Zamboni, L. Pavesi, *High-precision determination of the temperature dependence of the fundamental energy gap in gallium arsenide*, Phys. Rev. B **45**, 1638 (1992)

[70] C. Neumann, A. Nöthe, N. O. Lipari, *Two-photon magnetoabsorption of ZnTe, CdTe, and GaAs*, Phys. Rev. B **37**, 922 (1988)

[71] R. Dingle, D. D. Sell, S. E. Stokowski, M. Ilegems, *Absorption, reflectance, and luminescence of GaN epitaxial layers*, Phys. Rev. B **4**, 1211 (1971)

[72] P. Y. Yu, M. Cardona, *Fundamentals of semiconductors: Physics and materials properties (Fourth Edition)* (Springer, Heidelberg, 2010)

[73] G. Steude, B. K. Meyer, A. Göldner, A. Hoffmann an F. Bertram, J. Christen, H. Amano, I. Akasaki, *Optical investigations of AlGaN on GaN epitaxial films*, Appl. Phys. Lett. **74**, 2456 (1999)

[74] C. Weisbuch, R. C. Miller, R. Dingle, A. C. Gossard, W. Wiegman, *Intrinsic radiative recombination from quantum states in GaAs-$Al_xGa_{1-x}As$ multi-quantum well structures*, Solid State Commun. **37**, 219 (1981)

[75] J. J. Hopfield, *Theory of the contribution of excitons to the complex dielectric constant of crystals*, Phys. Rev. **112**, 1555 (1958)

[76] A. V. Kavokin, J. J. Baumberg, G. Malpuech, F. P. Laussy, *Microcavities* (Oxford University Press, Oxford, 2007)

[77] A. Honold, L. Schultheis, J. Kuhl, C.W. Tu, *Collision broadening of two-dimensional excitons in a GaAs single quantum well*, Phys. Rev. B **40**, 6442 (1989)

[78] R. Eccleston, B. F. Feuerbacher, J. Kuhl, W. W. Rühle, K. Ploog, *Density-dependent exciton radiative lifetimes in GaAs quantum wells*, Phys. Rev. B **45**, 11403 (1992)

[79] F. Binet, J. Y. Duboz, J. Off, F. Scholz, *High-excitation photoluminescence in GaN: Hot-carrier effects and the Mott transition*, Phys. Rev. B **60**, 4715 (1999)

[80] R. W. Martin, P. G. Middleton, K. P. O'Donnell, W. Van der Stricht, *Exciton localization and the Stokes' shift in InGaN epilayers*, Appl. Phys. Lett. **74**, 263 (1998)

[81] E. Feltin, D. Simeonov, J.-F. Carlin, R. Butté, N. Grandjean, *Narrow UV emission from homogeneous GaN/AlGaN quantum wells*, Appl. Phys. Lett. **90**, 021905 (2007)

[82] S. A. Moskalenko, *Reversible optico-hydrodynamic phenomena in a non ideal exciton gas*, Sov. Phys. Solid State **4**, 199 (1962)

[83] P. A. Martin, F. Rothen, *Problèmes à N-corps et champs quantiques* (Presses polytechniques et universitaires romandes, Lausanne, 1990)

[84] M. Perrin, *Relaxation des polaritons dans une microcavité contenant un gaz d'électrons*, PhD Thesis, Université Paris VI (2006)

[85] H. Hanamura, H. Haug, *Condensation effects of excitons*, Phys. Rep. **33**, 209 (1977)

[86] M. Kira, F. Jahnke, S. W. Koch, J. D. Berger, D. V. Wick, T. R. Nelson Jr., G. Khitrova, H. M. Gibbs, *Quantum theory of nonlinear semiconductor microcavity luminescence explaining "Boser" experiments*, Phys. Rev. Lett. **79**, 5170 (1997)

[87] N. F. Mott, *The transition to the metallic state*, Philos. Mag. **6**, 287 (1961)

[88] N. F. Mott, *Continuous and discontinuous metal-insulator transitions*, Philos. Mag. **37**, 377 (1978)

[89] L. M. Sander, D. K. Fairobent, *Mott transition of the electron-hole liquid in Ge*, Solid State Commun. **20**, 631 (1976)

[90] R. Zimmermann, *Many particle theory of highly excited semiconductors* (Teubner Verlag, Leipzig, 1988)

[91] L. J. Schowalter, F. M. Steranka, M. B. Salamon, J. P. Wolfe, *Evidence for separate Mott and liquid-gas transitions in photoexcited, strained germanium*, Phys. Rev. B **29**, 2970 (1984)

[92] J. Shah, M. Combescot, A. H. Dayem, *Investigation of exciton-plasma Mott transition in Si*, Phys. Rev. Lett. **38**, 1497 (1977)

[93] T. Ando, A. B. Fowler, F. Stern, *Electronic-properties of two-dimensional systems*, Rev. Modern Phys. **54**, 437 (1982)

[94] S. Schmitt-Rink, D. S. Chemla, D. A. B. Miller, *Theory of transient excitonic optical nonlinearities in semiconductor quantum-well structures*, Phys. Rev. B **32**, 6601 (1985)

[95] H. Reinholz, *Mott effect for an electron-hole plasma in a two-dimensional structure*, Solid State Commun. **123**, 489 (2002)

[96] Y. E. Lozovik, O. L. Berman, *The excitonic superfluid liquid in the system of spatially separated electrons and holes*, Physica Scripta **55**, 491 (1997)

[97] H. W. Yoon, M. D. Sturge, L. N. Pfeiffer, *Magnetic field induced Mott transition of a one-component electron plasma in GaAs quantum wells*, Solid State Commun. **104**, 287 (1997)

[98] L. Kappei, J. Szczytko, F. Morier-Genoud, B. Deveaud-Plédran, *Direct observation of the Mott transition in an optically excited semiconductor quantum well*, Phys. Rev. Lett. **94**, 147403 (2005)

[99] N. Peyghambarian, H. M. Gibbs, J. L. Jewell, A. Antonetti, A. Migus, D. Hulin, A. Mysyrowicz, *Blue shift of the exciton resonance due to exciton-exciton interactions in a multiple-quantum-well structure*, Phys. Rev. Lett. **53**, 2433 (1984)

[100] B. Deveaud-Plédran, F. Clérot, N. Roy, K. Satzke, B. Sermage, D. S. Katzer, *Enhanced radiative recombination of free excitons in GaAs quantum wells*, Phys. Rev. Lett. **67**, 2355 (1991)

[101] F. Tassone, Y. Yamamoto, *Exciton-exciton scattering dynamics in a semiconductor microcavity and stimulated scattering into polaritons*, Phys. Rev. B **59**, 10830 (1999)

[102] C. Ciuti, V. Savona, C. Piermarocchi, A. Quattropani, P. Schwendimann, *Role of the exchange of carriers in elastic exciton-exciton scattering in quantum wells*, Phys. Rev. B **58**, 7926 (1998)

[103] C. Ciuti, P. Schwendimann, B. Deveaud-Plédran, A. Quattropani, *Theory of the angle-resonant polariton amplifier*, Phys. Rev. B **62**, R4825 (2000)

[104] D. Hulin, A. Mysyrowicz, A. Antonetti, A. Migus, W. T. Masseling, H. Morkoç, H. M. Gibbs, N. Peyghambarian, *Well-size dependence of exciton blue shift in GaAs multiple-quantum-well structures*, Phys. Rev. B **33**, 4389 (1986)

[105] L. C. Andreani, *Radiative lifetime of free excitons in quantum wells*, Solid State Commun. **9**, 641 (1991)

[106] C. Weisbuch, B. Vinter, *Quantum semiconductor structures: Fundamentals and applications* (Academic Press Inc, San Diego, 1991)

[107] D. S. Citrin, *Radiative lifetimes of excitons in quantum wells: Localization and phase-coherence effects*, Phys. Rev. B **47**, 3832 (1993)

[108] J. Besbas, A. Gadalla, M. Gallart, O. Crégut, B. Hönerlage, P. Gilliot, E. Feltin, J.-F. Carlin, R. Butté, N. Grandjean, *Spin relaxation of free excitons in narrow GaN/$Al_x Ga_{1-x}N$ quantum wells*, Phys. Rev. B **82**, 195302 (2010)

[109] H. Yokoyama, *Physics and device applications of optical microcavities*, Science **256**, 66 (1992)

[110] H. Benisty, H. De Neve, C. Weisbuch, *Impact of planar microcavity effects on light extraction - Part I: basic concepts and analytical trends*, IEEE J. Quantum Elect. **1612**, 1998 (34)

[111] E. Feltin, J.-F. Carlin, J. Dorsaz, G. Christmann, R. Butté, M. Laügt, M. Ilegems, N. Grandjean, *Crack-free highly reflective AlInN/AlGaN Bragg mirrors for UV applications*, Appl. Phys. Lett. **88**, 051108 (2006)

[112] R. Houdré, R. P. Stanley, M. Ilegems, *Vacuum-field Rabi splitting in the presence of inhomogeneous broadening: Resolution of a homogeneous linewidth in an inhomogeneously broadened system*, Phys. Rev. A **53**, 2711 (1996)

[113] V. Savona, L. C. Andreani, P. Schwendimann, A. Quattropani, *Unified treatment of weak and strong coupling regimes*, Solid State Commun. **93**, 773 (1995)

[114] Y. Zhu, D. J. Gautier, S. E. Morin, Q. Wu, H. J. Carmichael, T. W. Mossberg, *Vaccum Rabi splitting as a feature of linear dispersion theory: analysis and experimental observations*, Phys. Rev. Lett. **64**, 2499 (1990)

[115] T. B. Norris, J.-K. Rhee, C.-Y. Sung, Y. Arakawa, M. Nishioka, C. Weisbuch, *Time-resolved vacuum Rabi oscillations in a semiconductor quantum microcavity*, Phys. Rev. B **50**, 14663 (1994)

[116] V. Savona, C. Weisbuch, *Theory of time-resolved light emission from polaritons in a semiconductor microcavity under resonant excitation*, Phys. Rev. B **54**, 10835 (1996)

[117] P. Corfdir, P. Lefebvre, J. Ristic, P. Valvin, E. Calleja, A. Trampert, J.-D. Ganière, B. Deveaud-Plédran, *Time-resolved spectroscopy on GaN nanocolumns grown by plasma assisted molecular beam epitaxy on Si substrates*, J. Appl. Phys. **105**, 013113 (2009)

[118] P. Corfdir, private communication (2012)

[119] G. Christmann, *III-nitride based microcavities: Towards polariton condensation at room temperature*, PhD Thesis, EPFL (2009)

[120] S. Sonderegger, E. Feltin, M. Merano, A. Crottini, J. F. Carlin, R. Sachot, B. Deveaud-Plédran, N. Grandjean, J. D. Ganière, *High spatial resolution picosecond cathodoluminescence of InGaN quantum wells*, Appl. Phys. Lett. **89**, 232109 (2006)

[121] P. Corfdir, *Physics of the ultrafast dynamics of excitons in GaN nanostructures*, PhD Thesis, École Polytechnique Fédérale de Lausanne (2011)

[122] G. Björk, H. Heitmann, Y. Yamamoto, *Spontaneous-emission coupling factor and mode characteristics of planar dielectric microcavity lasers*, Phys. Rev. A **47**, 4451 (1993)

[123] G. C. La Rocca, F. Bassani, V. M. Agranovich, *Biexcitons and dark states in semiconductor microcavities*, J. Opt. Soc. Am. B **15**, 652 (1998)

[124] L. Pitaevskii, S. Stringari, *Bose-Einstein condensation* (Oxford Science Publications, Oxford, 2003)

[125] L. V. Butov, A. Zrenner, G. Abstreiter, G. Böhm, G. Weimann, *Condensation of indirect excitons in coupled AlAs/GaAs quantum wells*, Phys. Rev. Lett. **73**, 304 (1994)

[126] T. Nikuni, M. Oshikawa, A. Oosawa, H. Tanaka, *Bose-Einstein condensation of dilute magnons in* $TlCuCl_3$, Phys. Rev. Lett. **84**, 5868 (2000)

[127] J. Klaers, J. Schmitt, F. Vewinger, M. Weitz, *Bose-Einstein condensation of photons in an optical microcavity*, Nature (London) **468**, 545 (2010)

[128] N. D. Mermin, H. Wagner, *Absence of ferromagnetism or antiferromagnetism in one- or two-dimensional isotropic Heisenberg models*, Phys. Rev. Lett. **17**, 1133 (1966)

[129] H. Deng, H. Haug, Y. Yamamoto, *Exciton-polariton Bose-Einstein condensation*, Rev. Modern Phys. **82**, 1489 (2010)

[130] H. P. Maruska, J. J. Tietjen, *The preparation and properties of vapor-deposited single crystalline GaN*, Appl. Phys. Lett. **15**, 327 (1969)

[131] H. Amano, Y. Toyoda, N. Sawaki, I. Akasaki, *Metalorganic vapor phase epitaxial growth of a high quality GaN film using an AlN buffer layer*, Appl. Phys. Lett. **48**, 353 (1986)

[132] H. Amano, M. Kito, K. Hiramatsu, I. Akasaki, *P-type conduction in Mg-doped GaN treated with low-energy electron beam irradiation (LEEBI)*, Jpn. J. Appl. Phys. **28**, L2112 (1989)

[133] S. Nakamura, T. Mukai, M. Senoh, *High-power GaN p-n junction blue-light emitting diodes*, Jap. J. Appl. Phys. **30**, L1998 (1991)

[134] T. Lei, M. Fanciulli, R. J. Molnar, T. D. Moustakas, R. J. Graham, J. Scanlon, *Epitaxial growth of zinc blende and wurtzitic gallium nitride thin films on (001) silicon*, Appl. Phys. Lett. **59**, 944 (1991)

[135] A. Muoz, K. Kunc, *High-pressure phase of gallium nitride*, Phys. Rev. B **44**, 10372 (1991)

[136] L. Görgens, O. Ambacher, M. Stutzmann, C. Miskys, F. Scholz, J. Off, *Characterization of InGaN thin films using high-resolution x-ray diffraction*, Appl. Phys. Lett. **76**, 577 (1999)

[137] H. Angerer, D. Brunner, F. Freudenberg, O. Ambacher, M. Stutzmann, R. Höpler, T. Metzger, E. Born, G. Dollinger, A. Bergmaier, S. Karsch, H.-J. Körner, *Determination of the Al mole fraction and the band gap bowing of epitaxial* $Al_xGa_{1-x}N$ *films*, Appl. Phys. Lett. **71**, 1504 (1997)

[138] T. Peng, J. Piprek, G. Qiu, J. O. Olowolafe, K. M. Unruh, C. P. Swann, E. F. Schubert, *Band gap bowing and refractive index spectra of polycrystalline* $Al_xIn_{1-x}N$ *films deposited by sputtering*, Appl. Phys. Lett. **71**, 2439 (1997)

[139] O. Ambacher, J. Majewski, C. Miskys, A. Link, M. Hermann, M. Eickhoff, M. Stutzmann, F. Bernardini, V. Fiorentini, V. Tilak, B. Shaff, L. F. Eastman, *Pyroelectric properties of Al(In)GaN/GaN hetero- and quantum well structures*, J. Phys.: Condens. Matter **14**, 3399 (2002)

[140] S.-H. Park, S.-L. Chuang, *Crystal-orientation effects on the piezoelectric field and electronic properties of strained wurtzite semiconductors*, Phys. Rev. B **59**, 4725 (1999)

[141] N. Akopian, G. Bahir, Gershoni, M. D. Craven, J. S. Speck, S. P. DenBaars, *Optical evidence for lack of polarization in* $(11\bar{2}0)$ *oriented GaN/(Al,Ga)N quantum structures*, Appl. Phys. Lett. **86**, 202104 (2005)

[142] P. Waltereit, O. Brandt, A. Trampert, H. T. Grahn, J. Menniger, M. Ramsteiner, M. Reiche, K. H. Ploog, *Nitride semiconductors free of electrostatic fields for efficient white light-emitting diodes*, Nature (London) **406**, 865 (2000)

[143] N. F. Gardner, J. C. Kim, J. J. Wierer, Y. C. Shen, M. R. Krames, *Polarization anisotropy in the electroluminescence of m-plane InGaN-GaN multiple-quantum-well light-emitting diodes*, Appl. Phys. Lett. **86**, 111101 (2005)

[144] K. Kojima, A. A. Yamaguchi, M. Funato, Y. Kawakami, , S. Noda, *Impact of nonpolar AlGaN quantum wells on deep ultraviolet laser diodes*, J. Appl. Phys. **110**, 043115 (2011)

[145] J. E. Northrup, *GaN and InGaN* $(11\bar{2}2)$ *surfaces: Group-III adlayers and indium incorporation*, Appl. Phys. Lett. **95**, 133107 (2009)

[146] Y. Yoshizumi, M. Adachi, Y. Enya, T. Kyono, S. Tokuyama, T. Sumitomo, K. Akita, T. Ikegami, M. Ueno, K. Katayama, T. Nakamura, *Continuous-wave operation of 520 nm green InGaN-based laser diodes on semi-polar* $\{20\bar{2}1\}$ *GaN substrates*, Appl. Phys. Express **2**, 092101 (2009)

[147] R. Robert, R. Reeber, K. Wang, *Lattice parameters and thermal expansion of important semiconductors and their substrates*, Mat. Res. Soc. Symp. **622**, T6.35.1 (2000)

[148] T. Detchprohm, K. Hiramatsu, K. Itoh, I. Akasaki, *Relaxation process of the thermal strain in the GaN/*α*-*Al_2O_3 *heterostructure and determination of the intrinsic lattice constants of GaN free from the strain*, Jpn. J. Appl. Phys. **31**, L1454 (1992)

[149] O. Ambacher, *Growth and applications of group III-nitrides*, J. Phys. D: Appl. Phys. **31**, 2653 (1998)

[150] H. Lahrèche, M. Leroux, M. Laügt, M. Vaille, B. Beaumont, P. Gibart, *Buffer free direct growth of GaN on 6H-SiC by metalorganic vapor phase epitaxy*, J. Appl. Phys. **87**, 577 (2000)

[151] L. Liu, J. H. Edgar, *Substrates for gallium nitride epitaxy*, Mat. Sci. Eng. R. **37**, 61 (2002)

[152] Y. Sun, S. E. Thompson, T. Nishida, *Strain effect in semiconductors: Theory and device applications* (Springer, New York, 2010)

[153] I. Vurgaftman, J. R. Meyer, *Band parameters for nitrogen-containing semiconductors*, J. Appl. Phys. **94**, 3675 (2003)

[154] U. M. E. Christmas, A. D. Andreev, D. A. Faux, *Calculation of electric field and optical transitions in InGaN/GaN quantum wells*, J. Appl. Phys. **98**, 073522 (2005)

[155] A. Bykhovski, B. Gelmont, M. Shur, *Strain and charge distribution in GaN-AlN-GaN semiconductor-insulator-semiconductor structure for arbitrary growth orientation*, Appl. Phys. Lett. **63**, 2243 (1993)

[156] F. Bernardini, V. Fiorentini, *Nonlinear macroscopic polarization in III-V nitride alloys*, Phys. Rev. B **64**, 085207 (2001)

[157] F. Bernardini, Vincenzo Fiorentini, *Spontaneous versus piezoelectric polarization in III-V nitrides: Conceptual aspects and practical consequences*, Phys. Stat. Sol. (b) **216**, 391 (1999)

[158] N. Grandjean, B. Damilano, S. Dalmasso, M. Leroux, M. Laügt, J. Massies, *Built-in electric-field effects in wurtzite AlGaN/GaN quantum wells*, J. Appl. Phys. **86**, 3714 (1999)

[159] Y. P. Varshni, *Temperature dependence of energy gap in semiconductors*, Physica **34**, 149 (1967)

[160] J. Wu, W. Walukiewicz, K. M. Yu, J. W. Ager, E. E. Haller, H. Lu, W. J. Schaff, Y. Saito, Y. Nanishi, *Unusual properties of the fundamental band gap of InN*, Appl. Phys. Lett. **80**, 3967 (2002)

[161] P. Rinke, M. Winkelnkemper, A. Qteish, D. Bimberg, J. Neugebauer, M. Scheffler, *Consistent set of band parameters for the group-III nitrides AlN, GaN, and InN*, Phys. Rev. B **77**, 075202 (2008)

[162] S.-H. Chuang, C.-S. Chang, *A band-structure model of strained quantum-well wurtzite semiconductors*, Semicond. Sci. Technol. **12**, 252 (1997)

[163] B. Gil, O. Briot, *Internal structure and oscillator strengths of excitons in strained* α*-GaN*, Phys. Rev. B **55**, 2530 (1997)

[164] K. Shimada, T. Sota, K. Suzuki, *First-principles study on electronic and elastic properties of BN, AlN, and GaN*, J. Appl. Phys. **84**, 4951 (1998)

[165] M. Suzuki, T. Uenoyama, A. Yanase, *First-principle calculations of effective-mass parameters of AlN and GaN*, Phys. Rev. B **52**, 8132 (1995)

[166] B. Gil, A. Alemu, *Optical anisotropy of excitons in strained GaN epilayers grown along the* $<10\bar{1}0>$ *direction*, Phys. Rev. B **56**, 12446 (1997)

[167] S. L. Chuang, C. S. Chang, *$k{\cdot}p$ method for strained wurtzite semiconductors*, Phys. Rev. B **54**, 2491 (1996)

[168] R. Wang, P. P. Ruden, J. Kolnik, I. Oguzman, K. F. Brennan, *Dielectric properties of wurtzite and zincblende structure gallium nitride*, J. Phys. Chem. Solids **58**, 913 (1997)

[169] H. Y. Zhang, X. H. He, Y. H. Shih, M. Schurman, Z. C. Feng, R. A. Stall, *Study of nonlinear optical effects in GaN:Mg epitaxial film*, Appl. Phys. Lett. **69**, 2953 (1996)

[170] N. A. Sanford, A. Munkholm, M. R. Krames, A. Shapiro, I. Levin, A. V. Davydov, S. Sayan, L. S. Wielunski, T. E. Madey, *Refractive index and birefringence of $In_xGa_{1-x}N$ films grown by MOCVD*, Phys. Stat. Sol. (c) **7**, 2783 (2005)

[171] N. A. Sanford, L. H. Robins, A. V. Davydov, A. Shapiro, D. V. Tsvetkov, A. V. Dmitriev, S. Keller, U. K. Mishra, S. P. DenBaars, *Refractive index study of $Al_xGa_{1-x}N$ films grown on sapphire substrates*, J. Appl. Phys. **94**, 2980 (2003)

[172] S. Shokhovets, R. Goldhahn, G. Gobsch, S. Piekh, R. Lantier, A. Rizzi, V. Lebedev, W. Richter, *Determination of the anisotropic dielectric function for wurtzite AlN and GaN by spectroscopic ellipsometry*, J. Appl. Phys. **94**, 307 (2003)

[173] D. Brunner, H. Angerer, E. Bustarret, F. Freudenberg, R. Höpler, R. Dimitrov, O. Ambacher, M. Stutzmann, *Optical constants of epitaxial AlGaN films and their temperature dependence*, J. Appl. Phys. **82**, 5090 (1997)

[174] T. Zhu, A. Dussaigne, G. Christmann, C. Pinquier, E. Feltin, D. Martin, R. Butté, N. Grandjean, *Nonpolar GaN-based microcavity using AlN/GaN distributed Bragg reflector*, Appl. Phys. Lett. **92**, 061114 (2008)

[175] G. Rossbach, J. Levrat, A. Dussaigne, G. Cosendey, M. Glauser, M. Cobet, R. Butté, N. Grandjean, H. Teisseyre, M. Bockowski, I. Grzegory, T. Suski, *Tailoring the light-matter coupling in anisotropic microcavities: Redistribution of oscillator strength in strained m-plane GaN/AlGaN quantum wells*, Phys. Rev. B **84**, 115315 (2011)

[176] M. Leroux, N. Grandjean, J. Massies, B. Gil, P. Lefebvre, P. Bigenwald, *Barrier-width dependence of group-III nitrides quantum-well transition energies*, Phys. Rev. B **60**, 1496 (1999)

[177] A. Bellabchara, P. Lefebvre, P. Christol, H. Mathieu, *Improved modeling of excitons in type-II semiconductor heterostructures by use of a three-dimensional variational function*, Phys. Rev. B **50**, 11840 (1994)

[178] F. Natali, Y. Cordier, J. Massies, S. Vezian, B. Damilano, M. Leroux, *Signature of monolayer and bilayer fluctuations in the width of (Al,Ga)N/GaN quantum wells*, Phys. Rev. B **79**, 035328 (2009)

[179] Y. Yamada, Y. Ueki, K. Nakamura, T. Taguchi, Y. Kawaguchi, A. Ishibashi, T. Yokogawa, *Biexciton luminescence from $Al_xGa_{1-x}N$ epitaxial layers*, Appl. Phys. Lett. **84**, 12 (2004)

[180] F. Stokker-Cheregi, A. Vinattieri, E. Feltin, D. Simeonov, J.-F. Carlin, R. Butté, N. Grandjean, M. Gurioli, *Biexciton kinetics in GaN quantum wells: Time-resolved and time-integrated photoluminescence measurements*, Phys. Rev. B **77**, 125342 (2008)

[181] S. Amloy, K. H. Yu, K. F. Karlsson, R. Farivar, T. G. Andersson, P. O. Holtz, *Size dependent biexciton binding energies in GaN quantum dots*, Appl. Phys. Lett. **99**, 251903 (2011)

[182] K. B. Lee, P. J. Parbrook, T. Wang, F. Ranalli, T. Martin, R. S. Balmer, , D. J. Wallis, *Optical investigation of exciton localization in $Al_xGa_{1-x}N$*, J. Appl. Phys. **101**, 053513 (2007)

[183] M. Gurioli A. Vinattieri, M. Colocci, *Temperature dependence of the radiative and nonradiative recombination time in GaAs/Al_xGa_{1-x}*, Phys. Rev. B **44**, 3115 (1991)

[184] J. Szczytko, L. Kappei, J. Berney, F. Morier-Genoud, M. T. Portella-Oberli, B. Deveaud-Plédran, *Determination of the exciton formation in quantum wells from time-resolved interband luminescence*, Phys. Rev. Lett. **93**, 137401 (2004)

[185] H. Haug, S. W. Koch, *Semiconductor laser theory with many-body effects*, Phys. Rev. A **39**, 1887 (1989)

[186] P. Corfdir, J. Levrat, G. Rossbach, R. Butté, E. Feltin, J.-F. Carlin, G. Christmann, P. Lefebvre, J.-D.Ganière, N. Grandjean, B. Deveaud-Plédran, *Impact of biexcitons on the relaxation mechanisms*

of polaritons in III-nitride based multiple quantum well microcavities, Phys. Rev. B **85**, 245308 (2012)

[187] K. Okada, Y. Yamada, T. Taguchi, F. Sasaki, S. Kobayashi, T. Tani, S. Nakamura, G. Shinomiya, *Biexciton luminescence from GaN epitaxial layers*, Jpn. J. Appl. Phys. **35**, L787 (1996)

[188] J. R. Haynes, *Experimental proof of the existence of a new electronic complex In silicon*, Phys. Rev. Lett. **4**, 361 (1960)

[189] J. Singh, D. Birkedal, V. G. Lyssenko, J. M. Hvam, *Binding energy of two-dimensional biexcitons*, Phys. Rev. B **53**, 15909 (1995)

[190] F. Stokker-Cheregi, A. Vinattieri, E. Feltin, D. Simeonov, J.Levrat, J.-F. Carlin, R. Butté, N. Grandjean, M. Gurioli, *Impact of confinement and quantum confined Stark effect on biexciton binding energy in GaN/AlGaN quantum wells*, Appl. Phys. Lett. **93**, 152105 (2008)

[191] W. Langbein, J. M. Hvam, *Localization-enhanced biexciton binding in semiconductors*, Phys. Rev. B **59**, 15405 (1999)

[192] C. H. Chia, T. Makino, K. Tamura, Y. Segawaa, A. Ohtomo, H. Koinuma, *Confinement-enhanced biexciton binding energy in ZnO/ZnMgO multiple quantum wells*, Appl. Phys. Lett. **82**, 1848 (2003)

[193] D. Birkedal, J. Singh, V. G. Lyssenko, J. Erland, J. M. Hvam, *Binding of quasi-two-dimensional biexcitons*, Phys. Rev. Lett. **76**, 672 (1996)

[194] P. Corfdir, M. Abid, A. Mouti, P. A. Stadelmann, E. Papa, J. P. Ansermet, J. D. Ganière, B. Deveaud-Plédran, *Biexciton emission and crystalline quality of ZnO nano-objects*, Nanotechnology **22**, 285710 (2011)

[195] J. C. Kim, D. R. Wake, J. P. Wolfe, *Thermodynamics of biexcitons in a GaAs quantum well*, Phys. Rev. B **50**, 15099 (1994)

[196] Y. Yamada, Y. Ueki, K. Nakamura, T. Taguchi, A. Ishibashi, Y. Kawaguchi, T. Yokogawa, *Stokes shift of biexcitons in* $Al_xGa_{1-x}N$ *epitaxial layers*, Phys. Rev. B **70**, 195210 (2004)

[197] S. T. Cundiff, T. Zhang, A. D. Bristow, D. Karaiskaj, X. Dai, *Optical two-dimensional fourier transform spectroscopy of semiconductor quantum wells*, Accounts Chem. Res. **42**, 1423 (2009)

[198] P. Borri, W. Langbein, U. Woggon, A. Esser, J. R. Jensen, J. M. Hvam, *Biexcitons in semiconductor microcavities*, Semicond. Sci. Technol. **18**, S351 (2003)

[199] F. Tassone, C. Piermarocchi, V. Savona, , A. Quattropani, P. Schwendimann, *Bottleneck effects in the relaxation and photoluminescence of microcavity polaritons*, Phys. Rev. B **56**, 7554 (1997)

[200] Y. G. Rubo, G. Malpuech, A. V. Kavokin, P. Bigenwald, *Dynamical theory of polariton amplifiers*, Phys. Rev. Lett. **91**, 156403 (2003)

[201] R. Butté, G. Delalleau, A. I. Tartakovskii, M. S. Skolnick, V. N. Astratov, J. J. Baumberg, G. Malpuech, A. Di Carlo, A. V. Kavokin, J. S. Roberts, *Transition from strong to weak coupling and the onset of lasing in semiconductor microcavities*, Phys. Rev. B **65**, 205310 (2002)

[202] E. Wertz, L. Ferrier, D. D. Solnyshkov, P. Senellart, D. Bajoni, A. Miard, A. Lemaître, G. Malpuech, J. Bloch, *Spontaneous formation of a polariton condensate in a planar GaAs microcavity*, Appl. Phys. Lett. **95**, 051108 (2009)

[203] A. I. Tartakovskii, M. Emam-Ismail, R. M. Stevenson, M. S. Skolnick, V. N. Astratov, D. M. Whittaker, J. J. Baumberg, J. S. Roberts, *Relaxation bottleneck and its suppression in semiconductor microcavities*, Phys. Rev. B **62**, R2283 (2000)

[204] J. Bloch, T. Freixanet, J. Y. Marzin, V. Thierry-Mieg, R. Planel, *Giant Rabi splitting in a microcavity containing distributed quantum wells*, Appl. Phys. Lett. **73**, 1694 (1996)

[205] G. Malpuech, A. V. Kavokin, A. Di Carlo, J. J. Baumberg, *Polariton lasing by exciton-electron scattering in semiconductor microcavities*, Phys. Rev. B **65**, 153310 (2002)

[206] M. Gallart, Private communication (2011)

[207] F. Bœuf, R. André, R. Romestain, Le Si Dang, E. Péronne, J. F. Lampin, D. Hulin, A. Alexandrou, *Evidence of polariton stimulation in semiconductor microcavities*, Phys. Rev. B **62**, R2279 (2000)

[208] B. Sermage, S. Long, I. Abram, J. Y. Marzin, J. Bloch, R. Planel, V. Thierry-Mieg, *Time-resolved spontaneous emission of excitons in a microcavity: Behavior of the individual exciton-photon mixed states*, Phys. Rev. B **53**, 16516 (1996)

[209] H. Deng, G. Weihs, D. Snoke, J. Bloch, Y. Yamamoto, *Polariton lasing vs. photon lasing in a semiconductor microcavity*, P. Natl. Acad. Sci. USA **100**, 15318 (2003)

[210] A. S. Brichkin, S. I. Novikov, A. V. Larionov, V. D. Kulakovskii, M. M. Glazov, C. Schneider, S. Höfling, M. Kamp, A. Forchel, *Effect of Coulomb interaction on exciton-polariton condensates in GaAs microcavities*, Phys. Rev. B **84**, 195301 (2011)

[211] D. Bajoni, P. Senellart, E. Wertz, I. Sagnes, A. Miard, A. Lemaître, J. Bloch, *Polariton laser using single micropillar GaAs-AlAs semiconductor cavities*, Phys. Rev. Lett. **100**, 047401 (2008)

[212] G. Roumpos, W. H. Nitsche, S. Höfling, A. Forchel, Y. Yamamoto, *Gain-induced trapping of microcavity exciton polariton condensates*, Phys. Rev. Lett. **104**, 123403 (2010)

[213] D. Sarchi, V. Savona, *Spectrum and thermal fluctuations of a microcavity polariton Bose-Einstein condensate*, Phys. Rev. B **77**, 045304 (2008)

[214] A. Huynh, J. Tignon, Ph. Roussignol, C. Delalande, *Experimental determination of intrinsic nonlinearities in semiconductor microcavities*, Phys. Rev. B **66**, 113301 (2002)

[215] R. Balili, V. Hartwell, D. Snoke, L. Pfeiffer, K. West, *Bose-Einstein condensation of microcavity polaritons in a trap*, Science **316**, 1007 (2007)

[216] M. Wouters, I. Carusotto, C. Ciuti, *Spatial and spectral shape of inhomogeneous nonequilibrium exciton-polariton condensates*, Phys. Rev. B **77**, 115340 (2008)

[217] L. Ferrier, E. Wertz, R. Johne, D. D. Solnyshkov, P. Senellart, I. Sagnes, A. Lemaître, G. Malpuech, J. Bloch, *Interactions in confined polariton condensates*, Phys. Rev. Lett. **106**, 126401 (2011)

[218] M. Vladimirova, S. Cronenberger, D. Scalbert, K. V. Kavokin, A. Miard, A. Lemaître, J. Bloch, D. D. Solnyshkov, G. Malpuech, A. V. Kavokin, *Polariton-polariton interaction constants in microcavities*, Phys. Rev. B **82**, 075301 (2010)

[219] Y. G. Rubo, A. V. Kavokin, I. A. Shelykh, *Suppression of superfluidity of exciton-polaritons by magnetic field*, Phys. Lett. A **358**, 227 (2007)

[220] M. Wouters, *Resonant polariton-polariton scattering in semiconductor microcavities*, Phys. Rev. B **76**, 045319 (2007)

[221] A. V. Kavokin, private communication (2011)

[222] M. Richard, J. Kasprzak, R. André, R. Romestain, Le Si Dang, G. Malpuech, A. V. Kavokin, *Experimental evidence for nonequilibrium Bose condensation of exciton polaritons*, Phys. Rev. B **72**, 201301 (2005)

[223] J. Kasprzak, R. André, Le Si Dang, I. A. Shelykh, A. V. Kavokin, Y. G. Rubo, K. V. Kavokin, G. Malpuech, *Build up and pinning of linear polarization in the Bose condensates of exciton polaritons*, Phys. Rev. B **75**, 045326 (2007)

[224] A. Baas K. G. Lagoudakis, M. Richard, R. André, Le Si Dang, B. Deveaud-Plédran, *Synchronized and desynchronized phases of exciton-polariton condensates in the presence of disorder*, Phys. Rev. Lett. **100**, 170401 (2008)

[225] H. Yokoyama, M. Suzuki, Y. Nambu, *Spontaneous emission and laser oscillation properties of microcavities containing a dye solution*, Appl. Phys. Lett. **58**, 2598 (1991)

[226] Y. Yamamoto, S. Machida, G. Björk, *Microcavity semiconductor laser with enhanced spontaneous emission*, Phys. Rev. A **44**, 657 (1991)

[227] J. J. Baumberg, P. G. Savvidis, R. M. Stevenson, A. I. Tartakovskii, M. S. Skolnick, D. M. Whittaker, J. S. Roberts, *Parametric oscillation in a vertical microcavity: A polariton condensate or micro-optical parametric oscillation*, Phys. Rev. B **62**, R16247 (2000)

[228] G. Malpuech, A. Di Carlo, A. V. Kavokin, J. J. Baumberg, P. Lugli, *Room-temperature polariton lasers based on GaN microcavities*, Appl. Phys. Lett. **81**, 412 (2002)

[229] J. Kasprzak, D. D. Solnyshkov, R. André, Le Si Dang, G. Malpuech, *Formation of exciton polariton condensate: thermodynamic versus kinetic regimes*, Phys. Rev. Lett. **101**, 146404 (2008)

[230] C.-K. Sun Y.-L. Huang, J.-C. Liang, S. Keller, M. P. Mack, U. K. Mishra, S. P. DenBaars, *Femtosecond Z-scan measurement of GaN*, Appl. Phys. Lett. **75**, 3524 (1999)

[231] M. H. Szymańska, J. Keeling, P. B. Littlewood, *Nonequilibrium quantum condensation in an incoherently pumped dissipative system*, Phys. Rev. Lett. **96**, 230602 (2006)

[232] E. Wertz, L. Ferrier, D. D. Solnyshkov, R. Johne, D. Sanvitto, A. Lemaître, I. Sagnes, R. Grousson, A. V. Kavokin, P. Senellart, G. Malpuech, J. Bloch, *Spontaneous formation and optical manipulation of extended polariton condensates*, Nature Phys. **6**, 860 (2010)

[233] H. Franke, C. Sturm, R. Schmidt-Grund, G. Wagner, M. Grundmann, *Ballistic propagation of exciton-polariton condensates in a ZnO-based microcavity*, New J. Phys. **14**, 013037 (2012)

[234] J. M. Kosterlitz, D. J. Thouless, *Ordering, metastability and phase-transition in 2 dimensional systems*, J. Phys. C Solid State **6**, 1181 (1973)

[235] V. L. Berezinsky, *Destruction of long-range order in one-dimensional and two-dimensional systems having a continuous symmetry group .1. Classical systems*, Soviet Physics JETP - USSR **32**, 493 (1971)

[236] V. L. Berezinsky, *Destruction of long-range order in one-dimensional and two-dimensional systems possessing a continuous symmetry group .2. Quantum systems*, Soviet Physics JETP - USSR **34**, 610 (1972)

[237] G. Malpuech, D. D. Solnyshkov, H. Ouerdane, M. M. Glazov, I. Shelykh, *Bose glass and superfluid phases of cavity polaritons*, Phys. Rev. Lett. **98**, 206402 (2007)

[238] M. G. A. Bernard, G. Durrafourg, *Laser conditions in semiconductors*, Phys. Stat. Sol. **1**, 699 (1961)

[239] G. Malpuech, Y. G. Rubo, F. P. Laussy, P. Bigenwald, A. V. Kavokin, *Polariton laser: thermodynamics and quantum kinetic theory*, Semicond. Sci. Technol. **18**, S395 (2003)

[240] B. Damski, J. Zakrzewski, L. Santos, P. Zoller, M. Lewenstein, *Atomic bose and Anderson glasses in optical lattices*, Phys. Rev. Lett. **91**, 080403 (2003)

[241] F. Kreller, M. Lowisch, J. Puls, F. Henneberger, *Role of biexcitons in the stimulated emission of wide-gap II-VI quantum wells*, Phys. Rev. Lett. **75**, 2420 (1995)

[242] Y. Kawakami, I. Hauksson, J. Simpson, H. Stewart, I. Galbraith, K. A. Prior, B. C. Cavenett, *Photoluminescence excitation spectroscopy of the lasing transition in ZnSe-(Zn,Cd)Se quantum wells*, J. Cryst. Growth **138**, 759 (1994)

[243] L. V. Butov, C. W. Lai, A. L. Ivanov, A. C. Gossard, D. S. Chemla, *Towards Bose-Einstein condensation of excitons in potential traps*, Nature (London) **417**, 47 (2002)

[244] J. Y. Jen, T. Tsutsumi, I. Souma, Y. Oka, H. Fujiyasu, *Stimulated emission processes in* $Zn_{1-x}Cd_xSe/ZnSe$ *multiquantum wells*, Jpn. J. Appl. Phys. **32**, L1542 (1993)

[245] J. Ding, T. Ishihara, M. Hagerott, A. V. Nurmikko, H. Luo, N. Samarth, J. Furdyna, *Excitonic gain and laser emission in ZnSe-based quantum wells*, Phys. Rev. Lett. **69**, 1707 (1992)

[246] J. Ding, M. Hagerott, T. Ishihara, H. Jeon, A. V. Nurmikko, *(Zn,Cd)Se/ZnSe quantum-well lasers: Excitonic gain in an inhomogeneously broadened quasi-two-dimensional system*, Phys. Rev. B **47**, 10528 (1993)

[247] M. Wouters, I. Carusotto, *Excitations in a nonequilibrium Bose-Einstein condensate of exciton polaritons*, Phys. Rev. Lett. **99**, 140402 (2007)

[248] R. Butté, G. Christmann, E. Feltin, A. Castiglia, J. Levrat, G. Cosendey, A. Altoukhov, J.-F. Carlin, N. Grandjean, *Room temperature polariton lasing in III-nitride microcavities: a comparison with blue GaN-based vertical cavity surface emitting lasers*, Proc. SPIE **7216**, 721619 (2009)

[249] D. Porras, C. Ciuti, J. J. Baumberg, C. Tejedor, *Polariton dynamics and Bose-Einstein condensation in semiconductor microcavities*, Phys. Rev. B **66**, 085304 (2002)

[250] J. Levrat, R. Butté, G. Christmann, E. Feltin, J.-F. Carlin, N. Grandjean, *Tailoring the strong coupling regime in III-nitride based microcavities for room temperature polariton laser applications*, Phys. Stat. Sol. (c) **6**, 2820 (2009)

[251] R. T. Philips, G. C. Nixon, T. Fujita, M. Y. Simmons, D. A. Ritchie, *Excitonic trions in undoped GaAs quantum wells*, Solid State Commun. **98**, 287 (1996)

[252] P. Corfdir, J. Levrat, A. Dussaigne, P. Lefebvre, H. Teisseyre, I. Grzegory, T. Suski, J.-D. Ganière, N. Grandjean, B. Deveaud-Plédran, *Intrinsic dynamics of weakly and strongly confined excitons in nonpolar nitride-based heterostructures*, Phys. Rev. B **83**, 245326 (2011)

[253] D. Bajoni, M. Perrin, P. Senellart, A. Lemaître, B. Sermage, J. Bloch, *Dynamics of microcavity polaritons in the presence of an electron gas*, Phys. Rev. B **73**, 205344 (2006)

[254] P. Tsotsis, P. S. Eldridge, T. Gao, S. I. Tsintzos, Z. Hatzopoulos, P. G. Savvidis, *Lasing threshold doubling at the crossover from strong to weak coupling regime in GaAs microcavity*, New J. Phys. **14**, 023060 (2012)

[255] M. Maragkou, A. J. D. Grundy, T. Ostatnický, P. G. Lagoudakis, *Longitudinal optical phonon assisted polariton laser*, Appl. Phys. Lett. **97**, 111110 (2010)

[256] L. Orosz, F. Réveret, F. Médard, P. Disseix, J. Leymarie, M. Mihailovic, D. Solnyshkov, G. Malpuech, J. Zuniga-Pérez, F. Semond, M. Leroux, S. Bouchoule, X. Lafosse, M. Mexis, C. Brimont, T. Guillet, *LO-phonon-assisted polariton lasing in a ZnO-based microcavity*, Phys. Rev. B **85**, 121201 (2012)

[257] K. D. Choquette, H. Q. Hou, *Vertical-cavity surface emitting lasers: Moving from research to manufacturing*, Proc. IEEE **85**, 1730 (1997)

[258] M. Z. Maialle, A. de Andrada e Silva, L. J. Sham, *Exciton spin dynamics in quantum wells*, Phys. Rev. B **47**, 15776 (1993)

[259] R. I. Dzhioev, H. M. Gibbs, E. L. Ivchenko, G. Khitrova, V. L. Korenev, M. N. Tkachuk, B. P. Zakharchenya, *Determination of interface preference by observation of linear-to-circular polarization conversion under optical orientation of excitons in type-II GaAs/AlAs superlattices*, Phys. Rev. B **56**, 13405 (1997)

[260] K. V. Kavokin, I. A. Shelykh, A. V. Kavokin, G. Malpuech, P. Bigenwald, *Quantum theory of spin dynamics of exciton-polaritons in microcavities*, Phys. Rev. Lett. **92**, 017401 (2003)

[261] Y. G. Rubo, *Kinetics of the polariton condensate formation in a microcavity*, Phys. Stat. Sol. (a) **201**, 641 (2003)

[262] M. Vladimirova, S. Cronenberger, D. Scalbert, M. Nawrocki, A. V. Kavokin, A. Miard, A. Lemaître, J. Bloch, *Polarization controlled nonlinear transmission of light through semiconductor microcavities*, Phys. Rev. B **79**, 115325 (2009)

[263] D. Read, T. C. H. Liew, Y. G. Rubo, A. V. Kavokin, *Stochastic polarization formation in exciton-polariton Bose-Einstein condensates*, Phys. Rev. B **80**, 195309 (2009)

[264] J. Levrat, R. Butté, T. Christian, M. Glauser, E. Feltin, J.-F. Carlin, N. Grandjean, D. Read, A. V. Kavokin, Y. G. Rubo, *Pinning and depinning of the polarization of exciton-polariton condensates at room temperature*, Phys. Rev. Lett. **104**, 166402 (2010)

[265] F. P. Laussy, I. A. Shelykh, G. Malpuech, A. V. Kavokin, *Effects of Bose-Einstein condensation of exciton polaritons in microcavities on the polarization of emitted light*, Phys. Rev. B **73**, 035315 (2006)

[266] E. del Valle, D. Sanvitto, A. Amo, F. P. Laussy, R. André, C. Tejedor, L. Viña, *Dynamics of the formation and decay of coherence in a polariton condensate*, Phys. Rev. Lett. **103**, 096404 (2009)

[267] A. P. D. Love, D. N. Krizhanovskii, D. M. Whittaker, R. Bouchekioua, D. Sanvitto, S. Al Rizeiqi, R. Bradley, M. S. Skolnick, P. R. Eastham, R. André, Le Si Dang, *Intrinsic decoherence mechanisms in the microcavity polariton condensate*, Phys. Rev. Lett. **101**, 067404 (2008)

[268] S. Krishnamurthy, M. van Schilfgaarde, N. Newman, *Spin lifetimes of electrons injected into GaAs and GaN*, Appl. Phys. Lett. **83**, 1761 (2003)

[269] I. A. Shelykh, G. Malpuech, K. V. Kavokin, A. V. Kavokin, P. Bigenwald, *Spin dynamics of interacting exciton polaritons in microcavities*, Phys. Rev. B **70**, 115301 (2004)

[270] S. V. Gupalov, E. L. Ivchenko, A. V. Kavokin, *Fine structure of localized exciton levels in quantum wells*, JETP **86**, 388 (1998)

[271] A. A: Toropov, E. L. Ivchenko, O. Krebs, S. Cortez, P. Voisin, J. L Gentner, *Excitonic contributions to the quantum-confined Pockels effect*, Phys. Rev. B **63**, 035302 (2000)

[272] M. D. Martin, G. Aichmayr, L. Viña, R. André, *Polarization control of the nonlinear emission of semiconductor microcavities*, Phys. Rev. Lett. **89**, 077402 (2002)

[273] A. V. Kavokin, P. G. Lagoudakis, G. Malpuech, J. J. Baumberg, *Polarization rotation in parametric scattering of polaritons in semiconductor microcavities*, Phys. Rev. B **67**, 195321 (2003)

[274] S. Ghosh, P. Misra, H. T. Grahn, B. Imer, S. Nakamura, S. P. DenBaars, J. S. Speck, *Polarized photoreflectance spectroscopy of strained A-plane GaN films on R-plane sapphire*, J. Appl. Phys. **98**, 026105 (2005)

[275] M. Litinskaya, P. Reineker, V. M. Agranovich, *Exciton-polaritons in a crystalline anisotropic organic microcavity*, Phys. Stat. Sol. (a) **201**, 646 (2004)

[276] B. M. Imer, F. Wu, S. P. DenBaars, J. S. Speck, *Improved quality* $(11\bar{2}0)$ *a-plane GaN with sidewall lateral epitaxial overgrowth*, Appl. Phys. Lett. **88**, 061908 (2006)

[277] X. Ni, Ü. Özgür, Y. Fu, N. Biyikli, J. Xie, A. A. Baski, H. Morkoç, Z. Liliental-Weber, *Defect reduction in* $(11\bar{2}0)$ *a-plane GaN by two-stage epitaxial lateral overgrowth*, Appl. Phys. Lett. **89**, 262105 (2006)

[278] M. A. Mastro, E. A. Imhoff, J A. Freitas, J. K. Hite, C. R. Eddy Jr, *Towards a polariton-based light emitter based on non-polar GaN quantum wells*, Solid State Comm. **149**, 2039 (2009)

[279] H. Teisseyre, J. Z. Domagala, B. Lucznik, A. Reszka, B. J. Kowalski, M. Bockowski, G. Kamler, I.Grzegory, *Characterization of the nonpolar GaN substrate obtained by multistep regrowth by hydride vapor phase epitaxy*, Appl. Phys. Express **5**, 011001 (2011)

[280] A. Dussaigne, P. Corfdir, J. Levrat, T. Zhu, D. Martin, P. Lefebvre, J.-D. Ganière, R. Butté, B. Deveaud-Plédran, N. Grandjean, Y. Arroyo, P. Stadelmann, *One-dimensional exciton luminescence induced by extended defects in nonpolar GaN/(Al,Ga)N quantum wells*, Semicond. Sci. Technol. **26**, 025012 (2011)

[281] P. Corfdir, P. Lefebvre, J. Levrat, J.-D. Ganière, D. Martin, J. Ristić, T. Zhu, N. Grandjean, B. Deveaud-Plédran, *Exciton localization on basal stacking faults in a-plane epitaxial lateral overgrown GaN grown by hydride vapor phase epitaxy*, J. Appl. Phys. **105**, 043102 (2009)

[282] S. Ghosh, P. Waltereit, O. Brandt, H. T. Grahn, K. H. Ploog, *Electronic band structure of wurtzite GaN under biaxial strain in the M plane investigated with photoreflectance spectroscopy*, Phys. Rev. B **65**, 075202 (2002)

[283] R. Mata, A. Cros, J. A. Budagosky, A. Molina-Sánchez, N. Garro, A. García-Cristóbal, J. Renard, S. Founta, B. Gayral, E. Bellet-Amalric C. Bougerol, B. Daudin, *Reversed polarized emission in highly strained a-plane GaN/AlN multiple quantum wells*, Phys. Rev. B **82**, 125405 (2010)

[284] P. Misra, O. Brandt, H. T. Grahn, H. Teisseyre, M. Siekacz, C. Skierbiszewski, B. Lucznik, *Complete in-plane polarization anisotropy of the A exciton in unstrained A-plane GaN films*, Appl. Phys. Lett. **91**, 141903 (2007)

[285] X. Fan, H. Wang, H. Q. Hou, B. E. Hammons, *Laser emission from semiconductor microcavities: Transition from nonperturbative to perturbative regimes*, Phys. Rev. B **56**, 15256 (1997)

[286] E. O. Kane, *Pollmann-Büttner variational method for excitonic polarons*, Phys. Rev. B **18**, 6849 (1978)

[287] T. Guillet, M. Mexis, J. Levrat, G. Rossbach, C. Brimont, T. Bretagnon, B. Gil, , R. Butté, N. Grandjean, L. Orosz, F. Réveret, J. Leymarie, J. Zúniga-Pérez, M. Leroux, F. Semond, S. Bouchoule, *Polariton lasing in a hybrid bulk ZnO microcavity*, Appl. Phys. Lett. **99**, 161104 (2011)

[288] M. Zamfirescu, A. Kavokin, B. Gil, G. Malpuech, M. Kaliteevski, *ZnO as a material mostly adapted for the realization of room-temperature polariton lasers*, Phys. Rev. B **65**, 161205 (2002)

[289] R. Shimada, J. Xie, Ü. Özgür V. Avrutin, H. Morkoç, *Cavity polaritons in ZnO-based hybrid microcavities*, Appl. Phys. Lett. **92**, 011127 (2008)

[290] J. R. Chen, T. C. Lu, Y. C. Wu, S. C. Lin, W. R. Liu, W. F. Hsieh, C. C. Kuo, C. C. Lee, *Cavity polaritons in ZnO-based hybrid microcavities*, Appl. Phys. Lett. **94**, 061103 (2009)

[291] R. Schmidt-Grund, B. Rheinländer, C. Czekalla, G. Benndorf, H. Hochmuth, M. Lorenz, M. Grundmann, *Exciton-polariton formation at room temperature in a planar ZnO resonator structure*, Appl. Phys. B **93**, 331 (2008)

[292] M. Nakayama, S. Komura, T. Kawase, D. Kim, *Observation of exciton polaritons in a ZnO microcavity with HfO_2/SiO_2 distributed Bragg reflectors*, J. Phys. Soc. Jpn. **77**, 093705 (2008)

[293] A. Trichet, L. Sun, G. Pavlovic, N. A. Gippius, G. Malpuech, W. Xie, Z. Chen, M. Richard, L. S. Dang, *One-dimensional ZnO exciton polaritons with negligible thermal broadening at room temperature*, Phys. Rev. B **83**, 041302(R) (2011)

[294] C. Sturm, H. Hilmer, R. Schmidt-Grund, M. Grundmann, *Observation of strong exciton-photon coupling at temperatures up to 410 K*, New J. Phys. **11**, 073044 (2009)

[295] T.-C. Lu, Y.-Y. Lai, Y.-P. Lan, S.-W. Huang, J.-R. Chen, Y.-C. Wu, W.-F. Hsieh, H. Deng, *Room temperature polariton lasing vs. photon lasing in a ZnO-based hybrid microcavity*, Opt. Lett. **20**, 5530 (2012)

[296] J. Frenkel, *On the transformation of light into heat in solids. I*, Phys. Rev. **37**, 17 (1931)

[297] D. G. Lidzey, D. D. C. Bradley, M. S. Skolnick, T. Virgili, S. Walker, D. M. Whittaker, *Strong exciton-photon coupling in an organic semiconductor microcavity*, Nature (London) **395**, 53 (1998)

[298] P. A. Hobson, W. L. Barnes, D. G. Lidzey, G. A. Gehring, D. M. Whittaker, M. S. Skolnick, S. Walker, *Strong exciton-photon coupling in a low-Q all-metal mirror microcavity*, Appl. Phys. Lett. **81**, 3519 (2002)

[299] L. G. Connolly, D. G. Lidzey, R. Butté, A. M. Adawi, D. M. Whittaker, M. S. Skolnick, R. Airey, *Strong coupling in high-finesse organic semiconductor microcavities*, Appl. Phys. Lett. **83**, 5377 (2003)

[300] R. J. Holmes, S. R. Forrest, *Exciton-photon coupling in organic materials with large intersystem crossing rates and strong excited-state molecular relaxation*, Phys. Rev. B **71**, 235203 (2005)

[301] J. Wenus, R. Parashkov, S. Ceccarelli, A. Brehier, J.-S. Lauret, M. S. Skolnick, E. Deleporte, D. G. Lidzey, *Hybrid organic-inorganic exciton-polaritons in a strongly coupled microcavity*, Phys. Rev. B **74**, 235212 (2006)

[302] S. Kéna-Cohen, S. R. Forrest, *Giant Davydov splitting of the lower polariton branch in a polycrystalline tetracene microcavity*, Phys. Rev. B **77**, 073205 (2008)

[303] R. Brückner, M. Sudzius, S. I. Hintschich, H. Fröb, V. G. Lyssenko, K. Leo, *Hybrid optical Tamm states in a planar dielectric microcavity*, Phys. Rev. B **83**, 033405 (2011)

[304] L. C. Andreani, G. Panzarini, J.-M. Gérard, *Strong-coupling regime for quantum boxes in pillar microcavities: Theory*, Phys. Rev. B **60**, 13276 (1999)

[305] T. Yoshie, A. Scherer, J. Hendrickson, G. Khitrova, H. M. Gibbs, G. Rupper, C. Ell, O. B. Shchekin, D. G. Deppe, *Vacuum Rabi splitting with a single quantum dot in a photonic crystal nanocavity*, Nature (London) **432**, 200 (2004)

[306] J. P. Reithmaier, G. Sęk, A. Löffler, C. Hofmann, S. Kuhn, S. Reitzenstein, L. V. Keldysh, V. D. Kulakovskii, T. L. Reinecke, A. Forchel, *Strong coupling in a single quantum dot-semiconductor microcavity system*, Nature (London) **432**, 197 (2004)

[307] M. Nomura, N. Kumagai, S. Iwamoto, Y. Ota, , Y. Arakawa, *Laser oscillation in a strongly coupled single-quantum-dot-nanocavity system*, Nature Phys. **6**, 279 (2010)

[308] N. Vico Triviño, G. Rossbach, U. Dharanipathy, J. Levrat, A. Castiglia, J.-F. Carlin, K. A. Atlasov, R. Butté, R. Houdré, N. Grandjean, *High quality factor two dimensional GaN photonic crystal cavity membranes grown on silicon substrate*, Appl. Phys. Lett. **100**, 071103 (2012)

[309] S. Sergent, M. Arita, S. Kako, S. Iwamoto, Y. Arakawa, *High-Q (>5000) AlN nanobeam photonic crystal cavity embedding GaN quantum dots*, Appl. Phys. Lett. **100**, 121103 (2012)

[310] A. Das, J. Heo, M. Jankowski, W. Guo, H. Deng L. Zhang, , P. Bhattacharya, *Room temperature ultralow threshold GaN nanowire polariton laser*, Phys. Rev. Lett. **107**, 066405 (2011)

[311] A. Das, P. Bhattacharya, A. Banerjee, M. Jankowski, *Dynamic polariton condensation in a single GaN nanowire-dielectric microcavity*, Phys. Rev. B **85**, 195321 (2012)

[312] D. Bajoni, A. Miard, A. Lemaître, S. Bouchoule, J. Bloch, J. Tignon, *Nonresonant electrical injection of excitons in an InGaAs quantum well*, Appl. Phys. Lett. **90**, 121114 (2007)

[313] S. I. Tsintzos, N. T. Pelekanos, G. Konstantinidis, Z. Hatzopoulos, P. G. Savvidis, *A GaAs polariton light-emitting diode operating near room temperature*, Nature (London) **453**, 372 (2008)

[314] S. I. Tsintzos, P. G. Savvidis, G. Deligeorgis, Z. Hatzopoulos, N. T. Pelekanos, *Room temperature GaAs exciton-polariton light emitting diode*, Appl. Phys. Lett. **94**, 071109 (2009)

[315] P. Bhattacharya, A. Das, S. Bhowmick, M. Jankowski, C. s. Lee, *Effect of magnetic field on polariton emission characteristics of a quantum well microcavity diode*, Appl. Phys. Lett. **100**, 171106 (2012)

[316] M. Glauser, G. Rossbach, G. Cosendey, J. Levrat, M. Cobet, J.-F. Carlin, J. Besbas, M. Gallart, P. Gilliot, R. Butté, N. Grandjean, *Investigation of InGaN/GaN quantum wells for polariton laser diodes*, Phys. Stat. Sol. (c) **9**, 1325 (2012)

[317] T.-C. Lu, J.-R. Chen, S.-C. Lin, S.-W. Huang, S.-C. Wang, Y. Yamamoto, *Room temperature current injection polariton light emitting diode with a hybrid microcavity*, Nano Lett. **11**, 2797 (2011)

[318] E. Thrush, O. Levi, W. Ha, G. Carey, L. J. Cook, J. Deich, S. J. Smith, W. E. Moerner, *Integrated semiconductor vertical-cavity surface-emitting lasers and PIN photodetectors for biomedical fluorescence sensing*, IEEE J. Quantum Elect. **40**, 491 (2004)

[319] E. O. Kane, *Band structure of indium antimonide*, J. Phys. Chem. Solids **1**, 249 (1957)

[320] Guy Fishman, *Semi-conducteurs: les bases de la théorie* $k \cdot p$ (Les Éditions de l'École Polytechnique, Palaiseau, 2010)

[321] V. Savona, *Confined photon systems: Fundamentals and applications* in *Linear optical properties of semiconductor microcavities with embedded quantum wells*, H. Benisty *et al.*, Editors (Springer Verlag, Berlin, New York, 1999), p. 173-242

[322] J. S. C. Prentice, *Coherent, partially coherent and incoherent ligth absorption in thin-film multi-layer structures*, J. Phys. D: Appl. Phys. **33**, 3139 (2000)

[323] H. Fujiwara, *Spectroscopic ellipsometry: Principles and applications* (Wiley, Tokyo, 2007)

[324] D. W. Berreman, *Optics in stratified and anisotropic media:* 4×4*-matrix formulation*, J. Opt. Soc. Am. **62**, 502 (1972)

[325] M. Schubert, *Infrared ellipsometry on semiconductor layer structures - Phonons, plasmons and polaritons* (Springer, Berlin, 2004)

[326] H. Wöhler, G. Haas, M. Fritsch, D. A. Mlynski, *Faster* 4×4 *matrix method for uniaxial inhomogeneous media*, J. Opt. Soc. Am. A **5**, 1554 (1988)

[327] P. Yeh, *Optics of anisotropic layered media: a new*4×4 *matrix algebra*, Surface Science **96**, 41 (1980)

Appendices

A Envelope function calculation in the Numerov approximation

We consider here the one-dimensional time-independent Schrödinger equation:

$$\begin{aligned}\left[-\frac{\hbar^2}{2m}\frac{d^2}{dx^2}+V(x)\right]\psi(x) &= E\psi(x) \\ \frac{d^2\psi}{dx^2} &= \underbrace{\frac{2m}{\hbar^2}(V(x)-E)}_{G(x)}\psi,\end{aligned} \tag{7.1}$$

where $\psi(x)$ is the wave function of a particle of mass m with energy E experiencing a potential energy $V(x)$ with boundary conditions $\lim_{x\to\pm\infty}\psi(x)=0$. In the Numerov procedure, one first considers an initial value of the wave function and its derivative ψ and ψ' at an initial position $x=x_0$ and propagate them on a spatial grid to some final point $x=x_\mathrm{f}$. Using the notation $\psi_\mathrm{n}=\psi(x=x_\mathrm{n})$ and $x_\mathrm{n}=x_0+nh$, where h is the spatial resolution used for the grid, one can estimate the value of the wave function around the position x_n by taking a Taylor series expansion. In the Numerov approximation, these series are truncated at sixth order:

$$\psi_{\mathrm{n}-1} = \psi_\mathrm{n}-h\psi'_\mathrm{n}+\frac{h^2}{2!}\psi''_\mathrm{n}-\frac{h^3}{3!}\psi^{(3)}_\mathrm{n}+\frac{h^4}{4!}\psi^{(4)}_\mathrm{n}-\frac{h^5}{5!}\psi^{(5)}_\mathrm{n}+\mathcal{O}(h^6) \tag{7.2}$$

$$\psi_{\mathrm{n}+1} = \psi_\mathrm{n}+h\psi'_\mathrm{n}+\frac{h^2}{2!}\psi''_\mathrm{n}+\frac{h^3}{3!}\psi^{(3)}_\mathrm{n}+\frac{h^4}{4!}\psi^{(4)}_\mathrm{n}+\frac{h^5}{5!}\psi^{(5)}_\mathrm{n}+\mathcal{O}(h^6), \tag{7.3}$$

where the derivatives ψ_n with order i higher than 2 are labeled $\psi^{(i)}_\mathrm{n}$ and with primes otherwise. Summing Equations 7.2 and 7.3, the wave function at point $x_{\mathrm{n}+1}$ can be expressed as a function of $\psi_{\mathrm{n}-1}$ and ψ_n with a precision $\mathcal{O}(h^6)$:

$$\psi_{\mathrm{n}+1}=-\psi_{\mathrm{n}-1}+2\psi_\mathrm{n}+h^2\psi''_\mathrm{n}+\frac{h^4}{12}\psi^{(4)}_\mathrm{n}. \tag{7.4}$$

Solving Equation 7.4 for ψ''_n leads to:

$$\psi''_\mathrm{n}=\frac{1}{h^2}\left(\psi_{\mathrm{n}+1}+\psi_{\mathrm{n}-1}-2\psi_\mathrm{n}-\frac{h^4}{12}\psi^{(4)}_\mathrm{n}\right). \tag{7.5}$$

As ψ is a solution of the Schrödinger equation 7.1, ψ''_n in Equation 7.5 can be replaced by $\psi''_\mathrm{n}=G_\mathrm{n}\psi_\mathrm{n}$, where $G_\mathrm{n}=G(x=x_\mathrm{n})$ is defined in Equation 7.1. This substitution allows expressing $\psi^{(4)}_\mathrm{n}$ as a function of $\psi_{\mathrm{n}-1}$, ψ_n and $\psi_{\mathrm{n}+1}$ only. Solving this expression for $\psi_{\mathrm{n}+1}$, one finally obtains:

$$\psi_{\mathrm{n}+1}=\frac{2\psi_\mathrm{n}-\psi_{\mathrm{n}-1}+\frac{h^2}{12}\left(G_{\mathrm{n}-1}\psi_{\mathrm{n}-1}+10G_\mathrm{n}\psi_\mathrm{n}\right)}{1-\frac{h^2}{12}G_{\mathrm{n}+1}}. \tag{7.6}$$

Relation 7.6 yields the Numerov's procedure. The values of ψ_0 and ψ_1 should be entered to start the calculation for a given energy E. Whereas $\psi_0=0$ is provided by the boundary conditions, the value of ψ_1 is vanishingly small but not strictly equal to zero. An appropriate choice for ψ_1 will depend on the spatial resolution and on the shape of the potential $V(x)$.

B Band structure calculation: an introduction to the $\boldsymbol{k}\cdot\boldsymbol{p}$ formalism

In the present appendix, the Kane theory of strained wurtzite semiconductors is presented for bulk wurtzite semiconductor layers. Near the Brillouin zone center, we consider the following basis functions for the two conduction and six valence bands accounting for the spin degree of freedom:

- **Conduction band basis ($\mathscr{B}_{\mathrm{cb}}$):**

  $\left|u_1^{\mathrm{cb}}\right\rangle = |iS\uparrow\rangle, \left|u_2^{\mathrm{cb}}\right\rangle = |iS\downarrow\rangle$

- **Valence band basis ($\mathscr{B}_{\mathrm{vb}}$):**

  $\left|u_1^{\mathrm{vb}}\right\rangle = \left|-\frac{X+iY}{\sqrt{2}}\uparrow\right\rangle, \left|u_2^{\mathrm{vb}}\right\rangle = \left|\frac{X-iY}{\sqrt{2}}\uparrow\right\rangle, \left|u_3^{\mathrm{vb}}\right\rangle = |Z\uparrow\rangle,$
  $\left|u_4^{\mathrm{vb}}\right\rangle = \left|\frac{X-iY}{\sqrt{2}}\downarrow\right\rangle, \left|u_5^{\mathrm{vb}}\right\rangle = \left|-\frac{X+iY}{\sqrt{2}}\downarrow\right\rangle, \left|u_6^{\mathrm{vb}}\right\rangle = |Z\downarrow\rangle.$

The electron spin σ is represented by arrows, i.e, $\sigma \in \{\uparrow,\downarrow\}$. Note that this basis can be expressed in terms of spherical harmonics $Y_{\mathrm{l}}^{\mathrm{m}}(\theta,\phi)$, which correspond to the $s\,(l=0)$ and $p\,(l=1)$ states, where l is the angular momentum quantum number and m (with $-l \le m \le l$) is the magnetic quantum number:

$$
\begin{aligned}
|S\rangle &= Y_0^0(\theta,\phi) = \sqrt{\frac{1}{4\pi}}\,,\\
|X\rangle &= Y_{-1}^1(\theta,\phi) = \sqrt{\frac{3}{8\pi}}\sin(\theta)\exp(-i\phi)\,,\\
|Y\rangle &= Y_1^1(\theta,\phi) = -\sqrt{\frac{3}{8\pi}}\sin(\theta)\exp(i\phi)\,,\\
|Z\rangle &= Y_0^1(\theta,\phi) = \sqrt{\frac{3}{4\pi}}\cos(\theta)\,.
\end{aligned}
\tag{7.7}
$$

In III-nitrides the band gap energy E_{G} (in the $1-6$ eV energy range) is large compared to the energy spacing between the different valence bands (in the $5-20$ meV energy range). As a consequence the influence of the conduction bands on the valence ones can be neglected. The conduction band Hamiltonian can thus be treated separately. In the $\mathscr{B}_{\mathrm{c}}$ basis, it reads [162]:

$$
\hat{H}_{\mathrm{cb}} = \frac{\hbar^2}{2}\left(\frac{1}{m_{\mathrm{t}}}\nabla_{\mathrm{t}}^2 + \frac{1}{m_{\mathrm{z}}}\frac{\partial^2}{\partial z^2}\right) + \hat{V}_{\mathrm{e}} + P_{\mathrm{cb}}(\bar{\bar{\varepsilon}})\,,
\tag{7.8}
$$

where $\nabla_{\mathrm{t}}^2 = \frac{\partial^2}{\partial y^2} + \frac{\partial^2}{\partial y^2}$ is the transverse Laplacian operator, m_{t} is the transverse effective mass, m_{z} is the effective mass along the polar c-axis, $\hat{V}_{\mathrm{e}}$ is the potential energy of the unstrained conduction band edge and $P_{\mathrm{cb}}(\bar{\bar{\varepsilon}})$ is the hydrostatic energy shift, which depends on the strain tensor $\bar{\bar{\varepsilon}}$ *via*:

$$
P_{\mathrm{cb}}(\bar{\bar{\varepsilon}}) = a_{\mathrm{cz}}\varepsilon_{\mathrm{zz}} + a_{\mathrm{ct}}(\varepsilon_{\mathrm{xx}} + \varepsilon_{\mathrm{yy}})\,,
\tag{7.9}
$$

where a_{cz} and a_{tz} are the deformation potentials of the conduction band along z and transverse directions, respectively. Note that the eigenvalues of Hamiltonian 7.8 with opposite spins are degenerate as Hamiltonian 7.8 does not include spin interaction and have a parabolic dispersion.

The situation is more complicated for the valence bands as the spin-orbit Hamiltonian mixes the different states. From Kane's model [319], the 6×6 band-edge Hamiltonian matrix for strained wurtzite semiconductors can be derived in the $\mathscr{B}_{\mathrm{vb}}$ basis [167]:

$$\hat{H}_{\text{vb}} = \begin{pmatrix} F & -K^* & -H^* & 0 & 0 & 0 \\ -K & G & H & 0 & 0 & \Delta \\ -H & H^* & \lambda & 0 & \Delta & 0 \\ 0 & 0 & 0 & F & -K & H \\ 0 & 0 & \Delta & -K^* & G & -H^* \\ 0 & \Delta & 0 & H^* & -H & \lambda \end{pmatrix}, \tag{7.10}$$

where the stars correspond to the complex conjugate of the quantities H and K defined hereafter:

$$\begin{aligned}
F &= \Delta_{\text{cr}} + \frac{1}{3}\Delta_{\text{so}} + \lambda + \theta\,, \\
G &= \Delta_{\text{cr}} - \frac{1}{3}\Delta_{\text{so}} + \lambda + \theta\,, \\
\lambda &= \frac{\hbar^2}{2m_0}\left[A_1 k_{\text{z}}^2 + A_2(k_{\text{x}}^2 + k_{\text{y}}^2)\right] + D_1\varepsilon_{\text{zz}} + D_2(\varepsilon_{\text{xx}} + \varepsilon_{\text{yy}})\,, \\
\theta &= \frac{\hbar^2}{2m_0}\left[A_3 k_{\text{z}}^2 + A_4(k_{\text{x}}^2 + k_{\text{y}}^2)\right] + D_3\varepsilon_{\text{zz}} + D_4(\varepsilon_{\text{xx}} + \varepsilon_{\text{yy}})\,, \\
K &= \frac{\hbar^2}{2m_0}\left[A_5(k_{\text{x}} + i\,k_{\text{y}})^2\right] + D_5(\varepsilon_{\text{xx}} + 2i\,\varepsilon_{\text{xy}} - \varepsilon_{\text{yy}})\,, \\
H &= \frac{\hbar^2}{2m_0}\left[A_6 k_{\text{z}}(k_{\text{x}} + i\,k_{\text{y}})\right] + D_6(\varepsilon_{\text{zx}} + i\,\varepsilon_{\text{yz}})\,, \\
\Delta &= \frac{\sqrt{2}}{3}\Delta_{\text{so}}\,.
\end{aligned}$$

The A_{i} parameters are related to the material hole effective mass in the i direction,[81] D_{i} are the corresponding deformation potentials and Δ_{cr} and Δ_{so} are the crystal-field and spin-orbit split-off energies, respectively. The energy dispersion as well as the relative oscillator strength of each band directly follow from the diagonalization of Hamiltonian 7.10. For more information on band structure calculation in semiconductors, the reader can refer to Ref. [320].

[81] with the notation convention $xx \to 1$, $yy \to 2$, $zz \to 3$, $yz = zy \to 4$, $xz = zx \to 5$, and $xy = yx \to 6$.

C Optical simulation in homogeneous planar multilayer systems: the transfer matrix formalism

C.1 Isotropic structures: the 2×2 matrix formalism

In an isotropic planar microcavity, free charges and current densities can be neglected and the in-plane translation invariance leads to a separation between in-plane and vertical (along z) components of the electromagnetic field $\mathscr{E}(\mathbf{r}_\parallel, z)$. In this case Maxwell equations reduce to the wave equation [321]:

$$\nabla^2 \mathscr{E}\left(\mathbf{r}_\parallel, z\right) + \left(\frac{\omega}{c}\right)^2 \epsilon(\omega, z)\, \mathscr{E}\left(\mathbf{r}_\parallel, z\right) = 0\,, \tag{7.11}$$

where $\mathbf{r}_\parallel$ is the in-plane coordinate and $\epsilon(\omega, z)$ is a stepwise function describing the homogeneous dielectric response of the structure along the z-direction. Because of the in-plane invariance, the solution to equation 7.11 can be written in the form $\mathscr{E}\left(\mathbf{r}_\parallel, z\right) = \boldsymbol{\epsilon}_{\mathbf{k}_\parallel} U_{\mathbf{k}_\parallel}(z) \exp\left(i\mathbf{k}_\parallel \mathbf{r}_\parallel\right)$, where $\boldsymbol{\epsilon}_{\mathbf{k}_\parallel}$ is the polarization vector and $U_{\mathbf{k}_\parallel}(z)$ is the modal wave function, which is the sum of a left (+ sign) and a right (− sign) traveling wave, i.e. $U_{\mathbf{k}_\parallel}(z) = E_+\left(\mathbf{k}_\parallel\right) \exp(i k_z z) + E_-\left(\mathbf{k}_\parallel\right) \exp(-i k_z z)$ where $k_z = \sqrt{\left(\frac{\omega}{c}\right)^2 \epsilon(\omega) - k_\parallel^2}$ is the wave vector in the growth direction. Equation 7.11 finally reduces to a 1D-equation for $U_{\mathbf{k}_\parallel}(z)$:

$$\frac{d^2 U_{\mathbf{k}_\parallel}(z)}{dz^2} - \left[\left(\frac{\omega}{c}\right)^2 \epsilon(\omega, z) - k_\parallel^2\right] U_{\mathbf{k}_\parallel}(z) = 0\,. \tag{7.12}$$

The solutions to equation 7.12 describe a propagating wave in the z-direction for $\left(\frac{\omega}{c}\right)^2 \epsilon(\omega) > k_\parallel^2$ and an evanescent one otherwise. $E_+\left(\mathbf{k}_\parallel\right)$ and $E_-\left(\mathbf{k}_\parallel\right)$ are complex electric field amplitudes determined by the boundary conditions at each interface between two successive layers. Considering a stack of N layers with well defined thicknesses and complex dielectric constants (see Fig. 7.1(a)), the electric field components have to be determined at each interface. Labeling $E_{\pm,l}^{i-1,i}$ and $E_{\pm,r}^{\mathrm{i-1,i}}$ the left and right components of $E_\pm$ at the interface between layers $i-1$ and i (see Fig.7.1(b)), one can can define the interface transfer matrix $\tilde{I}_{i-1,i}$ as [322]:

$$\begin{pmatrix} E_{+,l}^{i-1,i} \\ E_{-,l}^{i-1,i} \end{pmatrix} = \underbrace{\frac{1}{t_{\mathrm{i-1,i}}} \begin{pmatrix} 1 & r_{i-1,i} \\ r_{i-1,i} & 1 \end{pmatrix}}_{\tilde{I}_{i-1,i}} \begin{pmatrix} E_{+,r}^{i-1,i} \\ E_{-,r}^{i-1,i} \end{pmatrix}. \tag{7.13}$$

The complex reflection and transmission coefficients r and t depend on the polarization of light (TE or s when the electric field is orthogonal and TM or p when it is parallel to the plane of incidence), the refractive index of the medium and the angle of incidence according to Fresnel relations:

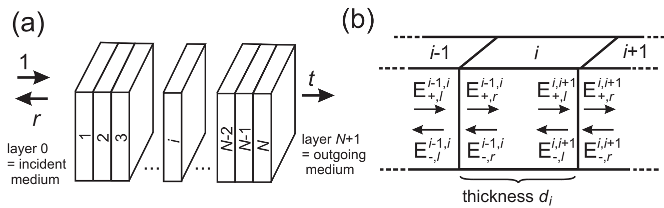

Fig. 7.1: (a) Schematic representation of a homogeneous thin-film multilayer structure. (b) Complex amplitudes of the electric field at each interface of the ith layer.

$$\begin{aligned} r^{\mathrm{TE}}_{\mathrm{i-1,i}} &= \frac{n_{\mathrm{i-1}}\cos(\theta_{\mathrm{i-1}}) - n_{\mathrm{i}}\cos(\theta_{\mathrm{i}})}{n_{\mathrm{i-1}}\cos(\theta_{\mathrm{i-1}}) + n_{\mathrm{i}}\cos(\theta_{\mathrm{i}})} \\ t^{\mathrm{TE}}_{\mathrm{i-1,i}} &= 1 + r^{\mathrm{TE}}_{\mathrm{i-1,i}} \\ r^{\mathrm{TM}}_{\mathrm{i-1,i}} &= \frac{n_{\mathrm{i}}\cos(\theta_{\mathrm{i-1}}) - n_{\mathrm{i-1}}\cos(\theta_{\mathrm{i}})}{n_{\mathrm{i}}\cos(\theta_{\mathrm{i-1}}) + n_{\mathrm{i-1}}\cos(\theta_{\mathrm{i}})} \\ t^{\mathrm{TM}}_{\mathrm{i-1,i}} &= \frac{n_{\mathrm{i-1}}}{n_{\mathrm{i}}}\left(1 + r^{\mathrm{TM}}_{\mathrm{i-1,i}}\right), \end{aligned} \tag{7.14}$$

where the indices $i-1$ and i refer to the incident and output media, respectively, and θ is the angle between the normal to the sample and the light wave vector. The reflection and transmission coefficients depend on the photon energy *via* the complex refractive index dispersion:

$$n(E) = n_{\mathrm{R}}(E) - i\, n_{\mathrm{I}}(E), \tag{7.15}$$

where $n_{\mathrm{R}}(E)$ is to the refractive index dispersion and $n_{\mathrm{I}}(E)$ the extinction coefficient. Between two successive interfaces, the phase of the electric field is increased by $\phi_{\mathrm{i}} = 2\pi d_{\mathrm{i}} n_{\mathrm{i}} \cos(\theta_{\mathrm{i}})/\lambda$. This allows defining the propagation transfer matrix $\tilde{L}_{\mathrm{i}}$ for a homogeneous layer i [322]:

$$\begin{pmatrix} E^{i-1,i}_{+,r} \\ E^{i-1,i}_{-,r} \end{pmatrix} = \underbrace{\begin{pmatrix} \exp(i\,\phi_{\mathrm{i}}) & 0 \\ 0 & \exp(-i\,\phi_{\mathrm{i}}) \end{pmatrix}}_{\tilde{L}_i} \begin{pmatrix} E^{i,i+1}_{+,l} \\ E^{i,i+1}_{-,l} \end{pmatrix}, \tag{7.16}$$

The relationship between incident, reflected (r) and transmitted (t) complex amplitudes of the electric field can now be determined for the full structure. Assuming an incident plane wave with normalized amplitude $E^{0,1}_{+,l} = 1$, the reflected and transmitted components are $E^{0,1}_{-,l} = r$ and $E^{N,N+1}_{+,r} = t$, where the indices 0 and $N+1$ correspond to the incident and exit media, respectively. The matrix of the full structure $\tilde{M}$ is obtained by propagating the external field from one layer to another according to [322]:

$$\begin{pmatrix} 1 \\ r \end{pmatrix} = \tilde{I}_{0,1}\tilde{L}_1\tilde{I}_{1,2}\tilde{L}_2 \ldots \tilde{I}_{\mathrm{N-1,N}}\tilde{L}_{\mathrm{N}}\tilde{I}_{\mathrm{N,N+1}} \begin{pmatrix} t \\ 0 \end{pmatrix} = \underbrace{\prod_{i=0}^{N} \tilde{I}_{\mathrm{i,i+1}}\tilde{L}_{\mathrm{i+1}}}_{\tilde{M}} \begin{pmatrix} t \\ 0 \end{pmatrix}, \tag{7.17}$$

For a given polarization direction $i \in \{\mathrm{s=TE}, \mathrm{p=TM}\}$ the complex reflectivity $r(E)$ and transmission $t(E)$ coefficients are obtained according to:

$$\begin{aligned} r(E) &= \frac{\tilde{M}_{2,1}}{\tilde{M}_{1,1}}, \\ t(E) &= \frac{1}{\tilde{M}_{1,1}}, \end{aligned} \tag{7.18}$$

where $\tilde{M}_{\mathrm{i,j}}$ correspond to the components of the $\tilde{M}$ matrix. The reflectance (R), transmittance (T) and absorptance (A) are finally obtained *via* [323]:

$$R(E) = |r(E)|^2, \tag{7.19}$$

$$T(E) = \frac{n_{\mathrm{t}}\cos(\theta_{\mathrm{t}})}{n_{\mathrm{in}}\cos(\theta_{\mathrm{in}})}\,|t(E)|^2, \tag{7.20}$$

$$A(E) = 1 - R(E) - A(E), \tag{7.21}$$

where the indices in and t refer the incident and output medium, respectively.

C.2 Anisotropic structures: the 4×4 matrix formalism

The case of anisotropic structures differs from the isotropic one since the optical response is affected by the sample orientation. In particular, the refractive index depends on the light polarization can be represented on an ellipsoid (see Fig. 7.2). Anisotropic media can be classified into two types: (i) uniaxial ones where the directions orthogonal to the optical z-axis have the same refractive index constants[82] ($n_x = n_y \neq n_z$) and (ii) biaxial ones where all crystal directions have different optical properties ($n_x \neq n_y \neq n_z$). As a consequence, the 2×2 matrix formalism no longer applies and 4×4 matrices must be used instead.

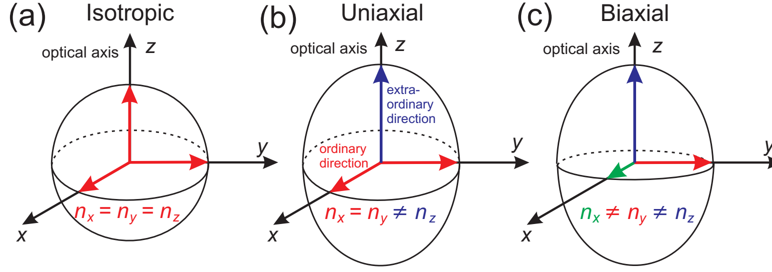

Fig. 7.2: Schematic representation of the refractive index ellipsoid of (a) an isotropic material ($n_x = n_y = n_z$), (b) an uniaxial material ($n_x = n_y \neq n_z$) and (c) a biaxial material ($n_x \neq n_y \neq n_z$).

Writing Maxwell's equation in a matrix form for the electric and magnetic fields $\mathscr{E} = (E_x, E_y, E_z)^T$ and $\mathscr{H} = (H_x, H_y, H_z)^T$,[83] Berreman derived in its seminal paper [324] the differential equation for the four-dimensional field vector $\mathbf{\Psi}(z) = \left(E_x, E_y, H_x, H_y\right)^T(z)$:

$$\frac{\partial \mathbf{\Psi}}{\partial z} = \frac{i\omega}{c}\tilde{\Delta}(z)\mathbf{\Psi}\,, \tag{7.22}$$

where ω is the wave frequency and $\tilde{\Delta}(z)$ is a matrix depending on the anisotropic dielectric tensor components for the homogeneous layers grown along the z-axis.[84] If $\mathbf{\Psi}$ is know for a given position z, then the solution to Equation 7.22 at position $z+h$ is given by:

$$\mathbf{\Psi}(z+h) = \exp\left(\frac{i\omega\tilde{\Delta}d}{c}\right)\mathbf{\Psi}(z)\,. \tag{7.23}$$

In 1996, Schubert established that a general solution of Equation 7.22 can be found for the vector $\mathbf{\Psi}(z) = \left(E_+^s, E_-^s, E_+^p, E_-^p\right)^T(z)$, where the $\pm$ sign stands for right/left traveling waves as in the 2×2 transfer matrix formalism and the $s(p)$ corresponds to TE (resp. TM) polarization of the electric field. He introduced three transfer matrices describing the optical response of the incident medium[85] $\tilde{L}_i^{-1}$, the exit medium $\tilde{L}_t$ and one for each individual layer $\tilde{T}_p$. Assuming that the incident medium is isotropic (usually air), $\tilde{L}_i^{-1}$ is given by:

[82] Note that x and y are usually referred to as the ordinary direction, i.e., $n_x = n_y = n_o$, and z as to the extraordinary one ($n_z = n_e$).

[83] The notation $\mathbf{v}^T$ corresponds to the transpose of vector $\mathbf{v}$.

[84] The expression of $\tilde{\Delta}(z)$ can be found in Ref. [323].

[85] Note that the inverse of the incident matrix $\tilde{L}_i$ is required to calculate the value of $\mathbf{\Psi}$ at $z=0$.

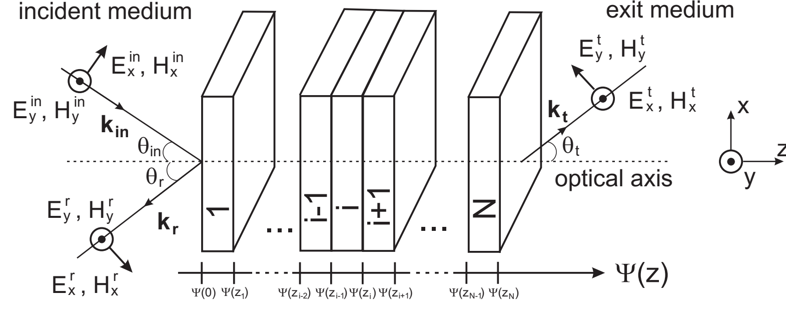

Fig. 7.3: Schematic representation of a homogeneous thin-film anisotropic multilayer structure. The x and y-components of the electric and magnetic field are shown for the incident, reflected and transmitted beam in an oblique configuration.

$$\tilde{L}_{\mathrm{i}}^{-1} = \frac{1}{2}\begin{pmatrix} 0 & 1 & -\frac{1}{n_{\mathrm{in}}\cos(\theta_{\mathrm{in}})} & 0 \\ 0 & 1 & \frac{1}{n_{\mathrm{in}}\cos(\theta_{\mathrm{in}})} & 0 \\ \frac{1}{\cos(\theta_{\mathrm{in}})} & 0 & 0 & \frac{1}{n_{\mathrm{in}}} \\ -\frac{1}{\cos(\theta_{\mathrm{in}})} & 0 & 0 & \frac{1}{n_{\mathrm{in}}} \end{pmatrix}. \tag{7.24}$$

The transfer matrix on the output medium side $\tilde{L}_{\mathrm{t}}$ is given by [325]:

$$\tilde{L}_{\mathrm{t}} = \begin{pmatrix} 0 & 1 & \cos(\theta_{\mathrm{z,t}}) & -\cos(\theta_{\mathrm{z,t}}) \\ 1 & 1 & 0 & 0 \\ -n_{\mathrm{y,t}}\cos(\theta_{\mathrm{t}}) & n_{\mathrm{y,t}}\cos(\theta_{\mathrm{t}}) & 0 & 0 \\ 0 & 0 & n_{\mathrm{x,t}} & n_{\mathrm{x,t}} \end{pmatrix}. \tag{7.25}$$

where $n_{\mathrm{m,t}}$, is the refractive index of the exit medium along the m-direction with $m \in \{x, y, z\}$ and $\cos(\theta_{\mathrm{m,t}}) = \sqrt{1-(n_{\mathrm{in}}/n_{\mathrm{m,t}})^2\sin^2(\theta_{\mathrm{in}})}$. Finally, the partial transfer matrix of the ith layer with thickness d_{i} is given by the expression:

$$\tilde{T}_{\mathrm{p}}^{\mathrm{i}}(-d_{\mathrm{i}}) = \exp\left(-\frac{i\omega\tilde{\Delta}d_{\mathrm{i}}}{c}\right). \tag{7.26}$$

Despite the difficulty of expressing Equation 7.26 in a simple matrix form, Wöhler and coworkers have shown in 1988 a fast way to calculate it by applying the theorem of Cayley-Hamilton [326]. They have shown that $\tilde{T}_{\mathrm{p}}^{\mathrm{i}}(d_{\mathrm{i}})$ can be developped with a finite series expansion up to third power:

$$\tilde{T}_{\mathrm{p}}^{\mathrm{i}}(-d_{\mathrm{i}}) = \beta_0\tilde{I}_4 + \beta_1\tilde{\Delta} + \beta_2\tilde{\Delta}^2 + \beta_3\tilde{\Delta}^3\,, \tag{7.27}$$

where $\tilde{I}_4$ is the 4×4 identity matrix. The β constants are given by [323]:

$$
\begin{aligned}
\beta_0 &= \sum_{j=1}^{4} q_k q_l q_m \frac{\exp\left(-i\omega q_j d_i/c\right)}{(q_j - q_k)(q_j - q_l)(q_j - q_m)}, \\
\beta_1 &= \sum_{j=1}^{4} (q_k q_l + q_k q_m + q_l q_m) \frac{\exp\left(-i\omega q_j d_i/c\right)}{(q_j - q_k)(q_j - q_l)(q_j - q_m)}, \\
\beta_2 &= \sum_{j=1}^{4} (q_k + q_l + q_m) \frac{\exp\left(-i\omega q_j d_i/c\right)}{(q_j - q_k)(q_j - q_l)(q_j - q_m)}, \\
\beta_3 &= \sum_{j=1}^{4} \frac{\exp\left(-i\omega q_j d_i/c\right)}{(q_j - q_k)(q_j - q_l)(q_j - q_m)},
\end{aligned}
\tag{7.28}
$$

where $q_{1,2,3,4}$ are the eigenvalues of $\tilde{\Delta}$ and $(k,l,m) = (2,3,4)$ for $j = 1$, $(1,3,4)$ for $j = 2$, $(1,2,4)$ for $j = 3$ and $(1,2,3)$ for $j = 4$. Finally, the transfer matrix of the full structure $\tilde{M}$ is obtained by:

$$
\tilde{M} = \tilde{L}_i^{-1} \prod_{i=1}^{N} \tilde{T}_p^i(-d_i) \tilde{L}_t. \tag{7.29}
$$

For a given polarization direction of excitation i and detection $j \in \{s,p\}$, the complex reflectivity and transmission coefficients $r_{ij}(E)$ and $t_{ij}(E)$, respectively, are obtained according to [327]:

$$
\begin{aligned}
r_{ss}(E) &= \frac{\tilde{M}_{2,1}\tilde{M}_{3,3} - \tilde{M}_{2,3}\tilde{M}_{3,1}}{\tilde{M}_{1,1}\tilde{M}_{3,3} - \tilde{M}_{1,3}\tilde{M}_{3,1}} \\
r_{sp}(E) &= \frac{\tilde{M}_{4,1}\tilde{M}_{3,3} - \tilde{M}_{4,3}\tilde{M}_{3,1}}{\tilde{M}_{1,1}\tilde{M}_{3,3} - \tilde{M}_{1,3}\tilde{M}_{3,1}} \\
r_{ps}(E) &= \frac{\tilde{M}_{1,1}\tilde{M}_{2,3} - \tilde{M}_{2,1}\tilde{M}_{1,3}}{\tilde{M}_{1,1}\tilde{M}_{3,3} - \tilde{M}_{1,3}\tilde{M}_{3,1}} \\
r_{pp}(E) &= \frac{\tilde{M}_{1,1}\tilde{M}_{4,3} - \tilde{M}_{4,1}\tilde{M}_{1,3}}{\tilde{M}_{1,1}\tilde{M}_{3,3} - \tilde{M}_{1,3}\tilde{M}_{3,1}} \\
t_{ss}(E) &= \frac{\tilde{M}_{3,3}}{\tilde{M}_{1,1}\tilde{M}_{3,3} - \tilde{M}_{1,3}\tilde{M}_{3,1}} \\
t_{sp}(E) &= \frac{-\tilde{M}_{3,1}}{\tilde{M}_{1,1}\tilde{M}_{3,3} - \tilde{M}_{1,3}\tilde{M}_{3,1}} \\
t_{ps}(E) &= \frac{-\tilde{M}_{1,3}}{\tilde{M}_{1,1}\tilde{M}_{3,3} - \tilde{M}_{1,3}\tilde{M}_{3,1}} \\
t_{pp}(E) &= \frac{\tilde{M}_{1,1}}{\tilde{M}_{1,1}\tilde{M}_{3,3} - \tilde{M}_{1,3}\tilde{M}_{3,1}}
\end{aligned}
\tag{7.30}
$$

The reflectance, transmittance , and absorptance are obtained using relations 7.19-7.21. Note that these relations now depend on the light polarization according to:

$$
\begin{aligned}
R_s(E) &= R_{ps}(E) + R_{ss}(E), \\
R_p(E) &= R_{sp}(E) + R_{pp}(E).
\end{aligned}
\tag{7.31}
$$

The same relations hold for $T_{s,p}$ and $A_{s,p}$. For more information on light propagation in anisotropic media, the reader should refer to Refs. [323] and [325].

JACQUES LEVRAT – Physicist engineer

Personal information

Born in Billens (FR) on
November 1st 1983
Citizenship: Swiss
Single

Contact information

E-mail j.levrat@gmail.com
Work: +41 (0) 21 693 54 29
Mobile: +41 (0) 79 224 03 67
Home: +41 (0) 21 634 31 00

Private address

Av. Du Tir Fédéral 40
CH-1024 Ecublens (VD)
SWITZERLAND

Current work address

Institute of Condensed Matter Physics
Station 6
CH-1015 Lausanne, SWITZERLAND

WORK EXPERIENCE & RESEARCH ACTIVITY

April 2008 – present (PhD thesis)

École Polytechnique Fédérale de Lausanne (EPFL), Switzerland
Laboratory of Advanced Semiconductors for Photonics and Electronics (LASPE)

- ✓ *Experimental research in the field of GaN-based semiconductor microcavities by means of UV-optical spectroscopy techniques*
- ✓ *Supervision of two master students and three semester students*
- ✓ *Webmaster of the laboratory website*
- ✓ *Expert for the non-linear optics Master lectures (2008)*

August 2007 – March 2008 (Master work, final grade 6/6)

École Polytechnique Fédérale de Lausanne (EPFL), Switzerland
Laboratory of Optics and Quantum Electronics (LOEQ)

- ✓ *Experimental research in the field of non-polar GaN-based quantum wells by means of time-resolved photoluminescence*

September 2006 – July 2007 (Bachelor work)

École Polytechnique Fédérale de Lausanne (EPFL), Switzerland
Laboratory of Optics and Quantum Electronics (LOEQ)

- ✓ *Experimental research in the field of CdTe-based semiconductor microcavities by means of time-resolved Fourier spectroscopy*

July 2007 – October 2007 (Internship)

Fribourg, Switzerland
Vibro-Meter SA, MEGGITT

- ✓ *Development of high temperature capacitance sensors (tip timing, tip clearance for airplane turbines)*

October 2005 – July 2007 (Student association)

Conference organizer for the department of the physicist student association at EPFL.

TEACHING ACTIVITIES

October 2007 – July 2007

Personal assistant to Prof. D. Pavuna (EPFL): active contribution to the teaching (*ex cathedra*) and preparation of the visual support for the lessons

April 2007 – July 2007

Assistant to Prof. A. Pasquarello (EPFL): student support

April 2008 – December 2011

Assistant to Prof. Nicolas Grandjean (EPFL): student support
Chief-assistant from September 2009 to June 2010

EDUCATION

September 2007 – December 2008

Master in Physics – École Polytechnique Fédérale de Lausanne (EPFL), Switzerland (grade: 5.76/6)

September 2003 – June 2007

Bachelor in Physics – École Polytechnique Fédérale de Lausanne (EPFL), Switzerland (grade: 5.32/6)

October 1999 – July 2003

Cantonal baccalaureate – Collège du Sud, Bulle (FR) – Economic type (grade: 5.45/6)

SKILLS

IT skills

- ✓ Scientific programming: C++, Matlab, Mathematica
- ✓ Web programming: PHP, MySQL, HTML
- ✓ Data acquisition/treatment: Labview, Origin
- ✓ Others: Office, LaTeX, Corel, Inkscape

Scientific background and laboratory techniques

- ✓ Advanced formation in optics and semiconductor physics
- ✓ Optical spectroscopy (photoluminescence, reflectivity, transmission, Fourier imaging, time-resolved)
- ✓ Optical setup design
- ✓ Vacuum and cryogenics

Others

- ✓ Scientific writing and oral presentations
- ✓ Student supervision – team management (passed *Venture Challenge*, formation for young entrepreneurs)

PRIZES/DINSTINCTIONS/AWARDS

Scientific awards

- ✓ 2012: Winner of the Chorafas Award *(innovative and high level research)* in the field of advanced data processing technology, life sciences *for the PhD work entitled "Physics of polariton condensates in GaN-based planar microcavities"*
- ✓ 2012: Best poster award: "*Coexistence of exciton and polariton-lasing in a non-polar GaN-based microcavity",* International School of Nanophotonics and Photovoltaics, Phuket, Thailand, March 30 - April 6 (1st prize, 2nd author)
- ✓ 2011: Best student paper award: "*Coexistence of excitonic and polariton-lasing in a m-plane GaN/AlGaN-based microcavity*" at the 38th International Symposium on Compound Semiconductors, Berlin, Germany, May 22-26 (2nd author)
- ✓ 2009: Best poster award: "*Polariton condensation from cryogenic to room temperature*", International Nano-Optoelectronic Workshop 2009, Stockholm and Berlin, Sweden and Germany, August 2-15 (2nd prize, 1st author)

Others

- ✓ 2007: Best SHS (Social and Human Sciences) work in Epistemology – *La problématique de la mesure en physique quantique* (Lausanne, EPFL)
- ✓ 2003: Best baccalaureate work (100 points/100)
- ✓ 1999: First prize of Latin version, cantonal competition (FR)

LANGUAGES

French	Mother tongue
English	Fluent
German	Very good knowledge

PUBLICATIONS

Publications published in international peer-reviewed journals (current h-factor: 5)
(Number of citations highlighted in dark blue (May 2012) for each refereed paper.)

[1] *Impact of quantum confinement and quantum confined Stark effect on biexciton binding energy in GaN/AlGaN quantum wells*

F. Stokker Cheregi, A. Vinattieri, E. Feltin, D. Simeonov, **J. Levrat**, J.-F. Carlin, R. Butté, N. Grandjean, and M. Gurioli, Appl. Phys. Lett. **93**, 152105 (2008). Times cited: 4

[2] *Room temperature polariton lasing in III-nitride microcavities, a comparison with blue GaN-based vertical cavity surface emitting lasers*

R. Butté, G. Christmann, E. Feltin, A. Castiglia, **J. Levrat**, G. Cosendey, A. Altoukhov, J.-F. Carlin, and N. Grandjean, OPTO2009 – SPIE Photonics West, **invited paper**, Proc. SPIE **7216**, 721619 (2009). Times cited: 6

[3] *Tailoring the strong coupling regime in III-nitride based microcavities for room temperature polariton laser applications*

J. Levrat, R. Butté, G. Christmann, E. Feltin, J.-F. Carlin, and N. Grandjean, **Invited paper**, Proceedings of the 15th Semiconducting and Insulating Materials Conference, Phys. Stat. Sol. (c) **6**, 2820 (2009). Times cited: 2

[4] *Exciton localization on basal stacking faults in a-plane epitaxial lateral overgrown GaN grown by hybride vapor phase epitaxy*

P. Corfdir, P. Lefebvre, **J. Levrat**, A. Dussaigne, J.-D. Ganière, D. Martin, J. Ristic, T. Zhu, N. Grandjean and B. Deveaud-Plédran, J. Appl. Phys. **105**, 043102 (2009). Times cited: 17

[5] *High reflectivity airgap distributed Bragg reflectors realized by wet etching of AlInN sacrificial layers*

A. Altoukhov, **J. Levrat**, E. Feltin, J.-F. Carlin, A. Castiglia, R. Butté, and N. Grandjean, Appl. Phys. Lett. **95**, 191102 (2009). Times cited: 2, **n° 19 in the Top 20 Most Downloaded Articles from Applied Physics Letters – November 2009.**

[6] *Phase diagram of a polariton laser from cryogenic to room temperature*

R. Butté, **J. Levrat**, G. Christmann, E. Feltin, J.-F. Carlin, and N. Grandjean, Phys. Rev. B **80**, 233301 (2009). Times cited: 9

[7] *Condensation phase diagram of cavity polaritons in GaN-based microcavities: experiment and theory*

J. Levrat, R. Butté, E. Feltin, J.-F. Carlin, N. Grandjean, D. Solnyshkov, and G. Malpuech, Phys. Rev. B **81**, 125305 (2010). Times cited: 23

[8] *Pinning and depinning of the polarization of exciton-polariton condensates at room temperature*

J. Levrat, R. Butté, T. Christian, M. Glauser, E. Feltin, J.-F. Carlin, N. Grandjean, D. Read, A.V. Kavokin, and Y.G. Rubo, Phys. Rev. Lett. **104**, 166402 (2010). Times cited: 7

[9] *One dimensional exciton luminescence induced by extended defects in nonpolar GaN/(Al,Ga)N quantum wells*

A. Dussaigne, P. Corfdir, **J. Levrat**, T. Zhu, D. Martin, P. Lefebvre, J.-D. Ganière, R. Butté, B. Deveaud-Plédran, N. Grandjean, Y. Arroyo, and P. Stadelmann, Semicond. Sci. Technol. **26**, 025012 (2011). Times cited: 3

[10] *Intrinsic dynamics of weakly and strongly confined excitons in nonpolar nitride-based heterostructures*

P. Corfdir, **J. Levrat**, A. Dussaigne, P. Lefebvre, H. Teisseyre, I. Grzegory, T. Suski, J.-D. Ganière, N. Grandjean and B. Deveaud-Plédran, Phys. Rev. B **83**, 245326 (2011). Times cited: 2

[11] *Tailoring the light-matter coupling in anisotropic microcavities: redistribution of oscillator strength in strained m-plane GaN/AlGaN quantum wells*

G. Rossbach, **J. Levrat**, A. Dussaigne, M. Glauser, M. Cobet, R. Butté, N. Grandjean, H. Teisseyre, M. Bockowski, I. Grzegory, and T. Suski, Phys. Rev. B **84**, 115315 (2011). Times cited: 1

[12] *Polariton lasing in a hybrid ZnO bulk microcavity*

T. Guillet, M. Mexis, **J. Levrat**, G. Rossbach, C. Brimont, T. Bretagnon, B. Gil, R. Butté, N. Grandjean, L. Orosz, F. Réveret, J. Leymarie, J. Zúñiga-Pérez, M. Leroux, F. Semond, and S. Bouchoule, Appl. Phys. Lett. **99**, 161104 (2011). Times cited: 4

[13] *Erratum: Condensation phase diagram of cavity polaritons in GaN-based microcavities: experiment and theory [Phys. Rev. B 81, 125305 (2010)]*

J. Levrat, R. Butté, E. Feltin, J.-F. Carlin, N. Grandjean, D. Solnyshkov, and G. Malpuech, Phys. Rev. B **84**, 199908(E) (2011). Times cited: 0

[14] *High quality factor two dimensional GaN photonic crystal cavity membranes grown on silicon substrate*

N. Vico Triviño, G. Rossbach, U. P. Dharanipathy, **J. Levrat**, A. Castiglia, J.-F. Carlin, K. A. Atlasov, R. Butté, R. Houdré, and N. Grandjean, Appl. Phys. Lett. **100**, 071103 (2012). Times cited: 2

[15] *Investigation of InGaN/GaN quantum wells for polariton laser diodes*

M. Glauser, G. Rossbach, G. Cosendey, J. Levrat, M. Cobet, J.-F. Carlin, J. Besbas, M. Gallart, P. Gilliot, R. Butté and N. Grandjean. Proceedings of 11th International Conference on Physics of Light-Matter Coupling in Nanostructures (PLMCN-11), Phys. Stat. Sol. (c) **9**, 1325 (2009). Times cited: 0

[16] *Impact of biexcitons on the relaxation mechanisms of polaritons in III-nitride based multi-quantum well microcavities*

P. Corfdir, **J. Levrat**, G. Rossbach, R. Butté, E. Feltin, J.-F. Carlin, G. Christmann, P. Lefebvre, J.-D. Ganière, N. Grandjean, and B. Deveaud-Plédran, Phys. Rev. B. **85**, 245308 (2012). Times cited: 0

[17] *On the nature of the non-linear emission properties of an optically anisotropic GaN-based microcavity*

J. Levrat, G. Rossbach, A. Dussaigne, G. Cosendey, M. Glauser, M. Cobet, R. Butté, N. Grandjean, H. Teisseyre, M. Bockowski, I. Grzegory, and T. Suski, submitted to Phys. Rev. B.

[18] *Generic picture of the emission properties of III-nitride polariton laser diodes: steady-state and current modulation response*

I. Iorsh, M. Glauser, G. Rossbach, J. Levrat, M. Cobet, R. Butté, N. Grandjean, M. A. Kaliteevski, R. A. Abram and A. V. Kavokin, submitted to Phys. Rev. B.

Book chapter

Toward quantum fluids at room temperature: polariton condensation in III-nitride based microcavities

Jacques Levrat, Georg Rossbach, Raphaël Butté, and Nicolas Grandjean

Chapter of *"Quantum fluids: hot topics and new trends"*, edited by Alberto Bramati and Michele Modugno, Springer Verlag, Berlin, 2012 (in press).

Publication published following colloquia without peer-reviewing

Giant Rabi splitting in semiconductor microcavities: towards polariton condensates at room temperature
J. Levrat, G. Christmann, R. Butté, E. Feltin, J.-F. Carlin, and N. Grandjean, Proceedings of the Enrico Fermi Summerschool on Coherence in Solid State, Varenna, Italy, July 2008.

ORAL PRESENTATIONS

Presentations in International Conferences

[1] *Condensation of cavity-polaritons in GaN-based semiconductor microcavities*

Jacques Levrat, Raphaël Butté, Gabriel Christmann, Eric Feltin, Jean-François Carlin, and Nicolas Grandjean.¨

15th Semiconducting and Insulating Materials Conference, Vilnius, Lithuania, June 15-19 2009. **Invited talk**.

[2] *Polarization behavior above the polariton condensation threshold in a GaN-based multiple quantum well microcavity*

J. Levrat, T. Christian, R. Butté, E. Feltin, J.-F. Carlin, and N. Grandjean.

Eleventh International Conference on Optics of Excitons in Confined Systems, Madrid, Spain, September 7-11 2009.

[3] *Pinning and depinning of the polarization of exciton-polariton condensates at room temperature*

J. Levrat, R. Butté, T. Christian, M. Glauser, E. Feltin, J.-F. Carlin, N. Grandjean, D. Read, A.V. Kavokin, and Y.G. Rubo.

Tenth International Conference on the Physics of Light-Matter Coupling in Nanostructures, Cuernavaca, Mexico, April 12-16 2010

[4] *Room temperature polariton lasing in III-nitride microcavities*

J. Levrat, R. Butté, G. Rossbach, M. Glauser, M. Cobet, T. Christian, E. Feltin, J.-F. Carlin, N. Grandjean, D. Read, A.V. Kavokin, Y.G. Rubo, D. Solnyshkov, and G. Malpuech.

NCCR – Quantum Photonics General Assembly, Muenchenwiler, Switzerland, July 7-8 2010.

[5] *Coexistence of excitonic and polariton-lasing in a non-polar GaN-based microcavity*

J. Levrat, G. Rossbach, A. Dussaigne, H. Teisseyre, M. Bockowski, M. Glauser, M. Cobet, I. Grzegory, T. Suski, R. Butté, and N. Grandjean.

11th International Conference on Physics of Light-Matter Coupling in Nanostructures (PLMCN-11), Berlin, Germany, April 4-8 2011.

[6] *Coexistence of excitonic and polariton-lasing in an m-plane GaN/AlGaN-based microcavity*

J. Levrat, G. Rossbach, A. Dussaigne, H. Teisseyre, G. Cosendey, M. Glauser, M. Cobet, M. Bockowski, I. Grzegory, T. Suski, R. Butté, and N. Grandjean.

9th International Conference on Nitride Semiconductors, Glasgow, UK, July 10-15 2011.

[7] *Impact of cavity biexcitons on the formation of polariton condensates in III-nitride based multiple quantum well microcavities*

J. Levrat, G. Rossbach, P. Corfdir, E. Feltin, J.-F. Carlin, J.-D. Ganière, R. Butté, B. Deveaud-Plédran and N. Grandjean

31th International Conference on the Physics of semiconductors, Switzerland, July 30-August 3 2012.

Seminars

[1] École Polytechnique Fédérale de Lausanne, Lausanne, Switzerland. "Condensation of exciton-polaritons in multiple quantum well GaN-based microcavities: *Phase diagram & Polarization behaviour above threshold*", 9th June 2009.

[2] École Polytechnique Fédérale de Lausanne, Lausanne, Switzerland. "Anisotropic III-nitride microcavities: *Coexistence of excitonic and polaritonic lasing*", 26th April 2011.

[3] Frauenhofer Institute, Freiburg in Breisgau, Germany. "Polariton condensation in GaN-based microcavities", 4th August 2011.

POSTER PRESENTATIONS

[1] *Nonlinear effects in III-nitride microcavities: evidence for polariton condensation at room temperature*

J. Levrat, G. Christmann, R. Butté, E. Feltin, A. Mouti, P.A. Stadelmann, A. Castiglia, J.-F. Carlin, and N. Grandjean.

Enrico Fermi Summerschool on Coherence in Solid State, Varenna, Italy, July 1-11 2008.

[2] *Impact of quantum confinement and quantum confined Stark effect on biexciton binding energy in GaN/AlGaN quantum wells*

F. Stokker-Cheregi, A. Vinattieri, **J. Levrat**, E. Feltin, D. Simeonov, J.-F. Carlin, R. Butté, N. Grandjean, and M. Gurioli.

International Workshop on Nitride Semiconductors 2008, Montreux, Switzerland, October 6-10 2008.

[3] *Polariton lasing in a GaN multiple quantum well microcavity at room temperature*

J. Levrat, G. Christmann, R. Butté, E. Feltin, J.-F. Carlin, and N. Grandjean.

Photonics Day, Lausanne, Switzerland, October 17 2008.

[4] *Polariton condensation from cryogenic to room temperature*

J. Levrat, R. Butté, G. Christmann, E. Feltin, J.-F. Carlin, D. Solnyshkov, G. Malpuech and N. Grandjean.

International Nano-Optoelectronic Workshop 2009, Stockholm and Berlin, Sweden and Germany, August 2-15 2009. **2nd Prize for the "Best Poster Award".**

[5] *Phase diagram of exciton-polaritons in multiple quantum well GaN-based microcavities*

J. Levrat, R. Butté, G. Christmann, E. Feltin, J.-F. Carlin, D. Solnyshkov, G. Malpuech, and N. Grandjean.

Eleventh International Conference on Optics of Excitons in Confined Systems, Madrid, Spain, September 7-11 2009.

[6] *Condensation of exciton-polaritons in multiple quantum well GaN-based microcavities*

J. Levrat, R. Butté, G. Christmann, E. Feltin, J.-F. Carlin, D. Solnyshkov, G. Malpuech, and N. Grandjean.

Eighth International Conference on Nitride Semiconductors, ICC Jeju, Korea, October 18-23 2009.

[7] *Condensation of exciton-polaritons in multiple quantum well GaN-based microcavities*

J. Levrat, R. Butté, G. Christmann, E. Feltin, J.-F. Carlin, D. Solnyshkov, G. Malpuech, and N. Grandjean.

Photonics Day 2009, EPFL, Switzerland, 6 November 2009.

[8] *Biexcitonic effects in a multiple quantum well GaN-based microcavity*

J. Levrat, G. Rossbach, M. Glauser, E. Feltin, J.-F. Carlin, R. Butté and N. Grandjean.

Photonics Day 2010, EPFL, Switzerland, 17 September 2010.

[9] *Biexciton-assisted relaxation mechanisms in III-nitride based microcavities*

J. Levrat, P. Corfdir, G. Rossbach, R. Butté, E. Feltin, J.-F. Carlin, J.-D. Ganière, B. Deveaud-Plédran and N. Grandjean.

11th International Conference on Physics of Light-Matter Coupling in Nanostructures (PLMCN-11), Berlin, Germany, April 4-8 2011.

[10] *Biexciton-assisted relaxation mechanisms in III-nitride based microcavities*

J. Levrat, P. Corfdir, G. Rossbach, R. Butté, E. Feltin, J.-F. Carlin, J.-D. Ganière, B. Deveaud-Plédran and N. Grandjean.

38th International Symposium on Compound Semiconductors (ISCS), Berlin, Germany, May 22-26, 2011

[11] Anisotropy and valence-band reordering in compressively strained GaN/AlGaN multiple quantum wells: prospects for non-polar III-nitride microcavities

J. Levrat, G. Rossbach, A. Dussaigne, M. Glauser, M. Cobet, R. Butté and N. Grandjean.

38th International Symposium on Compound Semiconductors (ISCS), Berlin, Germany, May 22-26, 2011

SCIENTIFIC COLLABORATIONS

Prof. J.J. Baumberg (Univ. Cambridge, UK), Prof. M. Gurioli, (LENS-Florence, Italy), Prof. A.V. Kavokin (Univ. Southampton, UK), Dr. G. Malpuech (LASMEA-CNRS, Univ. Blaise Pascal, Aubière – Clermont-Ferrand, France), Prof. T. Suski (Institute of High Pressure Physics “Unipress”, Polish Academy of Sciences, Warsaw, Poland), Prof. Y. G. Rubo (Centro de Investigacion en Energia, Universidad Nacional Autonoma de Mexico, Temixco, Morelos, Mexico), Dr. T. Guillet (Groupe d’Etude des Semiconducteurs, Université de Montpellier II, France)

REFERENCES

Prof. Nicolas Grandjean
Director, Institute of Condensed Matter Physics
EPFL, Switzerland
nicolas.grandjean@epfl.ch
+41 21 693 34 44

Prof. Benoit Deveaud-Plédran
Dean of Research
EPFL, Switzerland
benoit.deveaud-pledran@epfl.ch
+41 21 693 54 96

Dr. Raphaël Butté
Institute of Condensed Matter Physics
EPFL, Switzerland
raphael.butte@epfl.ch
+41 21 693 33 57